THE IMPACT OF OPEN SCIENCE FOR EVALUATION OF VOLCANIC HAZARDS

EDITED BY: Elisa Trasatti, Fidel Costa and Michelle Parks
PUBLISHED IN: Frontiers in Earth Science

frontiers Research Topics

ISSN 1664-8714
ISBN 978-2-88966-757-4
DOI 10.3389/978-2-88966-757-4

About Frontiers

Frontiers is more than just an open-access publisher of scholarly articles: it is a pioneering approach to the world of academia, radically improving the way scholarly research is managed. The grand vision of Frontiers is a world where all people have an equal opportunity to seek, share and generate knowledge. Frontiers provides immediate and permanent online open access to all its publications, but this alone is not enough to realize our grand goals.

Frontiers Journal Series

The Frontiers Journal Series is a multi-tier and interdisciplinary set of open-access, online journals, promising a paradigm shift from the current review, selection and dissemination processes in academic publishing. All Frontiers journals are driven by researchers for researchers; therefore, they constitute a service to the scholarly community. At the same time, the Frontiers Journal Series operates on a revolutionary invention, the tiered publishing system, initially addressing specific communities of scholars, and gradually climbing up to broader public understanding, thus serving the interests of the lay society, too.

Dedication to Quality

Each Frontiers article is a landmark of the highest quality, thanks to genuinely collaborative interactions between authors and review editors, who include some of the world's best academicians. Research must be certified by peers before entering a stream of knowledge that may eventually reach the public - and shape society; therefore, Frontiers only applies the most rigorous and unbiased reviews.
Frontiers revolutionizes research publishing by freely delivering the most outstanding research, evaluated with no bias from both the academic and social point of view. By applying the most advanced information technologies, Frontiers is catapulting scholarly publishing into a new generation.

What are Frontiers Research Topics?

Frontiers Research Topics are very popular trademarks of the Frontiers Journals Series: they are collections of at least ten articles, all centered on a particular subject. With their unique mix of varied contributions from Original Research to Review Articles, Frontiers Research Topics unify the most influential researchers, the latest key findings and historical advances in a hot research area! Find out more on how to host your own Frontiers Research Topic or contribute to one as an author by contacting the Frontiers Editorial Office: frontiersin.org/about/contact

THE IMPACT OF OPEN SCIENCE FOR EVALUATION OF VOLCANIC HAZARDS

Topic Editors:
Elisa Trasatti, Istituto Nazionale di Geofisica e Vulcanologia (INGV), Italy
Fidel Costa, Nanyang Technological University, Singapore
Michelle Parks, Icelandic Meteorological Office, Iceland

Citation: Trasatti, E., Costa, F., Parks, M., eds. (2021). The Impact of Open Science for Evaluation of Volcanic Hazards. Lausanne: Frontiers Media SA.
doi: 10.3389/978-2-88966-757-4

Table of Contents

frontiers in Earth Science

EDITORIAL
published: 19 March 2021
doi: 10.3389/feart.2021.659772

Editorial: The Impact of Open Science for Evaluation of Volcanic Hazards

Elisa Trasatti[1]*, *Fidel Costa*[2] *and Michelle Parks*[3]

[1]Istituto Nazionale di Geofisica e Vulcanologia, Osservatorio Nazionale Terremoti, Rome, Italy, [2]Asian School of the Environment and Earth Observatory of Singapore, Nanyang Technological University, Singapore, Singapore, [3]Icelandic Meteorological Office, Reykjavik, Iceland

Keywords: volcanic hazards and risk, remote sensing, natural hazards, open science, findable accessible interoperable and reusable principles, database (all types), volcanic unrest, eruptions

Editorial on the Research Article

The Impact of Open Science for Evaluation of Volcanic Hazards

The Open Science paradigm addresses the scientific process of producing and sharing knowledge and data as early as possible in the research development, through digital and collaborative technology. It includes findable and interoperable data, access to data processing platforms, and sharing of research products within the scientific community and with stakeholders. Open Science increases the quality and impact of science by fostering reproducibility and interdisciplinarity.

The growing interest for more Open Science in the Earth Sciences has stimulated this Research Topic that aimed at collecting contributions from the Volcanological scientific community. Anticipating volcanic eruptions and mitigating their associated hazards and risks can greatly benefit from the Open Science approach. In particular, proper management of volcanic crises, such as during unrest and eruption, needs rapid access to scientific data and results by stakeholders and decision-makers.

The contributions of this issue range from data-driven applications for volcanic hazard mitigation (Beauducel et al.; Coppola et al.; Fujita et al.; Tierz; Whitty et al.) to original research studies (Aranzulla et al.; Bignami et al.).

Fujita et al. present a new database and management system of volcanological information in Japan. It includes four themes focusing on observational data, forecasting of events, implementation of hazard mitigation measures, and a data-sharing system. This data-sharing system is named the Japan Volcanological Data Network and will serve as a platform for the analysis of branch nodes of probabilistic event trees for volcanic crises in the coming decades in Japan.

In a prospective-type article, Tierz discusses the importance of open databases for the volcanological community to be able to perform robust probabilistic volcanic hazard assessments. Given the complexity of volcanic processes and the relative scarcity of information on past eruptions, it is critical to have systems in place that allow for discoverability and accessibility to volcanological data. The author also clarifies some misunderstanding of the use and meaning of long term probabilistic volcanic hazard assessment.

Beauducel et al. have developed an open source software system called WebObs aimed at facilitating the tasks of data storage, visualization, and interpretation of volcanological observatories. The system allows efficient real-time access to monitoring data, metadata, modeling and estimation of uncertainties, which are fundamental for an efficient interpretation of the monitored signals. It supports data analysis and exchange between researchers, engineers, and technicians during periods of volcanic unrest or quiescence. WebObs is also open for further development and enhanced data processing.

OPEN ACCESS

Edited and reviewed by:
Valerio Acocella,
Roma Tre University, Italy

***Correspondence:**
Elisa Trasatti
elisa.trasatti@ingv.it

Received: *28 January 2021*
Accepted: *02 February 2021*
Published: *19 March 2021*

Citation:
Trasatti E, Costa F and Parks M (2021) Editorial: The Impact of Open Science for Evaluation of Volcanic Hazards. Front. Earth Sci. 9:659772. doi: 10.3389/feart.2021.659772

Aranzulla et al. present new methodology for modeling tropospheric delays with the aim of calculating tropospheric corrections for DInSAR (Differential Interferometric Synthetic Aperture Radar) data. Removal of atmospheric artifacts from interferograms remains a challenging task - especially in areas with highly variable weather conditions and steep topography, such as in the vicinity of stratovolcanoes. The authors test an improved tomography algorithm to estimate the wet-refractivity field on a synthetic dataset and also apply the method to correct Sentinel-1 interferograms at Mt Etna during 2015, incorporating water vapor measurements derived from MODIS instruments on-board Terra and Aqua satellites. The inclusion of MODIS data improves the tomographic resolution and the technique is successful in modeling the large-scale atmospheric effects.

Whitty et al. analyze open access data from the permanent air quality monitoring networks at the Island of Hawai'i, obtaining measurements of SO_2 and $PM_{2.5}$ for about 12 years. Additional air quality data were collected during the 2018 lower East Rift Zone eruption of Kilauea through a low-cost $PM_{2.5}$ network. The 2018 eruption caused severe excess of the air quality threshold for $PM_{2.5}$ even 100 km away from Kilauea. Data from the low-cost sensor network correlated well with data from permanent instruments, confirming that these low-cost sensors provide robust monitoring means with the added value of being an open access source of readily-available information to the public for community awareness toward air quality.

Coppola et al. present a web-based and open source system called MIROVA (Middle Infrared Observation of Volcanic Activity) that allows automatic volcano hot spot detection using Moderate Resolution Imaging Spectroradiometer. The system is able to detect, locate and quantify thermal anomalies in near real-time on over 200 volcanoes worldwide. MIROVA is currently used by several volcano observatories for daily monitoring activities and reporting.

Bignami et al. exploit multi-sensor images from mostly open access missions to retrieve key elements for volcanic crises management, such as lava flow patterns and volcanic source parameters related to the effusive eruption of Fogo volcano, Cape Verde, between November 2014 and January 2015. The main outcome of the work is the application of a new automatic change detection technique for estimating the lava field and its temporal evolution, combining the SAR intensity and the interferometric SAR coherence. These data are applied for the first time for lava mapping, providing an example of using the multi-temporal interferometric SAR coherence to automatically monitor lava flow evolution during an emergency phase.

The papers included in this Research Topic highlight the importance of making a bigger effort in global sharing of data and methods in an open way, showing the criticality for volcanic risk management in all its phases (e.g., before and during eruptions). Terrestrial and satellite monitoring techniques offer timely measurements for detecting volcanic activity at a global scale. Access to data, along with the availability of open processing tools and environments, and rapid sharing of results are vital for volcanic hazard assessment today and for growing future applications of data integration.

AUTHOR CONTRIBUTIONS

All authors contributed equally to this editorial and to the Research Topic management.

ACKNOWLEDGMENTS

We thank all authors for their contributions, the reviewers for valuable comments, and the Frontiers Editorial Office for improving the layout of this Research Topic.

Conflict of Interest: The authors declare that the research was conducted in the absence of any commercial or financial relationships that could be construed as a potential conflict of interest.

frontiers in Earth Science

ORIGINAL RESEARCH
published: 27 January 2020
doi: 10.3389/feart.2019.00362

Thermal Remote Sensing for Global Volcano Monitoring: Experiences From the MIROVA System

Diego Coppola[1,2], Marco Laiolo[1,2], Corrado Cigolini[1,2], Francesco Massimetti[1], Dario Delle Donne[3], Maurizio Ripepe[4], Hidran Arias[5], Sara Barsotti[6], Claudia Bucarey Parra[7], Riky Gustavo Centeno[8], Sandrine Cevuard[9], Gustavo Chigna[10], Carla Chun[10], Esline Garaebiti[9], Dulce Gonzales[10], Julie Griswold[11], Javier Juarez[10], Luis E. Lara[7], Cristian Mauricio López[12], Orlando Macedo[13], Celestin Mahinda[14], Sarah Ogburn[11], Oktory Prambada[15], Patricio Ramon[16], Domingo Ramos[17], Aline Peltier[18,19], Steve Saunders[20], Elske de Zeeuw-van Dalfsen[21], Nick Varley[22] and Ricardo William[9]*

[1] Dipartimento di Scienze della Terra, Università di Torino, Turin, Italy, [2] Centro Interdipartimentale sui Rischi Naturali in Ambiente Montano e Collinare, Università di Torino, Turin, Italy, [3] Istituto Nazionale di Geofisica e Vulcanologia, Osservatorio Vesuviano, Naples, Italy, [4] Dipartimento Scienze della Terra, Università degli Studi di Firenze, Florence, Italy, [5] Engineering Ingegneria Informatica S.p.A., Rome, Italy, [6] Icelandic Meteorological Office, Reykjavík, Iceland, [7] Servicio Nacional de Geología y Minería, Santiago, Chile, [8] Instituto GeoFísico del Perú, Lima, Peru, [9] Vanuatu Meteorology and Geohazards Department, Port Vila, Vanuatu, [10] Instituto Nacional de Sismologia, Vulcanologia, Meteorologia e Hidrologia, Guatemala City, Guatemala, [11] U.S. Geological Survey, Volcano Disaster Assistance Program, Reston, VA, United States, [12] Servicio Geológico Colombiano, Bogota, Colombia, [13] Facultad de Geología, Geofísica y Minas, Universidad Nacional de San Agustin de Arequipa, Arequipa, Peru, [14] Goma Volcano Observatory, Goma, Democratic Republic of Congo, [15] Center for Volcanology and Geological Hazard Mitigation, Bandung, Indonesia, [16] Instituto Geofísico, Escuela Politécnica Nacional, Quito, Ecuador, [17] Instituto Geologico Minero y Metalurgico, Lima, Peru, [18] Université de Paris, Institut de Physique du Globe de Paris, CNRS, Paris, France, [19] Observatoire Volcanologique du Piton de la Fournaise, Institut de Physique du Globe de Paris, La Plaine des Cafres, France, [20] Department of Mineral Policy and Geohazards Management, Port Moresby, Papua New Guinea, [21] Royal Netherlands Meteorological Institute, De Bilt, Netherlands, [22] Colima Intercambio e Investigación en Vulcanología, Universidad de Colima, Colima, Mexico

OPEN ACCESS

Edited by:
Fidel Costa, Nanyang Technological University, Singapore

Reviewed by:
Társilo Girona, NASA Jet Propulsion Laboratory (JPL), United States
Yosuke Aoki, The University of Tokyo, Japan
Christina Widiwijayanti, Earth Observatory of Singapore, Singapore

***Correspondence:**
Diego Coppola
diego.coppola@unito.it

Specialty section:
This article was submitted to Volcanology, a section of the journal Frontiers in Earth Science

Received: *17 September 2019*
Accepted: *30 December 2019*
Published: *27 January 2020*

Citation:
Coppola D, Laiolo M, Cigolini C, Massimetti F, Delle Donne D, Ripepe M, Arias H, Barsotti S, Parra CB, Centeno RG, Cevuard S, Chigna G, Chun C, Garaebiti E, Gonzales D, Griswold J, Juarez J, Lara LE, López CM, Macedo O, Mahinda C, Ogburn S, Prambada O, Ramon P, Ramos D, Peltier A, Saunders S, de Zeeuw-van Dalfsen E, Varley N and William R (2020) Thermal Remote Sensing for Global Volcano Monitoring: Experiences From the MIROVA System. Front. Earth Sci. 7:362. doi: 10.3389/feart.2019.00362

Volcanic activity is always accompanied by the transfer of heat from the Earth's crust to the atmosphere. This heat can be measured from space and its measurement is a very useful tool for detecting volcanic activity on a global scale. MIROVA (Middle Infrared Observation of Volcanic Activity) is an automatic volcano hot spot detection system, based on the analysis of MODIS data (Moderate Resolution Imaging Spectroradiometer). The system is able to detect, locate and quantify thermal anomalies in near real-time, by providing, on a dedicated website (www.mirovaweb.it), infrared images and thermal flux time-series on over 200 volcanoes worldwide. Thanks to its simple interface and intuitive representation of the data, MIROVA is currently used by several volcano observatories for daily monitoring activities and reporting. In this paper, we present the architecture of the system and we provide a state of the art on satellite thermal data usage for operational volcano monitoring and research. In particular, we describe the contribution that the thermal data have provided in order to detect volcanic unrest, to forecast eruptions and to depict trends and patterns during eruptive crisis. The current limits and requirements to improve the quality of the data, their distribution and interpretation are also discussed, in the light of the experience gained in recent years within the

volcanological community. The results presented clearly demonstrate how the open access of satellite thermal data and the sharing of derived products allow a better understanding of ongoing volcanic phenomena, and therefore constitute an essential requirement for the assessment of volcanic hazards.

Keywords: thermal remote sensing, global volcano monitoring, MIROVA, MODIS, thermal unrest, eruption forecasting

INTRODUCTION

Volcano monitoring consists of continuous, real-time, acquisition and processing of numerous data that describe the behavior of a volcano (e.g., earthquakes, ground movement, gas emissions, remote-sensed data) in order to detect any sign of change that may precede an eruption (Sparks et al., 2012; Pallister and McNutt, 2015; Newhall et al., 2017). It likely represents the only scientifically valid approach for short-term forecasts of a future eruption, or possible changes during an ongoing eruption (Tilling, 2008).

Volcanic monitoring can be viewed as a form of continuous learning by the scientific community, in which the greater the amount of information available, the greater the understanding of the volcanic phenomena in progress, and the better the ability to forecast future eruptive scenarios (Winson et al., 2014). In this context, satellite data are a reliable source of information, especially for monitoring the large number (∼50%) of potentially active volcanoes (∼1400) still lacking conventional ground-based instruments (Brown et al., 2015; Pritchard et al., 2018; Delgado et al., 2019). Nonetheless, even at well-monitored volcanoes, satellite data offer a spatio-temporal view of eruptive phenomena that may fill gaps left by ground based instruments (Ebmeier et al., 2018).

The acquisition of satellite images and data for volcanological applications is continuously and rapidly growing (Ramsey and Harris, 2013; Furtney et al., 2018; Pritchard et al., unpublished), so that big data analysis techniques (i.e., artificial intelligence and machine learning) are progressively used for research purposes and for monitoring activity (Piscini and Lombardo, 2014; Anantrasirichai et al., 2018; Valade et al., 2019). In particular, with the advent of the new millenium, and with the development of internet, the dissemination and sharing of satellite data/products can be considered a pillar of open science in volcanology, also thanks to the growing availability of open data by space agencies (Delgado et al., 2019).

At present, four main types of Remote Sensing Observations (RSO) provide different insights into the key processes occurring within a volcanic system. These are: (i) ground deformation, from microwaves; (ii) SO_2 degassing, from ultraviolet and infrared; (iii) ash emission, from infrared; and (iv) heat flux, from infrared.

Recent scientific pilot projects, as the European Volcano Observatory Space Services, EVOSS (Tait and Ferrucci, 2013) and the Committee on Earth Observation Satellite (CEOS) Volcano Pilot Project (Delgado et al., 2019), demonstrated the potential of integrating these space-based data for forecasting eruptions (Furtney et al., 2018), stressing the need to develop a volcanic monitoring system to support volcano observatories (Pritchard et al., unpublished). The Monitoring Unrest From Space (MOUNTS) project[1], although in an embryonic stage, can be considered a first prototype of such integrated system, since it includes near-real time multi-parametric analysis (UV, IR and microwaves) derived from the ESA Sentinel constellation, at several volcanoes (Valade et al., 2019). However, apart from this example, a comprehensive integration of space-based datasets into an operational system for global volcano monitoring is at this time only envisioned, with several distinct groups working on a single RSO (deformation, degassing, ash, thermal; Reath et al., 2019a).

During the past two decades, numerous volcanic hot-spot detection systems have been developed in order to detect, localize and quantify the presence of thermal anomalies produced by volcanic activity (Harris, 2013; Ramsey and Harris, 2013). In **Supplementary Table S1**, we have compiled a list of all the systems currently operating in real time of which we are aware, although other systems may be operated locally. These systems are based on different sensors having distinct spatial, temporal and radiometric resolution so that each of them is different from the others in terms of performance and usability for research and volcano monitoring (Steffke and Harris, 2011). The scientific results achieved thanks to the open data elaborated by these systems are remarkable and in continuous growth (Harris, 2013; Ramsey and Harris, 2013). However, their use from an operational point of view, that is, during the daily monitoring or during an eruptive crisis, remains little known and poorly described. In particular, what information is most useful to the observatories and how this information should be communicated/interpreted in (near) real time remains a topic of broad interest, especially for the future development of these systems and their integration with other satellite- or ground-based monitoring networks (Pritchard et al., unpublished).

In this work, we describe the architecture of the system named Middle Infrared Observations of Volcanic Activity (MIROVA) and its use by more than 17 volcano observatories/Institutions in charge of monitoring more than 650 volcanoes around the globe (**Supplementary Table S2**). Based on the experiences of the individual observatories (summarized in the **Supplementary Appendix**), we then deduced what is the contribution of the satellite thermal data to the daily monitoring of volcanoes in extremely different geological and socio-economic contexts. The use of the results provided by MIROVA makes it possible to understand the current limits of thermal remote sensing systems and the requirements to further develop an open science tool to support the assessment and mitigation of volcanic risk at global scale.

[1]http://mounts-project.com/

THE MIROVA SYSTEM

Architecture of the System

Middle Infrared Observations of Volcanic Activity is an automatic system for detecting thermal anomalies at high temperatures (>500K), based on the analysis of MODIS (Moderate Resolution Imaging Spectroradiometer) data. MODIS is a sensor mounted on board two NASA satellites, called Terra and Aqua, in sun-synchronous polar orbit since March 2000 and May 2002, respectively. The main features of MODIS, useful for volcano thermal monitoring, consist of its global coverage with spatial resolution of 1 km, temporal resolution of about four images/day (at the equator) and the presence of a dual channel in the mid-infrared (centered at 3.959 microm) with low/high gain settings (providing an extended range of unsaturated data). The general architecture of the MIROVA system can be divided into two main parts: (a) data download and processing (developed on a local computer) and (b) data dissemination (developed on a website: www.mirovaweb.it).

Unlike other systems that use MODIS data (e.g., MODVOLC; FIRMS; **Supplementary Table S1**) MIROVA is not strictly a global monitoring system. In fact, although the algorithm can be applied in any environmental context (Coppola et al., 2016a), the data processing chain actually operates only for a list of selected target volcanoes for which the near real time observation is requested. This list of selected targets is compiled from the list of the Holocene volcanoes (more than 1400) of the Global Volcanism Program (2013) by setting an "operational flag" to all the volcanoes that need to be monitored. Volcanoes are also given an identification number in accordance with the Global Volcanism Program. The number of monitored volcanoes has gradually increased since the start of the operational phase (in 2014) and has now reached a number equal to 216 units. These targets were gradually added to the MIROVA list based on a scientific interest, or following specific requests from the observatories. They now cover the most active volcanoes on the globe (Global Volcanism Program, 2013) with the current number actually limited by the hardware resources of the system and by the amount of data to be downloaded and processed daily (about 25 Gb per day). Despite this limitation, this architecture makes it possible to add other specific targets in case of need (i.e., unrest of a new volcano) without compromising the total system efficiency in terms of processing time, memory, storage capacity, etc. Access to archived MODIS data (available since 2000 and 2002 for Terra and Aqua, respectively) also allows analysis and reconstruction of 20-year time series for any volcano. However, building a complete thermal database for all the volcanoes currently monitored by MIROVA takes time and is in the development phase.

Download, Data Processing, and Sensibility

The original MODIS data (Level 1b – calibrated radiances) are downloaded from the LANCE system, which provides them with a latency of less than 3 h[2]. The continuous screening of the LANCE daily remote folders (every 5 min), allows timely downloading in the local computer of any newly acquired MODIS granule imaging at least one target volcano. The downloaded granules are then processed following several steps fully described in Coppola et al. (2016a).

For each analyzed volcano, the original spectral radiance data (recorded by MODIS in the Middle Infrared [MIR] at 3.959 μm and Thermal Infrared [TIR] at 12.02 μm) are resampled in regular grids of 50 × 50 km (in UTM coordinates) and processed in order to identify the pixels containing thermal anomalies. This step, or rather the hotspot detection algorithm, comprehends the application of spectral and spatial principles that, combined together, increase the ability to automatically detect hotspots. In particular, the MIROVA algorithm uses the middle infrared MIR bands at 3.959 μm and thermal TIR at 12.02 μm to calculate different spectral indices (such as the Normalized Thermal Index – NTI, Wright et al., 2004, and the Enhanced Thermal Index – ETI, Coppola et al., 2016a) that enhance the presence of hot objects inside the pixels. In addition, a series of spatial operations allow us to highlight the pixels having these indices in excess with respect to their surroundings, thus constituting a hybrid and contextual approach for any environmental condition.

Once the contaminated pixels have been identified, the volcanic radiative power (VRP) is calculated using the MIR-method (Wooster et al., 2003). Specifically, the VRP is calculated as:

$$VRP = 18.9 \cdot A_{pixel} \cdot \sum_{i=1}^{npix} \left(L_{\mathrm{MIR},alert} - L_{MIR,bk}\right)_i$$

where *npix* is the number of alerted pixels, $L_{MIR,alert}$ is the pixel integrated MIR radiance of the i^{th} alerted pixel, $L_{MIR,bk}$ is the MIR radiance of the background (average radiance of pixels surrounding the anomaly), A_{pixel} is the pixel size (1 km^2 for the resampled MODIS pixels), and 18.9 is a constant of proportionality (see Wooster et al., 2003).

The VRP is the main parameter calculated by the MIROVA system and represents the combined effect of the hotspot area (A_{hot}) and its integrated temperature (T_{hot}) according to Stephan Boltzmann's law ($VRP = \sigma\varepsilon A_{hot} T_{hot}^4$; being σ and ε the Boltzmann constant and emissivity, respectively).

It is important to underline that the application of the MIR method on hotspots of volcanic origin represents the thermal flux radiated exclusively from the surfaces with T > 500 K (only the portion of the warmer surface produces sufficient MIR radiances to be detected by MODIS) and returns the VRP with an error of ± 30%.

As a whole MIROVA may detect thermal anomalies with VRP spanning from less than ∼1 MW to about ∼50 GW. According to the Stephan-Boltzmann's law, the lower detection limit (1 MW) would correspond to two end-member cases: (i) a hot case characterized by a vent of ∼7 m^2 and a temperature of 1000°C, or (ii) a cold case characterized by a fumarole field having an area of ∼143 m^2 and a temperature of 300°C.

[2]https://lance-modis.eosdis.nasa.gov/

Website and Data Dissemination

In order to easily and quickly share the real-time observations of the system, a dedicated website[3] summarizes, and continuously updates, a series of tables and graphical outputs for any monitored volcano.

The home page (**Figure 1**) of this website is constituted by a world map showing all the monitored volcanoes, and by a table summarizing the latest thermal anomalies detected by the system (in chronological order). In order to quickly identify the "thermal magnitude" of the hotspot listed in this table, we represent each detection through a color scale, proportional to the logarithm of the detected VRP. This scale is divided into five distinct levels and each thermal detection is classified into these subdivisions, based on the recorded VRP (**Figure 1**).

The interactive map and table take the user to the page dedicated to each individual volcano, where specific graphical outputs are updated approximately four times per day (according to the number of MODIS overpasses) and available online from 1 to 4 h after image acquisition. These outputs consist of the "Latest IR Images," "VRP time series," "Distance from the summit," and a "Google Earth overlap" which are described in more detail below.

Latest IR Images

The latest IR Images screen summarizes the latest 10 MODIS acquisitions over the target volcano (**Figure 2**). This display provides an intuitive and fast overview of the thermal state of the volcano during the past 48 h (assuming four images per day). Each image displays a grayscale map according to the NTI relative to each pixel. When a hotspot is detected, the VRP (in MW) is reported below each image, and the frame colored according to the VRP Scale. The satellite zenith and azimuth are also displayed at the bottom of each image in order to permit a quick evaluation of the viewing geometry conditions. This information allows the user, who knows the topography of the volcano, to assess whether the observation conditions are favorable or unfavorable to the detection of a hotspot. For example, if a lava dome emerges at the bottom of a deep crater, the observation conditions are quite restricted, since in this case (high zenith angle over a deep crater) the crater's rim could block the line of sight of the sensor and, therefore, the sensor would not detect the hot dome. Similarly, a lava flow descending on a steep flank of a volcano will be poorly imaged by a satellite looking from the opposite side and with a high zenith angle. In this case the VRP could be underestimated and would not correspond to a real lowering of the thermal activity.

The visualization of the last 10 NTI maps allows also a first-order evaluation of the cloud fraction, essential for a correct interpretation of the data (e.g., presence/absence of hotspots, intensity and location of the thermal anomaly). In a general way, during the course of an eruption user can refer to the latest images (**Figure 2**) to follow the detection of thermal activity level and evaluate the quality of each VRP related to the weather conditions and the geometry of the satellite acquisition. It is however important to emphasize that the VRP and the color code provided by MIROVA are not corrected automatically for the acquisition conditions (i.e., clouds/geometry) but they simply represent a measurement of the thermal radiation reaching the sensor.

VRP Time Series

The *VRP time series* can be displayed in both Log and Linear scale, which summarizes the detected VRP values within the previous month and year of the MODIS observation (upper and lower panel, respectively in **Figure 3**). Each stem represents a single detection (one MODIS passage) with a distinction between proximal (hotspots located within 5 km from the summit are represented by blue stems) and distal anomalies (far hotspots located at more than 5 km from the summit, are represented by black stems).

The time series are displayed in a logarithmic scale (**Figure 3**) to allow the visualization of the large variations in the thermal intensity that may accompany a single eruption (up to five orders of magnitude). Also, the logarithmic scale permits to recognize subtle long-term trends and patterns such as the exponential decays (appearing linear in the log scale plot) that often accompany the waning phase of an eruption (Wadge, 1981). The extrapolation of these trends offers a rapid method to qualitatively detect a change from the expected values, possibly associated with a variation of the behavior of the ongoing volcanic activity (see section "Eruptive Evolution, Trends and Patterns"). The same VRP time series are also shown with a linear scale ("Rad Power" button on the left menu; **Figure 3**) in order to better visualize real intensity changes in thermal activity.

Distance From the Summit

This screen named "*Distance from summit*" shows the distance from the farthest hot pixel to the summit of the volcano, during the last month and last year of activity (upper and lower panel, respectively in **Figure 4**). This graph has the dual purpose of (*i*) identifying gradual displacements of the thermal anomaly, for example during the advancement of a lava front, or (*ii*) detecting sudden changes in the hot spot location, likely associated with the occurrence of forest fires or false alerts (in distal areas of the volcano).

Although the location accuracy remains significant ($\pm$ 1 km), in the case of km-long lava flows, this automatic analysis provides a useful estimate of lava front advancement. As an example, in **Figure 4** we show the case of the eruption of Erta Ale (**Figure 4**) during which the flow front advanced by 12 ± 1 km in 4 months (June–September 2017), with an average speed of 100 m day^{-1}. Isolated spikes showing thermal anomalies more than 25 km away from the summit (**Figure 4**), can be easily identified and associated with possible fires.

Google Earth Overlap

The Google Earth overlap screen shows the last processed image superimposed on google map which allows to locate the thermal anomaly and estimate its dimensions (**Figure 5**). In many cases, the overlap of the thermal images on google map can be used to verify if the hotspot is located inside or outside a summit crater, for hazard evaluation of the ongoing activity. The estimation of hotspot location is also very useful to verify if the thermal anomaly is possibly associated to a forest fire (e.g., located over

[3] www.mirovaweb.it

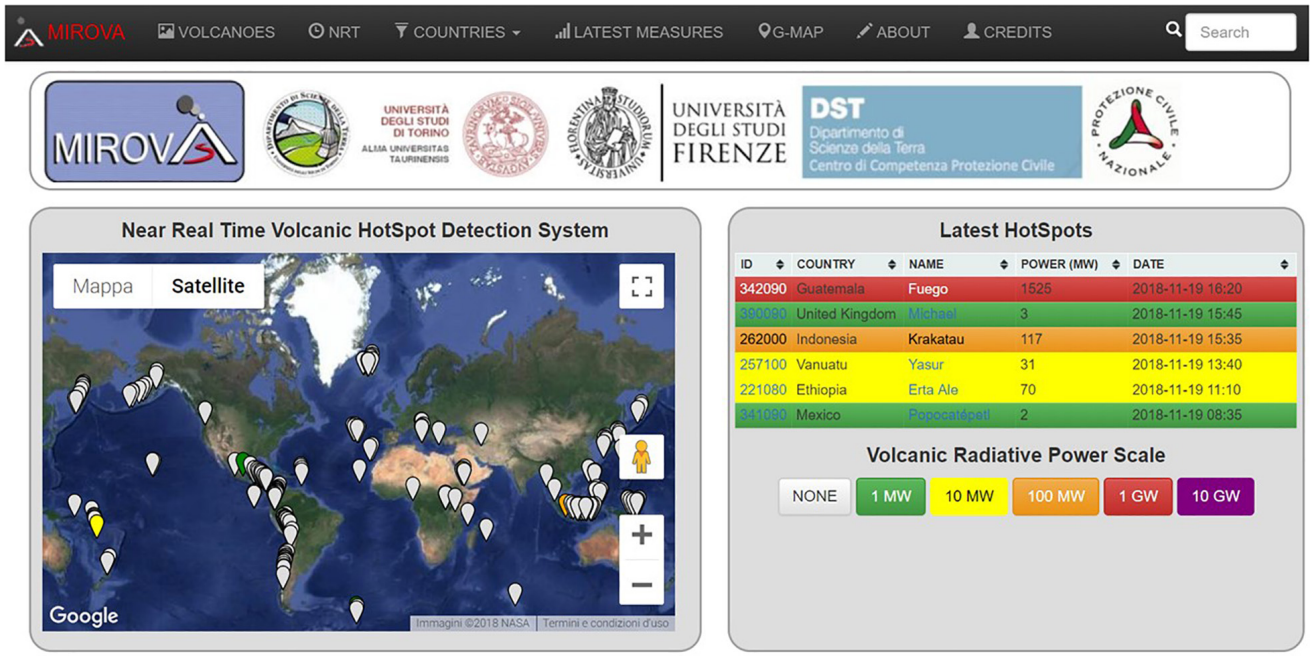

FIGURE 1 | Snapshot of the *home page* of the MIROVA website (www.mirovaweb.it; accessed on 19 November 2018).

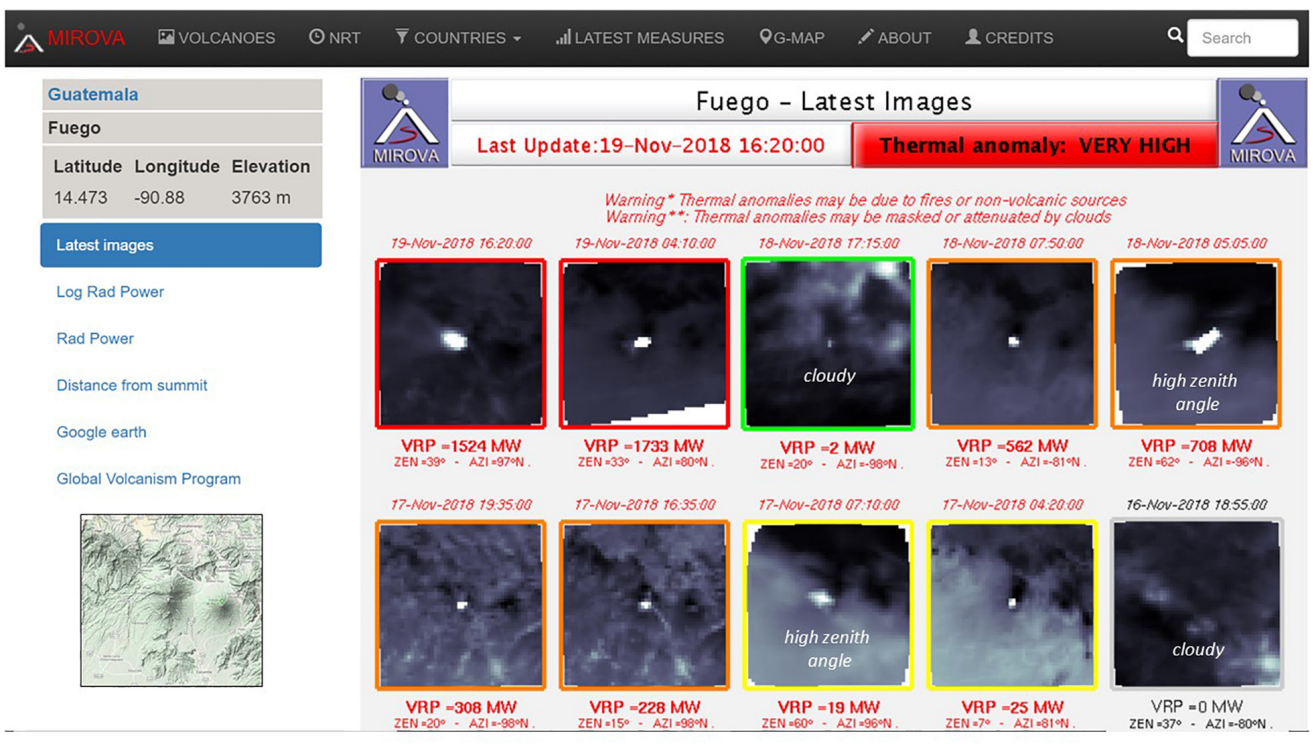

FIGURE 2 | Snapshot of the *Latest IR Images* display posted on MIROVA website for the Fuego volcano, Guatemala (accessed on 19 November 2018).

a vegetated area), anthropogenic source (e.g., located over an urban/industrial area), or it is a false alert (e.g., located above a body of water).

All the outputs described in the previous section are exclusively made up of static graphs that are continuously overwritten as newer data are processed. The original images

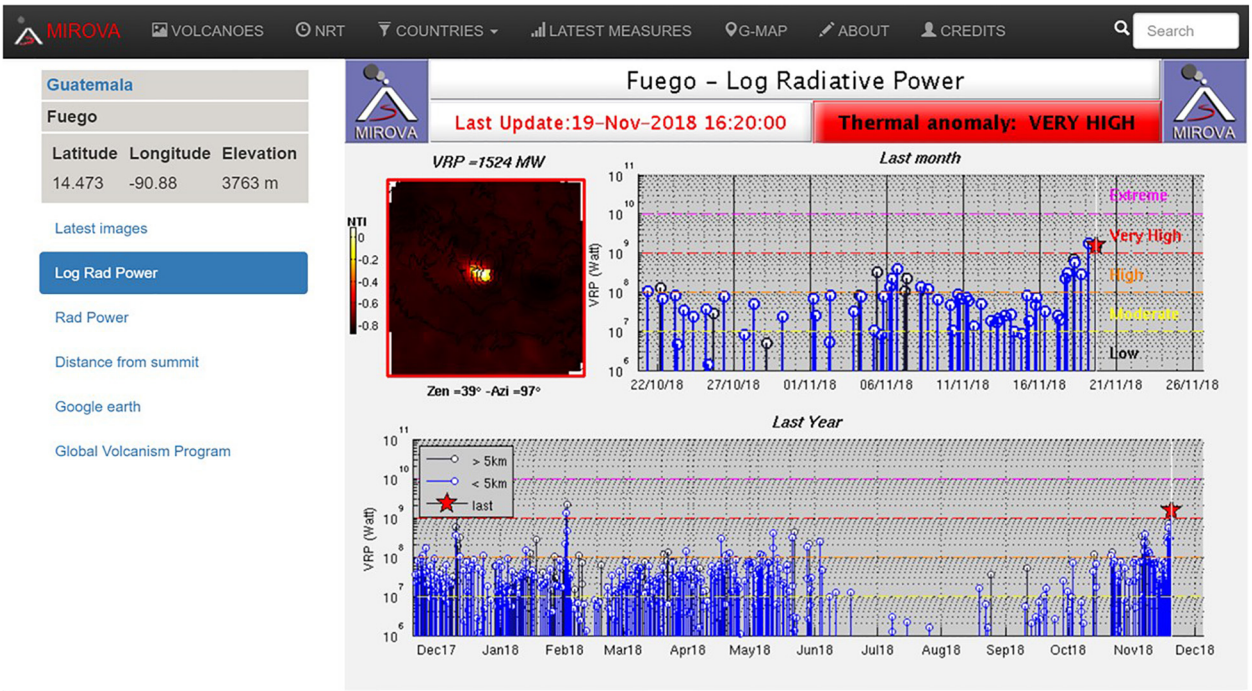

FIGURE 3 | Snapshot of the "*Log Radiative Power*" screen posted on the MIROVA website for the Fuego volcano, Guatemala (accessed on 19 November 2018). Note the fluctuations in thermal activity in the last month (top right panel), with an evident increase in VRP (almost 2 orders of magnitude) recorded from 14 to 19 November 2018. The trend of thermal anomalies recorded during the past year (lower panel) shows that after the eruption of the June 3, 2018 the thermal activity of Fuego was very low for at least 3 months. However, since September 2018 the radiate heat flux gradually intensified by means of repeated pulses culminating with the high VRP recorded on November 19, 2018.

(i.e., 50 × 50 km maps) and time series (numerical tables) are not archived on a web database and cannot be query and downloaded. Although this limitation prevents any direct data download, the management of the complete MIROVA database (that currently include a total of more than 2 million images) would require a large bandwidth and greatly slow down the use of the website.

Data sharing is currently done by request through email by the observatories. This practice, although slow and impractical from an operational point of view, allows a continuous exchange of information and discussions between the system developers and the end users, not necessarily experts in the interpretation of remote-sensed thermal data.

OPERATIONAL USE OF MIROVA FOR VOLCANO MONITORING: EXPERIENCES FROM THE OBSERVATORIES

The MIROVA system was developed in 2013 in collaboration with the University of Firenze (Italy) for monitoring Italian volcanoes on behalf of the Italian Department of Civil Protection (DPC). Since then, the satellite thermal data have been integrated with the ground-based data of the Laboratorio di Geofisica Sperimentale (LGS) of the University of Firenze to provide to the DPC daily/weekly and monthly reports regarding the activity of Stromboli and Etna (Italy) volcanoes[4]. During major eruptive crises of these volcanoes, the effusion rate and erupted volume calculated from MIROVA were presented and discussed at the daily briefing organized by the Volcano Risk management of the Italian Civil Protection Department (DPC) together with the scientific staff of the Istituto Nazionale di Geofisica e Vulcanologia (INGV).

In recent years, and thanks to its easy application on diverse volcanic environments, the MIROVA system has gradually turned into a small pilot project testing the capabilities for global volcano monitoring, with the observations now covering the full range of volcanic activities in near real time at 216 volcanoes (Coppola et al., 2016a). Currently, the website is routinely used by 17 volcanological observatories or other institutions in charge of volcano monitoring (**Figure 6** and **Supplementary Table S2**), supporting their daily monitoring duties and management during eruptive crises. Since 2016, MIROVA is included in the list of websites consulted by the ARISTOTLE2 program (All Risk Integrated System TOward *Trans*-boundary hoListic Early-warning – European Natural Hazards Scientific Partnership) for volcanic surveillance on a global scale by the Emergency Response Coordination Centre (ERCC[5]). Together with other remote sensing systems, MIROVA is currently used by the

[4]http://lgs.geo.unifi.it/

[5]http://aristotle.ingv.it/tiki-index.php

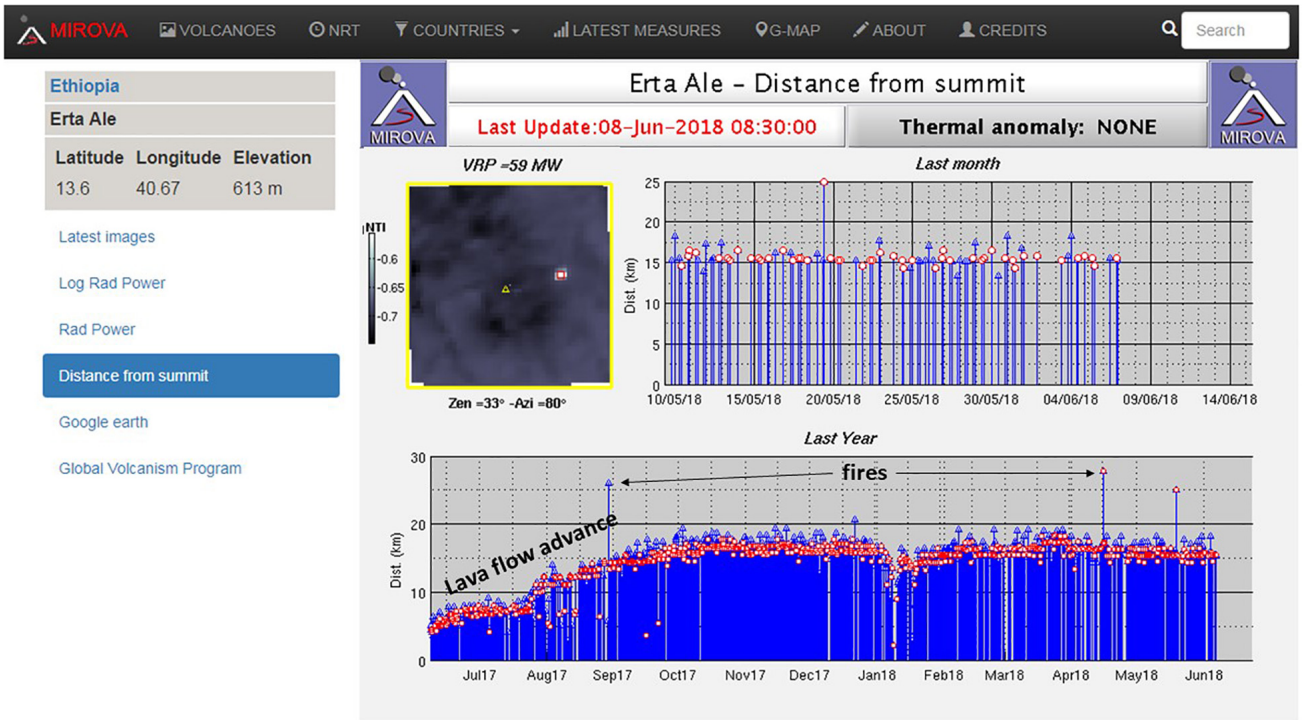

FIGURE 4 | Snapshot of the "*Distance from summit*" figure posted on MIROVA website for the Erta Ale volcano (accessed on 08 June 2018). Note the lengthening phase of the lava flow occurred between June and October 2017 with an average flow advancement velocity of 100 m day^{-1}.

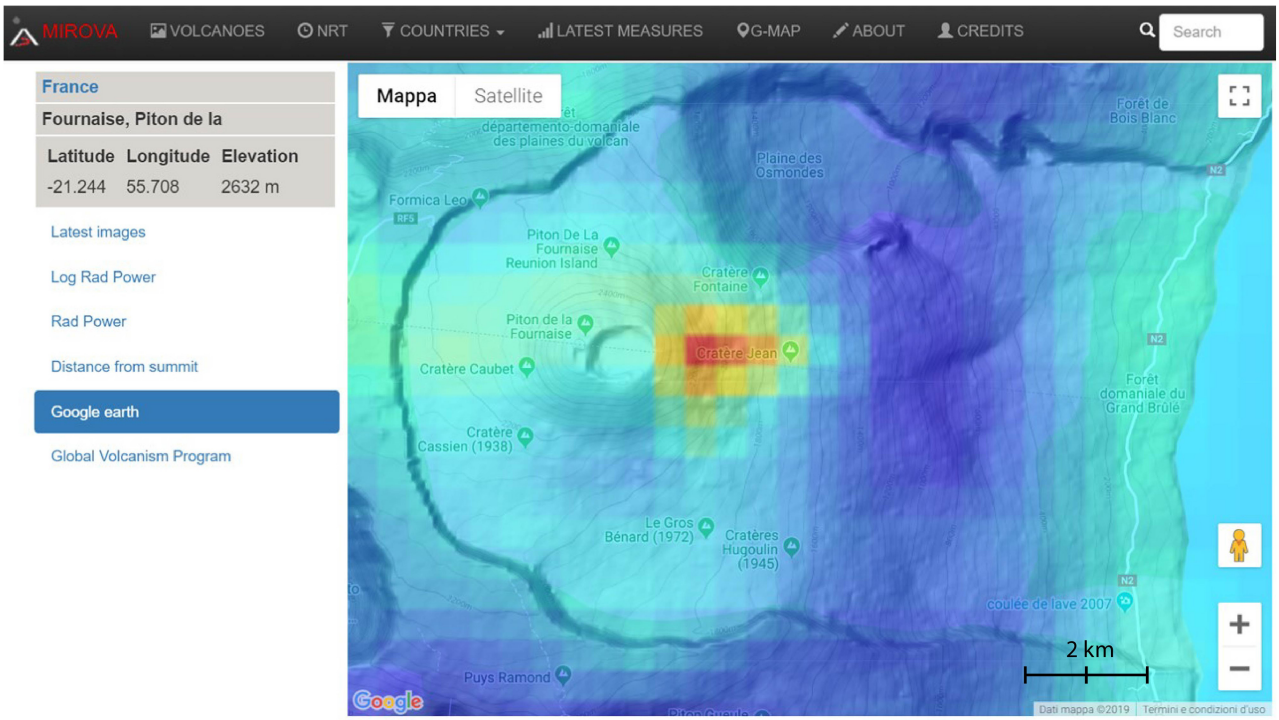

FIGURE 5 | Snapshot of the *Google Map's* overlay posted on MIROVA website for the Piton de la Fournaise volcano, La Réunion Island (accessed on 14 June 2019). The overlay image represents the Brightness Temperature (BT) recorded by MODIS in the MIR channel, resampled to a spatial resolution of 500 m. Yellow to red pixels indicate higher BT values associated to the presence of a cooling lava flow on the upper eastern flank of the volcano.

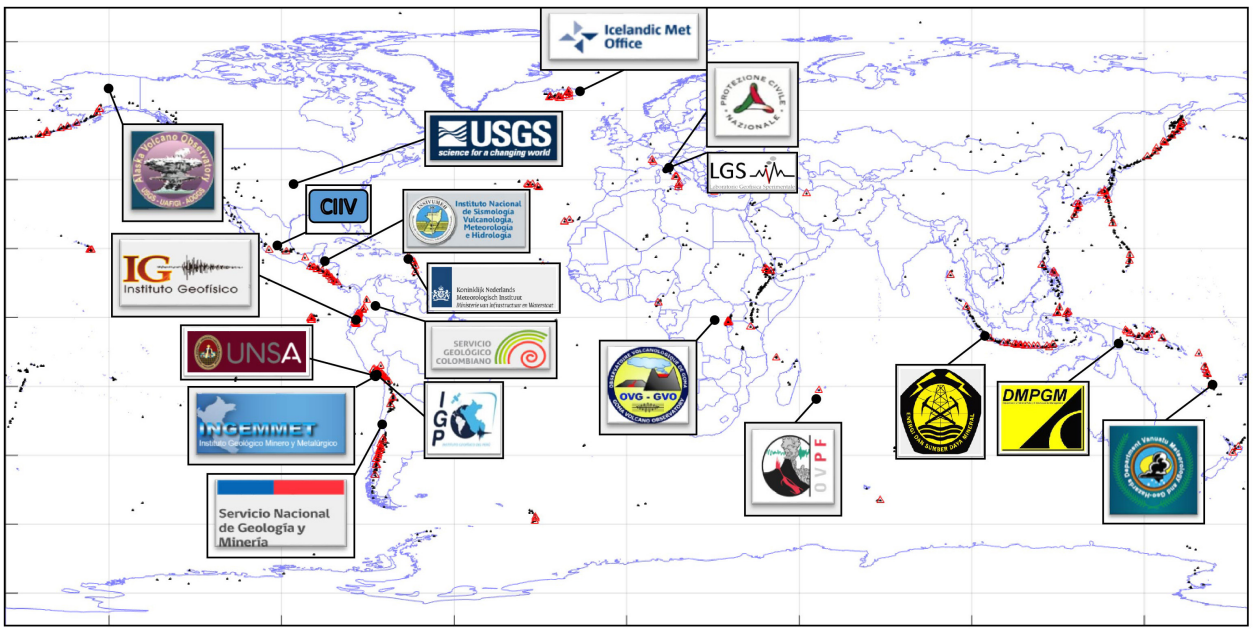

FIGURE 6 | Volcanoes currently observed by MIROVA (red triangles) with distribution of observatories (logos within insets) that use MIROVA in support of monitoring activities (see **Supplementary Table S2** for details).

Volcano Disaster Assistance Program (VDAP), formed in 1986 to assist foreign partners in mitigating hazards at their country's threatening volcanoes (Lowenstern and Ramsey, 2017).

In order to understand user' experiences and motivation in using the MIROVA system, a survey (see **Supplementary Appendix**) was recently conducted, whose results can be summarized in the following four main points.

State of the Art of Operational Thermal Remote Sensing Systems Currently Used by Volcano Observatories

None of the participating observatories has its own automatic detection/quantification hot spot system, but they rely on systems developed and maintained by external groups. Although there are many thermal remote sensing data available online (see **Supplementary Table S1**), most of them are not operational in near real time and in the area of interest. The most used remote sensing thermal monitoring systems are those based on moderate resolution sensors, such as MODIS data (MIROVA, MODVOLC, REALVOLC) or VIIRS (FIRMS), which provide approximately 2/4 images daily, at a resolution of 1 km. Some observatories also use automatic systems based on higher sampling rate data (e.g., HOTVOLC, HOTSAT based on SEVIRI data), which are particularly useful for tracking volcanic plumes or for detecting high-radiating effusive eruptions. Others use the available ASTER data (i.e., ASTER Image database for Volcanoes), based on TIR observations, which enable to detect low-level thermal activity (such as fumarole fields) but with longer revisit time (e.g., >15 days; Reath et al., 2019a). The lack of a near-real time data dissemination system makes this resource less used for monitoring purposes despite the fact that since 2011 the ASTER Urgent Request Protocol (URP) system has allowed the continuous increase of acquisitions of new volcanic activity as quickly as possible (Ramsey, 2016). Due to the lack of operational monitoring systems to analyze high-spatial resolution Short-Wave Infrared (SWIR) images, no observatory uses automatic systems focused on Sentinel 2 or Landsat 8, which have a typical revisit time of 5 to 16 days (see **Supplementary Table S1**). Only recently this gap has started to be covered by the MOUNTS pilot project that provides automatic Sentinel 2 hotspot detections alerts (together with other remote sensed parameters) on specific volcanic targets (Valade et al., 2019).

Frequency of Use of MIROVA Website and Volcano Alert Levels

The experiences reported by the observatories during the past 5 years allow us to state that the frequency of use of a satellite thermal monitoring system such as MIROVA strongly depends on the specific alert level of each monitored volcano. Many alert level systems exist in the world, with the majority based on four levels, e.g., the US system developed by the USGS (*Normal, Advisory, Watch, and Warning*). Each country (or volcano) has a specific scale which is adapted to the particular volcanological, environmental, social, political and economic context (Fearnley et al., 2012). For each level there is therefore a different need/urgency to have up-to-date data on the thermal state of the volcano which can be summarized as follows:

Normal

Volcano is in typical background, non-eruptive state or, after a change from a higher level, volcanic activity has ceased and

volcano has returned to non-eruptive background state. The thermal state of volcanoes at this level is typically checked on a monthly basis (e.g., Vesuvius, Italy) or occasionally, for example to verify reports or rumors (e.g., Cumbal, Colombia; Mt. Scenery, Saba Island – Netherlands). Automatic alerting systems (for example, by sending emails) can facilitate the immediate detection of hotspots. This is especially useful in remote volcanoes in a quiescent state (*Normal* alert level), when thermal state is irregularly controlled and for which there are no other operational monitoring systems.

Advisory

Volcano is exhibiting signs of elevated unrest above known background level or, after a change from a higher level, volcanic activity has decreased significantly but continues to be closely monitored for possible renewed increase. Several volcanoes may persist at this levels for several months or years showing persistent thermal anomalies (e.g., Stromboli, Italy; Villarrica, Chile). The typical frequency of use in this case is one to several times per week, in accordance with the reporting tasks of each observatory. In these cases, automatic alert systems, by setting up specific thresholds, can be used to warn the end-user(s) of a sudden increase in thermal activity that may lead to a higher alert level.

Watch

Volcano is exhibiting heightened or escalating unrest with increased potential of eruption, timeframe uncertain, or eruption is underway but poses limited hazards. In this case, the thermal data are typically checked on a daily basis, just before briefing or to write the daily reports (e.g., Etna, Italy, during major lava flows or paroxysms; Piton de la Fournaise, Réunion Island, during eruptions). At this alert level, the daily comparison of thermal data with other parameters (seismic, outgassing, deformation) is usually an integral part of the discussions within the observatory, and for analysis and evaluation of the ongoing volcanic activity.

Warning

Hazardous eruption is imminent, underway, or suspected. During imminent eruptions or ongoing eruptions, the thermal data are checked daily or hourly during crisis (e.g., Bardarbunga, Iceland [August 2014]; Agung, Indonesia [August 2017]; Kilauea, United States [May 2018]). In these warning conditions, each dataset must be more frequently updated. A screen grab of the MIROVA website is often displayed in the monitoring acquisition rooms during eruptive crisis (e.g., Nevado del Ruiz, Colombia; Manam, Papua New Guinea).

What Kind of Information Is Retrieved From MIROVA

The most useful information to get from a hotspot detection system such as MIROVA, according to volcano observatories, is summarized in the following four parameters:

Presence or Absence of Thermal Anomalies

The first and most direct information obtainable from a hotspot detection system is the presence/absence of thermal anomalies. During volcanic unrest, the appearance of a hotspot is indicative of the breaking of the magmatic system through the surface. In the case of MIROVA, which only detects high-temperature features, such appearance is commonly ascribed to the presence of magma at the surface, or at very shallow depths (Laiolo et al., 2019). For example, during the eruptive crisis of Ubinas in 2014, the detection of a small thermal anomaly inside the deep crater signaled the first appearance of a lava dome (confirmed only later by observations on the ground) after several days of seismic unrest. The opening of a magma path marked the beginning of an intense explosive activity that culminated few weeks later in a series of major explosions (Coppola et al., 2015). The fast detection of thermal anomalies is therefore very important to indicate the opening of the system, and coupled with other geophysical parameters often leads the rise of the alert level, as recently occurred at Sabancaya (Perù) (Reath et al., 2019b). On the other hand, the absence of a thermal anomaly is also important, and may help to discard any possible surface activity associated with deep seismic activity. This occurred for example at the Galeras and Chiles-Cerro Negro (Colombia) volcanoes, which experienced some seismic swarms in the last 4 years (2015–2019) without showing any kind of surface activity (Ebmeier et al., 2016). In other cases, and especially during clear waning phase, the persistence of thermal anomalies is useful to determine the thermal state of the associated lava bodies. At Momotombo (Nicaragua), where lava flowed down the flank during the 2015 eruption, from visual observation it appeared like the eruption had ceased and that the optically black lava had cooled. However, thermal data showed that the lava near the summit and along the flow was still hot. Thermal anomalies, combined with seismic activity, suggested that the lava extrusion was still feeding the flow and that the potential advancement for lava flow front/perimeter was still present. Generally, the presence or absence of thermal anomalies is often used to depict the beginning and the end of eruptive episodes, especially for which direct or indirect observations from other monitoring systems are not available.

Intensity

The intensity of the thermal anomaly, referred to as VRP, is the fundamental parameter of MIROVA and constitutes the main added value compared to other systems able to detect the presence/absence of hotspots, without quantifying their intensity in terms of radiated energy. Besides being a direct measurement of radiated thermal energy, the VRP can be used to calculate the area or the temperature of the lava body using Stephan-Boltzmann law (see details in section "Download, Data Processing, and Sensibility"), if at least one of the two variables can be estimated (or assumed) independently. The area or temperature of a lava dome is a parameter that can be easily understandable even by non-experts, and provides a clear idea of the size of the phenomenon underway. Moreover, during effusive eruptions, the VRP can be used to calculate the Time Averaged lava Discharge Rate (TADR) and the volume of erupted lava, subject to a calibration of the conversion factors or a basic knowledge of the type of erupted lava (Coppola et al., 2016a; Bernard et al., 2019). These second level products (Area, Temperature, TADR, Volume) are important for hazard

evaluation and communication, and require data independent of the satellite monitoring system as well as interpretation skills by the end-user. Finally, the quantification of the thermal activity by means of a parameter that compute in a standardized and consistent way (such as the VRP), allows for the comparison between different volcanoes or between different eruptions of the same volcano. Statistical analysis of the VRP allows identification of distinct thermal regimes (Coppola and Cigolini, 2013) and may be used to detect change of activity, such as from Strombolian activity to effusive activity (Coppola et al., 2013, 2019a; Naismith et al., 2019; see section "Forecasting Eruptive Trends"), or the occurrence of episodes of dome growth (Werner et al., 2017). During the growth of a new spatter cone on February 29, 2016 inside the Nyiragongo Crater, MIROVA data were used to eventually advise about anomalous large thermal emissions within the lava lake and/or the presence of active lava flows in areas around the volcano (see details in the following section).

Location/Dimension of the Hotspot and Its Distance From the Volcanic Summit

Locating the thermal anomaly with precision is fundamental to recognize the type of activity in progress, to assess the areas at risk and possibly to be able to run forecast models (for example, forecasting flooding of lava flows; Harris et al., 2016). The ability to promptly locate these anomalies is closely linked to the spatial and temporal resolution of the sensor used. With its 1 km pixel, the MIROVA system does not have the spatial resolution sufficient to locate the eruptive vents precisely. However, in most cases, this moderate resolution was found to be sufficient to discriminate between intra-crater anomalies (produced, for example, by the fissure opening, lava dome extrusion, development of high-temperature fumarole fields, appearance of lava lakes) and lateral anomalies (associated with lava flows or large pyroclastic flows descending the flanks of the volcano). This information, supplied in a relatively short time (e.g., few hours), was fundamental for hazard evaluation and to timely forecast the eruptive scenarios. It is also useful tool to detect lava flows generated from more distal flank fissures, although naturally, there are many false positives (i.e., fires). At effusive eruptions, thermal data can be used to map (at low resolution, e.g., 1 km) lava flow emplacement in order to detect the position of the flow front and track the formation of lava tubes (Coppola et al., 2019a). At dome-forming volcanoes, such as Sinabung (Indonesia), the spatial distribution/extension of the thermal anomalies allows for an assessment of stable dome growth, indicated by cluster of hot pixels at the summit, while for collapsing dome materials (large rock fall or pyroclastic density currents) and viscous lava flow, the hot pixels will be aligned with a channel down the flank. In the case of hot pixels down a channel, the sector and distance of furthest pixels provides a rapid estimate of hazardous areas that ought to be maintained as part of an exclusion zone. This becomes critical as eruption duration spans years and societal pressure on local officials to re-open evacuated areas increases (see **Supplementary Appendix** – VDAP Survey).

Eruptive Evolution, Trends, and Patterns

In conjunction with seismic, gas geochemistry, visual change and deformation data, MIROVA provides an initial check for level and type of activity at volcanoes, e.g., the occurrence of lava flows, domes or simply hot, degassing open vents. Being able to track relative changes in thermal output (i.e., VRP) as a time series, provides a useful assessment of any changes in activity, although a lack of thermal data does not necessarily means a volcano is cooling off (it can be due to cloud or thick ash cloud cover). Stationary, waning or intensifying trends obviously have different implications on the evaluation of the hazards and can be used (modeled) to define future eruptive scenarios, and possibly to make forecasts. At Piton de la Fournaise (La Réunion Island), the knowledge of the effusion rate trend (derived from thermal data), in combination with previously generated models of the likely lava flow path, has been useful to predict whether the flow will tend to lengthen or shorten, and whether the lava flows will reach the sea, cutting the national road that goes around La Réunion Island (Harris et al., 2017, 2019). Moreover, by comparing this variable with the gas flux and deformation rate, it is possible to analyze the balance of the erupted/degassed material and eventually to quantify magmatic intrusions or endogenous growth (Coppola et al., 2017, 2019a). During the Holuhraun (Iceland) eruption 2014–2015, MIROVA was regularly checked to monitor the level of activity at the eruption site (Barsotti et al., 2019), to estimate of lava discharge rate and, eventually, to declare the end of the eruption based on the observed eruptive trend (Coppola et al., 2017). In the case of Nevado del Ruiz (Colombia), MIROVA's thermal anomaly data matched very well with shallow seismicity increments, ash emissions (seismically associated to volcanic tremor), large SO_2 fluxes, tiltmeters inflationary trends, etc. The largest VRP values have been clearly associated with magma ascent to shallower levels of the volcanic conduit and surface magma extrusion process (lava dome emplacement within the inner part of crater). During the 2018–2019 Manam (Papua New Guinea) eruptions (Global Volcanism Program, 2019), the thermal trends provided confirmation that increased RSAM was due to renewed activity and that the activity involved the effusion of lava flows, and in what direction the flows were moving. After reaching the climax, the thermal data also indicated the waning of the activity, suggesting that the effusive event was coming to an end. Similarly, during the 2014 eruption of Ubinas (Peru), the increasing VRP values were compared with the state of seismicity, as well as with other parameters (such as ash or SO_1 missions, etc.; Coppola et al., 2015) to provide, eventually, recommendations to the civil protection authorities for the evacuation of the population.

How Thermal Data Are Used

The use of the observations/images/data obtained from MIROVA is highly varied and depends fundamentally on four factors: (i) the presence and (quality) of a ground-based monitoring network; (ii) the accessibility of the volcano; (iii) the alert level; and (iv) the type of activity in progress.

Remote-sensed thermal observations clearly provide invaluable information for volcanoes not monitored in other ways, and may represent the only evidence of ongoing volcanic

activity (Coppola et al., 2016a). These data may provide fundamental indications on the evolution of the unrest/eruption (e.g., stationary, increasing, decreasing), although incomplete.

When an eruption begins, remote sensing methods allow the surveillance of volcanic phenomena, and help minimizing the risks associated with direct exposure of observers to the activity. Often, it is very difficult, impossible, or too expensive to make frequent observations of the volcanoes' summit, as well as to measure directly lava flows, domes or fumarole temperatures. It is usually impossible to conduct frequent airborne observations within the crater, so MIROVA data are useful to get a longer time series for routine monitoring, to verify reports, rumors, or provide observations for internal and wider discussions before making a decision to assess the level of activity at the volcano.

At basaltic volcanoes equipped with a large ground-based monitoring network, such as Stromboli, Etna, Piton de la Fournaise, etc., MIROVA is commonly used to estimate time-averaged lava discharge rates (TADR) and erupted volumes in near real time (Coppola et al., 2019a; Laiolo et al., 2019), to define imminent eruptive scenarios (Ripepe et al., 2017) and to model the path and length of lava flows (Harris et al., 2017, 2019).

In summary, the processed data provided by MIROVA are used by the observatories in different ways, but essential for monitoring activities, internal discussions on the volcano's activity level and for real-time calculations of the erupted volume and eruptive trend. This information actually converges to activity reports (daily, weekly, monthly or extraordinary reports), in which the thermal data are integrated with other monitoring parameters in order to evaluate the state of activity and to maintain situational awareness.

The Volcano Disaster Assistance Program (VDAP) also includes the use of the website at trainings offered at volcano observatories where they are just starting to use remote sensing as part of their volcano monitoring. The MIROVA website is freely accessible to observers who do not necessarily have the background knowledge or funding support for more elaborate remote sensing analysis. Furthermore, the website is reliable, immediately accessible and requires no maintenance on their part beyond reliable internet connectivity.

KEY-CASE STUDIES

Below we summarize some case studies for which MIROVA satellite thermal data proved to be an essential element in the detection and characterization of volcanic (thermal) unrest, in the forecast of eruptions and in the recognition of particular trends and patterns.

Thermal Unrest

Volcanic unrest is commonly defined as a change from "normal state" at a volcano, or deviation from its background behavior (Gottsmann et al., 2017). Seismic activity, surface deformation, heat or gas emissions can be used as unrest indicators for a certain volcano and need to be interpreted to be able to implement timely mitigation actions (Phillipson et al., 2013). The appearance of thermal anomalies before an eruption is often considered as an important precursor and a clear symptom of volcanic unrest (Reath et al., 2016). A recent review (Furtney et al., 2018) suggests that about 19% of major eruptions are anticipated by thermal precursors detected by satellites, although the mere presence of thermal activity to a volcano does not necessarily constitute a change from its background level.

The MIROVA archive now embeds 65 of 72 volcanoes that after 2002 produced at least one VEI 3 eruption (Global Volcanism Program database, accessed on 26 June 2019). A preliminary analysis suggests that only 4 to 5 volcanoes of these 65 MIROVA targets, displays anomalies that can be considered as a thermal precursor of the upcoming VEI 3 eruption (**Figure 7**). This number possibly increases if we consider less explosive eruptions and changes from background activity at persistently active volcanoes. However, from our analysis, only 6–8% of the volcanoes seem to develop thermal unrest before a VEI 3 eruption detectable by MIROVA. It is interesting to note that the thermal unrest observed at these volcanoes shows unique behavior in terms of duration, pre- and post-eruption trends, as described below (**Figures 7a–e**):

Sabancaya, Perú (Development of Fumarole Fields – Figure 7a)

This is the archetype of thermal unrest consisting of the gradual appearance of very low-level thermal anomalies (< 1MW) localized at the bottom of a summit crater. It is associated with the slow (∼860 days for Sabancaya) development of a fumarole field within the crater area, showing a slight increase in the area and temperatures of fumaroles and almost constant water-vapor and SO2 plumes rising from the crater (Global Volcanism Program, 2016). The explosive VEI 3 eruption definitely opened the magma path and allowed the underlying magma to come to the surface producing evident and more persistent thermal anomalies (**Figure 7a**).

Santa Ana, El Salvador (Rupture of Hydrothermal System – Figure 7b)

In this case the thermal unrest has a pre-eruptive phase characterized by a long (∼376 days) and gradual development of a high-temperature fumarole field developing on the border of an acidic crater lake. Possibly, this type of thermal precursor develops in response to a magmatic injection at very superficial levels, which causes the rupture of the hydrothermal system feeding the acidic lake (Laiolo et al., 2017). Notably, the interaction between the fumarolic field and the crater lake may eventually cause a "decrease" in thermal activity due to self-sealing phenomena that may precede a major explosion (Laiolo et al., 2017). Unlike the previous case, the explosive event is not followed by a magmatic eruption (with lava dome extrusion and/or recurrent ash-explosions), but it is characterized by the almost total, definitive absence of a thermal anomaly (**Figure 7b**).

Llaima, Chile (Rise of Magmatic Column – Figure 7c)

This type of thermal precursor may occur in basaltic and basaltic-andesitic volcanoes characterized by the reactivation of the central vent after a period of quiescence. The unrest phase is typically characterized by an evident increase in thermal

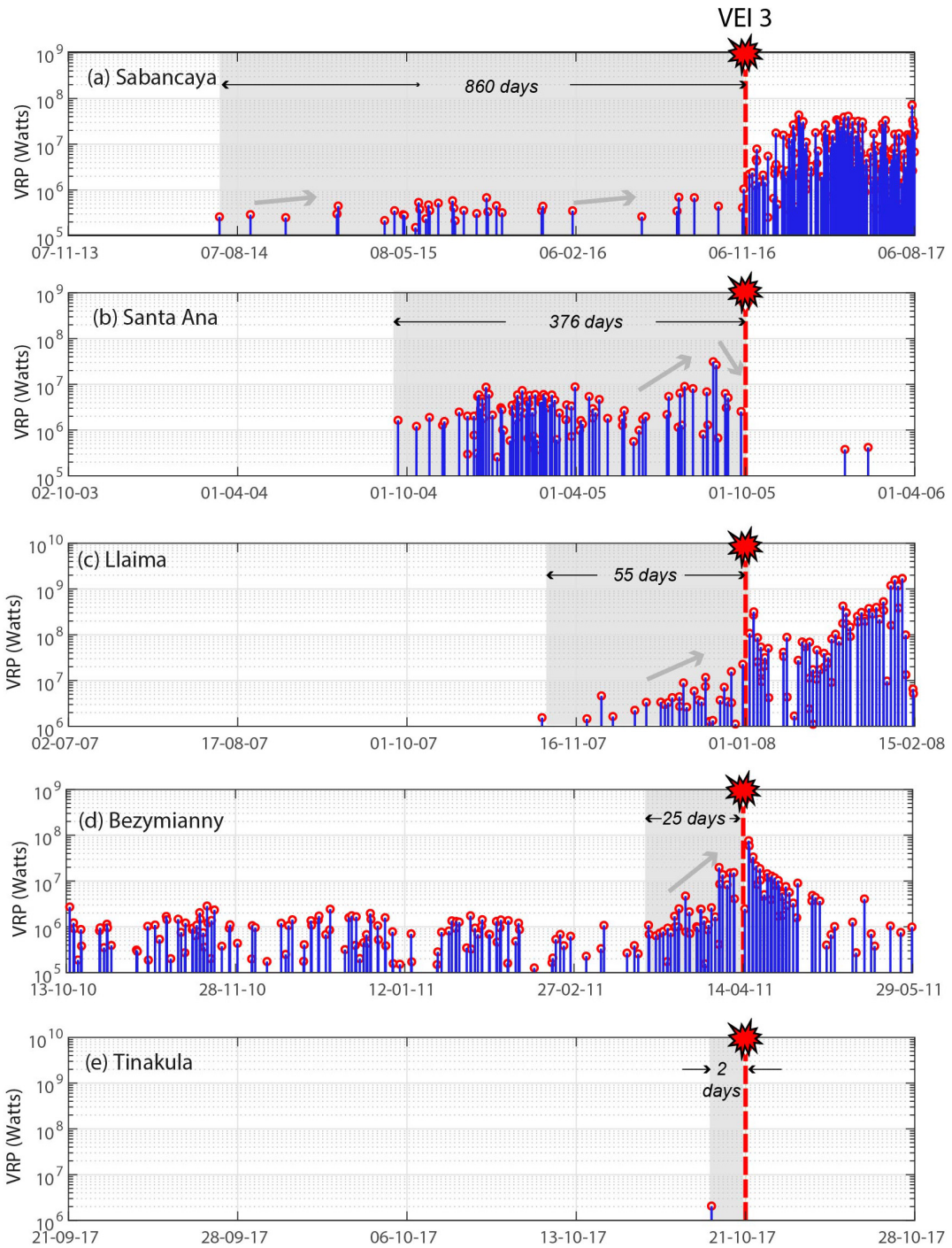

FIGURE 7 | Five cases of thermal unrest detected by MIROVA: **(a)** Sabancaya, **(b)** Santa Ana, **(c)** Llaima, **(d)** Bezymianny, **(e)** Tinakula. The red dashed line indicates the occurrence of a large explosion (VEI 3). The gray fields indicate the periods showing precursory thermal activity. The duration of each thermal unrest phase is indicated with arrows. Note how each volcano shows different behavior of thermal unrest in terms of duration, pre-eruptive level and trend, as well as post-eruptive pattern. See the text for more details.

anomalies inside the summit crater, corresponding to the opening of the system, followed by the ascent of the magmatic column and by increasing explosive activity (Franco et al., 2019), that culminates with a paroxysmal phase (**Figure 7c**). The explosive activity is followed by a further intensification of the effusive activity with the consequent emission of lava flows along the flanks of the volcano (Global Volcanism Program, 2008; Bouvet de Maisonneuve et al., 2012).

Bezymianny, Kamchatka (Increase in Dome Extrusion Rate – Figure 7d)

Activity of Bezymianny consists of ongoing lava-dome growth inside a large horseshoe-shaped crater, accompanied by intermittent explosive activity and pyroclastic flows. As already advised by previous works (van Manen et al., 2010, 2013), some major explosions of Bezymianny are preceded by weeks of gradual increase of the thermal anomaly, thus constituting one of the most robust precursors for this remote volcano. In this case the thermal precursor occurred at a volcano characterized by a persistent, low level thermal activity, associated with the presence of degassing hot cracks and minor explosions. The increase of VRP prior to large explosions (**Figure 7d**) has been attributed to an increase in the dome extrusion rate (van Manen et al., 2010, 2013).

Tinakula, Solomon Islands (Sudden Opening of Magma Path – Figure 7e)

After more than 5 years of quietness, on 19 October 2017, a low thermal anomaly was detected by MIROVA at the Tinakula volcano. This small thermal precursor was the unique sign of renewed eruptive activity at this remote volcano and preceded by only 2 days the large VEI 3 explosion which occurred on 21 October (Global Volcanism Program, 2018; Laiolo et al., 2018). This short unrest is probably a limit case for MIROVA-type systems (i.e., based on Moderate Resolution data) and suggests that the first thermal anomaly, detected after a several year-long period of quiescence, must be seriously evaluated and can represent a solitary short-term precursor of an incoming major eruption. On the other hand, it also outlines the need to have thermal satellite data with a high temporal resolution by keeping a high efficiency and a very limited number of false alerts. In the specific case of Tinakula it was necessary the post-event supervision (e.g., after the VEI 3 explosion) of the image of October 19, in order to exclude that it was a false alert. Actually, one real problem is how to assess the accuracy of each thermal alert, since there will always be a possibility of false or non-volcanic alerts. Fires constitute non-volcanic heat sources frequently detected in volcanic areas, but their distinction from volcanic hotspots cannot currently be done on a spectral basis. In addition, a smaller but variable percentage of false alerts, generally comprised between 0 and 3% (number of false alerts/number of MODIS overpasses), is detected by the MIROVA system at different volcanoes (Coppola et al., 2016b). These false alerts depend on the regional and local environmental conditions as climate, elevation, topography and land cover type.

With the exception of these five cases, our data suggest that most of VEI 3 eruptions are not preceded by thermal anomalies detectable by monitoring systems such as MIROVA. This is possibly due to the sensitivity of this type of systems that fail to detect small, low-intensity thermal anomalies. Indeed, the percentage of thermal unrest rises considerably if thermal data with higher spatial resolution are used as suggested by Furtney et al. (2018) and Reath et al. (2019a). On the other hand, it cannot be excluded that the appearance of thermal precursors and the explosivity index of the subsequent eruption are somehow related to the degree of openness of the shallow magmatic system. A more detailed analysis, which also considers the possible appearance/variation of thermal anomalies before the numerous VEI 1-2 eruptions that have occurred in the MODIS era, will surely help to clarify whether there is a correlation between the timing and intensity of thermal unrest and the magnitude of the explosive eruption.

Forecasting Eruptive Trends

Forecasting the time and scale of a volcano eruption is the goal of several monitoring and research efforts (see Marzocchi and Bebbington, 2012 for a review). Generally, with eruption forecasting we mean the ability to evaluate the occurrence of a volcanic eruption on the basis of a probabilistic approach. Forecasting what happens after eruption onset, or when an eruption will come to an end is also critical for the decision-making procedure and for updating eruptive scenarios (Bebbington and Jenkins, 2019).

As illustrated in the previous paragraph, in most cases, the MIROVA data do not record thermal precursors before > VEI 3 eruptions and therefore in many cases do not allow to make forecasts of imminent major explosive eruptions (with some important exceptions; **Figure 7**). However, thermal data show their strength during the course of eruptions, allowing, in some cases, the generation of forecasts of future activity based on the analysis of eruptive trends (Bonny and Wright, 2017).

Many effusive eruptions show a characteristic exponential decrease of effusion rates over time, ascribed to elastic or inelastic processes occurring within the decompressing magmatic system (Wadge, 1981; Coppola et al., 2017). In **Figure 8a** we show the TADR and erupted volumes, reconstructed through the MIROVA data, for the April 2018 eruption of Piton de la Fournaise (Harris et al., 2019) that can be considered as archetypal for this type of trend. Taking into account the uncertainty in the TADR estimates (typically between 30 and 50%; Coppola et al., 2019b), several types of predictions are possible. For example, the initial flow rate (Q_0) can be used (as soon as the MODIS data has been processed) within an effusive response protocol (Harris et al., 2017, 2019), to timely provide the observatory flow path projections and maximum run-out of the emplacing lava flow (**Figure 8b**).

Once the exponential trend has become recognizable, as in the case of the Bárðarbunga-Holuhraun (Iceland) 2014–2015 eruption, extrapolation from initial data can be used to evaluate final (or intermediate) erupted volumes (**Figure 9a**), useful, for example, to run simulation codes for lava flow invasion maps (Tarquini et al., 2019).

Projection of effusion rate trends to the future (black line **Figure 9b**) may also be used to forecast/predict the end of this type of eruptions (Coppola et al., 2017). In fact, before the end of the Bárðarbunga-Holuhraun eruption there was a drastic decrease in the effusion rates with respect to the model based upon the exponential curve. In this case, the phenomenon was attributed to the gradual closure of the dike, once the effusion rates (or driving pressure) dropped below a critical value (yellow star in **Figure 9b**). The detection in real-time of a change from the expected trend can therefore be useful information to estimate when the eruption end (Coppola et al., 2019a).

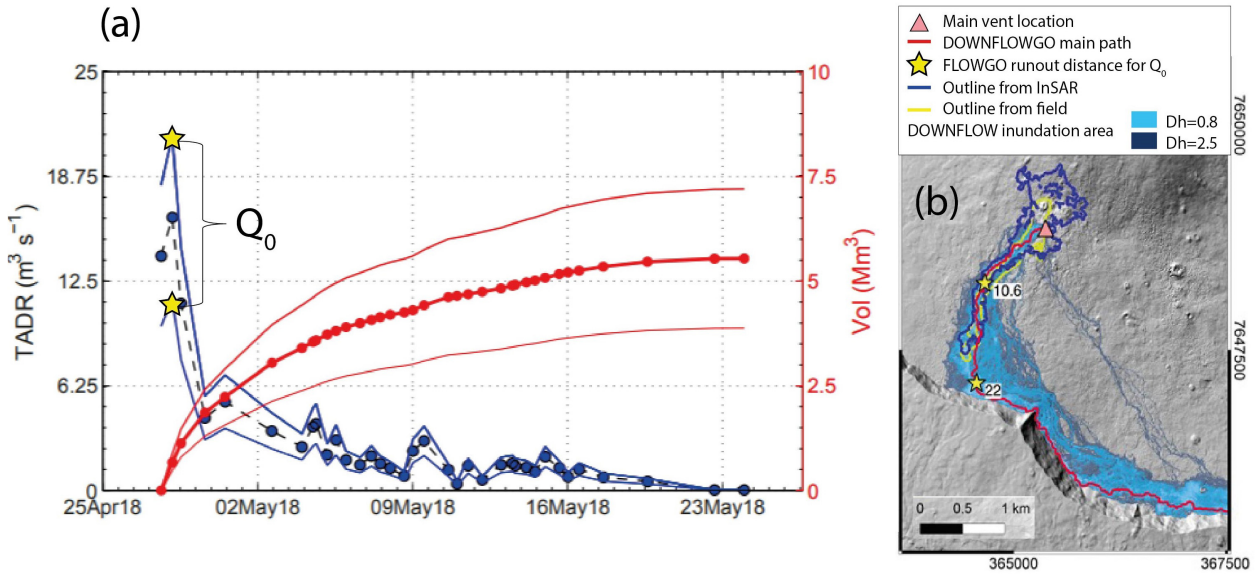

FIGURE 8 | (a) Middle Infrared Observations of Volcanic Activity-derived TADR (blue circles) and cumulative volume (red circles) provided to the Observatoire Volcanologique du Piton de la Fournaise (OVPF) during the April 2018 eruption. Q_0 is the initial flow rate, used to model the maximum runout of the emplacing lava flow (modified from Harris et al., 2019). **(b)** Lava flow inundation map derived from ingestion of MIROVA-derived TADR into DOWNFLOW-PyFLOWGO models. The numbers (in $m^3\ s^{-1}$) next to each star correspond to maximum and minimum estimate of Q_0 measured on 28 April 2018. Overlain are the limits of the flow field defined from InSAR incoherence (blue outline) and field mapping (yellow outline) on the same dates. Background shows the DOWNFLOW inundation area (modified from Harris et al., 2019).

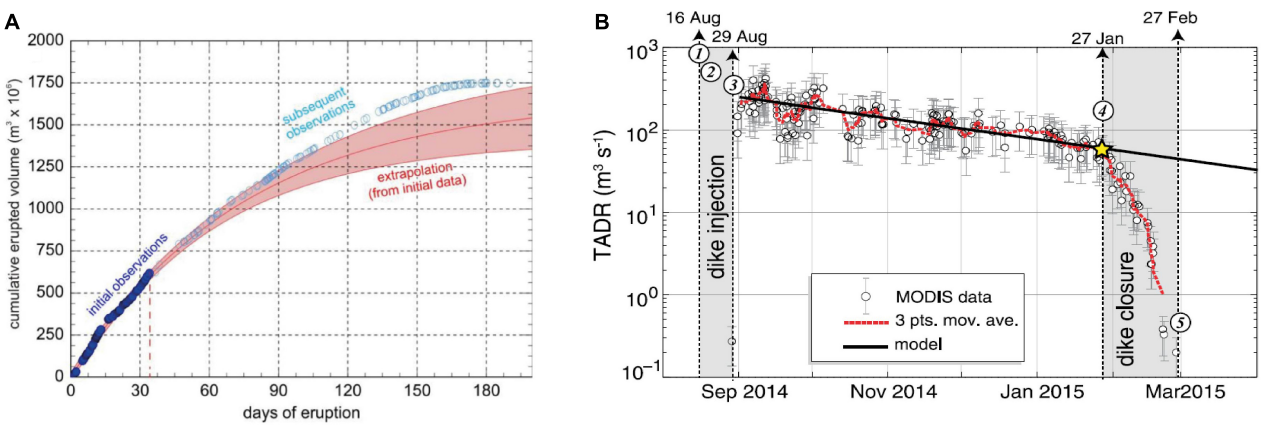

FIGURE 9 | (A) Extrapolation of the cumulative erupted volume during the Holuhraun 2014–2015 eruption, based on the initial 5 weeks of observations (modified from Tarquini et al., 2019), **(B)** Time-averaged lava discharge rate (TADR) measured during Holuhraun eruption (Iceland) (black circles; modified from Coppola et al., 2017) shows exponential decay of effusive activity. Departure from exponential trend began on 27 January 2015 and preluded the end of the eruption on 27 February. The yellow star indicates the critical flow rate Qc of ~50 $m^3\ s^{-1}$ when dike started to close. Numbered circles indicate main steps of eruption: (1) start of rifting episode and lateral magmatic injection; (2) start of caldera subsidence; (3) start of effusive eruption; (4) closure of lateral dike; and (5) end of eruption (modified from Coppola et al., 2017).

At persistently active volcanoes, such as Etna or Stromboli, the long-term analysis of MIROVA data has allowed the determination of specific thresholds (**Figure 10**) that separates the typical open-vent activity (with continuous degassing and intermittent strombolian activity), from more intense phases characterized by effusive activity and/or fountaining episodes (Coppola et al., 2013, 2019a). According to the authors, these thresholds represent a critical magma flux (about 0.1–0.3 $m^3\ s^{-1}$) above which the ascending magma can no longer be recycled in the conduit, and must be partially or completely extruded through effusive activity. The definition of these thresholds (blue dashed lines in **Figure 10**), allows the separation of the different regimes of activity, making it possible to track the rise of magma within the conduit and to advise about potential transitions toward magma effusion (Valade et al., 2016; Ripepe et al., 2017; Laiolo et al., 2019).

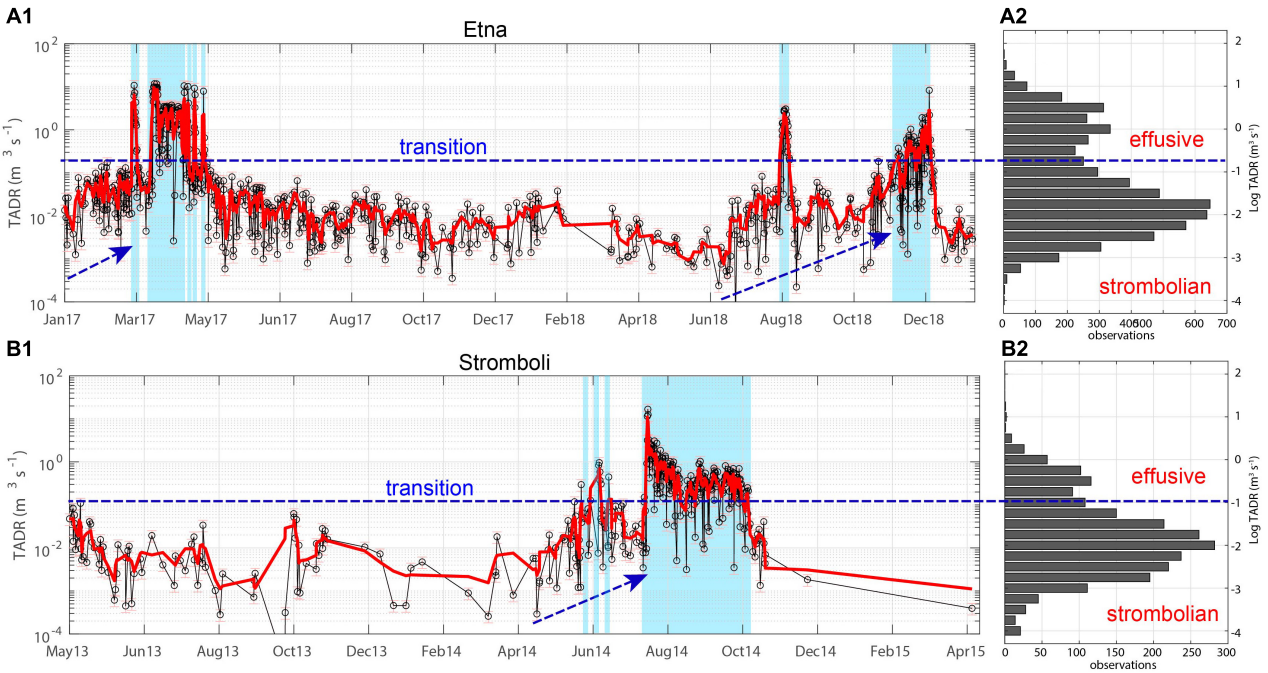

FIGURE 10 | Two-years long time-series of MIROVA-derived TADR for Etna **(A1)** and Stromboli **(B1)** volcanoes (modified from Valade et al., 2016 and Laiolo et al., 2019, respectively). A threshold separating the Strombolian and the effusive regime, is calculated from the statistical analysis of log-transformed TADRs **(A2,B2)** that outline the bimodal behaviors of magma flux.

LIMITS AND FUTURE DEVELOPMENTS

The surveys carried out by the observatories (**Supplementary Appendix**) highlight the current limits of the MIROVA system and provide guidelines for future development of an optimal satellite thermal monitoring system. In particular, the following points were highlighted:

Image Quality Assessment

Providing an evaluation of cloudiness and image/data quality is fundamental. In particular, any hot spot detection system should be able to quantify the effects of clouds and viewing geometry condition, within each acquired image (Coppola et al., 2016a). This fundamental step is currently absent in all the operational systems (**Supplementary Table S1**) and surely requires further efforts. One particular goal is to be able to determine automatically if the absence of a hotspot is real (no sign of thermal anomaly) or if it is due to the presence of clouds or to unfavorable viewing geometry. Typical estimates of the average cloud fraction within a region of interest may be useful for long-term analysis but not practical for operational monitoring in real time, where every single image must be interpreted. Moreover, when considered over large areas, the quantification of cloud fraction may cause misinterpretation of thermal data. In fact, in many cases thermal anomalies within high-altitude summit craters may be discarded or classified as strongly attenuated, because the surroundings pixels are cloudy (although the crater is actually without cloud cover). Quantification of cloud attenuation on a pixel per pixel basis would be an ideal solution (Koeppen et al., 2011), but this would require the collection and analysis of many more bands, including ancillary metadata and other atmospheric properties for every acquired image. Although this approach may provide excellent results, it remains time- and resource- consuming, especially for real time analysis. Similarly, as several volcanoes have steep slopes, the influence of topography on lava flow quantification from satellite thermal data may be important and require case by case correction models (Zakšek et al., 2017). An apparent decrease in heat flux may be due to unfavorable viewing conditions. This information must be accessible to users in order to correctly interpret each individual image. A promising solution is provided by machine learning (i.e., Valade et al., 2019), where an artificial intelligence is instructed on the basis of a supervised manual selection of cloud free images acquired in optimal viewing conditions.

Improve Spatial Resolution

The spatial resolution of the satellite thermal detection system is fundamental in every aspect of volcanic monitoring. In particular, it has been proved that the integration of high spatial resolution data in the TIR (i.e., ASTER; Landsat8-TIRS) as well as in the NIR/SWIR (i.e., Landsat8-OLI; Sentinel2) greatly improves the ability to detect smaller or low intensity thermal anomalies (Jay et al., 2013; Reath et al., 2019a; Valade et al., 2019). From an operational point of view, this translates into detecting a thermal precursor with respect to days/months earlier than moderate-resolution systems (Reath et al., 2019b). Nevertheless, integration of multisensor thermal data into a single volcanic hotspot detection system is still matter of development (Laiolo

et al., 2019), and currently no operative system exists that systematically provide this integrated information on the web (**Supplementary Table S2**).

Moreover, given the variability of wavelengths at which these sensors operate (from SWIR to MIR and TIR), the thermal information retrieved display different sensitivities to the wide range of temperatures of volcanological interest (i.e., from 50 to 1200°C) and is often inhomogeneous between the different datasets (for example, spectral radiance, hotspot area, temperature, radiative power).

A preliminary comparative study between MODIS-MIROVA and SENTINEL2 (Massimetti et al., 2018; Valade et al., 2019) showed that the two systems provide extremely coherent and complementary information. The example of **Figure 11** shows what could be an integrated output of these two datasets (Massimetti et al., 2018) for the case of Agung volcano. The frequent acquisition of SENTINEL2 images (every 5 days) allows the tracking of the evolution of the area of the thermal anomaly inside the Agung crater, with a discrete temporal detail (red circles in **Figure 11**). The latter is in excellent agreement with the thermal flux measured by the MODIS (blue stem in **Figure 11**) to which it adds a high spatial resolution (20 m in the NIR/SWIR) that allows the location and mapping of the thermal anomaly inside the crater with great detail. Small changes in the location, area and or temperature of the hot feature are thus easily tracked by SENTINEL 2 data, and are coherent with MIROVA dataset. An additional improvement can be obtained by integrating also the data provided by Landsat8-OLI sensor (30 m), considering the appropriate spectral bands in NIR/SWIR.

Moving toward the TIR-based systems, it has been shown that sensors such as ASTER (Ramsey et al., 2004) and LANDSAT8-TIRS (Blackett, 2014) allow the monitoring of low temperature thermal anomalies, such as fumaroles, hydrothermal systems, temperature of crater lakes, otherwise undetectable via systems using the NIR, SWIR or MIR bands. The integration of these data is certainly an opportunity that has not been currently exploited.

Improve Temporal Resolution of MIR Data

The temporal resolution is also extremely important to promptly detect a thermal anomaly, as well as to follow the course of an eruptive crisis. Increasing the frequency of thermal observations can be achieved through two ways: (*i*) adding new coherent datasets, from other similar polar sensors, and (*ii*) processing geostationary data.

The acquisition, processing and integration of thermal data from other sensors having MIR channels, such as the VIIRS or the SENTINEL 3, constitutes a relatively simple step to implement the VRP time series provided by MIROVA. In fact, these sensors have spatial and spectral characteristics very similar to MODIS (Blackett, 2015) that allow the direct application of the algorithms behind MIROVA on the new acquired data. Their processing would therefore allow thermal anomalies to be detected more frequently and with a greater probability of acquisition in optimal conditions. The main obstacle for such implementation remains the quantity of data to be analyzed and the storage capacity of the local server. These problems require the development of a more complex infrastructure than the existing one or, alternatively, the use of cloud computing services such as those provided by Google Earth Engine[6] or Amazon Web Services[7]. However, the products useful for the application of the MIROVA algorithm (geolocated, corrected spectral radiances) are not yet available on these platforms in near real time, making this option currently impossible.

Given the low spatial resolution of geostationary platforms (**Supplementary Table S1**), the hot spot detection systems based on these sensors are generally not able to detect low intensity thermal precursors. However, once an eruption has begun, it is possible to follow the event with temporal resolutions up to 5–15 min which make them extremely useful during crisis management (i.e., Ganci et al., 2011; Schneider et al., 2014; Gouhier et al., 2016; Lombardo, 2016; Patrick et al., 2016). The analysis of these data at high temporal frequency and their integration with systems based on polar satellites (such as MODIS) is not trivial and requires the processing of data in virtually streaming mode. The recent availability of geolocated and radiometrically pre-processed geostationary image data, provided by systems like EUMETVIEW[8] in near real time, is certainly a first fundamental step which needs further efforts and development to integrate these high-frequency datasets into an multiplatform satellite volcanic monitoring systems.

It is hoped that with the continuous technological development, future satellite missions will be specifically dedicated to volcanic monitoring, or at least will be characterized by sensors with appropriate features that would make a breakthrough in volcanic monitoring. In particular, it is absolutely necessary to maintain the continuity of observations in the MIR (such as MODIS and VIIRS), to continue the almost 20-years-long dataset, provided by MIROVA and MODVOLC, possibly improving both spatial and temporal resolution. The presence of SWIR and TIR data, co-registered with MIR and not saturated, would also be a significant improvement for future sensors that would permit the coverage, in a single system, of the wide range of temperature observed on volcanoes. This would allow a detailed characterization of thermal anomalies, potentially useful for real-time determination of the eruption style and composition of terrestrial lavas (Wright et al., 2011).

Data/Image Availability, Archive and Sharing

The availability of data and the possibility of them being searched, displayed and downloaded in real time is another important element to make a volcanic hot spot detection system fully operational. Currently, MIROVA does not allow this possibility, which is compensated by sharing data via email in the case of need. This step requires considerable and continuous efforts by the system developers, but allows the checking of the dataset for the presence of any false alerts, to remove other thermal emitters, such as fires, and to provide support for

[6]https://earthengine.google.com/

[7]https://aws.amazon.com

[8]https://eumetview.eumetsat.int/mapviewer/

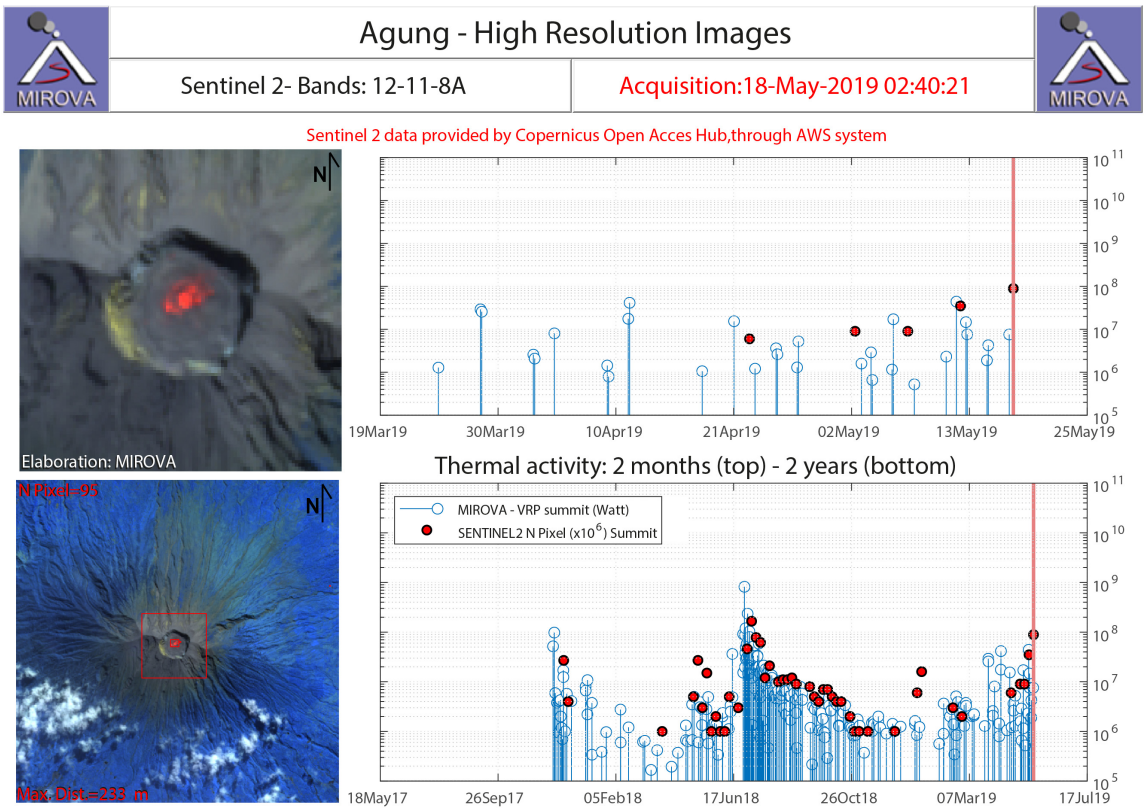

FIGURE 11 | Example of integration of MODIS-MIROVA (1 km) and SENTINEL2 (20 m) thermal data. The panels on the left show the SENTINEL 2 image of 18 May 2019 (combination of bands 12, 11, 8A) acquired over Agung volcano (Indonesia). On the top-left is shown a zoomed view of the crater area (2 km × 2 km) enhancing the presence of a hot lava body. The panels on the right show the MIROVA thermal flow time series (stems) and SENTINEL 2 hot pixel number (circles) of the last 2 months (high) and 2 years (low). The red circles represent the extension of the thermal anomaly within the Agung crater (N Pixel × 10^6). Note the excellent correlation between the volcanic radiative power, measured by the MODIS, and the extent of the anomaly (number of hot pixels), detected by SENTINEL 2.

the interpretation of the data, which in some cases can be ambiguous for non-experts. It can therefore be considered a sort of quality control service of the data that reduces the uncertainty (including cleaning of data sets of unreliable or untrustworthy data points) and any indirect, incidental or consequential damages arising out of any use of, or inability to use, the data.

Nevertheless, the creation of a web-based database for the entire MIROVA archive (time series) remains a task for future development to ensure faster information flow. The development of the apps (for mobiles and desktop pc) is an additional data sharing method, which would allow each individual user to select only the volcanoes of interest observed by MIROVA. Updates could be available through real-time notifications.

The system could be also improved by providing a simple display of daily, monthly and annual values (including cumulative curves) that could be easily accessed by volcano observatories for research/monitoring purposes.

Although the time series plots of VRP and distance are very useful for ongoing situation information, visualization of the image is useful to get the full sense for the spatial pattern of the thermal anomaly, or to verify the presence of clouds or ash plumes above the volcano. MIROVA offers the ability to check the latest 10 images on the web site, but is not possible to go back days, months, years and visualize the archived images, thermal alerts and hotspots. In addition to the time series, a data archive of thermal images, searchable and downloadable on line, is certainly a useful tool for the post-event analysis, but also for real-time assessments. Comparison of older data to the near-real time scenes allows for a quick reality check of the current situation to the last thermal events to see whether this is a repeat of normal behavior of whether this new thermal pattern is anomalous and atypical.

The integration of the thermal dataset with the satellite image viewing capabilities offered by cloud platforms such as WorldView[9] could be a particularly interesting solution to greatly simplify the visualization of MODIS images by local systems (such as MIROVA), by maintaining the possibility of linking the VRP time series with an independent image browser. However, building an online archive requires a major upgrade of the system and improved storage capacity (millions of images to manage). MODVOLC (Wright et al., 2004) offers an efficient ability to go back days, months, years and still get a quick plot of the distribution of thermal alerts, but it does not store the images.

[9]https://worldview.earthdata.nasa.gov/

True Global Detection Capabilities Keeping High Sensitivity

A final limit that could be overcome is the transformation of a system like MIROVA into a real global volcanic monitoring system. In fact, many observatories have shown interest in extending the satellite observations currently provided by MIROVA to many more volcanoes. However, the current limit of download and storage capacity of the system does not allow for such expansion, making MIROVA a potentially global system only. Hotspot detection systems that are really global, such as MODVOLC or FIRMS, offer effective coverage over the entire earth's surface, but at the expense of less efficiency in detecting low-intensity thermal anomalies (due to the simplicity of the algorithm). Moreover, they do not allow the display of original images, which we have seen to be fundamental for the correct interpretation of the thermal anomalies in real time. This major limitation, essentially technological, could possibly be overcome by a hardware upgrade of the current system, allowing the inclusion of all the Holocene volcanoes (about 1500) currently present in the Global Volcanism Database. This option would limit the amount of data to be analyzed only to areas of volcanic interest (not to the whole Earth's surface as it is done for MODVOLC or for FIRMS), retaining the possibility to add, in few hours at most, new targets in areas not yet covered. Alternatively, the development of 5 or 6 local systems (MIROVA clones), hosted by respective volcanological observatories, and focused only on regions (e.g., Asia, Africa, Europe, etc.) or countries can be a technologically easier solution to implement (it simply requires settling MIROVA on different targets in each region), which however involves an adaptation of the system to the specific hardware and networking requirements of each observatory.

CONCLUSION

Middle Infrared Observations of Volcanic Activity is a system that provides satellite observations, in near real time, regarding the thermal state of more than 200 volcanoes worldwide. The system provides on a specific website[10] thermal images and time series of VRP that are examined daily by more than 15 volcanological observatories. This information is being used daily to assess the presence/absence of thermal activity and eventually to locate and quantify these anomalies during phases of unrest or during eruptions. The recognition of particular thermal data trends or patterns, and the integration with other geophysical/geochemical parameters, permits an improved evaluation of the activity of a volcano. In many cases, the thermal data have been fundamental for the detection of the appearance of lava domes at the bottom of deep craters, or to quantify effusion rates and volumes erupted during effusive eruptions. In open vent volcanoes, the thermal data also permit to track the rise of the magmatic column that precedes effusive eruptions, although the detection of thermal precursors before major explosions remain currently a challenge for MIROVA.

[10]www.mirovaweb.it

All these applications are the result of a long chain of data sharing which, starting from the raw data generated by satellite and delivered by the space agency (NASA) via an open-data policy, finally reaches the observatories, as a useful product for volcanic monitoring.

The current system is, however, limited in a series of aspects that include: (i) the moderate spatial and temporal resolution of the data, (ii) the limited capacity to download and explore the entire archive of time series images, and (iii) the non-global coverage.

Several improvements can be made to partially overcome these limits. However, all these enhancements require human effort, as well as financial and technological resources that can be only partially supported by individual observatories or small research groups. As envisioned by Pritchard et al. (unpublished), the future development of a global volcano remote sensing observatory requires international support at each stage of the processing chain, from the acquisition and elaboration of the data, to their interpretation and dissemination to the volcano observatories or civil protection agencies.

Middle Infrared Observations of Volcanic Activity is a small pilot project, originally created to monitor only a few volcanoes. However, thanks to the sharing of open data and the growing collaboration with volcanological observatories, it has become a useful tool for monitoring hundreds of volcanoes around the world. Thanks to this experience, we are convinced that the role of thermal remote sensing will grow in the coming years, due to the great contribution provided by this open data to the comprehension of volcanic phenomena, and in particular for the hazard evaluation of volcanoes worldwide.

DATA AVAILABILITY STATEMENT

The datasets generated for this study are available on request to the corresponding author.

AUTHOR CONTRIBUTIONS

DC conceived and wrote the work. DC and ML have developed and analyzed the MIROVA data. FM analyzed the Sentinel2 images. All authors listed have made a substantial, direct and intellectual contribution to the work, and approved it for publication.

FUNDING

This research has benefited from funding provided by the Italian Presidenza del Consiglio dei Ministri, Dipartimento della Protezione Civile (DPC) as part of the DEVnet Program (2014–2016) that includes a collaborative project between the Earth Sciences departments of the University of Florence and the University of Turin. This research was partially supported by the Italian Ministry for Universities and Research (MIUR).

ACKNOWLEDGMENTS

We thank the three reviewers for their constructive comments and for the attention paid to revising this work. We acknowledge the LANCE-MODIS system (http://lance-modis.eosdis.nasa.gov/) for providing Level 1B MODIS data in near-real time. We thank many collaborators and students of the University of Turin who have contributed to the development and maintenance of the MIROVA system.

SUPPLEMENTARY MATERIAL

The Supplementary Material for this article can be found online at: https://www.frontiersin.org/articles/10.3389/feart.2019.00362/full#supplementary-material

TABLE S1 | Thermal Remote sensing systems available on the web, for operational volcano monitoring.

TABLE S2 | Synthesis of observatories currently using MIROVA in support of monitoring activity. From Global Volcanism Program (2013).

REFERENCES

Anantrasirichai, N., Biggs, J., Albino, F., Hill, P., and Bull, D. (2018). Application of machine learning to classification of volcanic deformation in routinely generated InSAR data. *J. Geophys. Res. Solid Earth* 123, 6592–6606.

Barsotti, S., Oddsson, B., Gudmundsson, M. T., Pfeffer, M. A., Parks, M. M., et al. (2019). Operational response and hazards assessment during the 2014–2015 volcanic crisis at Bárðarbunga volcano and associated eruption at Holuhraun, Iceland. *J. Volcanol. Geotherm. Res.* doi: 10.1016/j.jvolgeores.2019.106753

Bebbington, M. S., and Jenkins, S. F. (2019). Intra-eruption forecasting. *Bull. Volcanol.* 81:34. doi: 10.1007/s00445-019-1294-9

Bernard, B., Gibson, S., Ramon, P., Gleeson, M., Stock, M., Hernandez, S., et al. (2019). Chronology and phenomenology of the 1982 and 2015 wolf volcano eruptions, Galápagos Archipelago. *J. Volcanol. Geotherm. Res.* 374, 26–38. doi: 10.1016/j.jvolgeores.2019.02.013

Blackett, M. (2014). Early analysis of landsat-8 thermal infrared sensor imagery of volcanic activity. *Remote Sens.* 6, 2282–2295. doi: 10.3390/rs6032282

Blackett, M. (2015). An initial comparison of the thermal anomaly detection products of MODIS and VIIRS in their observation of Indonesian volcanic activity. *Remote Sens. Environ.* 171, 75–82. doi: 10.1016/j.rse.2015.10.002

Bonny, E., and Wright, R. (2017). Predicting the end of lava flow-forming eruptions from space. *Bull. Volcanol.* 79:52. doi: 10.1007/s00445-017-1134-1138

Bouvet de Maisonneuve, C., Dungan, M. A., Bachmann, O., and Burgisser, A. (2012). Insights into shallow magma storage and crystallization at Volcán Llaima (Andean Southern Volcanic Zone, Chile). *J. Volcanol. Geotherm. Res.* 211-212, 76–91. doi: 10.1016/j.jvolgeores.2011.09.010

Brown, S. K., Loughlin, S. C., Sparks, R. S. J., Vye-Brown, C., Barclay, J., Calder, E., et al. (2015). "Global volcanic hazard and risk," in *Global Volcanic Hazards and Risk* (Cambridge, MA: Cambridge University Press).

Coppola, D., Barsotti, S., Cigolini, C., Laiolo, M., Pfeffer, M. A., and Ripepe, M. (2019a). Monitoring the time-averaged discharge rates, volumes and emplacement style of large lava flows by using MIROVA system: the case of the 2014-2015 eruption at Holuhraun (Iceland). *Ann. Geophys.* 61:VO221. doi: 10.4401/ag-7812

Coppola, D., Campion, R., Laiolo, M., Cuoco, E., Balagizi, C., Ripepe, M., et al. (2016a). Birth of a lava lake: Nyamulagira volcano 2011-2015. *Bull. Volcanol.* 78, 1–13. doi: 10.1007/s00445-016-1014-7

Coppola, D., and Cigolini, C. (2013). Thermal regimes and effusive trends at Nyamuragira volcano (DRC) from MODIS infrared data. *Bull. Volcanol.* 75:744. doi: 10.1007/s00445-013-0744-z

Coppola, D., Laiolo, M., Cigolini, C., Donne, D. D., and Ripepe, M. (2016b). Enhanced volcanic hot-spot detection using MODIS IR data: results from the MIROVA system. *Geol. Soc. Lond. Spec. Publ.* 426, 181–205. doi: 10.1144/sp426.5

Coppola, D., Laiolo, M., Massimetti, F., and Cigolini, C. (2019b). Monitoring endogenous growth of open-vent volcanoes by balancing thermal and SO2 emissions data derived from space. *Sci. Rep.* 9:9394. doi: 10.1038/s41598-019-45753-4

Coppola, D., Macedo, O., Ramos, D., Finizola, A., Delle Donne, D., Del Carpio, J., et al. (2015). Magma extrusion during the Ubinas 2013–2014 eruptive crisis based on satellite thermal imaging (MIROVA) and ground-based monitoring. *J. Volcanol. Geotherm. Res.* 302, 199–210. doi: 10.1016/j.jvolgeores.2015.07.005

Coppola, D., Piscopo, D., Laiolo, M., Cigolini, C., Delle Donne, D., and Ripepe, M. (2013). Radiative heat power at stromboli volcano during 2000–2011: twelve years of MODIS observations. *J. Volcanol. Geotherm. Res.* 215–216, 48–60. doi: 10.1016/j.jvolgeores.2011.12.001

Coppola, D., Ripepe, M., Laiolo, M., and Cigolini, C. (2017). Modelling satellite-derived magma discharge to explain caldera collapse. *Geology* 45, 523–526. doi: 10.1130/G38866.1

Davies, D. K., Ilavajhala, S., Wong, M. M., and Justice, C. O. (2009). Fire information for resource management system: archiving and distributing modis active fire data. *IEEE Trans. Geosci. Remote Sens.* 47, 72–79. doi: 10.1109/tgrs.2008.2002076

Dean, K. G., Jon, D., Kevin, E., Pavel, I., and Ken, P. (2002). "Operational satellite monitoring of volcanoes at the alaska volcano observatory," in *Monitoring Volcanic Hotspots Using Thermal Remote Sensing, Advances in Environmental Monitoring and Modelling*, eds A. J. H. Harris, E. Wooster, and D. A. Rothery, (Anchorage: Alaska Volcano Observatory).

Delgado, F., Poland, M., Biggs, J., Ebmeier, S., Sansosti, E., Lundgren, P., et al. (2019). lessons learned from the ceos volcano pilot in latin american and the ongoing volcano demonstrator project. *Geophys. Res. Abstr.* 21, EGU2019–EGU14981.

Ebmeier, S. K., Andrews, B., Araya, M. C., Arnold, D. W. D., Biggs, J., Cooper, C., et al. (2018). Synthesis of global volcano deformation observations: implications for volcano monitoring and the lateral extent of magmatic systems. *J. Appl. Volcanol.* 7:2.

Ebmeier, S. K., Elliott, J. R., Nocquet, J.-M., Biggs, J., Mothes, P., Jarriìn, P., et al. (2016). Shallow earthquake inhibits unrest near chiles–cerro negro volcanoes, ecuador–colombian border. *Earth Planet Sci. Lett.* 450, 283–291. doi: 10.1016/j.epsl.2016.06.046

Elvidge, C. D., Zhizhin, M., Hsu, F., and Baugh, K. E. (2013). VIIRS nightfire: satellite pyrometry at night. *Remote Sens.* 5, 4423–4449. doi: 10.3390/rs5094423

Fearnley, C. J., McGuire, W. J., Davies, G., and Twigg, J. (2012). Standardisation of the USGS volcano alert level system (VALS): analysis and ramifications. *Bull. Volcanol.* 74, 2023–2036. doi: 10.1007/s00445-012-0645-6

Franco, L., Palma, J. L., Lara, L. E., Gil-Cruz, F., Cardona, C., Basualto, D., et al. (2019). Eruptive sequence and seismic activity of llaima volcano (Chile) during the 2007–2009 eruptive period: inferences of the magmatic feeding system. *J. Volcanol. Geotherm. Res.* 379, 90–105. doi: 10.1016/j.jvolgeores.2019.04.014

Furtney, M. A., Pritchard, M. E., Ebmeier, S. K., Jay, J. A., Carn, S. A., McCormick, B. T., et al. (2018). Synthesizing multi-sensor, multi-satellite, multi-decadal data sets for global volcano monitoring. *J. Volcanol. Geotherm. Res.* 365, 38–56. doi: 10.1016/j.jvolgeores.2018.10.002

Ganci, G., Vicari, A., Fortuna, L., and Del Negro, C. (2011). The HOTSAT volcano monitoring system based on combined use of SEVIRI and MODIS multispectral data. *Ann. Geophys.* 54, 544–550.

Global Volcanism Program, (2008). "Report on llaima (Chile)," in *Bulletin of the Global Volcanism Network*, ed. R. Wunderman, (Washington, DC: Smithsonian Institution), BGVN200801–BGVN357110.

Global Volcanism Program, (2013). "East diamante (284201)," in *Volcanoes of the World, v. 4.8.0*, ed. E. Venzke, (Washington, DC: Smithsonian Institution).

Global Volcanism Program, (2016). "Report on sabancaya (Peru)," in *Bulletin of the Global Volcanism Network, 41:5*, ed. E. Venzke, (Washington, DC: Smithsonian Institution).

Global Volcanism Program, (2018). "Report on tinakula (Solomon Islands)," in *Bulletin of the Global Volcanism Network, 43:2*, ed. E. Venzke, (Washington, DC: Smithsonian Institution).

Global Volcanism Program, (2019). "Report on manam (Papua New Guinea)," in *Bulletin of the Global Volcanism Network, 44:2*, eds A. E. Crafford, and E. Venzke, (Washington, DC: Smithsonian Institution).

Gordeev, E. I., Girina, O. A., Lupyan, E. A., Sorokin, A. A., Kramareva, L. S., Efremov, V., et al. (2016). The volsatview information system for monitoring the volcanic activity in Kamchatka and on the Kuril Islands. *J. Volcanol. Seismol.* 10, 382–394. doi: 10.1134/s074204631606004x

Gottsmann, J., Komorowski, J.-C., and Barclay, J. (2017). "Volcanic unrest and pre-eruptive processes: a hazard and risk perspective," in *Volcanic Unrest: from Science to Society. Advances in Volcanology*, (Berlin: Springer).

Gouhier, M., Guéhenneux, Y., Labazuy, P., Cacault, P., Decriem, J., and Rivet, S. (2016). HOTVOLC: a web-based monitoring system for volcanic hot spots. *Geol. Soc. Lond. Spec. Publ.* 426, 223–241. doi: 10.1144/sp426.31

Harris, A. (2013). *Thermal Remote Sensing of Active Volcanoes: A User's Manual*. Cambridge, MA: Cambridge university press.

Harris, A. J. L., Carn, S., Dehn, J., Del Negro, C., Guðmundsson, G., Cordonnier, B., et al. (2016). Conclusion: recommendations and findings of the red seed working group. detecting, modelling and responding to effusive eruptions. *Geol. Soc. Lond. Spec. Publ.* 426, 567–648. doi: 10.1144/SP426.11

Harris, A. J. L., Chevrel, M. O., Coppola, D., Ramsey, M., Hrysiewicz, A., Thivet, S., et al. (2019). Validation of an integrated satellite-data-driven response to an effusive crisis: the April-May 2018 eruption of Piton de la fournaise. *Ann. Geophys.* 61:2018. doi: 10.4401/ag-7972

Harris, A. J. L., Villeneuve, N., Di Muro, A., Ferrazzini, V., Peltier, A., Coppola, D., et al. (2017). - Effusive crises at piton de la fournaise 2014-2015: a multi-national response model. *J. Appl. Volcanol.* 6:11. doi: 10.1186/s13617-017-0062-9

Jay, J. A., Welch, M., Pritchard, M. E., Mares, P. J., Mnich, M. E., Melkonian, A. K., et al. (2013). Volcanic hotspots of the central and southern andes as seen from space by ASTER and MODVOLC between the years 2000-2010, remote sensing of volcanoes and volcanic processes: integrating observation and modelling. *Geol. Soc. Lond. Spec. Publ.* 380, 161–185. doi: 10.1144/SP380.1

Kaneko, T., Yasuda, A., Aoki, Y., Kajiwara, K., and Kitagawa, S. (2010). Realtime monitoring of active volcanoes in East Asia using MODIS and MTSAT data its advancement by GCOM-C1 SGLI. *Int. Arch. Photogramm. Remote Sens. Spatial Inform. Sci.* 38, 209–212.

Koeppen, W. C., Pilger, E., and Wright, R. (2011). Time series analysis of infrared satellite data for detecting thermal anomalies: a hybrid approach. *Bull. Volcanol.* 73, 577–593. doi: 10.1007/s00445-010-0427-y

Laiolo, M., Coppola, D., Barahona, F., Benítez, J. E., Cigolini, C., Escobar, D., et al. (2017). Evidences of volcanic unrest on high-temperature fumaroles by satellite thermal monitoring: the case of Santa Ana volcano, El Salvador. *J. Volcanol. Geotherm. Res.* 340, 170–179. doi: 10.1016/j.jvolgeores.2017.04.013

Laiolo, M., Massimetti, F., Cigolini, C., Ripepe, M., and Coppola, D. (2018). Long-term eruptive trends from space-based thermal and SO_2 emissions: a comparative analysis of Stromboli, Batu Tara and Tinakula volcanoes. *Bull. Volcanol.* 80 doi: 10.1007/s00445-018-1242-0

Laiolo, M., Ripepe, M., Cigolini, C., Coppola, D., Della Schiava, M., Genco, R., et al. (2019). Space- and ground-based geophysical data tracking of magma migration in shallow feeding system of mount etna volcano. *Remote Sens.* 11:1182. doi: 10.3390/rs11101182

Linick, J. P., Pieri, D. C., and Sanchez, R. M. (2014). "The JPL ASTER Volcano Archive: the development and capabilities of a 15 year global high resolution archive of volcano data," in *Proceedings of the Abstract ID. GC51E-0482 Presented at Fall Meeting 2014*, (San Francisco, CA: American Geophysical Union).

Lombardo, V. (2016). The AVHotRR: near-real time routine for volcano monitoring using IR satellite data. *Geol. Soc.* 426, 73–92. doi: 10.1144/sp426.18

Lowenstern, J. B., and Ramsey, D. W. (2017). The volcano disaster assistance program—helping to save lives worldwide for more than 30 years. *U.S. Geol. Survey Fact Sheet* 6, 2017–3071. doi: 10.3133/fs20173071

Marzocchi, W., and Bebbington, M. S. (2012). Probabilistic eruption forecasting at short and long time scales. *Bull. Volcanol.* 74, 1777–1805. doi: 10.1007/s00445-012-0633-x

Massimetti, F., Coppola, D., Laiolo, M., Cigolini, C., and Ripepe, M. (2018). "First comparative results from SENTINEL-2 and MODIS-MIROVA volcanic thermal dataseries," in *Proceedings of the CoV10 IAVCEI General Assembly*, Naples, Italy, 2–7.

Naismith, A., Watson, I., Quinillo, C. C., Chigna, G., Escobar-Wolf, R., Coppola, D., et al. (2019). Eruption frequency patterns through time for the current (1999 – 2018) activity cycle at Volcán de Fuego derived from remote sensing data: evidence for an accelerating cycle of explosive paroxysms and potential implications of eruptive activity. *J. Volcanol. Geotherm. Res.* 371, 206–219. doi: 10.1016/j.jvolgeores.2019.01.001

Newhall, C. G., Costa, F., Ratdomopurbo, A., Venezky, D. Y., Widiwijayanti, C., Win, N. T. Z., et al. (2017). WOVOdat – an online, growing library of worldwide volcanic unrest. *J. Volcanol. nd Geotherm. Res.* 345, 184–199. doi: 10.1016/j.jvolgeores.2017.08.003

Pallister, J., and McNutt, S. R. (2015). "Synthesis of volcano monitoring," in *The Encyclopedia of Volcanoes*, 2nd Edn, ed. H. Sigurdsson, (Cambridge, MA: Academic Press), 1151–1171. doi: 10.1016/b978-0-12-385938-9.00066-3

Patrick, M., Kauahikaua, J., Orr, T., Davies, A., and Ramsey, M. (2016). "Operational thermal remote sensing and lava flow monitoring at the hawaiian volcano observatory," in *Detecting, Modelling and Responding to Effusive Eruptions*, eds A. J. L. Harris, T. De Groeve, F. Garel, and S. A. Carn, (London: Special Publications), 426.

Pergola, N., Coviello, I., Filizzola, C., Lacava, T., Marchese, F., Paciello, R., et al. (2016). A review of RSTVOLC, an original algorithm for automatic detection and near-real-time monitoring of volcanic hotspots from space. *Geol. Soc. Lond. Spec. Publ.* 426:55. doi: 10.1144/SP426.1

Phillipson, G., Sobradelo, R., and Gottsmann, J. (2013). Global volcanic unrest in the 21st century: an analysis of the first decade. *J. Volcanol. Geotherm. Res.* 264, 183–196. doi: 10.1016/j.jvolgeores.2013.08.004

Piscini, A., and Lombardo, V. (2014). Volcanic hot spot detection from optical multispectral remote sensing data using artificial neural networks. *Geophys. J. Int.* 196, 1525–1535. doi: 10.1093/gji/ggt506

Pritchard, M. E., Biggs, J., Wauthier, C., Sansosti, E., Arnold, W. D., Delgado, F., et al. (2018). Towards coordinated regional multi-satellite InSAR volcano observations: results from the latin America pilot project. *J. Appl. Volcanol.* 7:5. doi: 10.1186/s13617-018-0074-70

Ramsey, M., Flynn, L., and Wright, R. (2004). Volcanic observations from space: new results from the eos satellite instruments. *J. Volcanol. Geotherm. Res.* 135, 1–219.

Ramsey, M. S. (2016). Synergistic use of satellite thermal detection and science: a decadal perspective using ASTER. *Geol. Soc. Lond. Spec. Publ.* 426, 115–136. doi: 10.1144/sp426.23

Ramsey, M. S., and Harris, A. J. L. (2013). Volcanology 2020: how will thermal remote sensing of volcanic surface activity evolve over the next decade? (invited review article). *J. Volcanol. Geotherm. Res.* 249, 217–233. doi: 10.1016/j.jvolgeores.2012.05.011

Reath, K., Pritchard, M., Moruzzi, S., Alcott, A., Coppola, D., and Pieri, D. (2019a). The. (AVTOD)(ASTER Volcano Thermal Output Database) latin america archive. *J. Volcanol. Geotherm. Res.* 376, 62–76. doi: 10.1016/j.jvolgeores.2019.03.019

Reath, K., Pritchard, M., Poland, M., Delgado, F., Carn, S., Coppola, D., et al. (2019b). Thermal, deformation, and degassing remote sensing time series (A.D. 2000-2017) at the 47 most active volcanoes in Latin America: implications for volcanic systems. *J. Geophys. Res. Solid Earth* 124, 195–218. doi: 10.1029/2018JB016199

Reath, K. A., Ramsey, M. S., Dehn, J., and Webley, P. W. (2016). Predicting eruptions from precursory activity using remote sensing data hybridization. *J. Volcanol. Geotherm. Res.* 321, 18–30. doi: 10.1016/j.jvolgeores.2016.04.027

Ripepe, M., Pistolesi, M., Coppola, D., Delle Donne, D., Genco, R., Lacanna, G., et al. (2017). Forecasting effusive dynamic and decompression rates by magmastatic model at open-vent volcanoes. *Sci. Rep.* 7:3885. doi: 10.1038/s41598-017-03833-3

Schneider, D. J., Randall, M., and Parker, T. (2014). "Volcview: a web-based platform for satellite monitoring of volcanic activity and eruption response," in *Proceedings of the Abstract ID IN41D-05 Presented at Fall Meeting 2014*, (San Francisco, CA: American Geophysical Union).

Sparks, R. S. J., Biggs, J., and Neuberg, J. W. (2012). Monitoring volcanoes. *Science* 335, 1310–1311.

Steffke, A. M., and Harris, A. J. L. (2011). A review of algorithms for detecting volcanic hot spots in satellite infrared data. *Bull. Volcanol.* 73, 1109–1137. doi: 10.1007/s00445-011-0487-487

Tait, S., and Ferrucci, F. (2013). "A real-time, space borne volcano observatory to support decision making during eruptive crises: european volcano observatory space services," in *proceedings of the 2013 UKSim 15th International Conference on Computer Modelling and Simulation*, (Washington, DC: IEEE Computer Society).

Tarquini, S., de' Micheli Vitturi, M., Jensen, E., Pedersen, G. M. B., Barsotti, S., Coppola, D., et al. (2019). Modeling lava flow propagation over a flat landscape by using MrLavaLoba: the case of the 2014-2015 eruption at holuhraun, Iceland. *Ann. Geophys.* 62:228. doi: 10.4401/ag-7812

Tilling, R. I. (2008). The critical role of volcano monitoring in risk reduction. *Adv. Geosci.* 14, 3–11. doi: 10.5194/adgeo-14-3-2008

Urai, M. (2011). "Volcano observations with aster and ASTER Image Database for Volcanoes," in *Proceedings of the IEEE International Geoscience and Remote Sensing Symposium*, (Piscataway, NJ: IEEE).

Valade, S., Lacanna, G., Coppola, D., Laiolo, M., Pistolesi, M., Delle Donne, D., et al. (2016). Tracking dynamics of magma migration in open-conduit systems. *Bull. Volcanol.* 78:78.

Valade, S., Ley, A., Massimetti, F., D'Hondt, O., Laiolo, M., Coppola, D., et al. (2019). Towards global volcano monitoring using multisensor sentinel missions and artificial intelligence: the MOUNTS monitoring system. *Remote Sens.* 11:528.

van Manen, S. M., Blake, S., Dehn, J., and Valcic, L. (2013). Forecasting large explosions at Bezymianny Volcano using thermal satellite data. *Geol. Soc. Lond. Spec. Publ.* 380, 187–201. doi: 10.1144/sp380.3

van Manen, S. M., Dehn, J., and Blake, S. (2010). Satellite thermal observations of the Bezymianny lava dome 1993–2008: precursory activity, large explosions, and dome growth. *J. Geophys. Res.* 115:B08205.

Wadge, G. (1981). The variation of magma discharge during basaltic eruptions. *J. Volcanol. Geotherm. Res.* 11, 139–168. doi: 10.1016/0377-0273(81)90020-2

Werner, C., Kern, C., Coppola, D., Lyons, J., Kelly, P., Wallace, K., et al. (2017). Magmatic degassing, lava dome extrusion, and explosions from mount cleveland volcano, alaska, 2011-2015: insight into the continuous nature of volcanic activity over multi-year timescales. *J. Volcanol. Geotherm. Res.* 337, 98–110. doi: 10.1016/j.jvolgeores.2017.03.001

Winson, A. E. G., Costa, F., Newhall, C. G., and Woo, G. (2014). An analysis of the issuance of volcanic alert levels during volcanic crises. *J. Appl. Volcanol.* 3:14. doi: 10.1186/s13617-014-0014-6

Wooster, M. J., Zhukov, B., and Oertel, D. (2003). Fire radiative energy for quantitative study of biomass burning: derivation from the BIRD experimental satellite and comparison to modis fire products. *Remote Sens. Environ.* 86, 83–107. doi: 10.1016/s0034-4257(03)00070-1

Wright, R., Flynn, L. P., Garbeil, H., Harris, A. J. L., and Pilger, E. (2004). MODVOLC: near-real-time thermal monitoring of global volcanism. *J. Volc. Geotherm. Res.* 135, 29–49. doi: 10.1016/j.jvolgeores.2003.12.008

Wright, R., Glaze, L., and Baloga, S. M. (2011). Constraints on determining the eruption style and composition of terrestrial lavas from space. *Geology* 39, 1127–1130. doi: 10.1130/g32341.1

Zakšek, K., Pick, L., Coppola, D., and Hort, M. (2017). Influence of topography on lava flow quantification from satellite thermal data. *EGU Gen. Assem. Geophys. Res. Abstr.* 19, EGU2017–EGU12016.

Conflict of Interest: The authors declare that the research was conducted in the absence of any commercial or financial relationships that could be construed as a potential conflict of interest.

frontiers in Earth Science

ORIGINAL RESEARCH
published: 11 February 2020
doi: 10.3389/feart.2020.00022

Synergic Use of Multi-Sensor Satellite Data for Volcanic Hazards Monitoring: The Fogo (Cape Verde) 2014–2015 Effusive Eruption

Christian Bignami[1], Marco Chini[2], Stefania Amici[1] and Elisa Trasatti[1]*

[1] Istituto Nazionale di Geofisica e Vulcanologia, Rome, Italy, [2] Luxembourg Institute of Science and Technology, Esch-sur-Alzette, Luxembourg

OPEN ACCESS

Edited by:
Nico Fournier, GNS Science, New Zealand

Reviewed by:
Thomas R. Walter, German Research Centre for Geosciences, Helmholtz Centre Potsdam, Germany
Eisuke Fujita, National Research Institute for Earth Science and Disaster Resilience (NIED), Japan

****Correspondence:***
Christian Bignami
christian.bignami@ingv.it

Specialty section:
This article was submitted to Volcanology, a section of the journal Frontiers in Earth Science

Received: *02 September 2019*
Accepted: *24 January 2020*
Published: *11 February 2020*

Citation:
Bignami C, Chini M, Amici S and Trasatti E (2020) Synergic Use of Multi-Sensor Satellite Data for Volcanic Hazards Monitoring: The Fogo (Cape Verde) 2014–2015 Effusive Eruption. Front. Earth Sci. 8:22. doi: 10.3389/feart.2020.00022

Monitoring volcanic eruptions provides key information for hazard assessment and its time evolution. Satellite remote sensing data are nowadays essential to perform such task, thanks to their capability to survey disastrous events also in remote and under-monitored regions, with frequent revisit time and accurate spatial resolution. Even though satellite imageries are presently used to analyze several phenomena related to eruptions, automatic methods and synergic exploitation of different sensors are rarely considered. In this work, we have analyzed satellite images coming from both synthetic aperture radar (SAR) and optical sensors, to study the effusive eruption of Fogo volcano, Cape Verde, which took place between November 2014 and January 2015. In particular, we have exploited multi-sensor images from Sentinel-1, COSMO-SkyMed, Landsat-8, and Earth-Observing-1 missions, to retrieve lava flow patterns and volcanic source parameters related to the eruption. The main outcome of our work is the application of a new automatic change detection technique for estimating the lava field and its temporal evolution, combining the SAR intensity and the interferometric SAR coherence. The innovative algorithm is able to take full advantage of the Sentinel-1 mission's 6-day repeat cycle. Such data are here used for the first time for lava mapping, thereby providing an unprecedented example of using the multi-temporal interferometric SAR (InSAR) coherence to automatically monitor lava flow evolution in emergency phase. This new technique, jointly used with optical satellite images, is capable of resolving with spatial and temporal detail the evolution of lava flows. We have also performed differential SAR interferometry (DInSAR) to map the ground deformation and retrieve the feeding dyke by inverting syn-eruptive signals. Results from source modeling show a SW-NE oriented dyke, located inside Chã das Caldeiras, SW of the Pico do Fogo. Our work highlights how multidisciplinary and satellite open data, along with innovative and automatic processing techniques, may be adopted for real-time hazard estimates in an operational environment.

Keywords: lava, volcanic source modeling, synthetic aperture radar, optical images, change detection, hierarchical-split-based approach, DInSAR coherence, Fogo volcano

INTRODUCTION

Hazards assessment in volcanic areas requires the combination and the coordination of many instruments, techniques, and expertise, in different fields such as volcanology, geology, seismology, data analysis, meteorology, human sciences, and so on. All these fields of knowledge support decision makers and authorities to address risk reduction and improve crises management capabilities when volcanic eruptions occur. Volcanic eruptions are complex natural events that involve several phenomena: lava flows, gas emission, ash dispersal and ash fall, and other secondary effects, e.g., earthquakes, pyroclastic flows, landslides, and lahars, producing a wide spectrum of impacts (e.g., Bosi and MIAVITA group, 2012). In this heterogeneous scenario, satellite remote sensing data and the associated techniques, with their intrinsic multidisciplinary capability, represent very powerful tools. Especially in the present era, many sensors, in particular optical and synthetic aperture radar (SAR), are available on several platforms and constellation missions [e.g., European Space Agency (ESA)—Sentinel missions, and Agenzia Spaziale Italiana (ASI)—COSMO-SkyMed (CSK) mission], and can provide supporting information for monitoring ongoing eruptions. However, even though satellite imageries are intensely used, automatic methods and synergic exploitation of different sensors are rarely considered. Our case study is the eruption that began on November 2014 in Fogo Island, Cape Verde. We mapped the lava flow and its evolution with time using satellite imagery. In particular, we exploited the complementarity of SAR and optical images acquired by the new SAR sensor on board of Sentinel-1mission (S1), and by optical sensors of Landsat-8 (L8) and Earth-Observing-1 (EO-1) missions (from NASA/USGS), plus the high-resolution capability of CSK SAR sensor. We tested the capability of a novel change detection algorithm, based on multiscale tiling approach, for deriving automatic surface change maps from SAR data. Secondarily, we complemented the lava flow analysis, with geodetic observations by means of differential SAR interferometry (DInSAR). DInSAR data coming from Sentinel-1 and CSK missions, have allowed mapping the ground deformation due to the lava ascent and, by inverting them, the estimation of the eruption source. We show how the synergic use of multi-sensor data gathers useful information for hazards during volcanic crisis related to both internal (i.e., the feeding dyke) and external (e.g., lava flow) processes.

THE FOGO ERUPTION (CAPE VERDE)

Located in the NW Atlantic Ocean, at about 500 km far from the coast of Senegal, Cape Verde is composed of 10 main islands, some of which are inhabited. Since the first settlements in 1460, only Fogo Island experienced volcanic eruptions. Fogo Island has nearly conical shape, with a diameter of about 30 km, an area of 471 km^2, and a population of about 37,000 inhabitants (Faria and Fonseca, 2014). The island is cut at about 2000 m a.s.l. by a lateral collapse (Day et al., 1999) that formed a plateau known as Chã das Caldeiras. About 700 farmers live in Chã das Caldeiras, close to cone of Pico do Fogo that with its summit, reaching 2898 m a.s.l., dominates the caldera. In the last five centuries, the eruptions occurred in the caldera, both at the summit of Pico do Fogo and, since 1785, from fissures near its base, and were characterized by an average recurring period of about 20 years, and an average duration of 2 months (Ribeiro, 1960; Day et al., 2000). The most relevant hazard in Fogo is the lava flow, in particular inside Chã das Caldeiras, and in the steep eastern coast where 30% of inhabitants live (Faria and Fonseca, 2014 and the references therein). Indeed, in 1951, the lava flow destroyed a village on the eastern coast, and in 1995 (Amelung and Day, 2002) and lastly in 2014 the villages inside Chã das Caldeiras were destroyed. In such hazardous context, the monitoring of lava flow and its evolution in time can be of crucial importance to provide useful information for planning rescue activities and save lives.

The last eruption in Fogo started on 23 November 2014 and lasted 78 days, and was characterized by an effusive activity originated from a fissure located at the base of Pico do Fogo, spreading the lava in Chã das Caldeiras. The lava flow traveled to the SW, and then was split into two main lobes toward NW and S (González et al., 2015; Cappello et al., 2016; Calvari et al., 2018).

DATA AND METHODS

A total of 21 images were used to map the lava emplacement in Chã das Caldeiras, nine from Sentinel-1A (S1A), six from CSK, and the remaining six from multispectral sensors on board of EO-1 (three images) and L8 (three images). **Table 1** shows the available dataset, divided by type and by orbit.

The optical dataset was used to perform the analysis of lava filed that occurred in Chã das Caldeiras. SAR imagery was used for a twofold objective: the automatic change detection by means of hierarchical-split-based approach (HSBA, Chini et al., 2017), to map the lava occurrence, and the retrieval of the volcanic source by taking advantage of SAR interferometry technique.

LAVA EMPLACEMENT ANALYSIS

SAR Data Exploitation

Synthetic aperture radar data occupy a privileged place as regards change detection algorithms thanks to the sensitivity of the backscattering toward differences in land covers and their quasi-all weather, day/night observation capacity. For these reasons, SAR-based change detection (SAR-CD) was developed over many years to provide useful and reliable information on land surface changes that occur across different temporal and spatial scales (Bovolo and Bruzzone, 2005). SAR-CD usually finds different domain of application, and in particular for all concerns natural hazard related to floods (Chini et al., 2013), volcanoes (Bignami et al., 2013; Valade et al., 2019), earthquakes (Pierdicca et al., 2018), and tsunamis (Chini et al., 2008). SAR-CD algorithms typically generates the difference image and then classifies it, which consists of a binary classification problem, aiming at separating the change and the no change classes (hereafter CC and NCC) (Ajadi et al., 2016). To do this, histogram thresholding

TABLE 1 | Available satellite dataset.

Mission	Sensor	Date of acquisition	Orbit direction
Sentinel-1	SAR	2014/11/03*	Ascending
Sentinel-1	SAR	2014/11/08*	Descending
Sentinel-1	SAR	2014/11/27*	Ascending
Sentinel-1	SAR	2014/12/02*	Descending
Sentinel-1	SAR	2014/12/09	Ascending
Sentinel-1	SAR	2014/12/14	Descending
Sentinel-1	SAR	2014/12/21	Ascending
Sentinel-1	SAR	2014/12/26	Descending
Sentinel-1	SAR	2015/01/02	Ascending
Lansat-8	OLI	2014/10/23	Descending
Lansat-8	OLI	2014/11/24	Descending
Earth-Observing-1	ALI	2014/12/16	Descending
Earth-Observing-1	ALI	2014/12/18	Descending
Earth-Observing-1	ALI	2014/12/24	Descending
Lansat-8	OLI	2015/01/11	Descending
COSMO-SkyMed	SAR	2014/11/21*	Ascending
COSMO-SkyMed	SAR	2014/11/29*	Ascending
COSMO-SkyMed	SAR	2014/11/30	Ascending
COSMO-SkyMed	SAR	2014/11/21*	Descending
COSMO-SkyMed	SAR	2014/11/29*	Descending
COSMO-SkyMed	SAR	2014/12/07	Descending

*OLI: Operational Land Imager; ALI: Advanced Land Imager. The * identifies the images of the interferograms used for the geodetic modeling.*

is one of the most commonly used methods (Rosin, 2002), having as a critical step the selection of an adequate threshold, affecting directly the classification results. Parametric approaches usually fit the probability density function (*PDF*) of CC and NCC (PDF_{CC} and PDF_{NCC}), which are assumed Gaussian, and then set the threshold where the two PDFs intersect (Bruzzone and Prieto, 2002). The classification accuracy heavily depends on the classes proportions within the scene and the overlap between the two PDFs. When CC and NCC are strongly unbalanced, it is difficult to robustly parameterize their PDFs, while the amount of overlap between PDFs directly affects the under- and over-detection. Here, to overcome the two aforementioned drawbacks, we used an adaptive threshold approach previously developed to map floodwater (Chini et al., 2017), and also applied to map buildings (Chini et al., 2018). The approach is composed of two main steps. It first parameterizes the PDF_{CC} and PDF_{NCC}, and then based on the two PDFs iteratively applies thresholding and region-growing to find the best threshold for seeds (TH_S) and the one for stopping the region growing (TH_{SRG}). The PDFs parameterization is performed by HSBA (Chini et al., 2017), which identifies regions, or tiles, of the image where the PDF_{CC} and PDF_{NCC} can be fitted more reliably and accurately. The size of the tiles depends on the possibility of parameterizing the PDFs attributed to two different classes. HSBA starts with bigger tiles, which reduce successively, depending on the spatial extension of changes on the surface with respect to the entire image. HSBA starts from the entire image and then reduce the tile size following a quad-tree decomposition of the image. In the second step, in order to reduce class overlap effects on the final classification, spatial information is introduced on the selection of the best threshold (Haralick and Shapiro, 1985). The latter is done by a region-growing approach assuming that pixels constituting CC are clustered rather than randomly spread out over the entire image (Giustarini et al., 2013; Chini et al., 2017). Therefore, we first classify as CC those pixels that have high magnitude of change and then we add to CC those pixels with a lower magnitude of change but which are spatially contiguous to the first guesses. To do this, we use the region-growing algorithm, where the PDF_{CC} and PDF_{NCC} will drive the selection of TH_S and TH_{SRG}. TH_S selects seeds, i.e., pixels with high change of magnitude. We can set TH_S to the mean value of PDF_{CC}, which are pixels with a high probability to belong to CC. In order to select TH_{SRG}, different thresholds are tested. The choice is based on the minimization of the root-mean-squared error between the PDF_{CC} and the histogram resulting from the region growing. The two thresholds are automatically selected in those areas defined by HSBA, and then they are applied to the entire image to get the final classification. This SAR-CD algorithm is applied to the intensity difference image (hereafter IDI), which is the difference between the two log-transformed images acquired on two different instants. The IDI registers changes in the roughness and the dielectric constant of the surface. In this particular case, the images acquired after the event onset were subtracted to the images acquired before the event, and the change image was mainly detecting an increase of the backscattering on those areas where new lava was flowing from the vent down to Chã das Caldeiras. This was probably due to the increased of roughness of the surface.

Another import SAR-related feature frequently used as change detector is the InSAR coherence. This quantity is mostly influenced by the phase difference between radar returns, a distinctive parameter measured by a coherent sensor such as SAR, and it is particularly related to the spatial arrangement of the scatterers within the pixel and thus to their possible random displacements. Its high sensitivity to surface changes is well-documented and enables the detection of damages caused by catastrophic events such as volcano eruptions, earthquakes, and floods (e.g., Hoffmann, 2007; Chini et al., 2012; Valade et al., 2019). Compared to the SAR intensity, the coherence sensitivity to surface changes is much higher, because even a target rotation can create a temporal decorrelation, while to detect changes in the intensity, it is necessary that the roughness and the dielectric properties of surface change. We compared the IDI with an InSAR coherence image (hereafter ICI) computed using the same couple of images, and although both localize the change in the same region, in **Figure 1** is possible to appreciate that the spatial extensions are not the same. The ICI (**Figure 1B**) is showing more changes with respect to the IDI (**Figure 1A**), and this could be due to the surface sliding of the lava flow without producing a substantial change to the surface roughness detectable by the intensity. It is worth noting that the change depicted by coherence includes the change detected by intensity, having a bigger extent. Moreover, the spatial transition of coherence values from low to high is quite sharp, and this is because the incoherent surface movement produced by the lava flow is quite important. Based on these evidences, we integrated the InSAR coherence information to that one provided by intensity reapplying a region growing

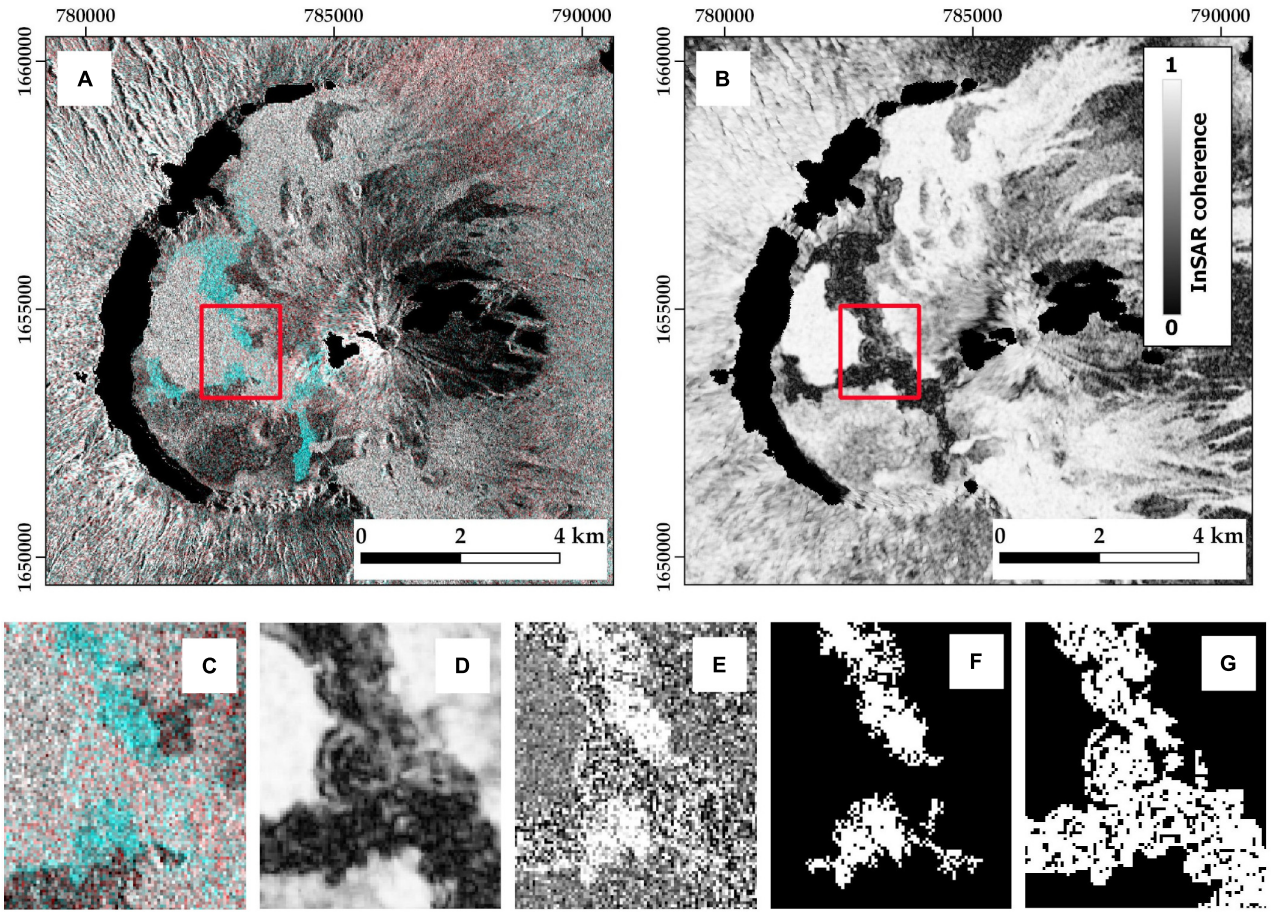

FIGURE 1 | Inputs, intermediate products, and final change map. **(A)** False color combination of SAR intensity images: R = pre-eruption SAR image on 2014/11/03, G = B = post-eruption SAR image on 2015/01/02. **(B)** ICI. **(C)** Detail of false color combination in **A**. **(D)** Detail of ICI. **(E)** IDI. **(F)** Intermediate HSBA output using IDI only. **(G)** Final HSBA output using IDI and ICI.

on the ICI. In this case, the seeds are those pixels depicted as change by the intensity and the rule to stop the growing is the standard deviation of seeds plus an epsilon. The rule to use the change maps from intensity as seed for the region growing on the coherence is motivated by the fact the coherence drop-off occurs also for reasons other than lava flow, e.g., vegetated areas (Valade et al., 2019). Indeed, looking at the coherence map in **Figure 1B**, the effect of the vegetation is quite evident in many areas (NNE zones of the volcano). Therefore, it is necessary to circumscribe the coherence loss only to those areas where a change in the SAR intensity has also occurred. In **Figure 1**, the inputs, the intermediate products, and the final change map are depicted. The latter obtained as a combination of IDI and ICI features. The increase in the intensity values is shown in **Figure 1C** (cyan areas) and in **Figure 1E** (white areas), while the decrease of coherence is in **Figure 1D** (dark areas), where it is highlighted that the InSAR coherence is detecting more changes than the only intensity. **Figure 1F** shows the intermediate product resulting from the IDI, while the final map is shown in **Figure 1G**, where the ICI was also integrated. The overall scheme for integrating ICI and IDI is reported in **Figure 2**.

It is worth to recall the S1 enhanced observational capabilities which reduce the drawbacks of previous moderate resolution SAR images and potentially enable the fully exploitation of the InSAR coherence capabilities for identifying surface changes. The high repeat cycle (i.e., small temporal baseline) and the relatively narrow orbit tube (i.e., small perpendicular interferometric baseline) of S1 mission reduce the temporal and the spatial decorrelation in vegetated areas and in the presence of structures with geometrical complexity, respectively. These peculiar characteristics of S1 have recently even enabled the detection of floodwater in urban areas using InSAR coherence (Chini et al., 2019), areas so far blind at 20 m spatial resolution.

Finally, SAR images captured by S1A spacecraft have been used for the first time to map the lava field in the caldera during the Pico do Fogo eruption. The dataset is composed of images in the innovative Terrain Observation with Progressive Scans SAR—TOPSAR—acquisition mode [aka Interferometric Wide (IW) swath]. The Fogo eruption is the first volcanic event captured by S1A mission in TOPSAR mode, and it was the first case study where SAR interferometry was applied to this very new imaging scan (González et al., 2015). Both ascending and

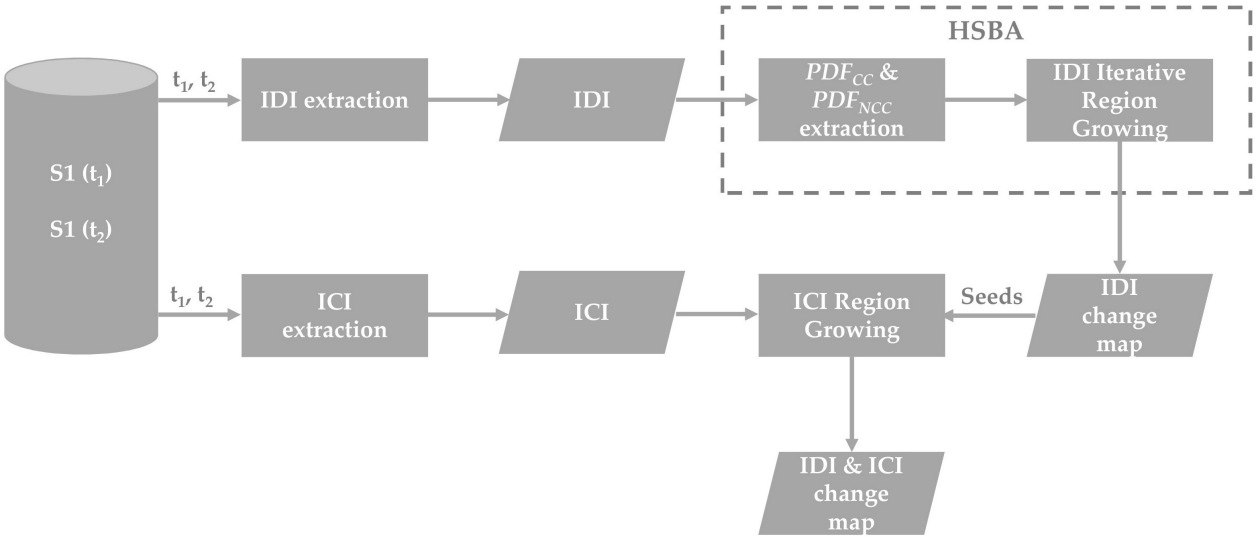

FIGURE 2 | Workflow of the change detection algorithm based on HSBA. See main text for acronyms definition.

descending orbit data were processed to estimate the lava flow coverage in the period between the eruption's onset and the last S1A image dated 2 January 2015. In addition to S1A data, we have taken advantage of CSK imageries. These data are high-resolution SAR images, at 3 m per pixel (full resolution). The TOPSAR images allowed the generation of seven change detection maps, four for the ascending data, and three for the descending ones. It is worth to note that the CSK were used to obtain some additional change maps but, unfortunately, they did not provide more information than those already provided by the S1 dataset.

The resulting change detection maps, from SAR intensity and phase coherence features, allowed the generation of the time series of lava emplacement (**Figure 3**). To do this, we computed the change maps using separately ascending and descending orbits, respectively. The change intensity images were all calculated with respect to the first available image of the time series (SAR_i–SAR_0), which is the one acquired before the event started. Instead, the InSAR coherence maps were calculated using two consecutive SAR images in order to reduce the temporal baseline, then the temporal decorrelation in vegetated areas.

Optical Data Exploitation

Multispectral satellite data, at medium spatial resolution (30 m) pixel, were acquired by EO-1 and L8 satellites. The EO-1 satellite was 1-year technology validation/demonstration mission that was extended due to its successful results. EO-1 is equipped with an Advanced Land Imager (ALI) instrument to validate and demonstrate technology for the Landsat Data Continuity Mission (LDCM) and Hyperion hyperspectral sensor[1]. L8[2] is a joint initiative between NASA and USGS, and it is equipped with two push-broom instruments: the Operational Land Imager (OLI) and the Thermal Infrared Sensor (TIRS). We have employed the bands positioned in visible (VIS), near infrared (NIR), and short wave infrared (SWIR) of the electromagnetic spectrum, to map the flow-field evolution.

In particular, the SWIR (2.2 μm), VNIR (1.6 μm), VNIR-Green (0.56 μm) of both L8-OLI and EO-1-ALI data were used to create a false color composite for Red, Green, and Blue channels, respectively (**Figure 4**). These false color images (similar to natural colors) visually enhance some features allowing to outline lava flows which appear black and brown in the images while vegetated areas appear green. Active lava flows (hot lava) show a change in color from red to yellow as a result of an increase in the temperature of the crustal component and/or an increase in the areas of high temperature fractures (Wright et al., 2001). In addition, clouds appear white in the images, while the plumes colored in blue can be related to gases emitted by the volcano (e.g., SO_2) (Flynn et al., 2000; Flynn et al., 2001; Lee et al., 2015). **Figure 4B** shows the active flow field on 24 November 2014, 1 day after the beginning of the eruption. Active lava flows from the eruptive fissure bifurcate originating two lava flows, one moving to the North in the direction of Portela and Bangaeira villages, and a second flow directed to South. The red haze surrounding the flows is a combined effect of smearing, i.e., high radiant pixels into adjacent pixels (Rothery et al., 1988), leading to an over representation of the size of the anomaly (Wright et al., 2001).

Lava flow mapping by using multispectral sensors relies generally on near-IR bands (1.6–2.2 μm) to map hot lava flow, and on Thermal IR bands (10–11 μm) to map cooling lava which tends to form lava tubes (Flynn et al., 1994). In this context, because of ALI sensor has not thermal infrared bands and L8-TIRS bands have a spatial resolution of 100 m per pixel, we have used two different approaches to map active and cooling lava flows. L8 and ALI images were synergically used to produce the chrono-contour of active lava flow (**Figure 5**) by visually inspecting the images at their best zoom (Flynn et al., 2001). The change detection was produced to explore the possibility to derive

[1]https://eo1.gsfc.nasa.gov/

[2]http://landsat.gsfc.nasa.gov/landsat-8

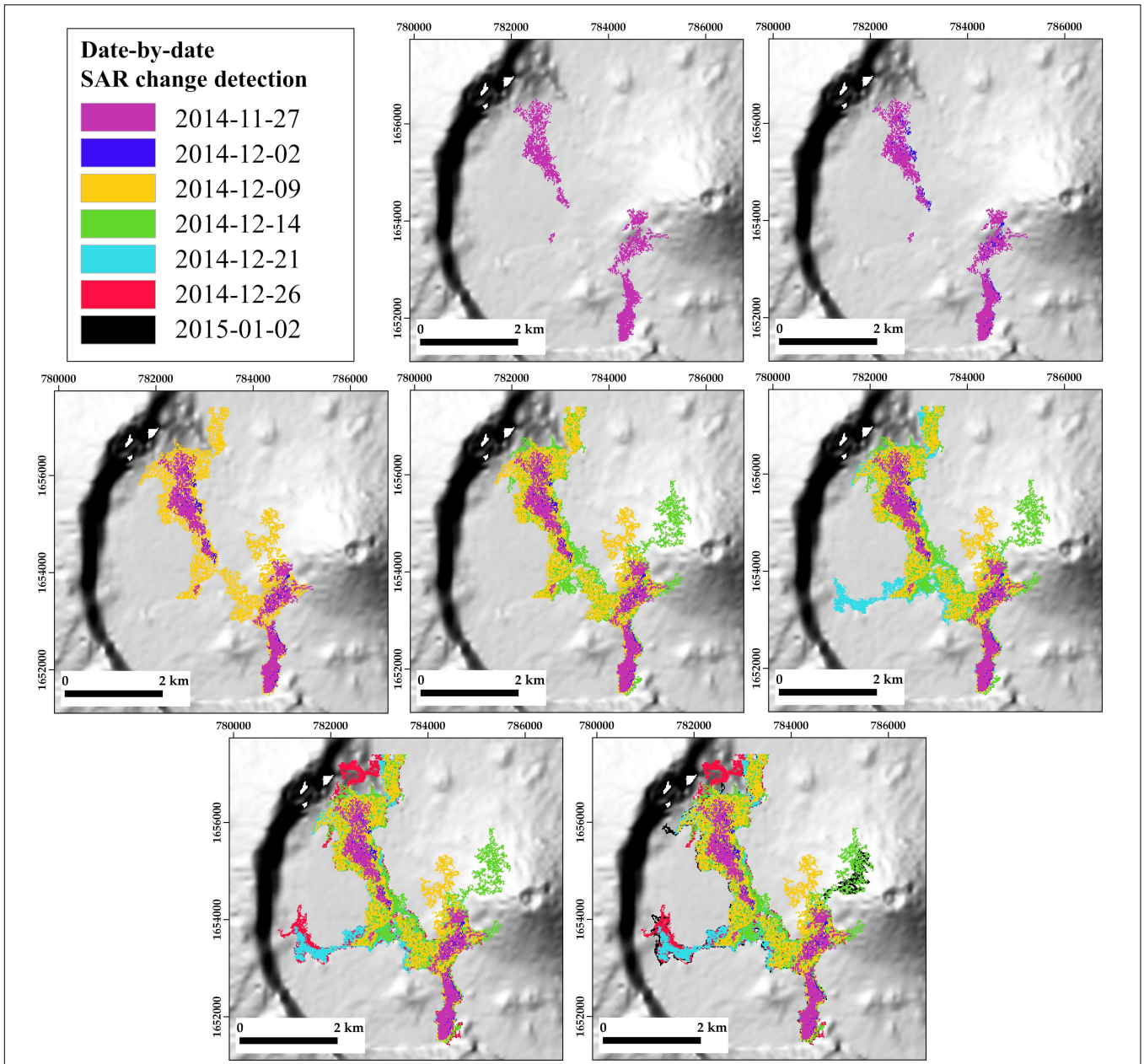

FIGURE 3 | Temporal evolution of the deposited lava obtained by using HSBA algorithm applied to S1 images. The figure shows the area affected by erupted lava at each S1 overpass, in different colors, on ascending and descending orbit. Both intensity and phase coherence data were processed.

additional information on cooling flow-fields besides hot lava characterization obtained by the optical multi-sensors time series.

In order to implement the change detection, the images were previously converted into reflectance, and to improve the spatial resolution of multispectral channels, we adopted the pan-sharpening Graham–Smidth method implemented in ENVI© software for resampling the bands originally at 30 m resolution into the 15 m resolution of L8-OLI panchromatic channel (band 8).

The pan-sharpened SWIR channel of L8-OLI was used to calculate a change detection map between the images captured on 23 October 2014 and 11 January 2015 (**Figure 6**) using the automatic co-registration option offered by ENVI©. Several bands were tested and best result was obtained by using the band 7. The change detection map highlights in gray scale the subsequent lava flows. The color of lava flow from light gray pixels to dark pixel can indicate a combined effect of lava thickness, composition and cooling areas. The thermal L8-TIRS band, at 10 μm and with a spatial resolution of 100 m, acquired on 11 January 2015 was used to support the interpretation regarding the cooling effect, although the TIR imagery is affected by reflectance component being acquired at daytime (see **Figure 6** inset).

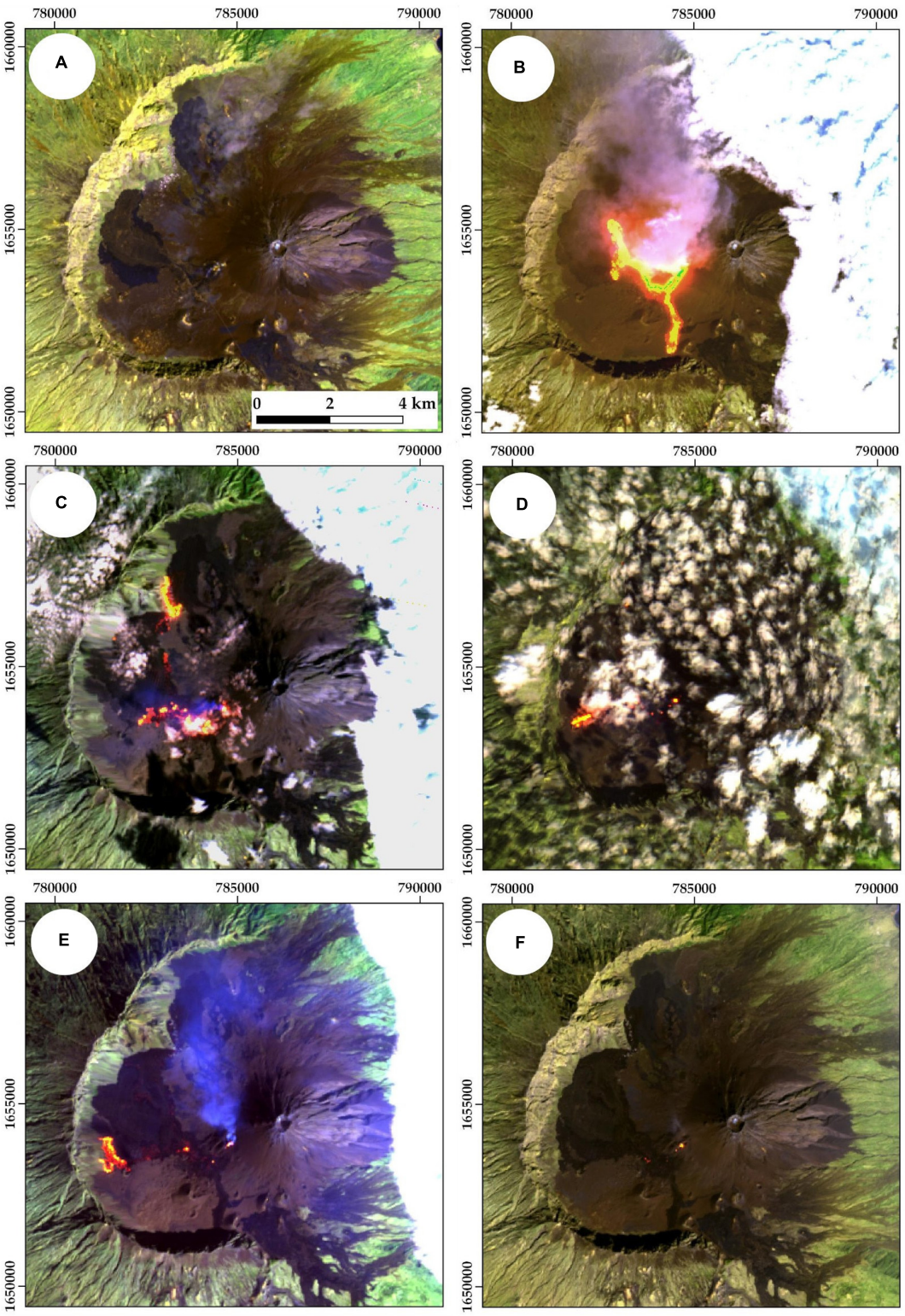

FIGURE 4 | False color representations of optical dataset (see main text for RGB assignment). **(A)** pre-eruptive (23 October 2014) image acquired by L8. **(B)** L8 acquired on 24 November 2014: it shows two active fresh lava flows. Bright yellow-orange pixels illustrate areas of very high temperature of crustal component and/or an increase in the areas of high temperature fractures and bright green pixels within the lava flow are related to saturated signal. **(C)** EO-1 image acquired on 16 December 2014; shows the advancement of the lava flow on west and north. **(D)** EO-1 acquired on 18 December 2014. **(E)** EO-1 acquired on 24 December 2014. **(F)** L8 image acquired on 11 January 2015.

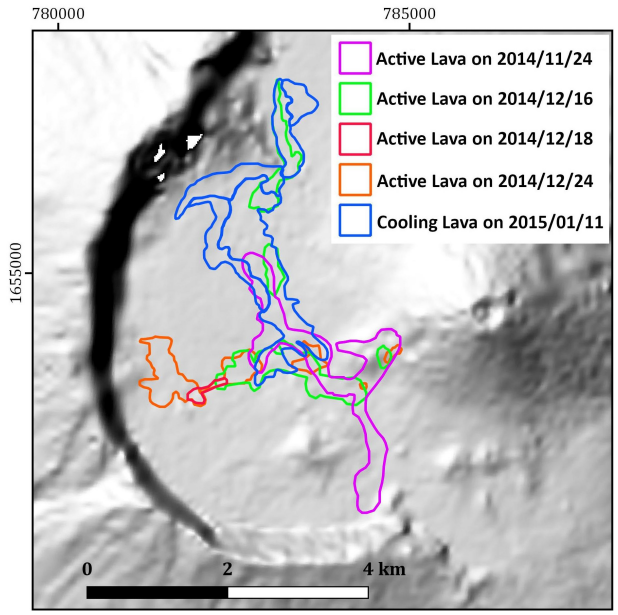

FIGURE 5 | Active lava perimeters derived by visual delineation of L8-OLI and EO1-ALI SWIR bands and change image from October 2014–January 2015 L8 data provide the flow fields evolution.

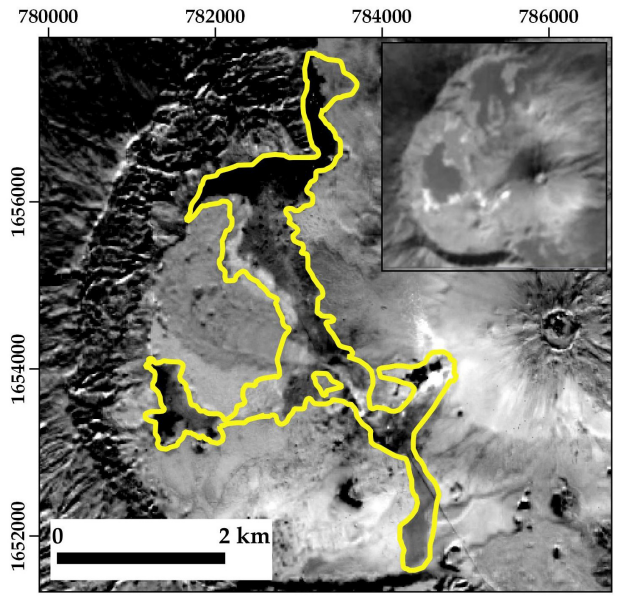

FIGURE 6 | The results of SWIR pan-sharp change detection between pre- (October 2014) and post-eruption (January 2015) data. The inset (top right) shows the L8-TIRS thermal band at 10 μm (January 2015). The variation of the gray tones mainly results by chronology, and cooling phases. The yellow polygon was drawn to highlight the detected whole change by visual inspection.

Lava Field Emplacement Evolution

The results about emitted lava estimated by SAR and optical images were compared in order to assess their capability to monitor the temporal evolution of the event. The plot reported in **Figure 7** shows four lines indicating the lava coverage in square km at each satellite time acquisition. The green and yellow lines refer to SAR data results, the blue line is the analysis performed with optical dataset, and the red one corresponds to the evaluation done by the Emergency Mapping Service (EMS) of Copernicus[3] by exploiting satellite images acquired by very high resolution sensors from many space missions.

Optical analysis has a very similar trend with respect to EMS data, showing a very close effusion rate (0.10 km^2/day for our data and 0.083 km^2/day for EMS) and few square km of bias (about 1 km^2) at the early stage of the effusion. These small discrepancies can be attributed to the ground resolution of the images used for the two estimates, i.e., medium resolution sensors in our dataset vs. very high resolution sensors in EMS study.

Synthetic aperture radar intensity only estimates the superficial effusion rate and lava total area smaller with respect to the one estimated from the other two datasets (green curve in **Figure 7**). The lava flow is a complex surface scenario, which cannot be explained with only change in roughness of the surface, which is the ground parameter that strongly affects SAR intensity signal. We think that the new emitted lava does not completely change the roughness of the soils, because the area of Chã das Caldeiras was already covered by lava (from previous eruptions) that can be characterized by similar texture. This can partially explain why the SAR intensity is underestimating it. Considering the SAR intensity and coherence results (yellow trend in **Figure 7**), two different temporal phases on the evolution of the surface changes are highlighted. The first section concerns the coverage estimation before the third SAR image taken on 9 December 2014. In this phase, SAR change detection underestimates the coverage with respect to the EMS maps. Actually, these set of data do not take into account the InSAR coherence information because the first two change coherence maps are related to SAR pairs that have a high temporal baseline, i.e., 24 days of separation (either ascending or descending pairs). For these maps, the coherence loss is not only due to changes in surface scattering because of lava emplacement, but also because of the effects of temporal decorrelation due to changes in the vegetation cover (Zebker and Villasenor, 1992). Moreover, in this first phase, the volcanic cloud was still present, and it represents another source of coherence loss (Jung et al., 2016). Therefore, we omitted the first two coherence maps because the decrease of coherence was also due to reasons other than lava within the caldera of Fogo Island (see **Supplementary Figure S1**). The second section of the trend (after 9 December 2014) concerns the merged information coming from both SAR intensity and coherence change maps. In this part, SAR results overestimate EMS results, and the total area coverage is 4 km^2 larger than the one measured by SAR intensity only (green line). Maps reported in **Figure 3** show where the overestimation occurred, and probably it is due to the InSAR coherence feature. The pictures highlight that the algorithm identifies some changes on the Pico do Fogo flanks (north sector) and few "false alarm" pixels in the northwest of Chã das Caldeiras (see lava coverage for dates 9 and

[3]https://emergency.copernicus.eu/

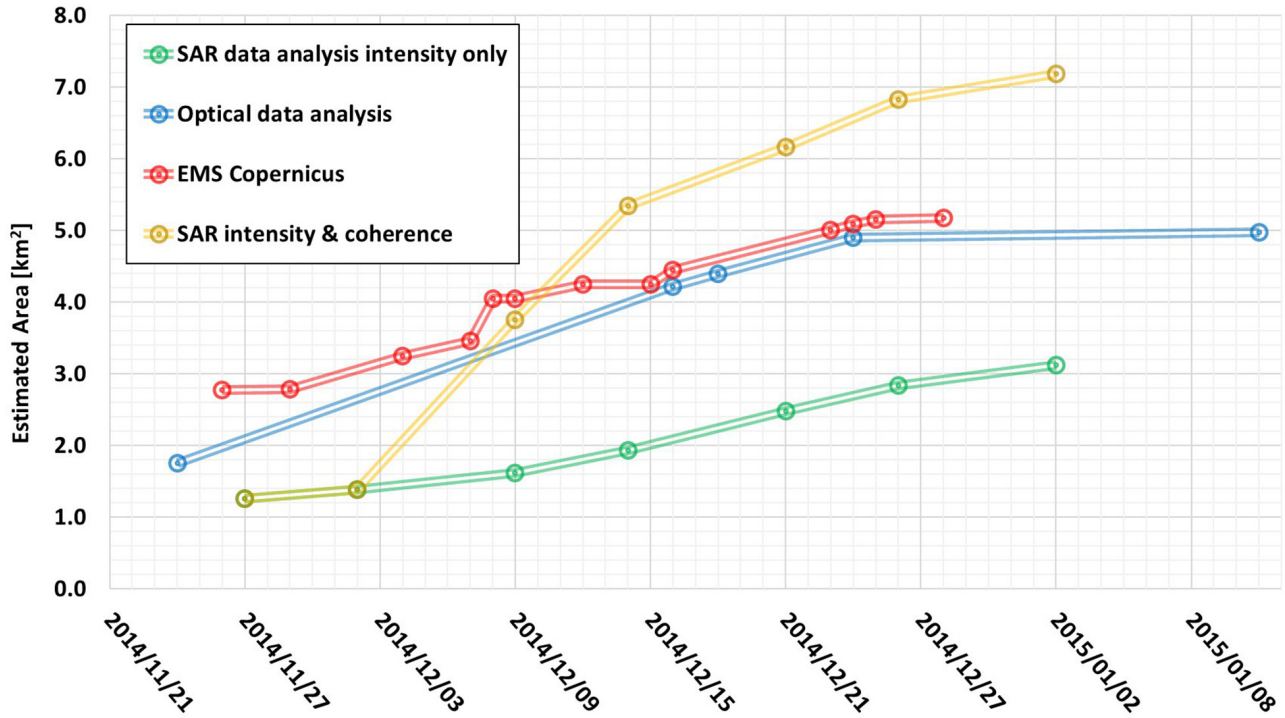

FIGURE 7 | Lava coverage trend from 24 November 2014 to 11 January 2015.

14 December 2014, in **Figure 3**). We calculated, by manually delineating "false alarms" areas, that the surface extension of these areas is about 2 km^2, which basically corresponds to the overestimation with respect to EMS maps and optical analysis. These changes, which were detected by S1 InSAR coherence drop off, are not mapped using other datasets. It is worth considering that here a "real ground truth" is not available, hence, in case we assume that S1 intensity and coherence method overestimate the surface effusion rate, a possible reason for coherence loss is still the presence of the volcanic cloud[4] (multispectral images in **Figure 4**), as discussed by Jung et al. (2016). Although SAR coherence seems to overestimate the lava emplacement, the information carried out by such feature is extremely useful to compensate the systematic underestimation of SAR intensity data only. This is clearly reported in **Figure 7**, where the line related to the SAR intensity only (in green) is constantly below the estimates from optical and EMS data. It is also important to point out that the results from S1 data are obtained using a completely automatic procedure and with lower resolution data, with respect to those from other datasets. Results clearly show the synergic role of SAR intensity and SAR InSAR coherence for lava mapping.

VOLCANIC SOURCE MODELING

Beside the change detection approach, S1 and CSK images were also exploited to map the ground deformation caused by the eruption. The master–slave images for each sensor and orbit are evidenced in **Table 1**, and they are all syn-eruptive. For this purpose, we processed the data by means of classical DInSAR (Zebker et al., 1994), and we calculated four interferograms. The SRTM DEM (Farr et al., 2007) was used to remove the topographic phase contribution, and the multi-looking technique was applied to reduce noise and to obtain products sampled at a square pixel size of 20 × 20 and 15 × 15 m^2 for S1 and CSK, respectively. Even though the two SAR systems operate with different bands (C and X band) and with different incidence angles (S1 at about 43.5° on ascending orbit and 35° on descending orbit; CSK at about 20° for both ascending and descending images), the patterns of the ground displacement are coherent (**Figure 8**). Indeed, inside the caldera, two lobes of deformation are visible on both S1 and CSK ascending interferograms. It is also worth to note the fringe pattern that is present on the south flank of Pico do Fogo on both S1 and CSK descending data. Of course, the fringe rate is different because of the different wavelengths.

These ground deformation estimates were exploited to retrieve the volcanic source modeling and to constrain the syn-eruptive feeding dyke. The four interferograms are subsampled with a step of 180 m in the inner caldera of Fogo, and 540 m outside, for a total of about 13,000 datapoints. The inversions were performed by means of the Volcano and Seismic source Modeling (VSM) tool (Trasatti, 2019). The code allows considering several analytical models of volcanic source, whose parameters are retrieved by non-linear inversion. The inversion is then followed by an appraisal stage based on a Bayesian approach

[4]https://volcano.si.edu/volcano.cfm?vn=384010

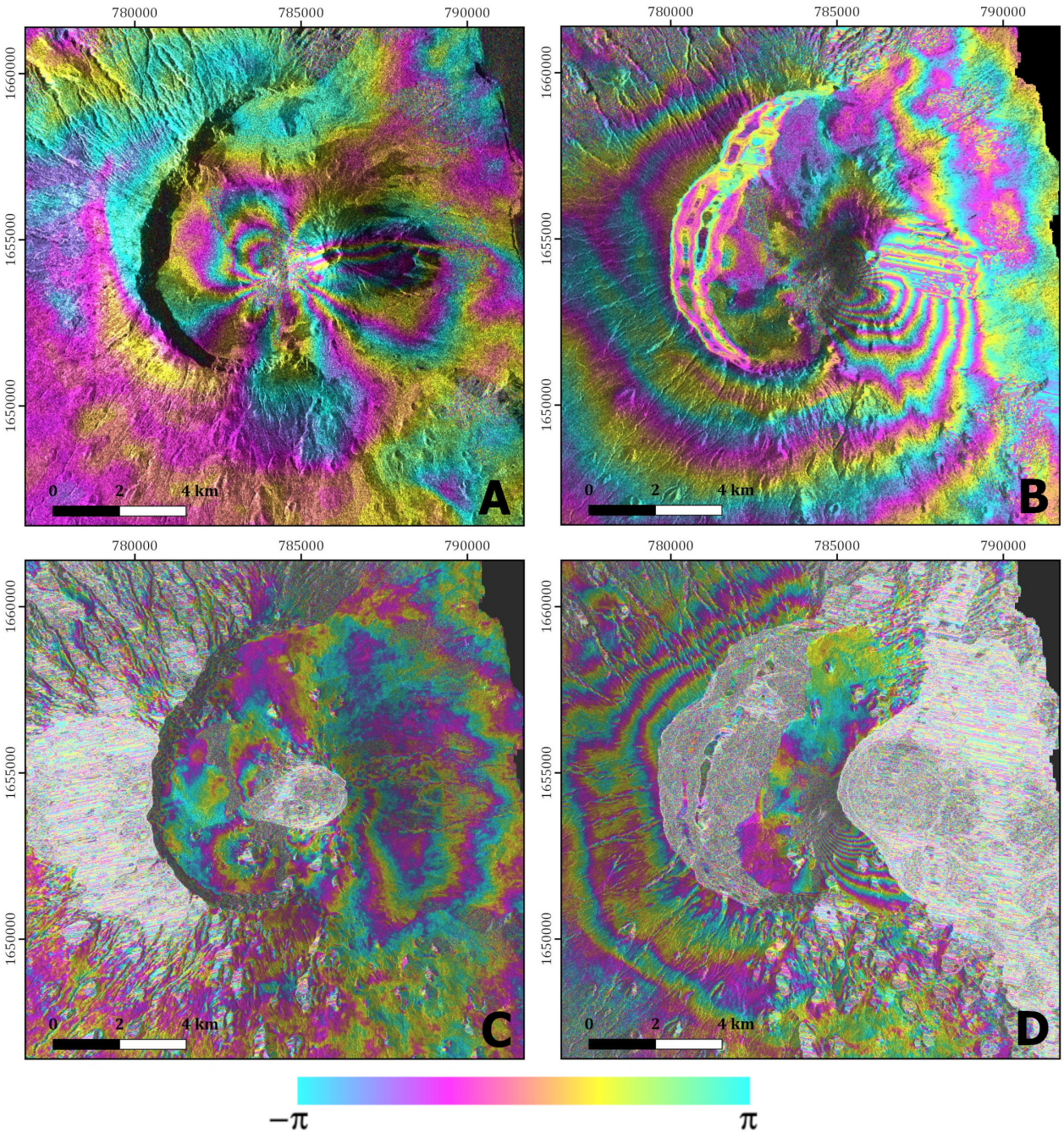

FIGURE 8 | Wrapped interferograms obtained from S1 ascending **(A)**, S1 descending **(B)**, CSK ascending **(C)**, and CSK descending **(D)** images. Two lobes of deformation are visible on both S1 and CSK ascending interferograms within the caldera. The south flank of Pico do Fogo is characterized by a very similar fringe arrangement, on S1 and CSK descending data.

aimed at finding the most probable parameters (instead the single best-fit model), obtaining posterior PDF (Sambridge, 1999). Several attempts were computed in order to find the most suitable geometrical source to reproduce the observed data. We find that pressurized sources such as a sphere or a spheroid are not suitable since they are unable to reproduce the wide negative line of sight (LOS) area in the eastern sector of the volcano. Instead, an opening dyke (Okada, 1992) reproduces the highest LOS values reaching 9–12 cm (opposite signs in the ascending/descending orbits, being the movement horizontal) and the corresponding opposite lobes (**Figure 9** and **Supplementary Figure S2** for CSK data). The misfit obtained, based on the chi-squared function, amounts to 14.8, while the null solution relating data to their uncertainties is 25.5.

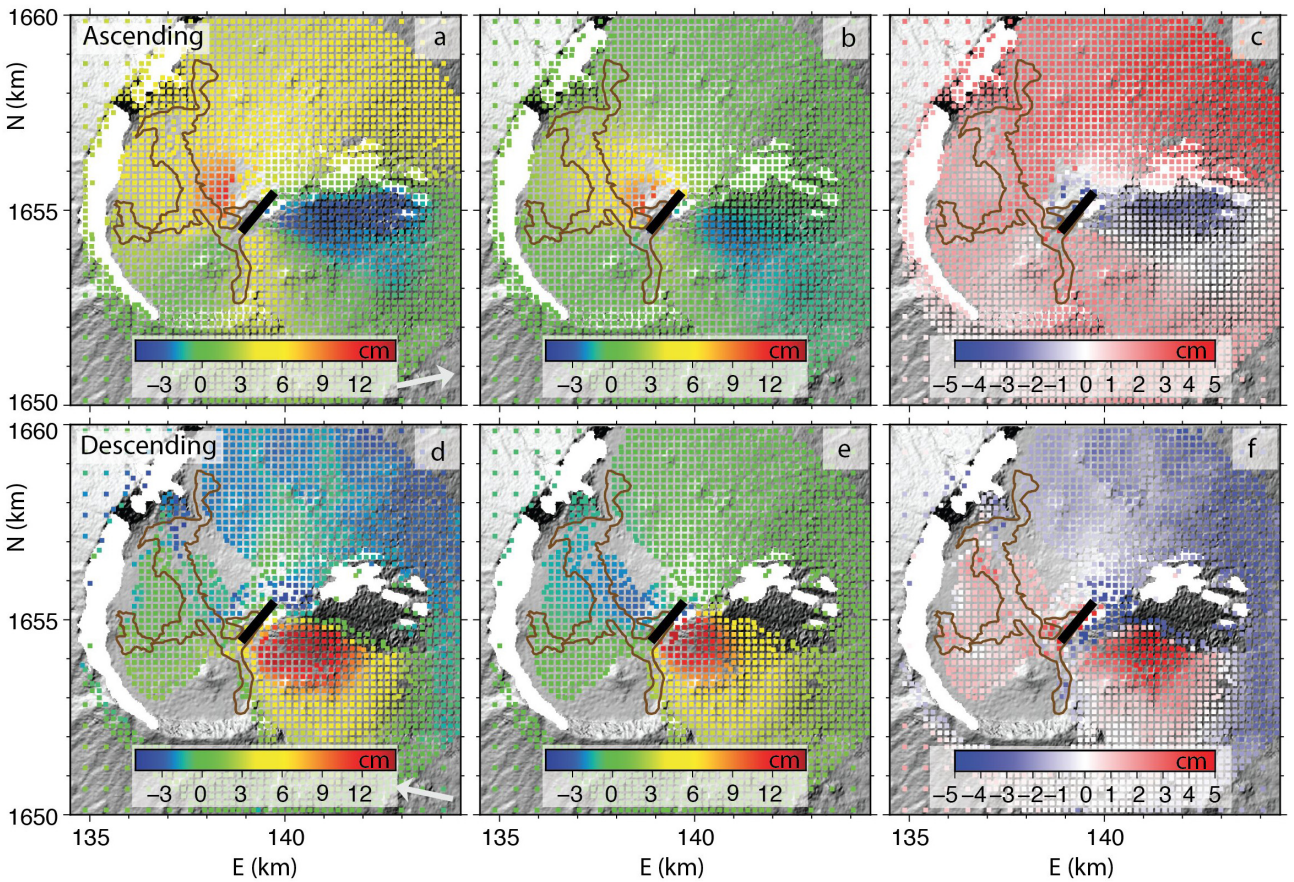

FIGURE 9 | Results of the VSM inversion. Comparison between observed **(a,d)** and modeled **(b,e)** data, and residuals **(c,f)** in ascending and descending orbits of S1 satellites. The black line is the surface projection of the feeding dyke. E and N are UTM projection, zone 27. The brownish transparency is the lava from SWIR pan-sharp change detection. Similar results for CSK mission are shown in **Supplementary Figure S2**.

The dyke, whose trace is represented with the black line in **Figure 9**, is SW-NE oriented, and it is located inside Chã das Caldeiras, SW of the Pico do Fogo. Our results show that it slightly dips of 86° toward SE, and opens about 60 cm, for a total volume change of 2.0 ± 0.6 10^6 m^3 in the observation time span (i.e., one month baseline and up to 8 days after the start of the eruption). The mean parameters' values are reported in **Table 2**, while the posterior PDFs are reported in **Supplementary Figure S3**. The top depth of the dyke was fixed at 100 m below the Fogo's mean altitude. **Figure 9** also shows the agreement between the constrained lava flow and the surface projection of the feeding dyke retrieved by an independent technique.

DISCUSSION

We have presented the results of a novel automatic technique to estimate the lava flow propagation during the effusive eruption of Fogo, adopting a multi-sensor approach. The area coverage obtained by visual analysis of medium resolution imagery (L8 and EO-1) is estimated equal to 4.97 km^2, in line with the results of EMS and by Cappello et al. (2016). This value is very close to the one estimated with more sophisticated techniques that require more computational efforts or *in situ* measurements, such as differential DEM (Bagnardi et al., 2016), and Terrestrial Laser Scanner (TLS) combined with structure from motion data (Richter et al., 2016). Bagnardi et al. (2016) and Richter et al. (2016) estimate a lava coverage for this eruption of 4.8 and 4.85 km^2, respectively, i.e., about 0.1 km^2 of difference with respect our results. This demonstrates that optical moderate resolution data are quite informative for this kind of application and are able to provide a cinematic estimate of lava emplacement. The temporal evolution information provided by the proposed approach can be delivered during an emergency phase. On the contrary, techniques such as DEM difference that require stereoscopic optical images, or TLS, that is based on field campaigns, are often prevented when an eruption is ongoing (e.g., with volcanic clouds and active lava flows). SAR data, on the other side, play a key role in such context, when prompt information is important for human rescue purposes, because of their all-weather and day-night capabilities, and their intrinsic suitability for a full automatic generation of change detection product. The HSBA presented in our work is more

TABLE 2 | Mean values of the dyke parameters as retrieved by the VSM tool.

E (km)	N (km)	L (m)	W (m)	Strike (°)	Dip (°)	Opening (m)
138.85 ± 0.2	1654.45 ± 0.2	1330 ± 150	2560 ± 250	48 ± 3	86 ± 5	0.58 ± 0.05

E and N are UTM projection, zone 27. L and W are the length and width of the dyke, respectively.

than a proof of concept of an operational tool, as in the case of flood mapping (Chini et al., 2017). The accuracy of SAR intensity and InSAR coherence lava maps seems to be lower than other approaches, giving under- and over-estimation of the total lava, at the beginning and at the end of the eruption (about 2 km^2), respectively. Of course, results from other methods based on earth observation data too are affected by errors as well. Moreover, it is worth to note that S1 mission was not fully operational at the time of Fogo eruption. Indeed, only one satellite was orbiting at that time, so that the temporal baseline between two consecutive acquisitions was twelve days (with two satellites it is reduced to 6 days). This latter is an important parameter for reducing false alarms caused by vegetation when InSAR coherence is used. The opportunity offered by SAR constellation missions, as in the case of ESA's S1, with weekly delivered acquisitions (or even more frequent as in the case of the CSK mission) was shown. Still some efforts have to be put in place to improve the results, correcting false alarms, and tuning algorithms, considering that volcanic areas during an eruption phase are quite challenging scenarios since different phenomena occur (e.g., ash and gas emissions). In synthesis, the comparison between the lava mapping results obtained from optical and SAR data suggests their possible automatic integration for supporting a crisis phase. Indeed, more complex approaches, such as DEM difference or TLS, even though they are expected to be more accurate (e.g., giving volume estimates too) cannot be applied easily or automatically when an eruption is ongoing. Despite some discrepancies are present in the analysis shown above, the synergic use of optical and SAR data could provide *high-rate* (almost daily) temporal information about lava evolution, thanks to the complementarity of such sensors, and automation of data processing.

The feeding dyke constrained by the geodetic inversion is located SW of the Pico do Fogo summit, in accordance with the area of the lava flow mapped by SAR change detection and optical images. The eruptive vent location follows the favorable calculated post-collapse stress field within the local crust (Maccaferri et al., 2017). The retrieved dyke shares position and dimension with previous analyses (González et al., 2015; Bagnardi et al., 2016) of the 2014–2015 eruption, and of the 1995 eruption (Amelung and Day, 2002). The volumes of the retrieved inflating dykes are comparable within uncertainty, being 3 ± 2 10^6 m^3 that inferred by González et al. (2015). The syn-eruptive dyke is referred for the 3–8 days of the eruption, being the SAR slave images taken on the 27th, 29th November, and 2nd December (**Table 1**), while the eruption lasted for 78 days. Even considering the area and volumes related to the first days of the eruption (one to few tens of 10^6 m^3, Bagnardi et al., 2016; Cappello et al., 2016; Calvari et al., 2018), the magma volume intruded is still only a small fraction of the erupted volume. This suggests that the shallow dyke inferred from SAR data is the lateral, sub-vertical pathway of the magma to be erupted and it is not representative of the volume actually extruded. From one hand, this is confirmed by the lack of pre-eruptive deformation and deflation after the end of the eruption (González et al., 2015), and from other hand, by the development of tubes (Calvari et al., 2018). We can conclude that the lava flow extension and volume, and the retrieved feeding dyke volume are not directly connected. Instead, we demonstrate that the full exploitation of SAR data allows quantifying multi-hazards in volcanic areas during eruptions.

As a final remark, a deeper magmatic source feeding the eruption was not retrieved both for the 1995 and 2014–2015 events (Amelung and Day, 2002; González et al., 2015). The eruptions at Fogo are fed by mantle-lithospheric source, according to petrological and geochemical data, assumed to be located below 16 km depth (Hildner et al., 2011; Calvari et al., 2018).

CONCLUSION

The present work is a multidisciplinary and multi-sensor study of the main hazards related to the 2014–2015 Fogo Island effusive eruption. In particular, we propose an innovative and automatic method to exploit SAR data, and their joint use with optical imageries to map the lava field emplacement. For these purposes, we have used the images acquired by the ESA's S1, ASI's CSK, and NASA/USGS L8 and EO-1 missions. The comparative and synergic use of this multi-sensor dataset has allowed estimating the temporal evolution of lava coverage in the Chã das Caldeiras by applying visual inspection of optical imagery and by testing the capability of a novel automatic change detection algorithm using SAR data. Our improved change detection algorithm is based on multiscale tiling approach to identify changes occurred on the SAR intensity and it combines information from the InSAR coherence to detect changes which are not directly related to changes on surface roughness. The approach is completely automatic and adaptive, showing high capability to detect different extent of lava flows. The lava flow analysis was then complemented by the geodetic observations. Indeed, thanks to DInSAR we have mapped the whole ground deformation due to the lava ascent. By inverting them, we have also identified the dyke feeding the eruption. The achieved results are in agreement with previous findings, even if based on different dataset and methods. We demonstrate how open access multi-sensor satellite imagery can be used in synergy to provide hazard information in an operational environment, when volcanic activity limits the use of single sensor data and/or on field measurements.

DATA AVAILABILITY STATEMENT

The Sentinel-1, Earth-Observing-1, and Landsat-8 datasets for this study can be found in the ESA (https://scihub.copernicus.eu/dhus/#/home) and USGS (https://earthexplorer.usgs.gov). CSK images are not publicly available because were provided by means of a direct agreement between ASI and INGV.

AUTHOR CONTRIBUTIONS

CB led the conception of the manuscript and processed SAR data for deformation mapping. MC worked on the SAR change detection analysis by developing and running the hierarchical approach. ET retrieved the volcanic source by inverting DInSAR deformation data. SA processed the satellite data to estimate change maps from Optical sensors. All authors contributed to the manuscript preparation and interdisciplinary analysis.

FUNDING

MC contribution was supported by the Luxembourg National Research Fund through the MOSQUITO project (Grant CORE C15/SR/10380137).

ACKNOWLEDGMENTS

The authors thank space agencies for data provision: ESA for Sentinel-1 dataset and ASI for the kind delivery of COSMO-SkyMed images, USGS for Landsat-8 and EO-1 set. Useful discussions with G. Ventura and M. Bagnardi are acknowledged.

SUPPLEMENTARY MATERIAL

The Supplementary Material for this article can be found online at: https://www.frontiersin.org/articles/10.3389/feart.2020.00022/full#supplementary-material

REFERENCES

Ajadi, O., Meyer, F., and Webley, P. (2016). Change detection in synthetic aperture radar images using a multiscale-driven approach. *Remote Sens.* 8:482. doi: 10.3390/rs8060482

Amelung, F., and Day, S. (2002). InSAR observations of the 1995 Fogo, cape verde, eruption: implications for the effects of collapse events upon island volcanoes. *Geophys. Res. Lett.* 2:1606. doi: 10.1029/2001GL013760

Bagnardi, M., González, P. J., and Hooper, A. (2016). High-resolution digital elevation model from tri-stereo Pleiades-1 satellite imagery for lava flow volume estimates at Fogo Volcano. *Geophys. Res. Lett.* 43, 6267–6275. doi: 10.1002/2016GL069457

Bignami, C., Ruch, J., Chini, M., Neri, M., Buongiorno, M. F., Hidayati, S., et al. (2013). Pyroclastic density current volume estimation after the 2010 Merapi volcano eruption using X-band SAR. *J. Volcanol. Geoth. Res.* 261, 236–243. doi: 10.1016/j.jvolgeores.2013.03.023

Bosi, V., and MIAVITA group, (2012). *Handbook for Volcanic Risk Management: Prevention, Crisis Management and Resilience*. France: BRGM Orleans.

Bovolo, F., and Bruzzone, L. (2005). A detail-preserving scale-driven approach to change detection in multitemporal SAR images. *IEEE Trans. Geosci. Remote Sens.* 43, 2963–2972. doi: 10.1109/TGRS.2005.857987

Bruzzone, L., and Prieto, D. F. (2002). An adaptive semiparametric and context-based approach to unsupervised change detection in multitemporal remote-sensing images. *IEEE Trans. Image Process.* 11, 452–466. doi: 10.1109/TIP.2002.999678

Calvari, S., Ganci, G., Victória, S., Hernandez, P., Perez, N., Barrancos, J., et al. (2018). Satellite and ground remote sensing techniques to trace the hidden growth of a lava flow field: the 2014–2015 effusive eruption at fogo volcano (Cape Verde). *Remote Sens.* 10:1115. doi: 10.3390/rs10071115

Cappello, A., Ganci, G., Calvari, S., Pérez, N. M., Hernández, P. A., Silva, S. V., et al. (2016). Lava flow hazard modeling during the 2014-2015 Fogo eruption. *Cape Verde. J. Geophys. Res.: Solid Earth* 121, 2290–2303. doi: 10.1002/2015JB012666

Chini, M., Bignami, C., Stramondo, S., and Pierdicca, N. (2008). Uplift and subsidence due to the 26 December 2004 Indonesian earthquake detected by SAR data. *Int. J. Remote Sens.* 29, 3891–3910. doi: 10.1080/01431160701871112

Chini, M., Hostache, R., Giustarini, L., and Matgen, P. (2017). A Hierarchical split-based approach for parametric thresholding of SAR images: flood inundation as a test case. *IEEE Trans. Geosci. Remote Sens.* 55, 6975–6988. doi: 10.1109/TGRS.2017.2737664

Chini, M., Pelich, R., Hostache, R., Matgen, P., and Lopez-Martinez, C. (2018). Towards a 20 m global building map from sentinel-1 SAR data. *Remote Sens.* 10:1833. doi: 10.3390/rs10111833

Chini, M., Pelich, R., Pulvirenti, L., Pierdicca, N., Hostache, R., and Matgen, P. (2019). Sentinel-1 InSAR coherence to detect floodwater in urban areas: houston and hurricane harvey as a test case. *Remote Sens.* 11:107. doi: 10.3390/rs11020107

Chini, M., Piscini, A., Cinti, F. R., Amici, S., Nappi, R., and DeMartini, P. M. (2013). The 2011 Tohoku (Japan) tsunami inundation and liquefaction investigated through optical. thermal, and SAR data. *IEEE Geosci. Remote Sens. Lett.* 10, 347–351. doi: 10.1109/LGRS.2012.2205661

Chini, M., Pulvirenti, L., and Pierdicca, N. (2012). Analysis and Interpretation of the COSMO-SkyMed Observations of the 2011 Japan Tsunami. *IEEE Geosci. Remote Sens. Lett.* 9, 467–471. doi: 10.1109/LGRS.2011.2182495

Day, S., Carracedo, J. C., Gillou, H., Fonseca, J. F. B. D., Heleno, S. I. N., Pais, J., et al. (2000). Comparison and cross-checking of evidence for the location and type of historical eruptions in ocean island volcanoes. in: the archaeology of geological catastrophes; McGuire, W., volcanoes, earthquakes and archeology. special publication. *Geol. Soc. Lon.* 171, 281–306. doi: 10.1144/gsl.sp.2000.171.01.21

Day, S. J., Heleno da Silva, S. I. N., and Fonseca, J. F. B. D. (1999). A past giant lateral collapse and present-day flank instability of Fogo. Cape Verde Islands. *J. Volcanol. Geothermal Res.* 94, 191–218. doi: 10.1016/S0377-0273(99)00103-101

Faria, B., and Fonseca, J. F. B. D. (2014). Investigating volcanic hazard in Cape Verde Islands through geophysical monitoring: network description and first results. *Nat. Hazards Earth Syst. Sci.* 14, 485–499. doi: 10.5194/nhess-14-485-2014

Farr, T. G., Rosen, P. A., Caro, E., Crippen, R., Duren, R., Hensley, S., et al. (2007). The shuttle radar topography mission. *Rev. Geophys.* 45, 1–33. doi: 10.1029/2005RG000183

Flynn, L. P., Harris, A. J. L., Rothery, R. D. A., and Oppenheimer, C. (2000). High-Spatial resolution thermal remote sensing of active volcanic features using Landsat and hyperspectral data. *Remote Sens. Active Volcanism AGU Geophys. Monogr. Ser.* 116, 161–177. doi: 10.1029/gm116p0161

Flynn, L. P., Harris, A. J. L., and Wright, R. (2001). Improved identification of volcanic features using Landsat 7 ETM+. *Remote Sens. Environ.* 78, 180–193. doi: 10.1016/S0034-4257(01)00258-259

Flynn, L. P., Mouginis-Mark, P. J., and Horton, K. A. (1994). Distribution of thermal areas on an active lava flow field: landsat observations of Kilauea, Hawaii, July 1991. *Bull.Volcanol.* 56, 284–296. doi: 10.1007/BF00302081

Giustarini, L., Hostache, R., Matgen, P., Schumann, G. J.-P., Bates, P. D., and Mason, D. C. (2013). A change detection approach to flood mapping in urban areas using terraSAR-X. *IEEE Trans. Geosci. Remote Sens.* 51, 2417–2430. doi: 10.1109/TGRS.2012.2210901

González, P. J., Bagnardi, M., Hooper, A. J., Larsen, Y., Marinkovic, P., Samsonov, S. V., et al. (2015). The 2014-2015 eruption of fogo volcano: geodetic modeling of Sentinel-1 TOPS interferometry. *Geophys. Res. Lett.* 42, 9239–9246. doi: 10.1002/2015GL066003

Haralick, R. M., and Shapiro, L. G. (1985). Image segmentation techniques. *Comput. Vis. Graph.Image Process.* 29, 100–132. doi: 10.1016/S0734-189X(85)90153-90157

Hildner, E., Klügel, A., and Hauff, F. (2011). Magma storage and ascent during the 1995 eruption of Fogo, Cape Verde Archipelago. *Contrib. Mineral. Petr.* 162, 751–772. doi: 10.1007/s00410-011-0623-6

Hoffmann, J. (2007). Mapping damage during the Bam (Iran) earthquake using interferometric coherence. *Int. J. Remote Sens.* 28, 1199–1216. doi: 10.1080/01431160600928567

Jung, J., Kim, D., Lavalle, M., and Yun, S.-H. (2016). Coherent change detection using InSAR Temporal decorrelation model: a case study for volcanic ash detection. *IEEE Trans. Geosci. Remote Sens.* 54, 5765–5775. doi: 10.1109/TGRS.2016.2572166

Lee, S.-K., Lee, C.-W., and Lee, S. (2015). A comparison of the Landsat image and LAHARZ-simulated lahar inundation hazard zone by the 2010 Merapi eruption. *Bull. Volcanol.* 77:46. doi: 10.1007/s00445-015-0920-924

Maccaferri, F., Richter, N., and Walter, T. R. (2017). The effect of giant lateral collapses on magmapathways and the location of volcanism. *Nat. Communi.* 8:1097. doi: 10.1038/s41467-017-01256-1252

Okada, Y. (1992). Internal deformation due to shear and tensile faults in a half-space. *B Seismol. Soc. Am.* 82, 1018–1040.

Pierdicca, N., Anniballe, R., Noto, F., Bignami, C., Chini, M., Martinelli, A., et al. (2018). Triple collocation to assess classification accuracy without a ground truth in case of earthquake damage assessment. *IEEE Trans. Geosci. Remote Sens.* 56, 485–496. doi: 10.1109/TGRS.2017.2750770

Ribeiro, O. (1960). *A ilha do Fogo e as Suas Erupções; Memórias, Série Geográfica*, 12th Edn. Lisbon: Junta de Investigações do Ultramar.

Richter, N., Favalli, M., de Zeeuw-van Dalfsen, E., Fornaciai, A., da Silva Fernandes, R. M., Pérez, N. M., et al. (2016). Lava flow hazard at fogo volcano, cabo verde, before and after the 2014-2015 eruption. *Nat. Hazards Earth Syst. Sci.* 16, 1925–1951. doi: 10.5194/nhess-16-1925-2016

Rosin, P. L. (2002). Thresholding for change detection. *Comput. Vis. Image Underst.* 86, 79–95. doi: 10.1006/cviu.2002.0960

Rothery, D. A., Francis, P. W., and Wood, C. A. (1988). Volcano monitoring using short wavelength infrared data from satellites. *J. Geophys. Res.* 93:7993. doi: 10.1029/JB093iB07p07993

Sambridge, M. (1999). Geophysical inversion with a neighbourhood algorithm - II. Appraising the ensemble. *Geophys. J. Int.* 138, 727–746. doi: 10.1046/j.1365-246x.1999.00900.x

Trasatti, E. (2019). *Volcano and Seismic source Modelling – VSM*. Avaliable at: http://www.rohub.org/rodetails/volcano_source_modelling_vsm-release/overview (accessed January 2020).

Valade, S., Ley, A., Massimetti, F., D'Hondt, O., Laiolo, M., Coppola, D., et al. (2019). Towards global volcano monitoring using multisensor sentinel missions and artificial intelligence: the MOUNTS monitoring system. *Remote Sens.* 11:1528. doi: 10.3390/rs11131528

Wright, R., Flynn, L., and Harris, A. (2001). Evolution of lava flow-fields at mount etna, 27-28 October 1999, observed by Landsat 7 ETM+. *Bull. Volcanol.* 63, 1–7. doi: 10.1007/s004450100124

Zebker, H. A., Rosen, P. A., Goldstein, R. M., Gabriel, A., and Werner, C. L. (1994). On the derivation of coseismic displacement fields using differential radar interferometry: the landers earthquake. *J. Geophys Res.: Solid Earth* 99, 19617–19634. doi: 10.1029/94JB01179

Zebker, H. A., and Villasenor, J. (1992). Decorrelation in interferometric radar echoes. *IEEE Trans. Geosci. Remote Sens.* 30, 950–959. doi: 10.1109/36.175330

Conflict of Interest: The authors declare that the research was conducted in the absence of any commercial or financial relationships that could be construed as a potential conflict of interest.

frontiers in Earth Science

ORIGINAL RESEARCH
published: 25 February 2020
doi: 10.3389/feart.2020.00036

Spatial and Temporal Variations in SO_2 and $PM_{2.5}$ Levels Around Kīlauea Volcano, Hawai'i During 2007–2018

Rachel C. W. Whitty[1], Evgenia Ilyinskaya[1], Emily Mason[2], Penny E. Wieser[2], Emma J. Liu[3], Anja Schmidt[4,5], Tjarda Roberts[6], Melissa A. Pfeffer[7], Barbara Brooks[8], Tamsin A. Mather[9], Marie Edmonds[2], Tamar Elias[10], David J. Schneider[11], Clive Oppenheimer[5], Adrian Dybwad[12], Patricia A. Nadeau[10] and Christoph Kern[13]*

[1] School of Earth and Environment, Institute of Geophysics and Tectonics, University of Leeds, Leeds, United Kingdom, [2] Department of Earth Sciences, University of Cambridge, Cambridge, United Kingdom, [3] Department of Earth Sciences, University College London, London, United Kingdom, [4] Department of Chemistry, University of Cambridge, Cambridge, United Kingdom, [5] Department of Geography, University of Cambridge, Cambridge, United Kingdom, [6] CNRS UMR7328, Laboratoire de Physique et de Chimie de l'Environnement et de l'Espace, Université d'Orléans, Orléans, France, [7] Icelandic Meteorological Office, Reykjavik, Iceland, [8] National Centre for Atmospheric Science, Leeds, United Kingdom, [9] Department of Earth Sciences, University of Oxford, Oxford, United Kingdom, [10] U.S. Geological Survey Hawaiian Volcano Observatory, Honolulu, HI, United States, [11] U.S. Geological Survey Alaska Volcano Observatory, Fairbanks, AK, United States, [12] PurpleAir LLC, Salt Lake City, UT, United States, [13] U.S. Geological Survey Cascades Volcano Observatory, Vancouver, WA, United States

OPEN ACCESS

Edited by:
Elisa Trasatti, Istituto Nazionale di Geofisica e Vulcanologia (INGV), Italy

Reviewed by:
Claudia Spinetti, Istituto Nazionale di Geofisica e Vulcanologia (INGV), Italy
Antonio M. Álvarez-Valero, University of Salamanca, Spain

***Correspondence:**
Rachel C. W. Whitty
eercww@leeds.ac.uk

Specialty section:
This article was submitted to Volcanology, a section of the journal Frontiers in Earth Science

Received: *23 October 2019*
Accepted: *03 February 2020*
Published: *25 February 2020*

Citation:
Whitty RCW, Ilyinskaya E, Mason E, Wieser PE, Liu EJ, Schmidt A, Roberts T, Pfeffer MA, Brooks B, Mather TA, Edmonds M, Elias T, Schneider DJ, Oppenheimer C, Dybwad A, Nadeau PA and Kern C (2020) Spatial and Temporal Variations in SO_2 and $PM_{2.5}$ Levels Around Kīlauea Volcano, Hawai'i During 2007–2018. Front. Earth Sci. 8:36. doi: 10.3389/feart.2020.00036

Among the hazards posed by volcanoes are the emissions of gases and particles that can affect air quality and damage agriculture and infrastructure. A recent intense episode of volcanic degassing associated with severe impacts on air quality accompanied the 2018 lower East Rift Zone (LERZ) eruption of Kīlauea volcano, Hawai'i. This resulted in a major increase in gas emission rates with respect to usual emission values for this volcano, along with a shift in the source of the dominant plume to a populated area on the lower flank of the volcano. This led to reduced air quality in downwind communities. We analyse open-access data from the permanent air quality monitoring networks operated by the Hawai'i Department of Health (HDOH) and National Park Service (NPS), and report on measurements of atmospheric sulfur dioxide (SO_2) between 2007 and 2018 and $PM_{2.5}$ (aerosol particulate matter with diameter <2.5 μm) between 2010 and 2018. Additional air quality data were collected through a community-operated network of low-cost $PM_{2.5}$ sensors during the 2018 LERZ eruption. From 2007 to 2018 the two most significant escalations in Kīlauea's volcanic emissions were: the summit eruption that began in 2008 (Kīlauea emissions averaged 5–6 kt/day SO_2 from 2008 until summit activity decreased in May 2018) and the LERZ eruption in 2018 when SO_2 emission rates reached a monthly average of 200 kt/day during June. In this paper we focus on characterizing the airborne pollutants arising from the 2018 LERZ eruption and the spatial distribution and severity of volcanic air pollution events across the Island of Hawai'i. The LERZ eruption caused the most frequent and severe exceedances of the Environmental Protection Agency (EPA) $PM_{2.5}$ air quality threshold ($35\ \mu g/m^3$ as a daily average) in Hawai'i in the period 2010–2018. In Kona, for example, the maximum 24-h-mean mass concentration of $PM_{2.5}$ was recorded as $59\ \mu g/m^3$ on the twenty-ninth of May 2018, which was one of eight recorded exceedances of the EPA air quality threshold during the 2018 LERZ eruption, where there had been no exceedances in the previous 8 years as measured by the

HDOH and NPS networks. SO_2 air pollution during the LERZ eruption was most severe in communities in the south and west of the island, as measured by selected HDOH and NPS stations in this study, with a maximum 24-h-mean mass concentration of 728 μg/m^3 recorded in Ocean View (100 km west of the LERZ emission source) in May 2018. Data from the low-cost sensor network correlated well with data from the HDOH $PM_{2.5}$ instruments, confirming that these low-cost sensors provide a robust means to augment reference-grade instrument networks.

Keywords: Kīlauea, volcano, $PM_{2.5}$, SO_2, emissions, air quality, Hawai'i

1. INTRODUCTION

Volcanic clouds are complex, evolving mixtures of volcanic and atmospheric gases, primary and secondary aerosol particles, ash and dust (Oppenheimer and McGonigle, 2004; Pfeffer et al., 2006b; von Glasow et al., 2009; Oppenheimer et al., 2010; Langmann, 2014). As well as the potential for global climatic consequences from explosive or large-scale volcanic emissions, low altitude volcanic clouds can have important impacts on air quality, human and animal health, and the environment on the local to regional scale (Hansell and Oppenheimer, 2004; Barsotti et al., 2010; Mather, 2015; Schmidt et al., 2015; Andronico and Del Carlo, 2016; Tam et al., 2016; Ilyinskaya et al., 2017).

Gaseous sulfur dioxide (SO_2) is usually highly concentrated in volcanic emissions compared to the background atmosphere and is often the focus of gas emission monitoring due to the relative ease of its measurement and its important environmental and air quality consequences (Cadle et al., 1971; Lambert et al., 1988; Loughlin et al., 2012; Schmidt et al., 2015). Population sub-groups including children, asthmatics and cardiac- or respiratory-compromised individuals are particularly vulnerable to exposure to SO_2 (ATSDR, 1998; CRI, 2004). For example, exposure to mass concentrations of 1,310 μg/m^3 SO_2 for 3 min can induce respiratory attacks in asthmatic individuals (Balmes et al., 1987; ATSDR, 1998). In 2010 the U.S. Environmental Protection Agency (EPA) set the National Ambient Air Quality Standard (NAAQS) for SO_2 mass concentration exposure limits at 195 μg/m^3 as an hourly average (EPA, 2010). Persistent volcanic SO_2 emissions on the Island of Hawai'i led the state of Hawai'i being designated as unclassifiable for the EPA 2010 NAAQS, and as such Hawai'i uses the pre-2010 EPA SO_2 exposure limit of 366 μg/m^3 as 24-h average (EPA, 2013). The European Commission (EC) air quality standards recommend a SO_2 mass concentration threshold of 350 μg/m^3 for a 3-h average, and 125 μg/m^3 as a daily average (EC, 2018).

Particulate matter (PM) in volcanic clouds is also significant in the context of environment and health. The chemical composition of volcanogenic $PM_{2.5}$ (PM with diameter <2.5 μm) is highly heterogeneous. Typical chemical species include sulfates (primary emissions or formed via oxidation of sulfur gases) (Cadle et al., 1971; Stockwell and Calvert, 1983; Allen et al., 2002; Mather et al., 2003; Langmann, 2014) and halides, with an array of metals and metalloids including environmentally-harmful species such as lead and cadmium (Longo, 2013; Langmann, 2014). $PM_{2.5}$ is a well-established indicator for air quality, since it commonly includes particulates derived from transport and industrial sources, fine wind-blown mineral dust, ambient matter, and volcanic material (Lim et al., 2012; Tam et al., 2016; Holgate, 2017; Butwin et al., 2019). It has been estimated that the health burden due to exposure to ambient $PM_{2.5}$ globally amounts to more than three million premature deaths each year (Lim et al., 2012), and is especially linked to increases in death from cardiovascular and respiratory diseases in vulnerable individuals (Holgate, 2017). EPA NAAQS thresholds recommend a $PM_{2.5}$ mass concentration exposure limit of 35 μg/m^3 as a daily average (EPA, 2013). This is higher than the 24-h mean exposure guideline of 25 μg/m^3 established by the World Health Organization (WHO, 2005).

2. KĪLAUEA ERUPTIVE ACTIVITY, 2007–2018

Kīlauea volcano on the Island of Hawai'i consists of a summit caldera at 1,200 m a.s.l. and rift zones to the south-west and east. From 1983 until 2008, activity at Kīlauea was concentrated on the middle East Rift Zone (ERZ), primarily near the Pu'u 'Ō'ō vent (Elias and Sutton, 2007; Poland et al., 2008) (**Figure 1A**). Between 2002 and 2006, average SO_2 flux from the ERZ was 1.7 ± 0.7 kt/day, while emissions from the summit were low at 0.1 kt/day (Elias and Sutton, 2007). From November 2007 to March 2008, SO_2 emissions at the summit increased to levels 10 times the long-term background (Wooten et al., 2009) (**Figure 2A**). On the twelfth of March 2008, a new vent opened within the Halema'uma'u summit crater, leading to sporadic explosive eruptions and increased degassing of SO_2.

Kīlauea's SO_2 emissions peaked in the summer of 2008, when a total emission rate of up to 20 kt/day was measured by satellite sensors (Beirle et al., 2014). At this time, emissions from both the ERZ and the summit were significant, with the two sources contributing variable amounts to the total degassing rate (Elias and Sutton, 2012). For the period 2009–2017, the dynamic activity at Kīlauea was reflected in variable emissions, with a long-term average of 5–6 kt/day based on satellite and ground-based measurements (Eguchi et al., 2011; Elias and Sutton, 2012; Carn et al., 2016; Elias et al., 2018) (**Figure 2A**). Lava was first observed in the Halema'uma'u summit crater in September 2008, with a permanent lava lake visible from February 2010 until May 2018 (Patrick et al., 2013; Neal et al., 2019).

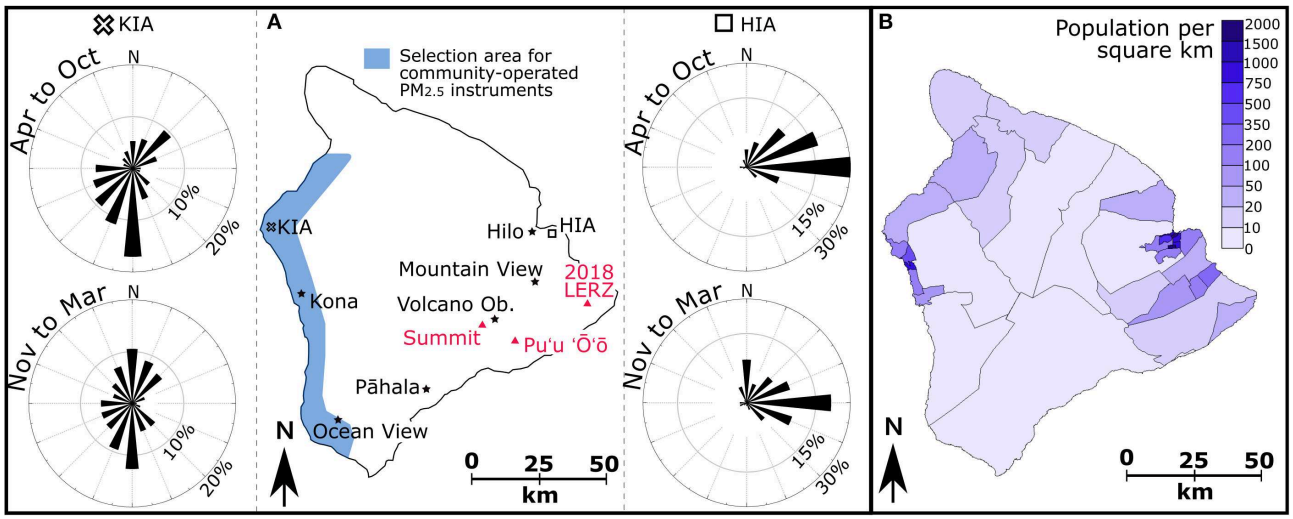

FIGURE 1 | Island of Hawai'i. **(A)** Ground-based sampling networks; HDOH and NPS stations indicated with black stars. Kīlauea summit, Pu'u 'Ō'ō vent and 2018 lower East Rift Zone eruption site indicated with red triangles. Selection area of community-operated $PM_{2.5}$ instruments indicated with blue highlight. Wind directions at Kona International Airport (KIA, empty black cross) and Hilo International Airport (HIA, empty black square) displayed as seasonal wind roses for period 2007–2018 (NOAA, 2019). Note "Volcano Ob." stands for Volcano Observatory. **(B)** Population density per square kilometer on the Island of Hawai'i, based on 2010 Census data. Highest population density is located in the east-coast city of Hilo (population ~45,700) and the west-coast city of Kailua-Kona (population ~28,500) (Hawai'i Department of Business Economic Development and Tourism, 2011).

The 2018 Kīlauea eruption in the lower East Rift Zone (LERZ) began following the collapse of the Pu'u 'Ō'ō vent on the thirtieth of April (Neal et al. 2019; HVO, 2018). Twenty-four fissures opened over a distance of 6.8 km in the vicinity of Leilani Estates (**Figure 1A**). During the first week of the LERZ eruption, spattering activity at individual fissures was typically short-lived (minutes to hours in duration) and lava was viscous with spatter deposition within tens of meters of individual fissures. On the eighteenth of May, the eruptive style evolved to less viscous lava and resulted in fast-moving lava flows which reached the ocean 2 days later (HVO, 2018). By the end of May 2018, activity had become focused at Fissure 8, and this remained the dominant fissure for the remainder of the LERZ eruption (Neal et al., 2019). Lava fountains from Fissure 8 reached heights of 80 m, and lava effusion rates ranged from 50 to 200 m^3/s (Neal et al., 2019). Lava from Fissure 8 flowed in a semi-stable channel to the ocean and eventually covered an area of land 35.5 km^2 in size (Neal et al. 2019; HVO, 2018). This eruption was the largest along Kīlauea's LERZ in the last two centuries and had far-reaching impacts around the Island of Hawai'i. With the collapse of the Pu'u 'Ō'ō vent and draining of Kīlauea's summit magma reservoir, the dominant source of volcanic SO_2 became the LERZ eruptive vents. SO_2 emissions reached an average of 200 kt/day in June 2018 (Kern et al. 2019), severely impacting island-wide air quality. The eruption declined rapidly at the end of July and lava effusion ceased on the fourth of August 2018 (Neal et al., 2019).

2.1. Downwind Processes and Impacts

Since initiation of intermittent fountaining activity at Kīlauea in 1983, SO_2 emissions have been a health concern among downwind communities on the Island of Hawai'i. As emissions from Kīlauea are dispersed downwind, communities are exposed to volcanic smog, locally known as vog, predominantly composed of SO_2 and fine particles of sulfuric acid aerosol (Longo, 2009; Longo et al., 2010; Halliday et al., 2015; Tam et al., 2016; Elias and Sutton, 2017). Prevailing trade winds from the north-east, particularly during the period from April to October, carry Kīlauea's emissions over the communities to the south and west (Longo et al., 2005, 2008; Michaud et al., 2007; Tam et al., 2016; Elias and Sutton, 2017) (**Figure 1A**). The Island of Hawai'i has relatively low population density in the south (**Figure 1B**), with ~4,400 residents in Ocean View and ~1,300 residents in Pāhala. Trade winds from the north-east are influenced by the high topography of Mauna Loa and Mauna Kea, generating more localized air movement in the lee of the island on the west coast (Michaud et al., 2007) (**Figure 1A**). This wind shadow allows a potentially longer residence time for air pollutants (volcanogenic or otherwise) along the densely-populated western coastline (**Figure 1B**). During the winter months (November to March), the trade winds weaken and southerly and westerly winds may distribute vog toward the densely-populated eastern coastline of the island (Wyrtki and Meyers, 1976; Mannino et al., 1996; Michaud et al., 2004) (**Figure 1B**).

Numerous studies have investigated the impact of Kīlauea's SO_2 emissions on the health of island residents, even at the relatively low levels of degassing prior to the emergence of the lava lake in 2008. Mannino et al. (1996) reviewed the frequency of visits to emergency departments and hospitalizations for respiratory issues during periods of continuous and discontinuous SO_2 emissions throughout the 1980s. Communities on the western side of the island frequently exposed to vog were found to have higher rates of

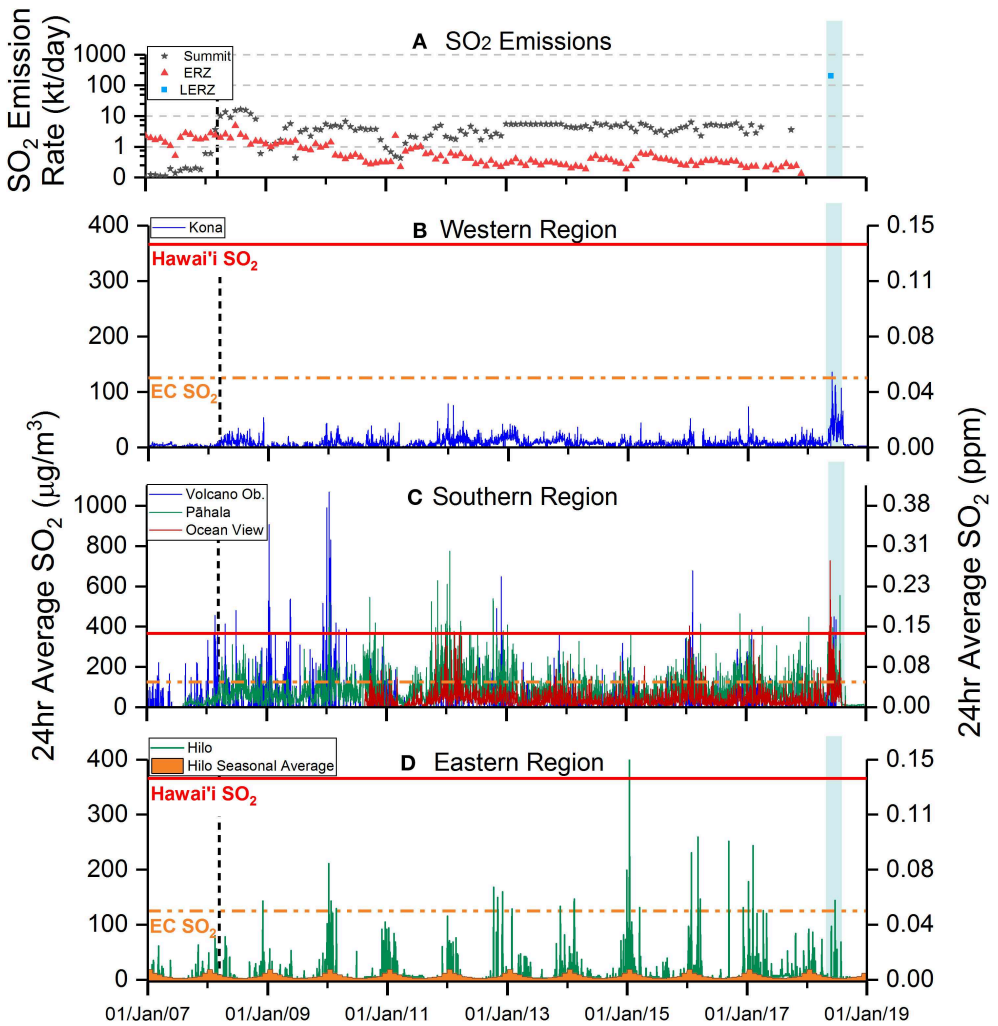

FIGURE 2 | SO_2 mass concentrations relative to health guidelines in selected populated areas of Island of Hawai'i. **(A)** SO_2 emissions from Kīlauea summit indicated with black stars; from ERZ indicated with red triangles; from 2018 LERZ eruption indicated with blue square. Note logarithmic scale. **(B–D)** SO_2 air quality (24-h mean) in communities from 2007 to the end of 2018. Solid red line: Hawai'i Standard air quality threshold (24-h mean of 366 $\mu g/m^3$); dashed orange line: European Commission (EC) air quality threshold (24-h mean of 125 $\mu g/m^3$). Dashed black line: 2008 initiation of summit activity; blue highlight: 2018 LERZ eruption duration. **(A)** SO_2 emissions data sourced from Elias and Sutton (2012), Beirle et al. (2014), Elias et al. (2018), and Elias et al. (in preparation). Summit emissions for 2008–2012 are from Beirle et al. (2014). LERZ data-point represents the average SO_2 emission from the LERZ eruption for June 2018, taken from Kern et al. (2019). **(B)** Note that "Volcano Ob." stands for Volcano Observatory; **(D)** seasonal average for Hilo between 2007 and 2017 indicated by orange bars.

hospitalizations for chronic obstructive pulmonary disease than the east-coast city of Hilo, which is rarely exposed to vog. Periods of weakened north-easterly trade winds coincided with a 15 % increase in emergency department visits for asthma in Hilo (Mannino et al., 1996). In 2004, the health of Hawai'i residents in vog-exposed and -unexposed communities was surveyed (Longo et al., 2008; Longo, 2009). Those in exposed communities were found to have a significantly increased prevalence of cough, phlegm, sinus congestion, rhinorrhoea, wheezing, eye irritation, and bronchitis than those in unexposed communities. Following the increase in SO_2 flux from Kīlauea's summit in 2008, Longo (2013) reassessed the vog-related health impacts on the residents of the Island of Hawai'i. The magnitude of cardio-respiratory issues in vog-exposed communities was found to have increased as compared to 2004 (Longo et al., 2008), with the risk factor of acute cardiac events in persons aged >50 years increased by 12 % (Longo, 2013). A study by Tam et al. (2016) investigated the effects of vog on the respiratory health of school children across Hawai'i, finding that chronic exposure to vog was associated with increased prevalence of cough and potential decrease in lung function, but not with the prevalence of asthma or bronchitis. The unprecedented emission rates of the 2018 LERZ eruption has presented a continued motivation to further characterize the severity and distribution of volcanic air pollution during elevated volcanic activity.

The 2018 Kīlauea LERZ eruption provided a unique opportunity to study the impacts arising from a large low-altitude cloud rich in SO_2 in a populated and well-instrumented part

of the world. Here we used open-access data from a network of reference-grade instruments in populated areas around the Island of Hawai'i to determine the severity of SO_2 and $PM_{2.5}$ impact on air quality from the LERZ eruption. We compare air quality during the LERZ eruption to that from a lower emission period, defined to be January 2007 to December 2017 for SO_2 and January 2010 to December 2017 for $PM_{2.5}$. We examine a network of community-operated $PM_{2.5}$ instruments and compare their measurements to those from reference-grade instruments. From these data, we demonstrate that SO_2 and $PM_{2.5}$ mass concentrations during the 2018 LERZ eruption in selected communities around the island were of a higher magnitude than during volcanic activity from Kīlauea during 2007 to 2017.

3. DATA AND METHODS

3.1. Continuous SO_2 and $PM_{2.5}$ Air Quality Monitoring

Hawai'i Department of Health (HDOH) ambient air quality stations continuously monitor SO_2 and $PM_{2.5}$ mass concentrations around the Island of Hawai'i (**Figure 1A**). Automated SO_2 monitoring stations have been operational since 1997 in Hilo, 2005 in Kona, 2007 in Pāhala and 2010 in Ocean View. A National Park Service (NPS) ambient air quality station monitors SO_2 inside of Hawai'i Volcanoes National Park at the Volcano Observatory. $PM_{2.5}$ has been autonomously monitored since 2005 in Mountain View and Kona, 2008 in Hilo and Pāhala and since 2010 in Ocean View.

SO_2 is measured by a pulsed fluorescence spectroscopy analyzer (model 43i manufactured by Thermo Scientific) that is designated by the EPA for measurements in the range of 0–1,000 ppb, with a lower detectable SO_2 limit of 0.5 ppb and a precision of 1 ppb (Thermo Scientific 2010; EPA, 2016). FEM-designated instruments (Forum for Environmental Measurements), such as this SO_2 analyzer, promote consistency in measurements and laboratory conditions ensuring that the instruments are of reference-grade quality (EPA, 2016). Following EPA regulations, the analyzers undergo *in-situ* calibration checks weekly, with a multi-point calibration run every 6 months. $PM_{2.5}$ mass concentrations are measured by a Beta Attenuation Monitor (BAM) with a 60-min sampling rate. The BAM instrument (model BAM-1020, manufactured by Met One Instruments) is FEM-designated for measurements of particles in the size range of 0–1,000 μm (with $PM_{2.5}$ being a small subset of the measured particle size range), with a resolution of 1 μm particle diameter and a lower detection limit of 4 $\mu g/m^3$ (MetOne 2008; EPA, 2016). The BAM instruments undergo calibration and auditing every 6 months. Permanent HDOH ambient air quality stations are kept in air-conditioned enclosures to maintain long-term stability. Data from the air quality stations are streamed in near-real time to the HDOH website, which is open-access and publicly-available (HDOH, 2019).

Data from the HDOH and NPS station networks used in this study have been categorized into regions for the purpose of data analysis. The western region includes Kona HDOH station on the west coast of the Island of Hawai'i. The southern region includes Volcano Observatory NPS station and Pāhala and Ocean View HDOH stations. The eastern region includes the Hilo and Mountain View HDOH stations. We compare the HDOH and NPS SO_2 timeseries data against the European Commission 24-h air quality threshold (125 $\mu g/m^3$) and the Hawai'i 24-h ambient air quality standard (366 $\mu g/m^3$). The HDOH $PM_{2.5}$ timeseries data is compared to the World Health Organization 24-h exposure limit (25 $\mu g/m^3$) and the Environmental Protection Agency NAAQS 24-h limit (35 $\mu g/m^3$).

3.2. Community-Operated $PM_{2.5}$ Instruments

PurpleAir (Utah, USA) instruments are low-cost (approximately $250 per unit) particulate sensors that are purchased and operated by individuals and provide open access data online (PurpleAir, 2019). PurpleAir instruments contain Plantower PMS5003 nephelometer sensors, which use a small fan to draw air through a laser-induced light, and a photo-diode detector converts 90°-scattered light into a voltage pulse (Kelly et al., 2017). PMS5003 sensors have a 10 s response time and detect particles between 0.3 and 10 μm in diameter (Kelly et al., 2017; Sayahi et al., 2019). The maximum consistency error of the sensors is stated by the manufacturer to be ± 10 $\mu g/m^3$ between 0 and 100 $\mu g/m^3$ (Plantower, 2016). The instruments are factory calibrated prior to sale (PurpleAir, 2019). PM mass concentration measurements are calculated using an atmospheric calibration factor, details of which are not provided by the manufacturer (Kelly et al., 2017; Zheng et al., 2018; Sayahi et al., 2019). PurpleAir instruments contain two Plantower PMS5003 sensors mounted in one housing, allowing self-consistency checks to alert when significant differences are reported between the internal sensors. An ESP8266 wireless chip is included in PurpleAir instruments to upload data via WiFi to an online cloud database, which is open-access (Sayahi et al., 2019).

Prior to the 2018 LERZ eruption, six community-operated PurpleAir instruments were located on the Island of Hawai'i, three of which were in the Kona area in the western region. Installation dates ranged from August 2017 to February 2018. Following the onset of the LERZ eruption and island-wide increase in atmospheric pollutants, the number of PurpleAir instruments increased, with a further twenty instruments installed across the western region of the island over the course of May to July 2018.

We carried out fieldwork during the 2018 LERZ eruption and co-located PurpleAir instruments with HDOH ambient air quality stations at Kona and Ocean View (**Figure 1A**). Two PurpleAir instruments were installed at the Kona station, one from the fifth of June to September 2018 and a second from the nineteenth of July to the third of August, and one PurpleAir instrument was installed at the Ocean View station from the nineteenth of July to the third of August 2018. The PurpleAir instruments were installed close to the inlet for the BAM instruments, on the roofs of the air quality shelters and away from obstructions. Other than the coordinates of the instrument,

no environmental information is provided in association with the PurpleAir instruments. For this reason, measurement uncertainty arising from factors such as installation in proximity to potential contamination sources in community-operated PurpleAir instruments should be considered significantly higher than those placed in optimal conditions near HDOH stations. Community-operated PurpleAir instruments were selected for analysis along the region highlighted in blue in **Figure 1A**.

4. RESULTS

4.1. SO_2 Mass Concentrations 2007–2018

4.1.1. Western Region: Kona

During 2007–2017, the west-coast city of Kailua-Kona was commonly exposed to low mass concentrations of SO_2, with a maximum recorded 24-h-mean mass concentration of 79 μg/m^3 recorded at the Kona HDOH station (**Table 1**). SO_2 air pollution in Kona increased with the onset of summit activity in 2008 (2008–2017 average mass concentrations were 7.7 μg/m^3 compared to 3 μg/m^3 in 2007) (**Figure 2B**). During 2007–2017 there were no 24-h periods where SO_2 mean mass concentrations at the HDOH Kona station exceeded Hawai'i or EC recommended thresholds (**Figure 2B**).

Kona experienced elevated SO_2 mass concentrations during the 2018 LERZ eruption, with a peak 24-h-mean mass concentration of 136 μg/m^3 measured at the Kona station. During the 2018 LERZ, SO_2 mass concentrations in Kona did not exceed the Hawai'i SO_2 threshold of 366 μg/m^3 (**Figure 2B**), but did exceed the 125 μg/m^3 EC threshold on one occasion (**Table 1**).

4.1.2. Southern Region: Volcano Observatory, Pāhala and Ocean View

Following initiation of Kīlauea's summit activity in 2008, the HDOH-operated Pāhala station and the NPS-operated Volcano Observatory station routinely recorded high concentrations of SO_2 (**Figure 2C**), with SO_2 mass concentrations exceeding the Hawai'i 366 μg/m^3 24-h-mean threshold 0.7 % of the time at both Volcano Observatory (twenty-eight exceedance events) and Pāhala (thirty exceedance events) (**Table 1**). The maximum 24-h-mean mass concentration recorded by the NPS station at Volcano Observatory during 2007–2017 was 1,068 μg/m^3, and by the HDOH station in Pāhala was 776 μg/m^3. The Ocean View HDOH station is located farther to the south-west than Pāhala and Volcano Observatory, at a greater distance from Kīlauea's summit and the ERZ (**Figure 1A**). During the period 2010–2017, SO_2 mass concentrations recorded at Ocean View exceeded the Hawai'i 24-h-mean threshold 0.1 % of the time (three exceedance events). The maximum 24-h-mean mass concentration recorded at Ocean View was 403 μg/m^3, significantly lower than measured at Volcano Observatory and Pāhala (**Table 1**).

In comparison, during the 3-months of the 2018 LERZ eruption, SO_2 mass concentrations exceeded the Hawai'i 366 μg/m^3 threshold 2.1 % of the time at Volcano Observatory (two exceedance events), 5.3 % of the time at Pāhala (five exceedance events) and 4.2 % at Ocean View (four exceedance events). Maximum 24-h-mean mass concentrations at Volcano Observatory and Pāhala were lower than those measured during 2008–2017 (450 and 555 μg/m^3, respectively), but the relative frequency of exceedance events increased (**Table 1**). During the 2018 LERZ eruption, the Ocean View station recorded a peak 24-h-mean mass concentration of 728 μg/m^3, almost double the previous peak measurement of 403 μg/m^3 recorded at that station in January 2016.

4.1.3. Eastern Region: Hilo

During the period 2007–2017, SO_2 mass concentrations in Hilo followed a distinct seasonality (**Figure 2D**). Peak SO_2 mass concentrations were commonly observed in Hilo in November to March (average monthly concentration of 11 μg/m^3) with low mass concentrations in the intervening months of April to October (average monthly mass concentration of 3.6 μg/m^3, as calculated from 2007 to 2017) (**Figure 2D**). Exceedances of the EC 24-h-mean threshold (125 μg/m^3) rarely occurred outside this peak season. In the period 2007–2017 there were twenty-one exceedance events during November to March, compared with just three between April to October. The seasonal variations in SO_2 mass concentrations observed in Hilo can be explained by the strong prevalence of northeasterly trade winds during April to October (Wyrtki and Meyers, 1976) (**Figure 1A**). During these months, emissions from Kīlauea's summit and the ERZ were dispersed predominantly to the south-west of the Island. The trade winds weaken between November to March, allowing SO_2 to be dispersed to the east of the island (Mannino et al., 1996; Michaud et al., 2004; Elias and Sutton, 2017).

During the third of May to fourth of August LERZ eruption, the HDOH station in Hilo recorded a maximum 24-h-mean mass concentration of 144 μg/m^3, which was recorded on the twenty-first of June (**Table 1**), and was the only exceedance of the EC 24-h-mean threshold during the 3-month eruption. The SO_2 mass concentrations measured during the LERZ eruption were lower than the average measurements during the 2007–2017 period. SO_2 mass concentrations in Hilo are usually low during the months when the LERZ eruption occurred. Nevertheless, during the 2018 LERZ eruption, SO_2 mass concentrations in Hilo rose significantly above the average for the season (average 24-h-mean SO_2 mass concentration during 2018 LERZ eruption was 6.9 μg/m^3, in comparison to the usual seasonal average of 3.6 μg/m^3).

4.2. $PM_{2.5}$ Mass Concentrations 2010–2018

4.2.1. Western Region: Kona

In the period 2010–2017, $PM_{2.5}$ recorded by HDOH Kona station never exceeded the EPA 24-h-mean threshold of 35 μg/m^3 (**Figure 3A**). The WHO 24-h-mean guideline of 25 μg/m^3 was exceeded 1.2 % of the time at the Kona site (33 exceedance events). The maximum $PM_{2.5}$ 24-h-mean mass concentrations was 33 μg/m^3, recorded in April 2016 (**Table 1**).

During the 2018 LERZ eruption, $PM_{2.5}$ exceeded the 24-h-mean 35 μg/m^3 EPA threshold 8.4 % of the time at the Kona station (eight exceedance events). The lower guideline of 25 μg/m^3 established by the WHO was exceeded 34.7 % of the time at the Kona site (33 exceedance events). The maximum

TABLE 1 | Impact of the 2018 LERZ eruption on concentrations of SO_2 and $PM_{2.5}$.

Station location	Measurement period	Sulfur dioxide (SO_2)			Particulates ($PM_{2.5}$)		
		(SO_2) ($\mu g/m^3$) 24-h mean	Exceedance Hawai'i threshold (24-h > 366 $\mu g/m^3$)	Exceedance EC threshold (24-h > 125 $\mu g/m^3$)	($PM_{2.5}$) ($\mu g/m^3$) 24-h mean	Exceedance EPA threshold (24-h > 35 $\mu g/m^3$)	Exceedance WHO guideline (24-h > 25 $\mu g/m^3$)
Hilo Elevation: 121 m asl 40 km NE of summit 35 km NW of Fissure 8	Low Emission *	Average 7 σ 19 Max 403	1 day 0%	24 days 0.6%	Average – σ – Max –	[No Data]	[No Data]
	High Emission 2018 LERZ **	Average 6 σ 21 Max 144	0 days 0%	1 day 1.1%	Average 5 σ 2 Max 15	0 days 0%	0 days 0%
Mountain View Elevation: 426 m asl 26 km NE of summit 23 km NW of Fissure 8	Low Emission ***	Average – σ - Max –	[No Data]	[No Data]	Average 4 σ 4 Max 35	1 day 0%	3 days 0.1%
	High Emission 2018 LERZ **	Average – σ – Max -	[No Data]	[No Data]	Average 7 σ 6 Max 18	0 days 0%	0 days 0%
Volcano Observatory Elevation: 1,161 m asl 2 km NW of summit 35 km W of Fissure 8	Low Emission *	Average 24 σ 67 Max 1068	28 days 0.7%	204 days 5.1%	Average – σ – Max –	[No Data]	[No Data]
	High Emission 2018 LERZ ***	Average 56 σ 106 Max 450	2 days 2.1%	10 days 10.5%	Average σ – Max –	[No Data]	[No Data]
Pāhala Elevation: 320 m asl 30 km SW of summit 66 km SW of Fissure 8	Low Emission *	Average 81 σ 72 Max 776	30 days 0.7%	729 days 18.1%	Average 6 σ 5 Max 97	2 days 0.1%	3 days 0.1%
	High Emission 2018 LERZ **	Average 129 σ 108 Max 555	5 days 5.3%	34 days 35.8%	Average 10 σ 5 Max 24	0 days 0%	0 days 0%

(Continued)

TABLE 1 | Continued

Station location	Measurement period	Sulfur dioxide (SO_2)			Particulates ($PM_{2.5}$)		
		(SO_2) ($\mu g/m^3$) 24-h mean	Exceedance Hawai'i threshold (24-h > 366 $\mu g/m^3$)	Exceedance EC threshold (24-h > 125 $\mu g/m^3$)	($PM_{2.5}$) ($\mu g/m^3$) 24-h mean	Exceedance EPA threshold (24-h > 35 $\mu g/m^3$)	Exceedance WHO guideline (24-h > 25 $\mu g/m^3$)
Ocean View Elevation: 862 m asl 61 km W of summit 100 km W of Fissure 8	Low Emission ***	Average 26	3 days 0.1%	93 days 3.5%	Average 12	4 days 0.1%	25 days 0.9%
		σ 39			σ 5		
		Max 403			Max 42		
	High Emission 2018 LERZ **	Average 117	4 days 4.2%	27 days 28.4%	Average 26	10 days 10.5%	44 days 46.3%
		σ 114			σ 8		
		Max 728			Max 56		
Kona Elevation: 517 m asl 67 km W of summit 106 km W of Fissure 8	Low Emission *	Average 7	0 days 0%	0 days 0%	Average 12	0 days 0%	33 days 1.2%
		σ 7			σ 5		
		Max 79			Max 33		
	High Emission 2018 LERZ **	Average 39	0 days 0%	1 days 1.1%	Average 24	8 days 8.4%	33 days 34.7%
		σ 25			σ 9		
		Max 136			Max 59		

*All units in $\mu g/m^3$. Exceedances of air quality standards are indicated for 24 h means, and calculated as percentage of total measurement duration. Distances between emission points and measurements sites are straight line distances; the emissions will not always follow the most direct route from near- to far-field. Note: no data available for $PM_{2.5}$ at Volcano Observatory, or Hilo for 2010–2017; no data available for SO_2 at Mountain View. *Low emission period for SO_2 from the first of January 2007 to the thirty-first of December 2017 and for $PM_{2.5}$ from the first of September 2010 to the thirty-first of December 2017; **high emission 2018 LERZ period for SO_2 and $PM_{2.5}$ from the third of May 2018 to the sixth of August 2018. ***Exceptions due to data availability: Mountain View low emission for $PM_{2.5}$ from the first of December 2010 to the thirty-first of December 2017; Volcano Observatory high emission 2018 LERZ period for SO_2 from the third of May 2018 to the third of July 2018; Ocean View low emission for SO_2 from twenty-third of August 2010 to the thirty-first of December 2017.*

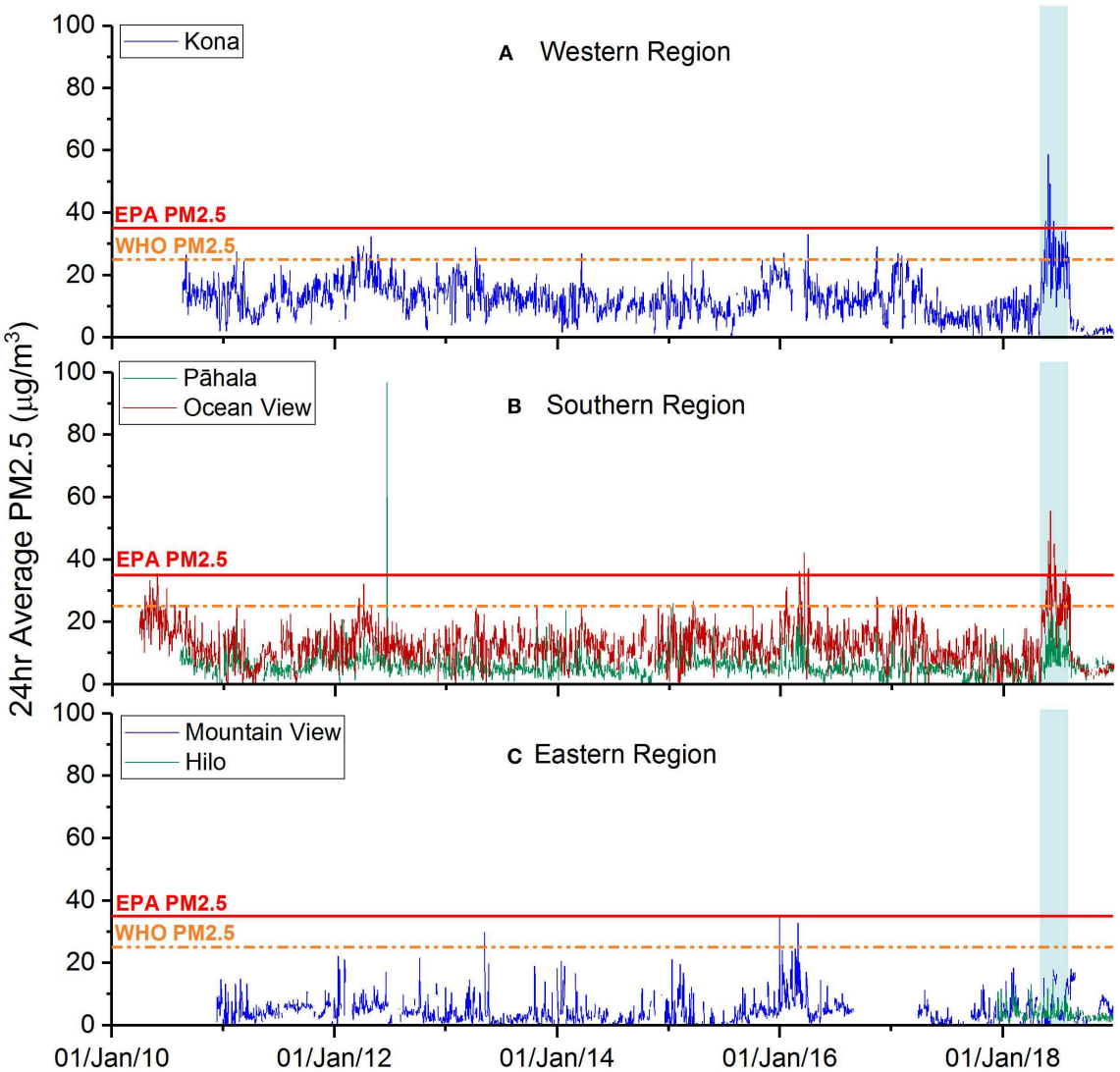

FIGURE 3 | $PM_{2.5}$ mass concentrations relative to health guidelines in select populated areas of Island of Hawai'i. **(A–C)** Concentrations of $PM_{2.5}$ (24-h mean) in populated areas from 2010 to the end of 2018. Solid red line: EPA Federal Standard air quality threshold (24-h mean of 35 µg/m^3); dashed orange line: World Health Organization (WHO) air quality guideline (24-h mean of 25 µg/m^3); blue highlight: 2018 LERZ eruption duration.

$PM_{2.5}$ 24-h-mean mass concentration at the site was recorded as 59 µg/m^3 on the twenty-ninth of May 2018.

4.2.2. Southern Region: Pāhala and Ocean View

During the period 2010–2017, the southern region of the Island of Hawai'i experienced variable levels of $PM_{2.5}$ (**Figure 3B**). The maximum $PM_{2.5}$ 24-h-mean mass concentration recorded in Ocean View was 42 µg/m^3, recorded in March 2016. In Pāhala the maximum recorded $PM_{2.5}$ 24-h-mean mass concentration was 97 µg/m^3, recorded on the eighteenth of June 2012, and coincident with two brush fires in the vicinity of Pāhala which burned approximately 5,600 acres (Hawai'i Emergency Management Agency, 2018). The EPA 35 µg/m^3 $PM_{2.5}$ threshold was exceeded 0.1 % of the time at both Ocean View and Pāhala (four exceedance events and two exceedance events, respectively). The lower $PM_{2.5}$ guideline of 25 µg/m^3 established by the WHO was exceeded 0.9 % of the time at Ocean View (25 exceedance events) and 0.1 % of the time at Pāhala (three exceedance events).

Mean $PM_{2.5}$ mass concentrations in Pāhala during the 2018 LERZ eruption were higher than the 2010–2017 average (10 µg/m^3 with respect to 6 µg/m^3) (**Table 1**), however there were no 24-h periods which exceeded either the EPA or WHO 24-h-mean thresholds. During the 2018 LERZ eruption, $PM_{2.5}$ recorded in Ocean View exceeded the 35 µg/m^3 EPA threshold 10.5 % of the time (ten exceedance events) and exceeded the WHO 24-h-mean guideline 46.3 % of the time (44 exceedance events). In mid-June 2018, the Ocean View HDOH station recorded 3 consecutive days where 24-h-mean mass concentrations exceeded 35 µg/m^3, unprecedented in the period 2010–2017. The maximum 24-h-mean mass concentration

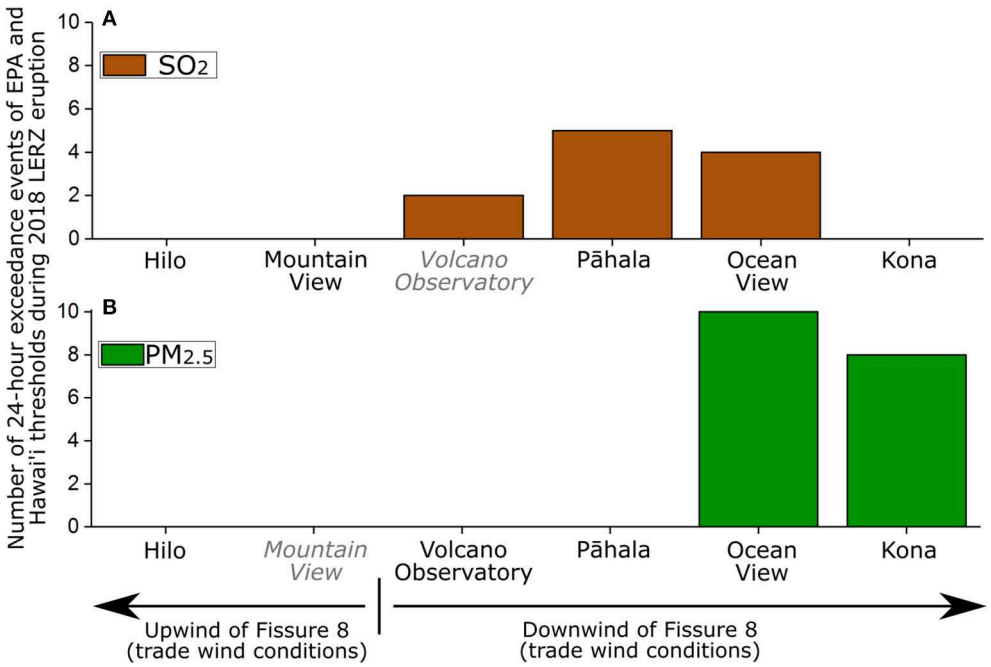

FIGURE 4 | Exceedances of **(A)** 24-h Hawai'i Standard for SO_2 during 2018 LERZ eruption and **(B)** EPA threshold for $PM_{2.5}$ during 2018 LERZ eruption. Note: data were unavailable for $PM_{2.5}$ at Volcano Observatory and SO_2 at Mountain View.

recorded in Ocean View during the 2018 LERZ eruption was 56 μg/m^3, somewhat higher than the peak 24-h-mean mass concentration recorded at Ocean View in 2016 (42 μg/m^3).

4.2.3. Eastern Region: Hilo and Mountain View

HDOH stations in the eastern region of the Island of Hawai'i recorded variable levels of $PM_{2.5}$ during 2010–2017 (**Figure 3C**). The maximum $PM_{2.5}$ 24-h-mean mass concentration in Mountain View was 35 μg/m^3, which was recorded in December 2015, and was the only exceedance of the 35 μg/m^3 24-h-mean EPA threshold during the period 2010–2017 (**Figure 3C**). The lower $PM_{2.5}$ 24-h-mean guideline of 25 μg/m^3 established by the WHO was exceeded 0.1 % of the time at Mountain View (three exceedance events).

During the 2018 LERZ eruption, $PM_{2.5}$ mass concentrations in Mountain View were higher than the average mass concentrations for 2010–2017 (7 and 4 μg/m^3, respectively) (**Table 1**). However, during the 2018 LERZ eruption, $PM_{2.5}$ mass concentrations did not exceed either the EPA threshold of 35 μg/m^3 or the WHO guideline of 25 μg/m^3.

5. DISCUSSION

5.1. Dispersal of Volcanic Emissions

Time series of SO_2 mass concentrations were analyzed in five populated areas on the Island of Hawai'i; Hilo, Volcano Observatory, Pāhala, Ocean View and Kona, for the period 2007–2018 (**Figure 2**). Time series of $PM_{2.5}$ were analyzed in Hilo, Mountain View, Pāhala, Ocean View, and Kona for the duration 2010–2018 (**Figure 3**). Significant escalations in emissions from Kīlauea volcano can be identified (**Figure 2A**), which were registered by the air quality monitoring instruments around the Island of Hawai'i (**Table 1**, section 4.1 and 4.2).

High mass concentrations of SO_2 and $PM_{2.5}$ generally occurred in the southern and western parts of the Island of Hawai'i. Prevailing trade winds from the north-east dispersed SO_2 emissions from Kīlauea volcano toward communities in the south and west of the island, as reported in previous studies (Longo et al., 2005, 2008; Michaud et al., 2007; Tam et al., 2016). During the 2018 LERZ eruption, the EPA 24-h-mean threshold for $PM_{2.5}$ (35 μg/m^3) and the Hawai'i threshold for SO_2 (366 μg/m^3) were exceeded in the south and west of the island (**Figure 4**). HDOH stations in the south of the island, 35–100 km away from Fissure 8, recorded 24-h events where SO_2 exceeded Hawai'i thresholds (note that there were no HDOH or NPS permanent monitoring stations for SO_2 in proximal location to the 2018 LERZ eruption site), but $PM_{2.5}$ EPA exceedance events only occurred at HDOH stations 100 km or further away from Fissure 8 (**Figure 4**). This spatial variance between distribution of $PM_{2.5}$ and SO_2 is well-documented and thought to reflect the timescale of oxidation of sulfur dioxide gas into sulfate aerosol during dispersion (Cadle et al., 1971; Stockwell and Calvert, 1983; Porter et al., 2002; Ilyinskaya et al., 2017).

Volcanic emissions at source commonly consist of a mixture of silicate ash particles, various gases and non-silicate aerosol (Oppenheimer and McGonigle, 2004; von Glasow et al., 2009; Langmann, 2014). The lifetime of SO_2 in the lower troposphere is generally considered to be on the order of 1–3 days to a week (Allen et al., 2002; Rotstayn and Lohmann, 2002; Pfeffer et al., 2006a; Pattantyus et al., 2018), the rate of conversion

depending on relative humidity and temperature, the availability of oxidants, and interaction with cloud or fog (Saxena and Seigneur, 1987; Oppenheimer et al., 1998). However, the SO_2 oxidation pathways in a volcanic cloud are not necessarily the same as under background conditions (Galeazzo et al., 2018). Through a variety of reaction pathways (including oxidation with the hydroxyl radical, OH, and with hydrogen peroxide, H_2O_2, and O_3), SO_2 in volcanic clouds is gradually converted to sulfate aerosol (Stockwell and Calvert, 1983; Allen et al., 2002), which is a dominant component of volcanic $PM_{2.5}$ (Tam et al., 2016; Pattantyus et al., 2018). The conversion rate of SO_2 to sulfate aerosol is important for estimating the potential hazard of volcanic $PM_{2.5}$ to human health and the downwind environments (Kroll et al., 2015).

HDOH stations measure the ambient air, which contains SO_2 and $PM_{2.5}$ derived from anthropogenic sources as well as natural non-volcanic and volcanic sources. In order to determine the influence of the volcanic eruption on the measured SO_2 and aerosol abundances, it is first necessary to calculate the volcanic component of the HDOH measurements. During the 2018 LERZ eruption, Fissure 8 was the dominant source of volcanic SO_2 emissions on the island, and following the decline of the eruption, the SO_2 and $PM_{2.5}$ mass concentrations decreased to below pre-LERZ eruption levels at all HDOH stations analyzed in this study (**Figures 2**, **3**). The mass of pollutants recorded at HDOH stations during this post-LERZ eruption period (mid-August 2018 to the first of February 2019) are therefore used to define the background abundances arising from all other non-volcanic sources. During this time there was some SO_2 emitted from Kīlauea's summit but at the lowest rate measured in decades at 0.1 kt/year (Nadeau et al., 2019). The volcanic component of the HDOH measurements was calculated by subtracting the average $PM_{2.5}$ and SO_2 mass concentration following the end of the 2018 LERZ eruption for each station from the mass concentrations measured during the LERZ eruption, to estimate the volcanogenic component. The sulfate aerosol component within the volcanic $PM_{2.5}$ mass concentration was then estimated to be in the range 77–92 %, following the methods of Mather et al. (2012) and Kroll et al. (2015), of $PM_{2.5}$ composition from Kīlauea.

Estimating the conversion rate of SO_2 to sulfate from SO_2 and SO_4^{2-} datasets is not straightforward because several processes can occur simultaneously, including SO_2 oxidation to sulfate, dispersion-dilution and deposition of SO_2 and/or SO_4^{2-} to the surface.

Here, a first-order decay constant for SO_2 is estimated by the relationship between volcanic components of SO_2 and SO_4^{2-}, as follows;

$$\ln\left(\frac{S_{gas}}{S_{total}}\right) = -kt \quad (1)$$

where S_{gas} is the sulfur component of the volcanic SO_2 mass concentration (μg/m^3), S_{total} is the sum of sulfur components of the volcanic SO_4^{2-} and SO_2 mass concentrations (μg/m^3), t is the age of the volcanic cloud (seconds) and $-k$ is a first-order decay constant.

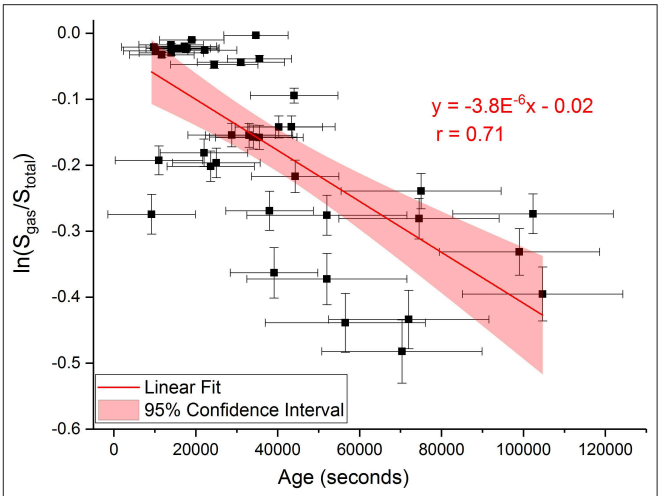

FIGURE 5 | Relationship between the age of the volcanic cloud and the volcanic sulfur components measured at Pāhala, Ocean View and Kona HDOH ambient air quality stations. S_{gas} is the sulfur component of the volcanic SO_2 mass concentration, S_{total} is the sum of sulfur components of the volcanic SO_4^{2-} and SO_2 mass concentrations. Age is derived from HYSPLIT back-trajectory simulations (Ilyinskaya et al., in preparation). Y axis error bars indicate range of SO_4^{2-} component in volcanic $PM_{2.5}$ composition from Kīlauea. X axis error bars indicate one standard deviation of HYSPLIT back-trajectory results specific to Kona, Ocean View and Pāhala. Correlation trendline based on the data points, with a first-order decay constant of 3.8×10^{-6} s^{-1} with a 95 % confidence interval of $\pm$ 1.26×10^{-6} s^{-1}.

The age of the volcanic cloud is here considered to be the time between emission of the cloud at the LERZ eruption source point and subsequent measurement at the HDOH station. From back-trajectory HYSPLIT simulations run between the HDOH ambient air quality stations and Fissure 8, the average age of the emissions and dispersal distance was calculated for dates between the eighteenth of July to the second of August 2018 (Ilyinskaya et al., in preparation). An estimate of the average first-order decay constant from our data-set is indicated in **Figure 5**. Although there is considerable scatter in the data, a broad trend of decreasing S fraction in the gas phase is apparent and a linear fit allows us to estimate a first-order rate constant of 3.8×10^{-6} s^{-1} with a 95 % confidence interval of $\pm$ 1.26×10^{-6} s^{-1}. This first-order decay constant for SO_2 relative to total sulfur can represent an estimate of the average rate of SO_2 oxidation to sulfate only if negligible sulfur deposition has occurred. Nevertheless, our value is similar to the SO_2 oxidation rate calculated by Kroll et al. (2015) from direct measurements of sulfur in gas and particle phase in Kīlauea's emission cloud from the summit to Pāhala. Kroll et al. (2015) identified a diurnal cycle in measured sulfate as a fraction of total sulfur, from which they calculated a noontime instantaneous SO_2 oxidation rate of 2.4×10^{-6} s^{-1}.

5.2. Reliability Assessment of Community-Operated $PM_{2.5}$ Instruments

A subset of the community-operated PurpleAir instruments on the Island of Hawai'i were selected for intercomparison

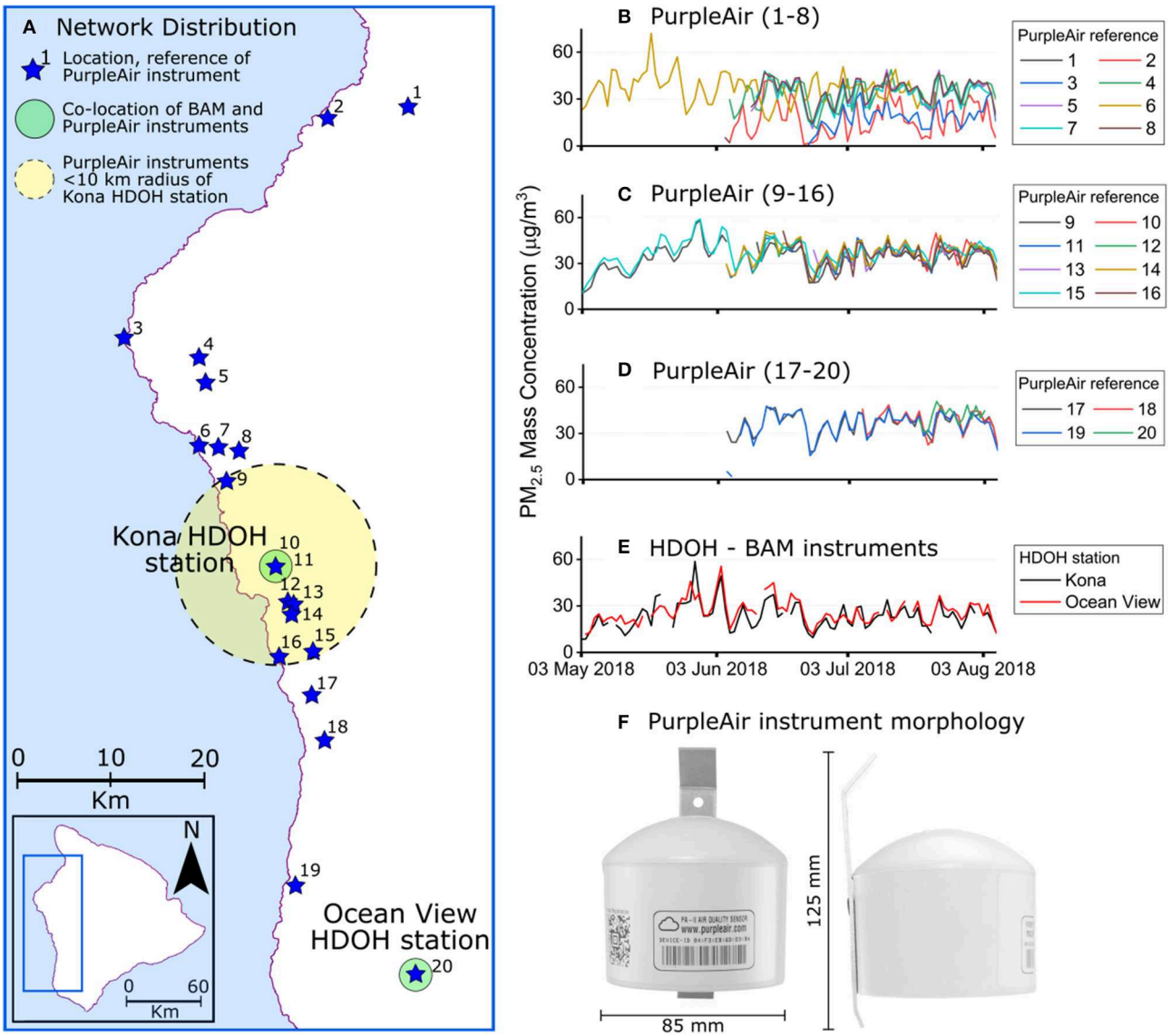

FIGURE 6 | Hawai'i Department of Health ambient air quality stations and community-operated PurpleAir instruments along the western region of the Island of Hawai'i selected for analysis in this study. **(A)** Distribution of publicly-owned PurpleAir instruments, indicated by blue stars with reference numbers, distribution of Kona and Ocean View HDOH stations indicated by green circles. PurpleAir instruments within 10 km radius of Kona HDOH station indicated by dashed yellow circle. **(B–D)** 24-h average mass concentration measurements from 20 PurpleAir instruments during the 2018 LERZ eruption; **(E)** 24-h average $PM_{2.5}$ from BAM instruments at Kona and Ocean View HDOH ambient air quality stations during the 2018 LERZ eruption. **(F)** Size and morphology of the PurpleAir instruments, seen from the front (left image) and side (right image). Photos by kind permission of PurpleAir LLC.

with the established institutional data-sets across the western region of the island. The low-cost and portable nature of the PurpleAir instruments (**Figure 6F**) facilitated installation of a monitoring network across the western region (**Figure 6A**), with a high spatial resolution of measurements in comparison to the locations of HDOH ambient air quality sites (**Figure 6A**). This can be advantageous to capture the effects of local topographic and meteorological factors, which may influence dispersion of and deposition from volcanic plumes. Mass concentrations from PurpleAir instruments and HDOH $PM_{2.5}$ instruments during the course of the 2018 LERZ eruption are presented in **Figures 6B–E**.

Small differences were found between individual PurpleAir instruments in the same location. Two PurpleAir instruments (**Figure 6A**, PurpleAir references 10 and 11) were co-located at the Kona HDOH station, and the PurpleAir instruments ran together for 16 days. During this time, the maximum absolute differences in 24-h average measurements between the PurpleAir instruments was 2.3 $\mu g/m^3$; which was 6 % of the total

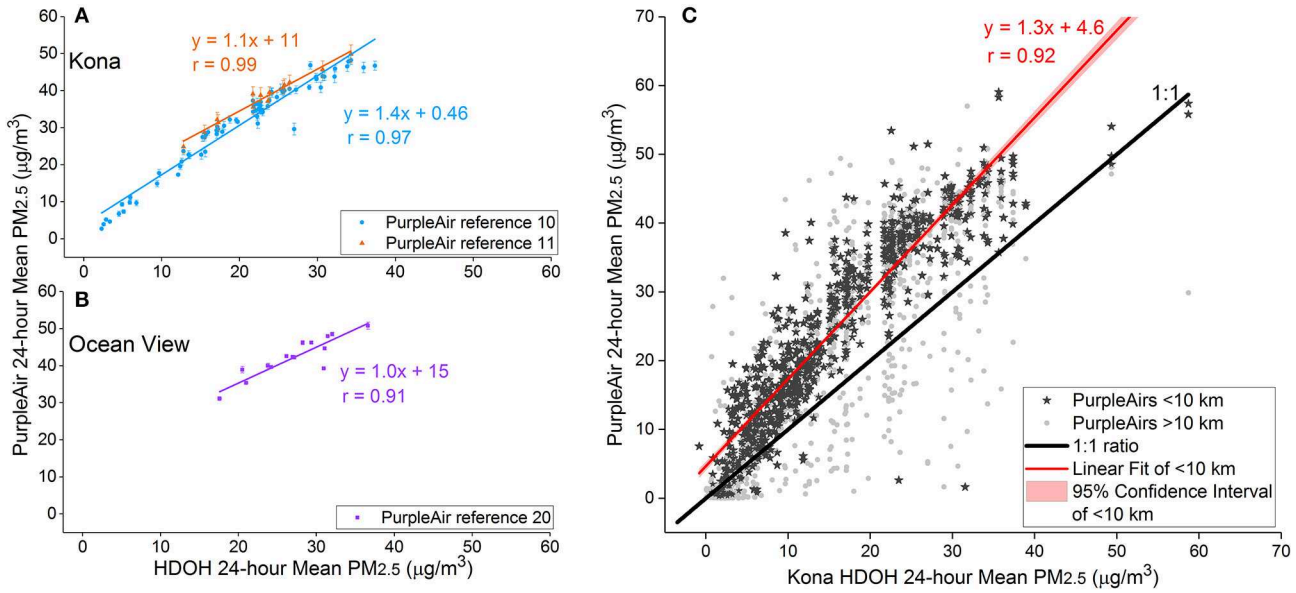

FIGURE 7 | PurpleAir and HDOH $PM_{2.5}$ comparison. **(A)** Two PurpleAir instruments co-located with Kona HDOH station. **(B)** One PurpleAir instrument co-located with Ocean View HDOH station. **(C)** Comparison of all PurpleAir instruments along the western region of the Island of Hawai'i compared with Kona HDOH measurements. PurpleAir instruments within 10 km of Kona HDOH indicated by dark gray stars, PurpleAir instruments at greater distances are indicated by light gray circles. Linear regression and 95 % confidence interval fit to instruments <10 km from Kona HDOH ambient air quality station. Measurement periods vary with earliest PurpleAir data from August 2017 and most recent from January 2019. **(A,B)** PurpleAir error bars show measurement variations between the two sensors within a single PurpleAir instrument, and therefore indicate the minimum error.

measured concentration. Correlation between the two PurpleAir instruments was very strong (Pearson's $r = 0.99$). Similar results were found by Malings et al. (2019) with co-location of nine PurpleAir instruments at a site in Pennsylvania for a period of 66 days (Pearson's $r > 0.9$). The high correlation between co-located individual PurpleAir instruments indicates high standardization. With this being the case, relative $PM_{2.5}$ mass concentrations measured by PurpleAir instruments over a wider geographical area should be comparably reliable.

Three PurpleAir instruments were co-located with HDOH $PM_{2.5}$ instruments (BAM) to determine the accuracy of PurpleAir instrument $PM_{2.5}$ measurements in relation to reference-grade instruments (**Figure 6A**, PurpleAir references 10, 11, and 20). The co-located PurpleAir measurements correlated well with the BAM measurements, with Pearson's r values of 0.99, 0.97, and 0.91 (**Figures 7A,B**). However, PurpleAir instruments did record higher mass concentrations of $PM_{2.5}$ in comparison to the BAM analyzers (**Figures 7A,B**). PurpleAir reference 10 (co-located with Kona HDOH station) (**Figure 6A**) recorded the greatest measurement off-set, with up to 40 % higher mass concentrations of $PM_{2.5}$ relative to the Kona BAM analyzer measurements (**Figure 7A**). This trend was also found when the community-operated PurpleAir instruments across the western region of the island were compared to the BAM at Kona HDOH station (**Figure 7C**), with strong correlation between PurpleAir instruments and BAM (Pearson's $r = 0.92$) but an average 30 % higher mass concentrations measured by PurpleAir instruments within 10 km of the Kona BAM instrument. Previous testing of PurpleAir instruments in Pennsylvania and California has yielded similar findings (AQ-SPEC, 2017; Malings et al., 2019), with over-estimation of $PM_{2.5}$ mass concentrations measured by PurpleAir instruments relative to BAM reference-grade analyzers.

Some discrepancy between PurpleAir and BAM measurements may be expected, as it is well-known that low-cost instruments measuring $PM_{2.5}$ with light scattering methods have not historically agreed with measurements obtained from reference grade instruments with different operating principles (Watson et al., 1998; Wilson et al., 2002; Chow et al., 2008; Burkart et al., 2010). In comparison with sensors of other operating principles, light-scattering optical particle sensors have been shown to suffer effects of relative humidity (Wang et al., 2015; Crilley et al., 2018), since the operating principle relies on indirect measurement of particle size and shape based on scattered light, and an assumed particle shape and refractive index. Conversely, BAM instruments measure direct changes in aerosol mass concentrations based on the loss of electrons on a filter which the aerosol has been deposited on (Watson et al., 1998; Manikonda et al., 2016), and so are not influenced by the hygroscopic growth of individual particles. Zheng et al. (2018) analyzed the performance of Plantower PMS3003 (an earlier version of the Plantower PMS5003 housed in PurpleAir instruments used in this study) against a reference grade scattered light spectrometer (with good correlation of $R^2 = 0.8$) and a BAM instrument (with lower correlation of $R^2 = 0.5$). They concluded that a likely

explanation contributing to the discrepancy is the potential for hygroscopic growth of aerosol particles due to ambient humidity, which alters the light-scattering properties of the aerosol and therefore the measurement made by the optical sensor (Watson et al., 1998; Cabada et al., 2004; Spinetti and Buongiorno, 2007; Jayaratne et al., 2018). In this instance, Zheng et al. (2018) found that the low-cost light-scattering sensor correlated best with the reference-grade instrument of the same operating principle, finding a lower correlation against the reference-grade instrument operating on principles other than light-scattering. The PurpleAir instrument over-estimation of $PM_{2.5}$ relative to the BAM reference-grade instrument may therefore be due to influences of humidity acting on the light scattering (Zheng et al., 2018).

An additional consideration in explaining the overestimation of $PM_{2.5}$ by the PurpleAir instruments relative to the reference-grade BAM is the particle density of the measured particulates. The Plantower PMS5003 sensors contained within the PurpleAir instruments provide mass concentration measurements which are calculated by an unreported atmospheric calibration factor (Zheng et al., 2018). We assume that this calibration factor uses an average particle density, likely similar to that for an urban environment, such as 1.65 g cm^{-3} (Pitz et al., 2003; Liu et al., 2015; Crilley et al., 2018). If the Plantower PMS5003 sensor measures ambient air with a particle density dissimilar to the average particle density used in the atmospheric calibration factor, the resulting sensor output would be biased. For example, introduction of volcanic aerosol, primarily sulfate with an average particle density of 1.77 g cm^{-3} (Sarangi et al., 2016), into the air measured by the sensor could result in sensor output bias as a result of dissimilarity between the real and assumed particle density.

Despite the $PM_{2.5}$ over-estimation, the strong correlation between the PurpleAir and BAM instruments indicates that the PurpleAir instruments provided qualitatively valuable measurements of the atmospheric conditions. The high degree of intra-instrument performance, similar to findings by Malings et al. (2019), indicates that the PurpleAir instruments are reliable for determining relative variations in $PM_{2.5}$. The dense network of instruments with a high spatial resolution along the western region of Hawai'i during the 2018 LERZ eruption gives a good indication of the relative amounts of $PM_{2.5}$ across the region, at a finer spatial resolution than available from the sparsely-located BAM instruments (**Figure 6A**). Low-cost community-operated networks, such as the PurpleAir instruments across the western region of Hawai'i during the 2018 LERZ eruption, can therefore be invaluable in providing insights into smaller-scale heterogeneities in air quality across a regional area at a scale inaccessible by the usually more disperse reference-grade instruments (**Figures 6B–E**). Additionally, as far as the authors are aware, this is the first validation of PurpleAir instruments in a volcanic environment. Their strong correlation to the BAM instruments along the west coast of the Island of Hawai'i during the 2018 LERZ eruption indicates that they are suitable for augmenting reference-grade instrument networks in periods of volcanic unrest. Considering that these instruments also provide a source of open-access data to the public, they present an opportunity to improve community awareness and inclusion of the general public in hazard assessment of downwind volcanic $PM_{2.5}$ air pollution.

6. CONCLUSIONS

Kīlauea's 2018 eruption was the largest LERZ eruption in the last two centuries. SO_2 emissions reached a monthly average of 200 kt/day during June (Kern et al. 2019), significantly exceeding emissions from Kīlauea during 2008–2017, which averaged 5–6 kt/day (Eguchi et al., 2011; Beirle et al., 2014; Carn et al., 2016; Elias et al., 2018). During the 2018 LERZ eruption, SO_2 mass concentrations exceeding the Hawai'i 24-h-mean threshold (366 $\mu g/m^3$) primarily occurred in the south of the island, at Volcano Observatory and in Pāhala and Ocean View (2.1, 5.3, and 4.2 % of the time during the 3-month long eruption, respectively). SO_2 mass concentrations were elevated at the HDOH Kona station (average 24-h-mean mass concentration of 39 $\mu g/m^3$ during the LERZ eruption, relative to 7 $\mu g/m^3$ during 2007–2017), but mass concentrations were highest in Ocean View, Pāhala and at Volcano Observatory (average 24-h-mean mass concentrations of 117 , 129 , and 56 $\mu g/m^3$, respectively). The Hawai'i 24-h-mean threshold was exceeded five times in Pāhala and twice at Volcano Observatory, but peak mass concentrations did not exceed those from the period 2007–2017. In Ocean View, the Hawai'i 24-h-mean threshold was exceeded four times and 24-h-mean mass concentrations peaked at 728 $\mu g/m^3$, almost double the previous peak measurement of 403 $\mu g/m^3$ recorded at that station in January 2016.

$PM_{2.5}$ mass concentrations recorded at HDOH stations around the island from 2010 to 2017 rarely exceeded the EPA 24-h-mean threshold of 35 $\mu g/m^3$ (0.1 % of the time at both Ocean View and Pāhala). The lower 24-h-mean $PM_{2.5}$ limit (25 $\mu g/m^3$) set by the World Health Organization was exceeded with greater frequency, particularly in Kona and Ocean View (1.2 and 0.9 % of the time, respectively). During the 2018 LERZ eruption, $PM_{2.5}$ air pollution was significantly higher than 2010–2017 levels in Kona and Ocean View, exceeding WHO guidelines 34.7 and 46.3 % of the time, respectively. Peak 24-h-mean mass concentrations in Ocean View were recorded at 56 $\mu g/m^3$, and 3 consecutive days in June were recorded with mean 24-h mass concentrations exceeding 35 $\mu g/m^3$. The Kona HDOH stations recorded eight 24-h periods which exceeded EPA thresholds, unprecedented in the 2010–2017 period.

Following the decline of the 2018 LERZ eruption, mass concentrations of both SO_2 and $PM_{2.5}$ measured at the HDOH stations decreased to below pre-LERZ eruption levels, indicating that a large proportion of the air quality anomalies measured during the eruption were volcanogenic. The post-LERZ HDOH measurements are here assumed to be representative of the background (non-volcanically-perturbed) atmosphere, and subtracting these abundances from those recorded during the LERZ eruption provides an estimate of the purely volcanogenic $PM_{2.5}$ and SO_2. The sulfate aerosol component within the volcanic $PM_{2.5}$ is calculated as between 77 and 92 %, following Mather et al. (2012). HYSPLIT back-trajectory

simulations provide an estimate of emission age following dispersion from source to measurement point (Ilyinskaya et al., in preparation), and a first-order SO_2 decay constant is estimated at 3.8×10^{-6} s^{-1}.

Community-operated PurpleAir instruments provided a high spatial resolution network across the western region of the island, informing the public regarding $PM_{2.5}$ mass concentrations in their locality. Low measurement variability (Pearson's $r = 0.99$) was found between co-located individual PurpleAir instruments, indicating a high level of intra-instrument performance. Observations recorded by co-located PurpleAir and BAM instruments correlated well (Pearson's $r = 0.99$, 0.97, and 0.94), but PurpleAir instruments were found to overestimate the $PM_{2.5}$ mass concentration by up to 40 %, relative to the BAM instrument. This likely reflects inherent differences in instrument operating principles and may be associated with changes in optical-properties of aerosol arising from hygroscopic growth in ambient humidity. Nevertheless, the PurpleAir instruments are suitable for providing a low-cost network to augment reference-grade instruments, and contribute an open-access source of readily-available information to the public leading to development of community awareness toward air quality.

This study has assessed the impacts to air quality in downwind communities around the Island of Hawai'i from 2007 to 2018. Spatial variability of air quality around the island during the 2018 LERZ eruption was comparable to patterns identified over the previous decade, but $PM_{2.5}$ and SO_2 pollution levels resulting from the 2018 LERZ eruption were significantly higher in western and southern regions of the island. A study of the potential health burden of these significant impacts on air quality might further illuminate aspects of the dose-response to volcanogenic emissions in addition to the impacts of public health protection measures put in place during the eruption.

DATA AVAILABILITY STATEMENT

The datasets analyzed for this study can be found in the Hawai'i Department of Health Ambient Air Quality Data repository [http://health.hawaii.gov/cab/hawaii-ambient-air-quality-data/], and in the PurpleAir sensor list repository [https://www.purpleair.com/sensorlist].

AUTHOR CONTRIBUTIONS

RW performed the data analysis and wrote the original draft. EI, AS, TR, MP, and TM contributed to data interpretation. All co-authors contributed to draft review and editing.

FUNDING

RW is funded by the Leeds-York Natural Environment Research Council (NERC) Doctoral Training Partnership (DTP) NE/L002574/1, in CASE partnership with the Icelandic Meteorological Office. RW, EI, EM, PW, and EL were funded for campaign-fieldwork by the Centre for the Observation and Modeling of Earthquakes, Volcanoes and Tectonics (COMET) grant COME3001. The authors also acknowledge support to EI from the NERC urgency grant NE/M021130/1 Source and longevity of sulfur in Icelandic flood basalt eruption plumes and GCRF NE/P015271/1 and NE/R009465/1 Unseen but not unfelt: resilience to persistent volcanic emissions (UNRESP). We acknowledge support from the NERC ESS DTP to PW, EPSRC CASE funding to EM, Alfred P. Sloan Foundation through support of the Deep Carbon Observatory to ME and EL and Leverhulme Early Career Fellowship to EL, and ANR Projet de Recherche Collaborative VOLC-HAL-CLIM ANR-18-CE01-0018 and Orléans Labex Voltaire ANR-10-LABX-100-0 to TR. CO acknowledges support from NERC grant NE/N009312/1, and EI, TM, ME, and CO further acknowledge support from NERC grant NE/S00436X/1: Volcanic plume understanding and forecasting: Integrating remote-sensing, *in-situ* observations and models (V-PLUS).

ACKNOWLEDGMENTS

We thank James Ciszewski at the Hawai'i Department of Health for assistance with fieldwork and data-gathering; Lacey Holland and Steven Businger at the University of Hawai'i at Manoa for volcanic emissions trajectory and HYSPLIT discussions; and the National Park Service and Hawai'i Volcanoes National Park for their contributions.

Any use of trade, firm, or product names is for descriptive purposes only and does not imply endorsement by the U.S. Government.

REFERENCES

Allen, A., Oppenheimer, C., Ferm, M., Baxter, P., Horrocks, L., Galle, B., et al. (2002). Primary sulfate aerosol and associated emissions from Masaya Volcano, Nicaragua. *J. Geophys. Res. Atmos.* 107, ACH5–ACH8. doi: 10.1029/2002JD002120

Andronico, D., and Del Carlo, P. (2016). PM10 measurements in urban settlements after lava fountain episodes at Mt. Etna, Italy: pilot test to assess volcanic ash hazard to human health. *Nat. Hazards Earth Syst. Sci.* 16, 29–40. doi: 10.5194/nhess-16-29-2016

AQ-SPEC (2017). *PurpleAir PA-I Sensor Evaluation Report*. Available online at: http://www.aqmd.gov/aq-spec/product/purpleair-pa-ii (accessed Feburary 13, 2019).

ATSDR (1998). *Public Health Statement Sulfur Dioxide*. 7446-09-5. Agency for Toxic Substances and Disease Registry.

Balmes, J. R., Fine, J. M., and Sheppard, D. (1987). Symptomatic bronchoconstriction after short-term inhalation of sulfur dioxide. *Am. Rev. Respir. Dis.* 136, 1117–1121. doi: 10.1164/ajrccm/136.5.1117

Barsotti, S., Andronico, D., Neri, A., Del Carlo, P., Baxter, P., Aspinall, W., et al. (2010). Quantitative assessment of volcanic ash hazards for health and infrastructure at Mt. Etna (Italy) by numerical simulation. *J. Volcanol. Geotherm. Res.* 192, 85–96. doi: 10.1016/j.jvolgeores.2010.02.011

Beirle, S., Hörmann, C., Penning de Vries, M., Dörner, S., Kern, C., and Wagner, T. (2014). Estimating the volcanic emission rate and atmospheric lifetime of SO_2 from space: a case study for Kīlauea volcano, Hawai'i. *Atmos. Chem. Phys.* 14, 8309–8322. doi: 10.5194/acp-14-8309-2014

Burkart, J., Steiner, G., Reischl, G., Moshammer, H., Neuberger, M., and Hitzenberger, R. (2010). Characterizing the performance of two optical particle counters (Grimm OPC1. 108 and OPC1. 109) under urban aerosol conditions. *J. Aerosol Sci.* 41, 953–962. doi: 10.1016/j.jaerosci.2010.07.007

Butwin, M. K., von Löwis, S., Pfeffer, M. A., and Thorsteinsson, T. (2019). The effects of volcanic eruptions on the frequency of particulate matter suspension events in Iceland. *J. Aerosol Sci.* 128, 99–113. doi: 10.1016/j.jaerosci.2018.12.004

Cabada, J. C., Khlystov, A., Wittig, A. E., Pilinis, C., and Pandis, S. N. (2004). Light scattering by fine particles during the Pittsburgh Air Quality Study: measurements and modeling. *J. Geophys. Res. Atmos.* 109. doi: 10.1029/2003JD004155

Cadle, R., Wartburg, A., and Grahek, P. (1971). The proportion of sulfate to sulfur dioxide in Kīlauea Volcano fume. *Geochim. Cosmochim. Acta* 35, 503–507. doi: 10.1016/0016-7037(71)90046-9

Carn, S., Clarisse, L., and Prata, A. J. (2016). Multi-decadal satellite measurements of global volcanic degassing. *J. Volcanol. Geothermal Res.* 311, 99–134. doi: 10.1016/j.jvolgeores.2016.01.002

Chow, J. C., Doraiswamy, P., Watson, J. G., Chen, L.-W., Ho, S. S., and Sodeman, D. A. (2008). Advances in integrated and continuous measurements for particle mass and chemical composition. *J. Air Waste Manage. Assoc.* 58, 141–163. doi: 10.3155/1047-3289.58.2.141

CRI (2004). *Health Effects of Project Shad Chemical Agent: Sulfur Dioxide* [cas 7446-09-5]. National Academies. The Centre for Research Information.

Crilley, L. R., Shaw, M., Pound, R., Kramer, L. J., Price, R., Young, S., et al. (2018). Evaluation of a low-cost optical particle counter (Alphasense OPC-N2) for ambient air monitoring. *Atmos. Meas. Tech.* 11, 709–720. doi: 10.5194/amt-11-709-2018

Eguchi, K., Uno, I., Yumimoto, K., Takemura, T., Nakajima, T. Y., Uematsu, M., et al. (2011). Modulation of cloud droplets and radiation over the North Pacific by sulfate aerosol erupted from Mount Kīlauea. *SOLA* 7, 77–80. doi: 10.2151/sola.2011-020

Elias, T., Kern, C., Horton, K., Sutton, A. J., and Garbeil, H. (2018). Measuring SO_2 emission rates at Kīlauea Volcano, Hawai'i USA, 2014-2017. *Front. Earth Sci.* 6:214. doi: 10.3389/feart.2018.00214

Elias, T., and Sutton, A. J. (2007). *Sulfur Dioxide Emission Rates from Kīlauea Volcano, Hawai'i, an Update: 2002-2006*. US Geological Survey.

Elias, T., and Sutton, A. J. (2012). *Sulfur Dioxide Emission Rates From Kīlauea Volcano, Hawai'i, 2007–2010.* Technical report, US Geological Survey.

Elias, T., and Sutton, A. J. (2017). *Volcanic Air Pollution Hazards in Hawai'i*. Technical report, US Geological Survey. Available online at: https://pubs.usgs.gov/fs/2017/3017/fs20173017.pdf

Environmental Protection Agency (2010). *Primary National Ambient Air Quality Standard for Sulfur Dioxide; Final Rule*. Available online at: https://www.govinfo.gov/content/pkg/FR-2010-06-22/pdf/2010-13947.pdf, 40 CFR Parts 50, 53, and 58 (accessed January 15, 2019)

Environmental Protection Agency (2013). *Federal and State Ambient Air Quality Standards*. Available online at: http://health.hawaii.gov/cab/files/2013/05/naaqs_jan_2013.pdf (accessed January 15, 2019)

Environmental Protection Agency (2016). *List of Designated Reference and Equivalent Methods*. National Exposure Research Laboratory.

European Commission (2018). *Environment Air Quality Standards*. Available online at: http://ec.europa.eu/environment/air/quality/standards.htm (accessed January 21, 2019)

Galeazzo, T., Bekki, S., Martin, E., Savarino, J., and Arnold, S. R. (2018). Photochemical box modelling of volcanic SO_2 oxidation: isotopic constraints. *Atmos. Chem. Phys.* 18, 17909–17931. doi: 10.5194/acp-18-17909-2018

Halliday, T., Lynham, J., and de Paula Neto, A. (2015). *Vog: Using Volcanic Eruptions to Estimate the Health Costs of Particulates and SO_2*. College of Social Sciences; Department of Economics.

Hansell, A., and Oppenheimer, C. (2004). Health hazards from volcanic gases: a systematic literature review. *Arch. Environ. Health Int. J.* 59, 628–639. doi: 10.1080/00039890409602947

Hawai'i Department of Business Economic Development and Tourism (2011). *Research and Economic Analysis Division. Statistics and Data Support Branch. Hawai'i State Data Center. 2010 Census Tract Names and Their Population, Housing and Land Area for the State of Hawai'i* Honolulu. *Hawai'i State Data Center Report Number 2010-2.*

Hawai'i Emergency Management Agency (2018). *2018 State of Hawai'i Hazard Mitigation Plan*. Section 4.15; Wildfire Available online at: https://dod.hawaii.gov/hiema/files/2018/06/Draft-Section-4.15-Wildfire-Placeholder.pdf (accessed August 9, 2019)

HDOH (2019). *Hawai'i Department of Health Clean Air Branch, Hawai'i Ambient Air Quality Data*. Available online at: http://health.hawaii.gov/cab/hawaii-ambient-air-quality-data/ (accessed August 13, 2019)

Holgate, S. (2017). "Every breath we take: the lifelong impact of air pollution" - a call for action. *Clin. Med.* 17, 8–12. doi: 10.7861/clinmedicine.17-1-8

Ilyinskaya, E., Schmidt, A., Mather, T. A., Pope, F. D., Witham, C., Baxter, P., et al. (2017). Understanding the environmental impacts of large fissure eruptions: aerosol and gas emissions from the 2014–2015 Holuhraun eruption (Iceland). *Earth Planet. Sci. Lett.* 472, 309–322. doi: 10.1016/j.epsl.2017.05.025

Jayaratne, R., Liu, X., Thai, P., Dunbabin, M., and Morawska, L. (2018). The influence of humidity on the performance of a low-cost air particle mass sensor and the effect of atmospheric fog. *Atmos. Meas. Tech.* 11, 4883–4890. doi: 10.5194/amt-11-4883-2018

Kelly, K. E., Whitaker, J., Petty, A., Widmer, C., Dybwad, A., Sleeth, D., et al. (2017). Ambient and laboratory evaluation of a low-cost particulate matter sensor. *Environ. Pollut.* 221, 491–500. doi: 10.1016/j.envpol.2016.12.039

Kern, C., Elias, T., Nadeau, P., Lerner, A., Werner, C., Cappos, M., et al. (2019). "Sulfur dioxide emissions associated with Kīlauea Volcano's 2018 fissure eruption; V43C-0209," in *American Geophysical Union Fall Meeting*.

Kroll, J. H., Cross, E. S., Hunter, J. F., Pai, S., et al. (2015). Atmospheric evolution of sulfur emissions from Kılauea: real-time measurements of oxidation, dilution, and neutralization within a volcanic plume. *Environ. Sci. Technol.* 49, 4129–4137. doi: 10.1021/es506119x

Lambert, G., Le Cloarec, M., and Pennisi, M. (1988). Volcanic output of SO_2 and trace metals: a new approach. *Geochim. Cosmochim. Acta* 52, 39–42. doi: 10.1016/0016-7037(88)90054-3

Langmann, B. (2014). On the role of climate forcing by volcanic sulphate and volcanic ash. *Adv. Meteorol.* 2014, 1–17. doi: 10.1155/2014/340123

Lim, S. S., Vos, T., Flaxman, A. D., Danaei, G., Shibuya, K., Adair-Rohani, H., et al. (2012). A comparative risk assessment of burden of disease and injury attributable to 67 risk factors and risk factor clusters in 21 regions, 1990–2010: a systematic analysis for the Global Burden of Disease Study 2010. *Lancet* 380, 2224–2260.

Liu, Z., Hu, B., Ji, D., Wang, Y., Wang, M., and Wang, Y. (2015). Diurnal and seasonal variation of the $pm_{2.5}$ apparent particle density in Beijing, China. *Atmos. Environ.* 120, 328–338. doi: 10.1016/j.atmosenv.2015.09.005

Longo, B. M. (2009). The Kīlauea Volcano adult health study. *Nurs. Res.* 58, 23–31. doi: 10.1097/NNR.0b013e3181900cc5

Longo, B. M. (2013). Adverse health effects associated with increased activity at Kīlauea Volcano: a repeated population-based survey. *ISRN Public Health* 2013:475962. doi: 10.1155/2013/475962

Longo, B. M., Grunder, A., Chuan, R., and Rossignol, A. (2005). SO_2 and fine aerosol dispersion from the Kīlauea plume, Kau district, Hawai'i, USA. *Geology* 33, 217–220. doi: 10.1130/G21167.1

Longo, B. M., Rossignol, A., and Green, J. B. (2008). Cardiorespiratory health effects associated with sulphurous volcanic air pollution. *Public Health* 122, 809–820. doi: 10.1016/j.puhe.2007.09.017

Longo, B. M., Yang, W., Green, J. B., Crosby, F. L., and Crosby, V. L. (2010). Acute health effects associated with exposure to volcanic air pollution (vog) from increased activity at Kīlauea Volcano in 2008. *J. Toxicol. Environ. Health A* 73, 1370–1381. doi: 10.1080/15287394.2010.497440

Loughlin, S., Aspinall, W., Vye-Brown, C., Baxter, P., Braban, C., Hort, M., et al. (2012). *Large-Magnitude Fissure Eruptions in Iceland: Source Characterisation*. BGS Open File Report, OR/12/098.

Malings, C., Tanzer, R., Hauryliuk, A., Saha, P. K., Robinson, A. L., Presto, A. A., et al. (2019). Fine particle mass monitoring with low-cost sensors: corrections and long-term performance evaluation. *Aerosol Sci. Technol.* 54, 1–40. doi: 10.1002/essoar.10500022.5

Manikonda, A., Zíková, N., Hopke, P. K., and Ferro, A. R. (2016). Laboratory assessment of low-cost PM monitors. *J. Aerosol Sci.* 102, 29–40. doi: 10.1016/j.jaerosci.2016.08.010

Mannino, D. M., Ruben, S., Holschuh, F. C., Holschuh, T. C., Wilson, M. D., and Holschuh, T. (1996). Emergency department visits and hospitalizations for respiratory disease on the Island of Hawai'i, 1981 to 1991. *Hawai'i Med. J.* 55.

Mather, T., Allen, A., Oppenheimer, C., Pyle, D., and McGonigle, A. (2003). Size-resolved characterisation of soluble ions in the particles in the tropospheric plume of Masaya volcano, Nicaragua: origins and plume processing. *J. Atmos. Chem.* 46, 207–237. doi: 10.1023/A:1026327502060

Mather, T., Witt, M., Pyle, D., Quayle, B., Aiuppa, A., Bagnato, E., et al. (2012). Halogens and trace metal emissions from the ongoing 2008 summit eruption of Kīlauea volcano, Hawai'i. *Geochim. Cosmochim. Acta* 83, 292–323. doi: 10.1016/j.gca.2011.11.029

Mather, T. A. (2015). Volcanoes and the environment: lessons for understanding Earth's past and future from studies of present-day volcanic emissions. *J. Volcanol. Geothermal Res.* 304, 160–179. doi: 10.1016/j.jvolgeores.2015.08.016

MetOne (2008). *BAM 1020 Particulate Monitor Operation Manual*. [BAM-1020-9800 Rev H].

Michaud, J.-P., Grove, J. S., and Krupitsky, D. (2004). Emergency department visits and 'vog'-related air quality in Hilo, Hawai'i. *Environ. Res.* 95, 11–19. doi: 10.1016/S0013-9351(03)00122-1

Michaud, J. D., Michaud, J.-P., and Krupitsky, D. (2007). Temporal variability in SO_2 exposures at Hawai'i Volcanoes National Park, USA. *Environ. Geol.* 52, 81–92. doi: 10.1007/s00254-006-0459-y

Nadeau, P., Elias, T., Kern, C., Lerner, A., et al. (2019). *The 2018 Eruption and Beyond: A New Era of Degassing at Kīlauea Volcano*. IUGG19-1696.

National Oceanic and Atmospheric Administration (2019). *Climate Data Online Data Tools*. Available online at: https://www.ncdc.noaa.gov/cdo-web/datatools (accessed May 1, 2019)

Neal, C. A., Brantley, S. R., Antolik, L., Babb, J. L., Burgess, M., Calles, K., et al. (2019). The 2018 rift eruption and summit collapse of Kīlauea Volcano. *Science* 363, 367–374. doi: 10.1126/science.aav7046

Oppenheimer, C., Francis, P., and Stix, J. (1998). Depletion rates of sulfur dioxide in tropospheric volcanic plumes. *Geophys. Res. Lett.* 25, 2671–2674. doi: 10.1029/98GL01988

Oppenheimer, C., Kyle, P., Eisele, F., Crawford, J., Huey, G., Tanner, D., et al. (2010). Atmospheric chemistry of an Antarctic volcanic plume. *J. Geophys. Res. Atmos.* 115. doi: 10.1029/2009JD011910

Oppenheimer, C., and McGonigle, J. (2004). Exploiting ground-based optical sensing technologies for volcanic gas surveillance. *Ann. Geophys.* 47.

Patrick, M. R., Orr, T., Sutton, A. J., Tamar, E., and Swanson, D. (2013). *The First Five Years of Kīlauea's Summit Eruption in Halema'uma'u Crater, 2008–2013*. U.S. Geological Survey Fact Sheet 2013–3116. Available online at: https://pubs.er.usgs.gov/publication/fs20133116

Pattantyus, A. K., Businger, S., and Howell, S. G. (2018). Review of sulfur dioxide to sulfate aerosol chemistry at Kīlauea Volcano, Hawai'i. *Atmos. Environ.* 185, 262–271. doi: 10.1016/j.atmosenv.2018.04.055

Pfeffer, M., Langmann, B., and Graf, H.-F. (2006a). Atmospheric transport and deposition of Indonesian volcanic emissions. *Atmos. Chem. Phys.* 6, 2525–2537. doi: 10.5194/acp-6-2525-2006

Pfeffer, M., Rietmeijer, F., Brearley, A., and Fischer, T. P. (2006b). Electron microbeam analyses of aerosol particles from the plume of Poás Volcano, Costa Rica and comparison with equilibrium plume chemistry modeling. *J. Volcanol. Geothermal Res.* 152, 174–188. doi: 10.1016/j.jvolgeores.2005.10.009

Pitz, M., Cyrys, J., Karg, E., Wiedensohler, A., Wichmann, H.-E., and Heinrich, J. (2003). Variability of apparent particle density of an urban aerosol. *Environ. Sci. Technol.* 37, 4336–4342. doi: 10.1021/es034322p

Plantower (2016). *Digital Universal Particle Concentration Sensor PMS5003 Series Data Manual*. Available online at: http://www.aqmd.gov/docs/default-source/aq-spec/resources-page/plantower-pms5003-manual_v2-3.pdf (accessed November 13, 2018)

Poland, M., Miklius, A., Orr, T., Sutton, J., Thornber, C., and Wilson, D. (2008). New episodes of volcanism at Kīlauea Volcano, Hawai'i. *Eos Trans. Am. Geophys. Union* 89, 37–38. doi: 10.1029/2008EO050001

Porter, J. N., Horton, K. A., Mouginis-Mark, P. J., Lienert, B., Sharma, S. K., Lau, E., et al. (2002). Sun photometer and lidar measurements of the plume from the Hawai'i Kilauea Volcano, Hawai'i Volcano Pu'u 'Ō'ō vent: aerosol flux and SO_2 lifetime. *Geophys. Res. Lett.* 29, 30–31. doi: 10.1029/2002GL014744

PurpleAir (2019). *PurpleAir: Air Quality Monitoring*. Available online at: https://www.purpleair.com/ (accessed October 26, 2018).

Rotstayn, L. D., and Lohmann, U. (2002). Simulation of the tropospheric sulfur cycle in a global model with a physically based cloud scheme. *J. Geophys. Res. Atmos.* 107. doi: 10.1029/2002JD002128

Sarangi, B., Aggarwal, S. G., Sinha, D., and Gupta, P. K. (2016). Aerosol effective density measurement using scanning mobility particle sizer and quartz crystal microbalance with the estimation of involved uncertainty. *Atmos. Meas. Tech.* 9, 859–875. doi: 10.5194/amt-9-859-2016

Saxena, P., and Seigneur, C. (1987). On the oxidation of SO_2 to sulfate in atmospheric aerosols. *Atmos. Environ.* 21, 807–812. doi: 10.1016/0004-6981(87)90077-1

Sayahi, T., Butterfield, A., and Kelly, K. (2019). Long-term field evaluation of the Plantower PMS low-cost particulate matter sensors. *Environ. Pollut.* 245, 932–940. doi: 10.1016/j.envpol.2018.11.065

Schmidt, A., Leadbetter, S., Theys, N., Carboni, E., Witham, C., Stevenson, J., et al. (2015). Satellite detection, long-range transport, and air quality impacts of volcanic sulfur dioxide from the 2014–2015 flood lava eruption at Bárðarbunga (Iceland). *J. Geophys. Res. Atmos.* 120, 9739–9757. doi: 10.1002/2015JD023638

Spinetti, C., and Buongiorno, M. (2007). Volcanic aerosol optical characteristics of Mt. Etna tropospheric plume retrieved by means of airborne multispectral images. *J. Atmos. Solar Terrest. Phys.* 69, 981–994. doi: 10.1016/j.jastp.2007.03.014

Stockwell, W. R., and Calvert, J. G. (1983). The mechanism of the HO-SO_2 reaction. *Atmos. Environ.* 17, 2231–2235. doi: 10.1016/0004-6981(83)90220-2

Tam, E., Miike, R., Labrenz, S., Sutton, A. J., Elias, T., Davis, J., et al. (2016). Volcanic air pollution over the Island of Hawai'i: emissions, dispersal, and composition. association with respiratory symptoms and lung function in Hawai'i Island school children. *Environ. Int.* 92, 543–552. doi: 10.1016/j.envint.2016.03.025

Thermo Scientific (2010). *Model 43i Sulphur Dioxide Analyser - Product Specifications*.

US Geological Survey Hawai'ian Volcano Observatory (2018). *Cooperator Report to Hawai'i County Civil Deference; Preliminary Analysis of the Ongoing Lower East Rift Zone (LERZ) Eruption of Kīlauea Volcano, Fissure 8 Prognosis and Ongoing Hazards*. Available online at: https://volcanoes.usgs.gov/vsc/file_mngr/file-185/USGS%20Preliminary%20Analysis_LERZ_7-15-18_v1.1.pdf (accessed Feburary 27, 2019)

von Glasow, R., Bobrowski, N., and Kern, C. (2009). The effects of volcanic eruptions on atmospheric chemistry. *Chem. Geol.* 263, 131–142. doi: 10.1016/j.chemgeo.2008.08.020

Wang, Y., Li, J., Jing, H., Zhang, Q., Jiang, J., and Biswas, P. (2015). Laboratory evaluation and calibration of three low-cost particle sensors for particulate matter measurement. *Aerosol Sci. Technol.* 49, 1063–1077. doi: 10.1080/02786826.2015.1100710

Watson, J., Chow, J., Moosmüller, H., Green, M., Frank, N., and Pitchford, M. (1998). *Guidance for Using Continuous Monitors in PM2.5 Monitoring Networks*. EPA-454/R-98-012. Environmental Protection Agency, Office of Air Quality.

Wilson, W. E., Chow, J. C., Claiborn, C., Fusheng, W., Engelbrecht, J., and Watson, J. G. (2002). Monitoring of particulate matter outdoors. *Chemosphere* 49, 1009–1043. doi: 10.1016/s0045-6535(02)00270-9

Wooten, K. M., Thornber, C. R., Orr, T. R., Ellis, J. F., and Trusdell, F. A. (2009). *Catalog of Tephra Samples From Kīlauea's Summit Eruption, March-December 2008*. U.S. Geological Survey Open-File Report 2009-1134, 26.

World Health Organization (2005). *WHO Air Quality Guidelines for Particulate Matter, Ozone, Nitrogen Dioxide and Sulfur Dioxide*. Global update.

Wyrtki, K., and Meyers, G. (1976). The trade wind field over the Pacific Ocean. *J. Appl. Meteorol.* 15, 698–704. doi: 10.1175/1520-0450(1976)015<0698:TTWFOT>2.0.CO;2

Zheng, T., Bergin, M. H., Johnson, K. K., Tripathi, S. N., Shirodkar, S., Landis, M. S., et al. (2018). Field evaluation of low-cost particulate matter sensors in high-and low-concentration environments. *Atmos. Meas. Tech.* 11, 4823–4846. doi: 10.5194/amt-11-4823-2018

Conflict of Interest: AD was employed by company PurpleAir LLC.

The remaining authors declare that the research was conducted in the absence of any commercial or financial relationships that could be construed as a potential conflict of interest.

frontiers in Earth Science

ORIGINAL RESEARCH
published: 27 February 2020
doi: 10.3389/feart.2020.00048

WebObs: The Volcano Observatories Missing Link Between Research and Real-Time Monitoring

François Beauducel[1,2]*, *Didier Lafon*[1], *Xavier Béguin*[1], *Jean-Marie Saurel*[1], *Alexis Bosson*[1], *Didier Mallarino*[3], *Patrice Boissier*[1], *Christophe Brunet*[1], *Arnaud Lemarchand*[1], *Christian Anténor-Habazac*[1], *Alexandre Nercessian*[1] and *Ahmad Ali Fahmi*[2]

[1] Institut de Physique du Globe de Paris, Université de Paris, Paris, France, [2] Institut de Recherche Pour le Développement, Yogyakarta, Indonesia, [3] CNRS, OSU Pythéas, Aix-Marseille, Marseille, France

Volcanological observatories have common needs and often common practical issues for multi-disciplinary data monitoring applications. Real-time access to integrated data, technical metadata, modeling and estimation of uncertainties are fundamental for an efficient interpretation. But in fact, the heterogeneity of instruments or acquisition systems and the inherent problems to produce rapid models using real-time data lead to difficulties that may hinder crisis management. In an attempt to globally address these questions, the French volcanological and seismological observatories have developed a specific operational software system over the past 19 years. Based on GNU/Linux open source tools and a Web interface, the WebObs system mainly offers: (1) a modular database for equipment network management; (2) a dozen of evolving dedicated periodic tasks for each monitoring technique like seismology, deformations and geochemistry that use standard data formats with automated execution of periodic tasks that produce high-quality graphs on preset moving time intervals, data exports, optional event notifications including e-mail alerting, instruments status controls based on their data validity; (3) web-form interfaces for manual data input/editing and export; (4) a user request form to adjust the tasks parameters for a single execution and to produce customized graphs and data exports. This system hence constitutes a web-based tool that performs integrated, centralized and automated real-time volcano monitoring. It has therefore become a strong support for data analysis and exchange between researchers, engineers, and technicians during periods of unrest as well as periods of long-term quiescence. WebObs is also widely open for development of interdisciplinary modeling and enhanced data processing. This allows scientists to test new methods with real-time data flux and to instantaneously share their results in the community.

Keywords: volcanology, seismology, monitoring, real-time, modeling, database, metadata, web-services

OPEN ACCESS

Edited by:
Fidel Costa, Nanyang Technological University, Singapore

Reviewed by:
Sonia Calvari, National Institute of Geophysics and Volcanology, Italy
Silvio De Angelis, University of Liverpool, United Kingdom

***Correspondence:**
François Beauducel
beauducel@ipgp.fr

Specialty section:
This article was submitted to Volcanology, a section of the journal Frontiers in Earth Science

Received: *30 November 2019*
Accepted: *12 February 2020*
Published: *27 February 2020*

Citation:
Beauducel F, Lafon D, Béguin X, Saurel J-M, Bosson A, Mallarino D, Boissier P, Brunet C, Lemarchand A, Anténor-Habazac C, Nercessian A and Fahmi AA (2020) WebObs: The Volcano Observatories Missing Link Between Research and Real-Time Monitoring. Front. Earth Sci. 8:48. doi: 10.3389/feart.2020.00048

1. INTRODUCTION

Any operational volcano observatory faces the complex mission of: (1) detecting changes in the behavior of the volcano through the acquisition of continuous as well as periodic long time-series of instrumental observations produced by multidisciplinary techniques in real-time as much as is possible; (2) quantifying and monitoring the spatio-temporal dynamics of those changes

with respect to parameter and process critical thresholds; (3) assessing the short-term potential hazard for the population; and (4) informing the authorities and the population of the state of activity of the volcano and the potential hazards. This implies a good understanding of natural phenomena, i.e., through the use of interpretative models, ideally with quantitative physical parameters like seismic energy, pressure source depth, fluid composition and thermodynamics or potential eruptive volumes. Although today this quantitative approach is still strongly limited by our current knowledge of complex non-linear volcanic processes and their uncertainties, volcanological fundamental research anchored in high-resolution observations and monitoring data provides a framework to continuously improve this knowledge. A volcano observatory hence constitutes a unique environment where fundamental and applied sciences must coexist and where academic researchers necessarily have to intimately collaborate with engineers and technicians to correctly interpret the observations.

But in the real world, during phases of volcanic unrest as well as periods of long-term quiescence, observatories have to face common practical issues for multi-disciplinary data monitoring applications. Indeed, accessing to integrated data in real-time and estimating uncertainties are fundamental tasks to achieve in order to guarantee efficient interpretation and decision making. However, the variety of instruments, the wide range of data sampling, the heterogeneity of acquisition systems and the challenges and constraints of technical maintenance lead to practical difficulties that may hinder efficient and timely crisis management. Moreover, during unrest, scientists must produce manually interpretative models that should ideally use data in real-time. Only few hours of delay in the updating of data processing can generate interpretations that might have serious consequences.

On the other hand, researchers that have developed new ideas and models might want to finally apply them on real-time data in order to contribute to observatory task in addition to other standard monitoring methods. Testing models on real-time data may be also a robust way to validate them. But this implementation is not straightforward if the monitoring system has not been designed at an early stage for integrating new modules that use the input and output data streams.

Furthermore, a volcanological observatory must record the activity of one or more volcanoes for very long periods of time. Beyond the preservation of scientific measurements and observations, an observatory is a structure that must transmit a lot of information of different kinds to the people who work there and elsewhere in collaboration. The centralization and the perpetuation of these scientific, technical and administrative data is a long-term challenge because the actors of observatories need to access rapidly and in a user-friendly interface to past knowledge and data; a task that turns out to be fundamental in case of crisis management, for example.

To address the needs of real-time data monitoring and long-term research in such a context, most observatories have developed their own dedicated solutions. Some are focused on single scientific method while others are concentrated on access to data through a global database. Noteworthy among these are the pioneer software PC-BOB for time series data management (Murray, 1990), μGRAPH utility for data analysis (Beauducel, 1998), FFM software for eruption forecasting (Cornelius and Voight, 1995), VALVE system for multidisciplinary database (Cervelli et al., 2002, 2011), SWARM tool for real-time seismic data streams (Cervelli et al., 2004), dMODELS software package for supervised deformation modeling (Battaglia et al., 2013), and the WOVODat platform for worldwide volcanic unrests datasets (Newhall et al., 2017).

In the French volcanological and seismological observatories which are responsible for La Soufrière de Guadeloupe, La Montagne Pelée, Piton de la Fournaise and recently the new Mayotte submarine volcano, we have developed since late 2000 an operational system named WebObs (WO) that attempts to address these common questions in the context of a generic pluri-instrumental volcanological and seismological observatory (Beauducel and Anténor-Habazac, 2002; Beauducel et al., 2004, 2010; Beauducel, 2006).

2. MATERIALS AND METHODS

2.1. Ambivalence Between Research and Monitoring

Researches that use observations of natural phenomena must lead to a gradual characterization of a conceptual model of physical, chemical, and geological processes. During crisis management, operational scientific advisories (i.e., forecast) have to be based on the real-time observations through the use of such an interpretative model, in a context that leaves no time to spend on fundamental research. Thus, any instrumental network in an observatory has, besides the apparently unique objective of monitoring, a second implicit objective which is to constrain and maintain up-to-date conceptual models.

Figure 1A shows this approach using the example of ground deformations study: here the model is for instance the hypothetic location of the magma reservoir. Used as an a priori information, scientists implement a GNSS network optimized to detect any pressure changes at depth, then they perform the measurements at the surface, process the raw data to compute displacements, search for source models that are consistent with the data, interpret the results in terms of a new plausible depth, and finally confirm or re-assess the initial location of the magma reservoir. A single loop of this experiment might take months or years, and each of the different steps is important and must be undertaken while keeping in mind the overall purpose of improving the model toward a better quantitative representation of reality. **Figure 1B** transposes this long-term research cycle in general terms adapted to any scientific domain that uses instrumental data or observations.

The action of monitoring is not such a separated task in this framework. Using validated data in real-time, monitoring also constitutes an interpretation of the data through the current conceptual model. Any volcano monitoring service uses an interpretative conceptual model, explicitly or not: an experimented scientist looking at time series on a screen is using his own interpretative model in his mind to make the raw data

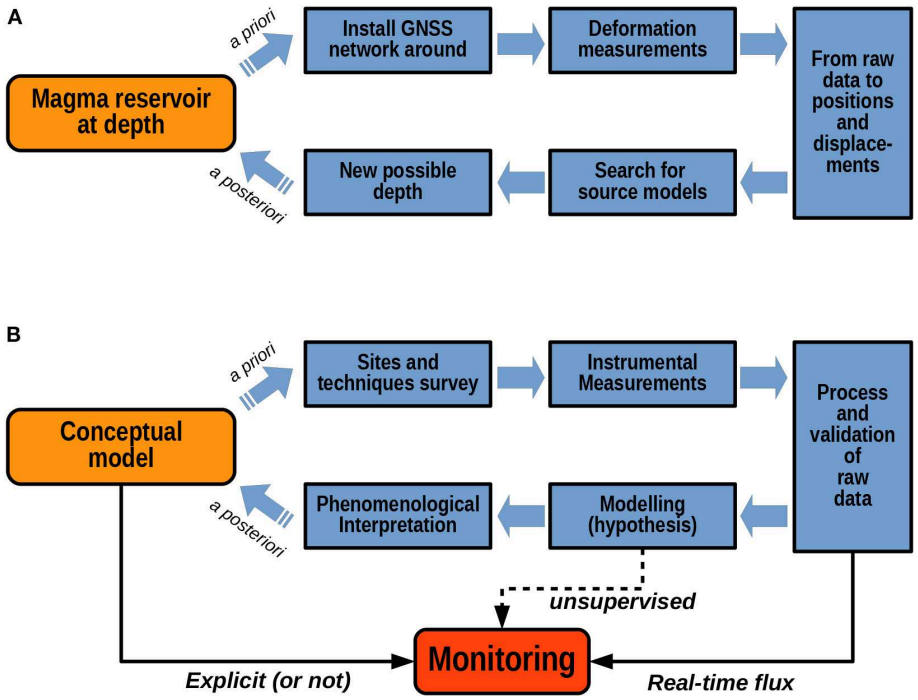

FIGURE 1 | Long-term research and real-time monitoring coexistence for instrumental approach in observatories. **(A)** Shows an example of long-term research cycle for volcano ground deformation studies, **(B)** extends the concept to any scientific method. The monitoring is using real-time validated data and the current phenomenological model to interpret them. Dashed arrow places the automatic unsupervised modeling as a new tool for monitoring.

meaningful. An automatic system that could produce real-time unsupervised modeling with clearly identified hypothesis would help scientists in achieving their tasks by providing a rational, structured, accountable and quantitative framework to interpret the data.

2.2. Objectives

The overall objective of WO is to design an integrated operational tool, through a centralized web-based interface, that addresses most of the observatory daily needs from technical management to scientific analysis of real-time data even with quantitative modeling. In fact, especially during a crisis management, scientists must have a broad and exhaustive view of the whole acquisition chain, in order to correctly evaluate the effective uncertainty of any observations, especially when the results are not straightforward if an anomaly is detected in the data. In order to accomplish these goals, we propose a system with the following specifications:

- instant access to raw and processed data, to quantitative parameters from unsupervised data modeling, all techniques, and over any time period in real-time and/or upon request;
- access to all technical characteristics of the acquisition systems, as metadata, including to equipment maintenance data that may affect a measurement;
- a unique level of information, technical, scientific and operational, shared with all the people involved;
- a robust, efficient, and light standalone system open for development and fast integration of new multidisciplinary data streams and innovative monitoring methods.

2.3. Strategy and Pragmatic Solutions

In order to reach these objectives, elegant overall solutions obviously exist but they rely on extensive technical means and long-term investment particularly in the case of: (1) building a single, huge, multidisciplinary new database for all the data; (2) upgrading all sensors, telemetry and acquisition systems to make them homogeneous in standard data formats; (3) making automatic the manual measurements, when technically possible; and finally (4) using a large computer to process any user's requests without delay. Thus, in the project we have discarded from the beginning the perspective of structurally reforming existing overall solutions and opted for the development of a more pragmatic and less costly solution.

The strategy that we have proposed has been efficient on the short-term in order to:

- keep existing acquisition systems and data archives as they are,
- connect and make accessible all data in their native formats, even though we promote standard formats and protocols since WO has implemented many,
- process the data through dedicated scheduled tasks to anticipate the most common real-time requests,
- facilitate manual data edition and access through simple text databases.

2.3.1. Technical Specifications

WO can run on a single computer server under the *GNU/Linux* operating system on *IA-32* (*i386*) or *x86-64* architectures. It is an installable package of *bash* scripts and using a combination of several languages: *Perl* and *Javascript* for the web interface, *Matlab* standalone binaries (no license needed), *Python* and some *C* binaries for the data processings, but any other Linux-compatible language are compatible welcome.

In account of the obvious heterogeneity of acquisition systems, data formats and the specificity of data archiving in every observatory, we decided that for automatic systems WO should not recreate a database of existing monitoring data but will be able to read the raw data in their native format, on-the-fly, adapting itself to existing archives or data streams. This concept is consistent with real-time needs but had also the advantage to not impose extensive data conversion or migration to observatories. Presently, the available data formats include seismological standards for waveforms and hypocenters (SEED, *Earthworm*, Hypo71, FDSN web-services, QuakeML, ...), GNSS solutions (*Gipsy*, *Gamit/GlobK*, ...), some data loggers (*Campbell Sci.*), any delimiter-separated values files, and customisable SQL requests. New data formats can be easily added with little development. Data export of validated data or any processing results is made in simple text format (delimiter separated values).

However, observatories also still have to deal with manual data besides automatic acquisitions, such as the results of chemical analysis of water or gas samples, laser distance measurements, data from geophysical surveys (e.g., gravimetry, electrical resistivity, spontaneous potential, magneto-telluric). Due to very low sampling rate, these data account for a negligible size of storage but they still are of primary importance and must be equally considered in the monitoring system. WO proposes few web-form interfaces to input/edit and export this kind of data, and each are associated to a dedicated process to also produce automatic graphs, in the same way as high sampling rate automatic methods.

Although there are some internal databases in *sqlite3* format for the system management itself, most of the system uses text files for configuration parameters and symbolic links under a basic folders architecture, easy to edit or share with other systems.

WO provides a web portal using a HTTP server for the graphical user interface and web services, and provides user authentication associated with an extended resources access management. WO can be used as an internal web portal, and/or connected to the internet for external access, restricted or even public. But the main goal is to be able to run standalone, even under offline internet conditions. This aim leads to voluntarily limit the use of any external internet services.

The web pages use a customizable menu with sub-menus using HTML and CSS facilities. The welcome page contains fixed areas with customizable content: a title banner, an information area, a news area, an extract of agenda events. Additional free text-content web pages can be created and accessed through the main menu. All text zones can use the *MarkDown* syntax.

One of the main tools of WO is a modular databank to manage information on site measurements, stations, sensors, any equipment or observations. The proposed network architecture can be adapted to various objects with a very broad concept of what is metadata: interactive maps, log history, customizable features, photos, documents. Any object can be linked to some data channels, data processing, manual web-form editing, and any feature can be linked to the features of an object. The network management can handle any type of multidisciplinary method, permanent or temporary experiments, instrumental or not (i.e., a journal of observations or activity).

Geolocation and network maps are usually a good base for discussion. WO will automatically produce individual maps of stations or sites using global digital elevation models (DEM) downloaded when necessary and stored locally. This allows to have up-to-date offline maps available at any time. Background maps are built using an automatic merge of SRTM and ETOPO1 global topography files, or any user defined DEM. Coordinates are defined in latitude and longitude in the WGS84 referential, and will be automatically converted to UTM and cartesian ECEF, with text file and KML export facilities.

For the data processing, we have adopted a near real-time solution which consists of producing static images (PNG and EPS formats), automatically updated by periodic tasks under control of a dedicated jobs scheduler. Pre-set moving time windows are defined for each method, from hours to decades, so all the standard graphs are instantaneously accessible for users, without additional server solicitation. User manual requests of any other time interval are available at any time but will have lower priority than periodic tasks.

For historical reasons, the most advanced data processing modules have been written in the *Matlab* language, a choice justified by the native matrix computing capabilities perfectly suited to signal processing, numerical modeling, inverse problem and high-quality graphical outputs. Take note of the fact that no license is needed since these modules have been compiled in standalone and freely distributable binaries. Source codes are also available for development, running under compatible free environment like *GNU Octave*, or translation to other languages. Note that the job scheduler is able to run any *GNU/Linux* compatible program or code. Besides the *Matlab* library, a package of *bash* functions is available to import WO parameters into any external programs.

2.3.2. Relational Structure

2.3.2.1. Nodes

WO relational structure is built around one basal element named a "node." A node is an object with a list of characteristics, mostly optional, all user-editable: name, alias (short name), lifetime dates, geographical location, text-content user-defined features that can be linked to other node(s), sensor(s) and channels description (calibration file), data processing related format and parameters, radio transmission path, photos, documents, dated events and sub-events with additional images and links to features and channels, text-content project. In practice, a node can be, while this is not an exhaustive list:

- an instrumental multi-parameter station,
- a measurement or sampling site,
- a mobile equipment,
- spare parts of an equipment,
- a journal of observations,

TABLE 1 | Example of nodes, associated feature list (any of them can be linked to an other node), types of documents and events.

Node	Features	Documents	Events
Instrumental Station	Acquisition Sensor Power Infrastructure Transmission	User's manual Sensor's calibration	Maintenance log
Mobile Equipment	Description Protocole	User's manual	Calibration Maintenance log
Sampling Site	Infrastructure Protocole	–	Sampling log Site layout
Volcanic Eruption	VEI Seismicity Deformations Gas Deposits Casualties	Data Technical Reports Scientific Papers	Chronology
Journal of Observations	–	Press release	Observations Testimonies
Building	Description Furniture Land Equipments Vehicles Staff	Any related	Maintenance log Inspection

The list is non-exhaustive and completes the common characteristics of any node which are: name, alias, type, lifetime, coordinates, installation, access, information, photos and schemes.

- a description of historical event like an eruption.

Some examples of nodes, associated features and possible documents and events content are given in **Table 1** and **Figure S4**.

2.3.2.2. Grids and domains

Nodes can be combined into a "grid," a higher level object of WO. There are 3 types of grids:

- a "view" is a simple group of nodes for display purposes, like a network of stations or sites, that will produce a table list, location maps, and descriptive text-contents (purpose, references, dated events). Association or disassociation of nodes to a view is immediate and will produce easy customizable lists and maps.
- a "proc" is a group of nodes for dedicated data processing purpose. It has the same characteristics as a view, but in addition has the capacity of producing graphs and data export, as a periodic task and/or upon user request, through a generic processing named a "superproc" (see the detailed list in section 3.2). Association or disassociation of nodes to a proc has immediate incidence on data processing outputs.
- a "form" is a manually editable small database, adapted to non-automatic data acquisitions. A form has a table data display with search parameters, editable form inputs with value checking, data export, and can be linked to a proc to produce automatic graphs.

Views and procs are associated with a "domain," a higher level object to group several grids into general categories, mainly for retrieval and display purposes. Default domains are Seismology, Deformation, Geochemistry, Geophysics, Imagery, Phenomenology, and Acquisition. This list is fully customizable, for example: domains can be a list of different volcanoes. Examples are given in **Tables S1, S2**.

A global search tool allows to find any event contents in all grids and nodes.

2.3.2.3. Users, groups and authorizations

WO uses its own authorization system in addition to the HTTP server authentication, to identify its users and control their individual access level to WO resources (e.g., files, processes, web pages, etc).

Users can be managed individually and/or as members of groups. A user or group is given an explicit access level to a given resource. Possible access levels are "admin" (full control including creation and deletion), "edit" (modifiable) or "read" (only readable). Lack of access level for a resource means no access to this resource; there is no explicit restriction level concept.

Default groups provided on first installation are: ADMIN, DUTY, OBSERVER, VISITOR with adapted and editable resource access levels. The main web menu can be extended by user or group individual menus that will appear only for the corresponding user or group.

2.3.2.4. The gazette

Management of the time schedule of an observatory team is one of the pillars of work efficiency, while activity archives are very useful to make reports. Since its creation in 2001, WO includes a shared agenda named *The Gazette*, that provides such observatory's logbook and calendar functions. It can be considered as a collection of timestamped and categorized articles. Default pre-defined categories are: Duty Scientist, Staff Missions, Off/Holiday, Field work, Meeting/Officials, Medias, Outreach, Teaching, Visitors, Students Training, Buildings, Miscellaneous. An option allows to include node's and grid's events. The Gazette is fully customizable, including the definitions of local day-off dates, and exportable.

Each category is considered as a resource and can be associated to specific access level for user/group. For example, access to staff leaves of absence data can be restricted to superiors.

Figure 2 resumes the WO structure, objects and links between them.

2.3.3. Principles of Procs

A proc drives the processing of any available data from its associated nodes using one of the available superproc as its processing core. The proc's configuration file defines parameters that apply to all nodes, including a default data format, preset moving time windows, filtering options or specific processing variables. Each node has its own configuration file, possible specific data format and channels description (names, unit, offset,

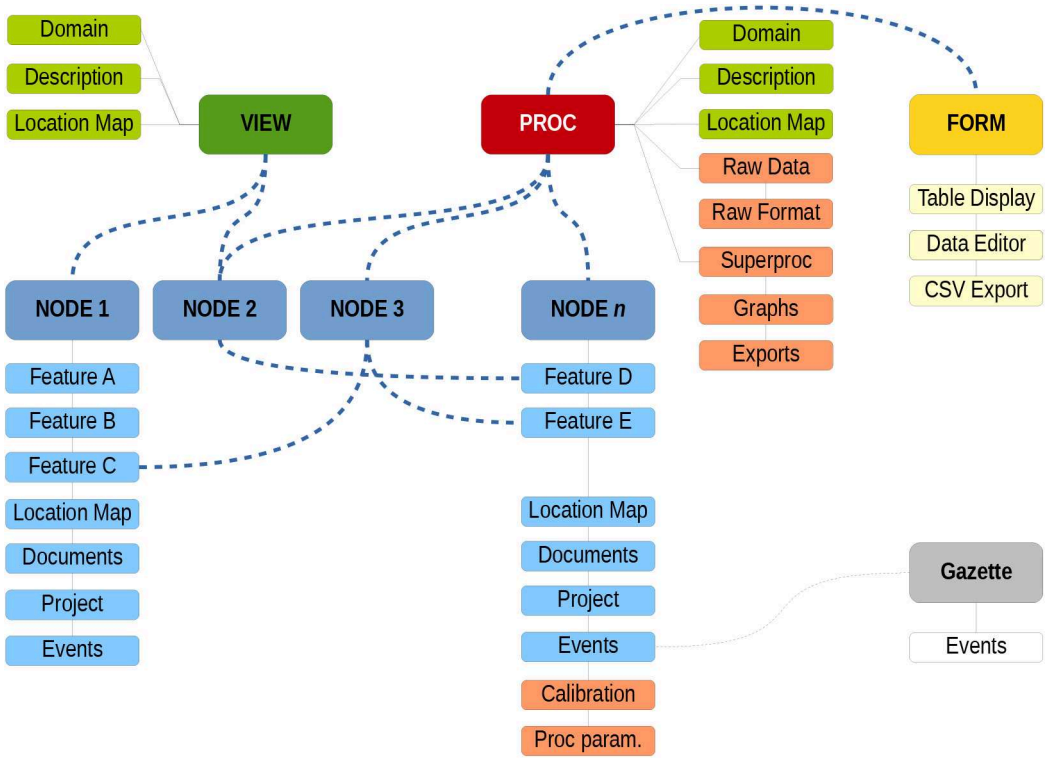

FIGURE 2 | Overview of WebObs structure and objects: dashed line stands for editable association between two objects, solid line stands for preset attribute to an object (see text for explanation).

gain, min/max values, location, …). Once imported, data from nodes have the same variable structure: a vector of timestamps and a matrix of corresponding data values. Some types of data may have a matrix of errors and a matrix of text-content additional data. The proc uses data samples as dated numerical values and the current time as a reference. Because of the required real-time context, all the signal processing must be causal, i.e., outputs will depend only on past and present inputs. Time zones are taken into account individually for each node, and one for the proc outputs.

A proc is constructed to produce, for each time window, one graph per node and a series of "summary" graphs that combine all the nodes and/or make elaborated calculation that uses all nodes together, e.g., for an integrated model. Each graph is written in vectorial format (EPS or PDF), converted to raster image (PNG) for fast display and a thumbnail (JPG), and is associated with an exportable data file in simple text format. Automatic tasks overwrite the outputs to keep them up-to-date with constant names, and display them on standard web pages with automatic refresh (see an example at **Figure S5**). An other output of procs is the status of a node: the last valid data timestamp is compared to a time delay to set if the node is active or not, while the amount of valid data on a certain period is compared to the theoretical acquisition period to compute a sampling rate performance. These indicators are displayed in the main proc's table to give an overview of a network health status. Some specific procs may produce per-event outputs, e.g., for earthquake events, in that case all former outputs will be stored and accessible by date.

Any user may submit a proc request after filling a web-form of dates interval, graphical options and some selected proc's parameters. This request will run exactly the same proc code and data as used for periodic task, but the outputs (graphical and data exports) will be written in a separated folder and an email will notify the user of the end of the job. This functionality is also useful to test proc's parameters and adjust the configuration of periodic tasks.

2.3.4. System Administration, Install and Upgrade

WO is distributed with a single binary package, a detailed README file, and a user manual. A bash script creates the disk structure, detects missing dependencies and installs the system with default jobs, examples of views and procs. The same setup script is used to upgrade code, documentation and configuration to a new version. The results presented in this paper correspond to version v2.1.4, dated November 2019.

System administration can be achieved using shell commands after logging in on the server, while some important tools can be handled through the web interface: grids and nodes management, tasks scheduler (see **Figure S8**), user administration, configuration files editor, wiki pages. Each proc can activate a debug mode to increase log verbosity.

WO is delivered with English and French interface, but the system is open to other languages as the code uses an internationalization system.

Finally, the code development, projects and issues tracking is achieved through a GIT repository (see Data Availability section).

3. RESULTS

In the French observatories, WO has become a key tool for data monitoring but also for most of the everyday use as it centralizes any information on technical equipments, team management and other observatory activities. Over the years, scientists have used the WO environment to develop their own procs dedicated to each monitoring method. Here we describe how observatories are using the WO system and what are the main outputs in the light of observatory goals. An overview of WO screenshots is also available in the **Supplementary Materials**.

3.1. Observatory Equipment and Team Management

The combination of nodes and grids is mainly used for instrumental stations and sites of measurement on the volcano or for regional tectonic surveys. For a station, the node regroups all the technical information on the equipment, including the log of maintenance, exploiting node's features to describe, for example, sensor(s), digitizer, power supply, transmission, firmware version, network addresses, monument dimensions, serial numbers, connector types, length of cables, etc. For instrumental stations, the calibration table stores the gain or offset changes in time for each channel or sensor component, using simple linear formula:

$$D = G \times F \times d + O \quad (1)$$

where d is the raw data, G the instrumental gain, F a calibration factor in physical unit per count or raw data unit), O an offset, and D the calibrated data in physical unit. There is also the possibility to filter raw values using minimum and/or maximum thresholds in order to exclude outliers.

A station can be also a simple radio repeater, a satellite hub, without any sensor. Since any node's feature can be linked to another node's feature, it is possible for example to link two stations that use the same power or same transmission system. A text description of how to access the station, eventually with contact numbers or site opening hours, completes the list. The aim of a node page for stations is to include all the necessary information for a technician who must act on the equipment (see an example of instrumental node full page in **Figure S3**).

For a measurement or sampling site like an EDM reflector, a hot spring or a fumarole, the node also describes the access and environment of each site. Accessing the WO page from the field, or bring a hard copy is one of the good practices to improve the field work efficiency. Of course, the staff must fill out the forms after each maintenance task.

The nodes are also used for non-instrumental equipments like data archive collections, buildings, electricity (power generator, inverter, …), pool of computers, vehicles, health and safety procedures (hurricane season, safety equipment, …). Other important uses of non-instrumental nodes are journals of phenomenological observations, like historical volcanic unrests, major earthquakes, tsunamis or volcano-related visual observations or meteorological events, especially to collect testimonies. This is a fundamental feature because it allows to constitute an electronic log-book of all events occurring and actions taken during a crisis event with the ability to have keywords in the observation made and a time stamp. A search for keywords can then later be done. In these cases, the node's features are adapted to describe each "object" and the dated events and associated photos and documents are the main utilities.

When a node has geographical coordinates, an automatic location map will be associated with it (see **Figure 3**). A global interactive map of all the grid's nodes is also updated.

Additional web pages offering static content have been created for more specific uses, when a list of nodes is not necessary, e.g.,:

- team members contact address and number,
- assistance, maintenance and local suppliers contacts,
- crisis management instructions,
- publication list.

3.2. Periodic Data Processing

Besides the management of sites, sensors, equipment, and measurements, the second pillar of WO is the capacity to make periodic data processing with dedicated automatic scripts for some standard techniques of monitoring.

3.2.1. Seismic Chart and Bulletin

For the seismic continuous and high frequency data flux, WO proposes an innovative combination of a digital stripchart paper for multiple data streams, a manual and semi-automatic detection and classification of events, and a bulletin with dynamic graphs of event types: hourly/daily/moving histogram, cumulated number of events, cumulated seismic moment and Gutenberg-Richter diagram. The system accepts SEED and Earthworm data protocols, some basic filtering (median/trend removal, low/high/band pass or bandstop Butterworth/Bessel/Chebyshev N-order filters) and the catalog can be linked to external earthquake databases (local QuakeML or any web-service FDSN compatible) and a raw data access in miniSEED format.

The objective of these tools is to construct and update a human-controlled earthquake bulletin, offering the possibility to visually detect and/or check automatic triggered events, and classifying the type from a customized list. The system offers a synthetic view of up to 15 simultaneous channels at different time scales, an efficient way to immediately detect and recognize the origin of events (see **Figure 4** and **Figure S7**). The seismic bulletin named "main courante" (handtrail) can be linked to multiple stripcharts 'sefran' (named after a former French seismograph system), allowing for example one stripchart with volcano stations and one for the regional tectonic activity. The

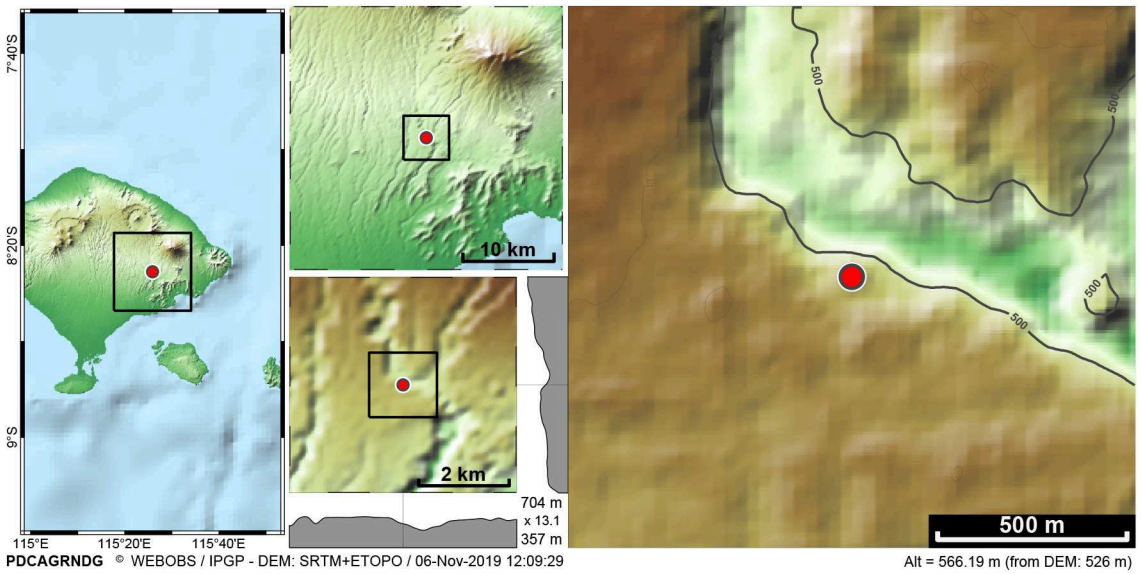

FIGURE 3 | Example of a node location map: Four levels of zooms around the station (red circle) using automatic downloading and merging of SRTM1 and ETOPO1 data for global topography and bathymetry. Cross sections to look at possible topography incidence and estimation of altitude value interpolated from the DEM itself. The right frame might use a user-defined DEM if available.

sefran includes a broom-wagon process that fills up the gaps due to real-time data packet loss.

At Piton de la Fournaise volcano, La Soufrière of Guadeloupe volcano, and Mayotte volcano, we have also implemented an automatic classification method based on the machine learning approach, and tested the possible integration into WO as an automatic suggestion of event types during the human validation (Maggi et al., 2017).

3.2.2. Seismic Swarms

This superproc uses seismic catalogs and bulletins to compute and plot the seismic rate, the cumulated moment, and to detect seismic swarms using thresholds over moving intervals (see an example in **Figure S6**).

3.2.3. Generic Time Series

This superproc will produce time series graphs of any node channels, with some filtering possibilities (moving median, moving average, picks cleanup, decimation), plotted as one graph per node and one summary graph with selected common channels. Combined with input data formats capabilities, these procs allow the basic generic plot of any non-specific real-time data (see **Figure 5**).

3.2.4. Seismic Helicorders

WO proposes its own drum helicorder graphs, from single component and customizable time sheet length, rotating speed and colors (see **Figure 6**).

3.2.5. Hypocenter Maps

Hypocenter maps operate earthquake catalogs at customizable geographic scales with vertical cross-sections, magnitude and quality filters, depth or time color scale (see **Figure 7**), and possible time series of earthquake location, depth and magnitude. For this superproc, the associated nodes are the catalogs, so it is possible to merge different formats, e.g., some *Hypo71* files for historical catalog and a FDSN web-service request for recent data.

3.2.6. Felt Earthquake Reports

This superproc produces automatic reports for earthquakes that are potentially felt. Based on a catalog of events defined by the associated nodes, it uses location and magnitude to compute theoretical ground acceleration and macroseismic intensities through a combination of ground motion prediction equation and ground motion intensity conversion equation. The report includes a map of average and maximum peak ground accelerations and intensities, considering potential site effects, for selected local towns (see **Figure 8**). The text content and language is fully customizable (templates are in English and French). This report is produced automatically at each new event or reassessment of the epicenter, depth or magnitude, so it is possible to send it to medias and authorities within few minutes after the event (Beauducel et al., 2011).

The seismic bulletin media contains a link to the existing reports when applicable.

3.2.7. RSAM

Real-time Seismic Amplitude Measurement (RSAM) is a useful tool to follow the time evolution of a seismic crisis (Endo and Murray, 1991). At the moment WO does not compute the RSAM values since standard acquisition systems are able to produce RSAM data streams efficiently. The superproc imports RSAM channels from standard data streams to make time-series plots (linear and log scales) for each station. A dedicated

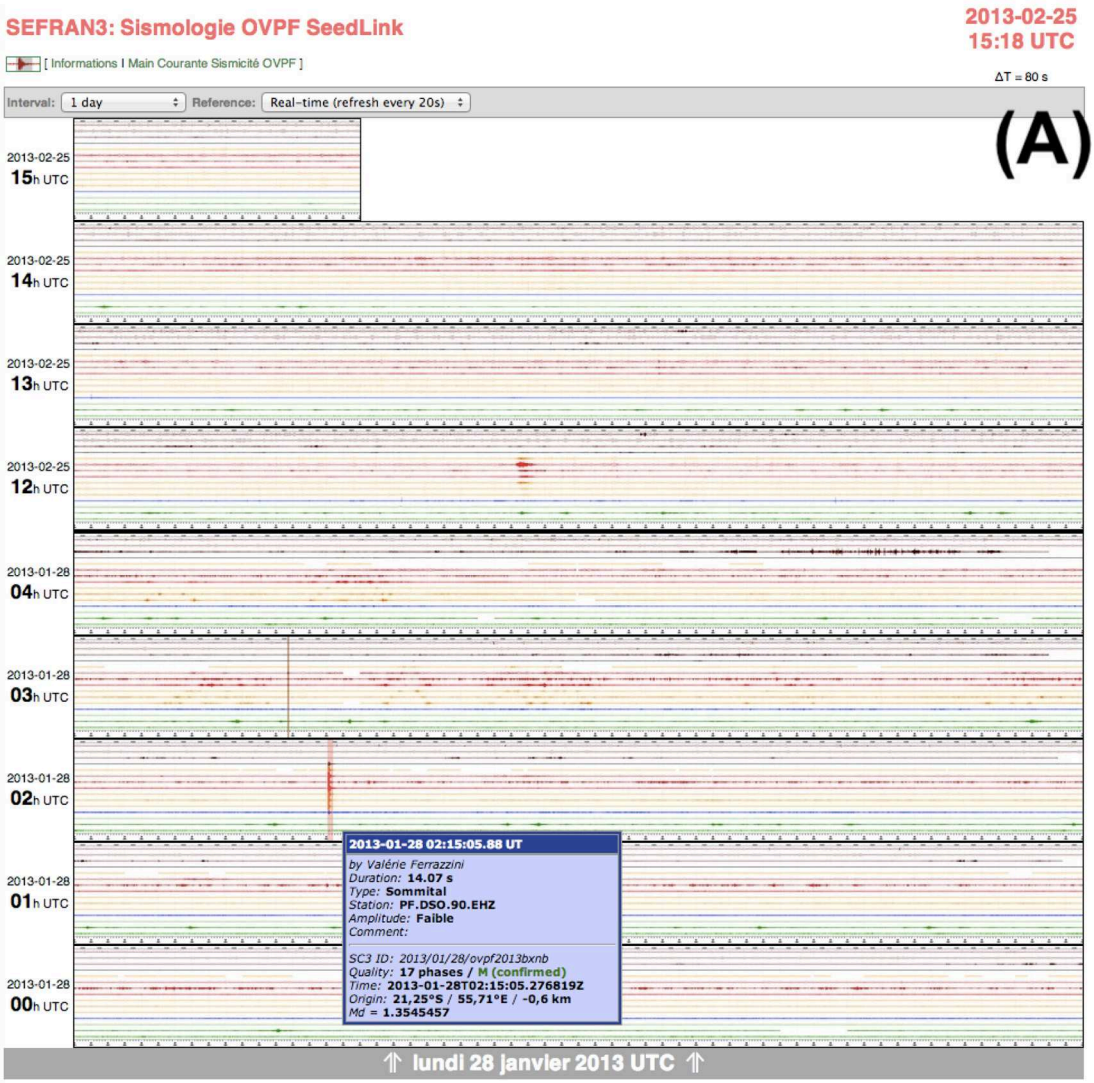

Informations

#	Alias	Channel	Calibration (count/(m/s))	Offset	Peak-Peak (m/s)	Signal statistics						SeedLink server				Status
						Offset (µm/s)	Asym.	RMSΔ (µm/s)	Acq. (%)	Samp. (Hz)		Oldest data	Last data	Buffer	ΔT	
1.	PROZ	PF.PRO.00.EHZ	8.229220e+08	auto	3e-5	1,0481	10%	0%	0,0532	100%	100	2013/02/25 12:05:30.8083	2013/02/25 15:16:13.4583	3 h	2 s	OK
2.	RERZ	PF.RER.90.EHZ	5.513050e+07	auto	3e-5	0,7800	8%	0%	0,0499	100%	100	2013/02/24 21:02:21.1600	2013/02/25 15:16:10.2200	18 h	5 s	OK
3.	CILZ	PF.CIL.00.EHZ	8.254400e+08	auto	3e-5	-1,7070	-25%	1%	0,1946	100%	100	2013/02/25 12:22:34.0083	2013/02/25 15:16:12.5883	3 h	3 s	OK
4.	NSRZ	PF.NSR.90.EHZ	2.476470e+07	auto	3e-5	-1,5344	-76%	-2%	0,0491	100%	100	2013/02/24 19:55:55.5200	2013/02/25 15:16:12.3400	19 h	3 s	OK
5.	PJSZ	PF.PJS.00.EHZ	8.211510e+08	auto	3e-5	10,0457	96%	-1%	0,0389	100%	100	2013/02/25 11:52:18.1883	2013/02/25 15:16:13.1083	3 h	2 s	OK
6.	SNEZ	PF.SNE.00.EHZ	8.268908e+08	auto	3e-5	-2,7198	-18%	-0%	0,4359	100%	100	2013/02/25 12:55:01.9683	2013/02/25 15:16:13.7083	2 h	2 s	OK
7.	dsoZ	PF.DSO.90.EHZ	7.553000e+09	auto	3e-5	0,0000	0%	-0%	0,1917	100%	100	2013/02/25 09:17:52.7200	2013/02/25 15:16:09.2500	6 h	6 s	OK
8.	BORZ	PF.BOR.00.EHZ	2.474965e+07	auto	3e-5	-0,0404	-1%	1%	0,1063	100%	100	2013/02/25 09:22:26.3300	2013/02/25 15:16:10.9500	6 h	5 s	OK
9.	FLRZ	PF.FLR.00.EHZ	8.228290e+08	auto	3e-5	0,3512	3%	0%	0,0507	100%	100	2013/02/25 11:42:24.7683	2013/02/25 15:16:11.9683	4 h	4 s	OK
10.	FORZ	PF.FOR.00.EHZ	8.177960e+08	auto	3e-5	-2,5232	-17%	1%	0,0527	100%	100	2013/02/25 11:44:02.5883	2013/02/25 15:16:11.5083	4 h	4 s	OK
11.	RVLZ	PF.RVL.00.EHZ	8.186350e+08	auto	3e-5	-0,0342	-0%	2%	0,1143	100%	100	2013/02/25 12:25:06.3983	2013/02/25 15:16:13.2283	3 h	2 s	OK
12.	NTRZ	PF.NTR.90.EHZ	2.545810e+07	auto	3e-5	-1,6105	-64%	0%	0,0429	100%	100	2013/02/24 19:38:16.0100	2013/02/25 15:16:10.3000	20 h	5 s	OK
13.	ttrZ	PF.TTR.90.EHZ	3.000000e+09	auto	3e-5	153,8753	26424%	1%	0,0467	100%	100	2013/02/25 08:26:35.8983	2013/02/25 15:16:13.7983	7 h	2 s	HS
14.	FEUZ	PF.FEU.00.EHZ	1.000000e+08	auto	3e-5	88,7900	2084%	-0%	0,2860	100%	100	2013/02/25 11:22:55.8500	2013/02/25 15:16:13.6500	4 h	2 s	HS
15.	HDLZ	PF.HDL.00.EHZ	8.345710e+08	auto	3e-5	-9,7595	-149%	-1%	0,1106	100%	100	2013/02/25 12:19:37.0983	2013/02/25 15:16:13.5883	3 h	2 s	OK

Sefran3 configuration file: **SEFRAN3_OVPF.conf**

Channels parameters file: **SEFRAN3_OVPF_Channels.conf**

FIGURE 4 | Continued

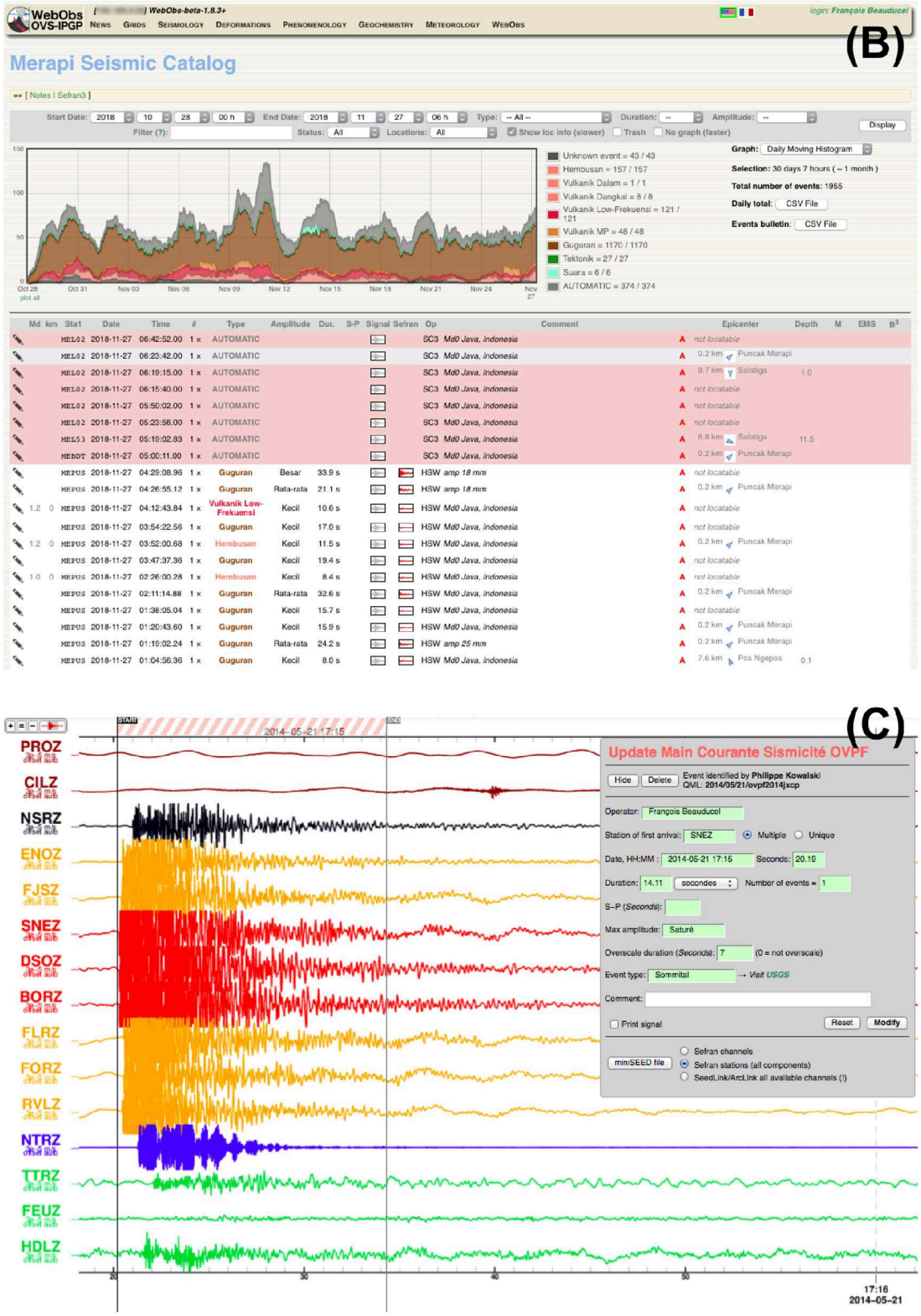

FIGURE 4 | Seismic stripchart and bulletin: **(A)** real-time last hours of the multichannel seismogram as hourly thumbnails, indication of events, statistics on channels. **(B)** Seismic bulletin table of classified events and graphs, red background stand for automatic unclassified events. **(C)** Form to edit and submit an event with high-speed scale seismograms, channels are North-South sorted, colors have been set to areas related to the volcano (data from BPPTKG/CVGHM and OVPF/IPGP).

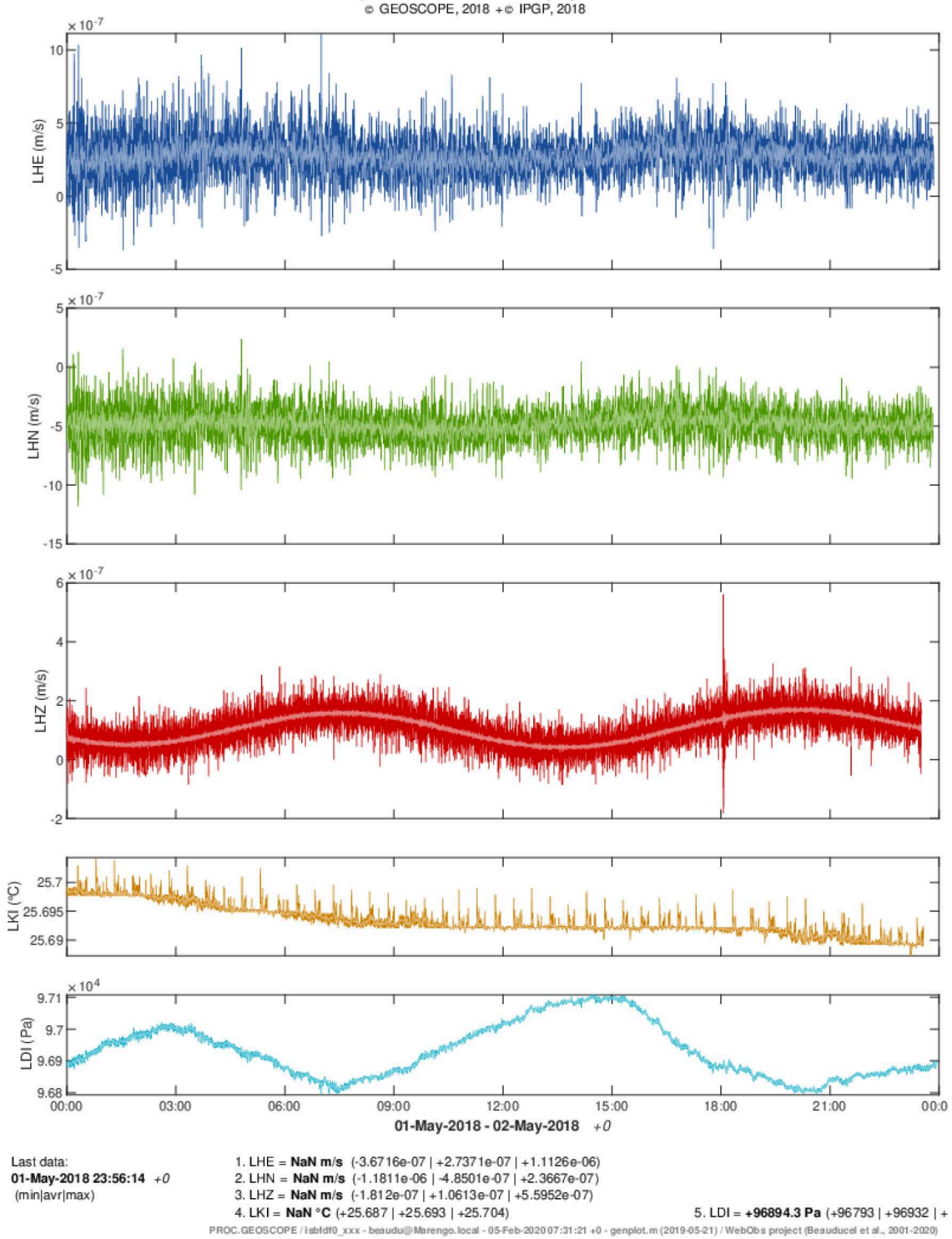

FIGURE 5 | Example of a generic time series proc: channels from a very broadband seismic station (STS-2 3-component, atmospheric temperature and pressure) using *SeisComP3 Arclink* data request. Station codes, data format and data source are defined in the node configuration, channels description and codes are set in the calibration file. Each subplot has 10-sample moving average as lighter color lines. Channel subplot order and relative height is configurable in the proc parameters (data from GEOSCOPE).

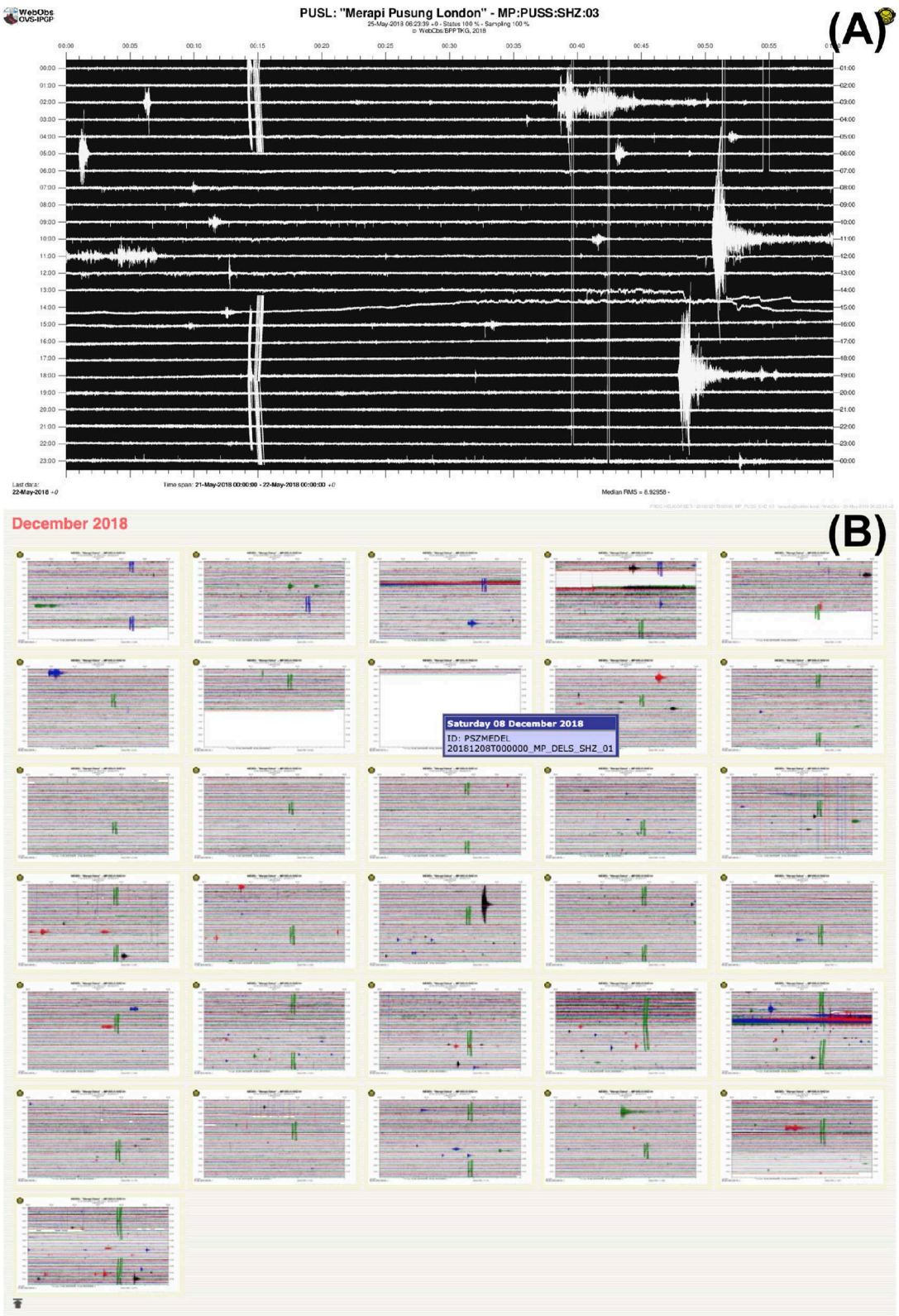

FIGURE 6 | Example of seismic helicorder with an analog short-period station: **(A)** smoked-paper colors and pen-rotating effect, **(B)** screen-shot of daily thumbnails page over one full month of recording (data from BPPTKG/CVGHM).

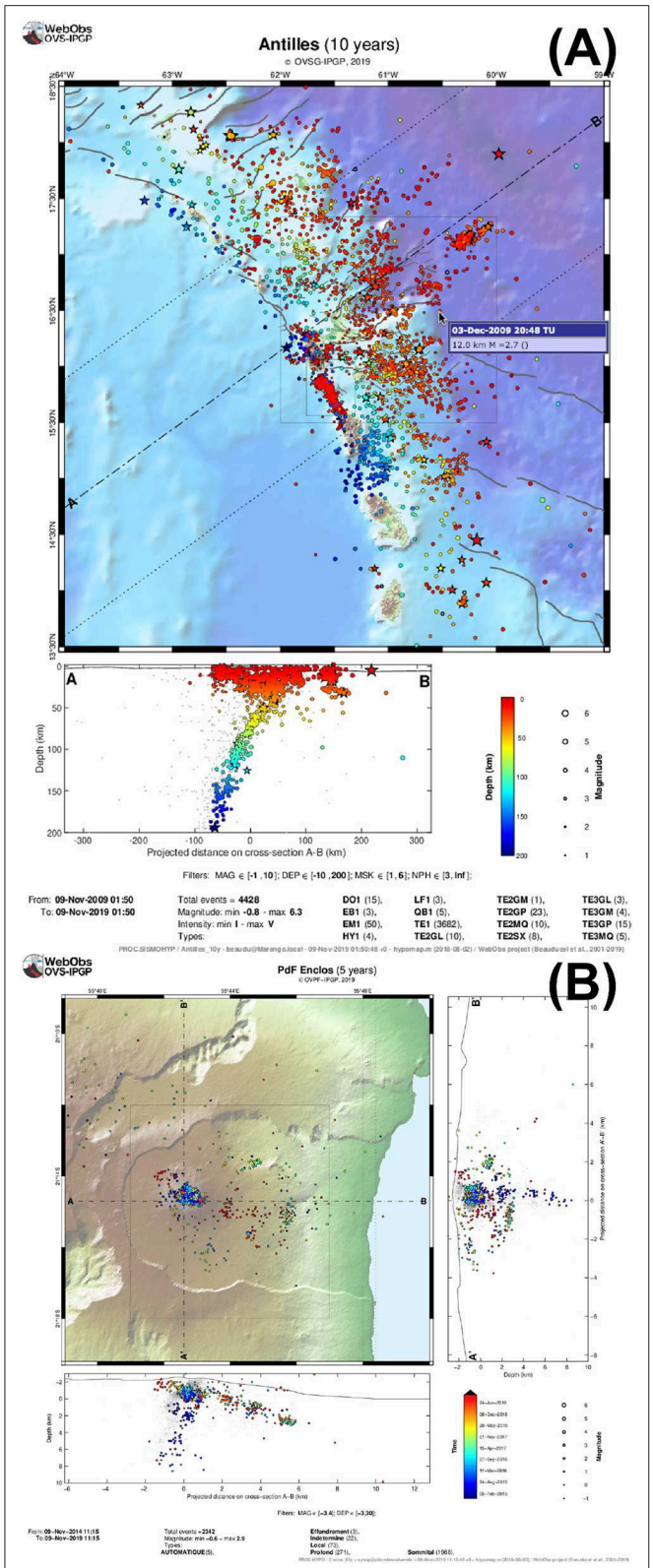

FIGURE 7 | Example of seismic hypocenter maps: **(A)** regional map with oblique cross-section, and mouse pointer showing an event details, **(B)** zoomed map on a volcano with time colormap and two vertical cross-sections (data from OVSG/IPGP and OVPF/IPGP).

graph computes time-dependent maps of the seismic source from spatial RSAM amplitudes, a simple and efficient method to locate the origin of an eruptive tremor (**Figure 9**).

3.2.8. Tilt

Tiltmeter data can be processed using a dedicated superproc that plots time series of the two components and a soil temperature, per node and integrated in a summary graph, a map of vector trends, and a source modeling using an isotropic point of inflation/deflation through exhaustive grid search to determine the spatial probability of a source and volume variation (Beauducel and Carbone, 2015). It is possible to add an a priori target location to plot tilt amplitudes vs. distances from the target.

3.2.9. GNSS

For GNSS solution data, WO proposes enhanced processing and graphs that includes (Beauducel et al., 2014): tectonic trend correction, absolute or relative velocity referencing (using one or more stations as reference), per node and summary time series plots of the three components (East, North, Up), principal component analysis, customizable baselines between pairs of stations, velocity vector map, particle motion map, source modeling using an isotropic point of inflation/deflation through exhaustive grid search to determine the spatial probability of a source and volume variation, and finally, time series of the best model parameters using different periods of integration for trend estimation (see **Figure 10**). Among the large number of parameters, it is possible to model only the horizontal components, to add an a priori target location to plot displacement amplitudes vs. distances from the target, and to constrain the source location using a gaussian-shape distance probability function.

This superproc is able to read several GNSS solution formats like Gipsy-Oasis/GipsyX (Desai et al., 2014), Gamit/Globk (Herring et al., 2010), and USGS "rneu" GPS files. When the orbit type is available, it is indicated on the graphs as shaded colors (e.g., final, rapid and ultra orbits from Gipsy/JPL software). Node's calibration file can be used to apply offset corrections due to antenna or benchmark changes or to correct local earthquake co-seismic displacements.

3.2.10. Extensometry

Extensometers are useful to monitor active cracks and fractures. The superproc makes time series of linear distance, air temperature and wind strength for each station, a summary graph of all distances grouped in geographic zones and a map showing extensive or compressive oriented arrows of displacements (Tamburello et al., 2019). A specific form is available to manage manual data input in a dedicated database (see section 3.3.3).

3.2.11. Volcanic Gas

This superproc plots simple time series of physical and chemical parameters from fumarole sampling on-site measurements and laboratory analysis: temperature, pH, velocity, major elements, isotopes and sulfur/carbon ratio. A specific form is available to manage manual data input in a dedicated database (see section 3.3.1).

Rapport préliminaire de séisme concernant la Guadeloupe et Îles du Nord

Observatoire Volcanologique et Sismologique de Guadeloupe – IPGP
Le Houëlmont – 97113 Gourbeyre – Guadeloupe (FWI)
Tél: +590 (0)590 99 11 33 – Fax: +590 (0)590 99 11 34 – infos@ovsg.univ–ag.fr – www.ipgp.fr

Gourbeyre, mardi 29 août 2017 à 09:36 (locale)

Magnitude 2.5, 16.05°N, 61.66°W, profondeur moins de 1 km mardi 29 août 2017 06:29 TU

Un séisme faible (magnitude **2.5** sur l'Échelle de Richter) a été enregistré le mardi 29 août 2017 à 02:29 (heure locale) et identifié de type **Volcano–Tectonique**. L'épicentre a été localisé à **3 km** à l''est–nord–est de **Saint–Claude**, à moins de 1 km de profondeur (soit une distance hypocentrale d'environ 3 km). Ce séisme a pu générer, dans les zones concernées les plus proches, une accélération moyenne du sol de **4.1 mg** (*), correspondant à une intensité macrosismique **III** (faiblement ressentie). Suivant le type de sols, les intensités peuvent cependant avoir atteint localement l'intensité **IV–V** (secousse forte).

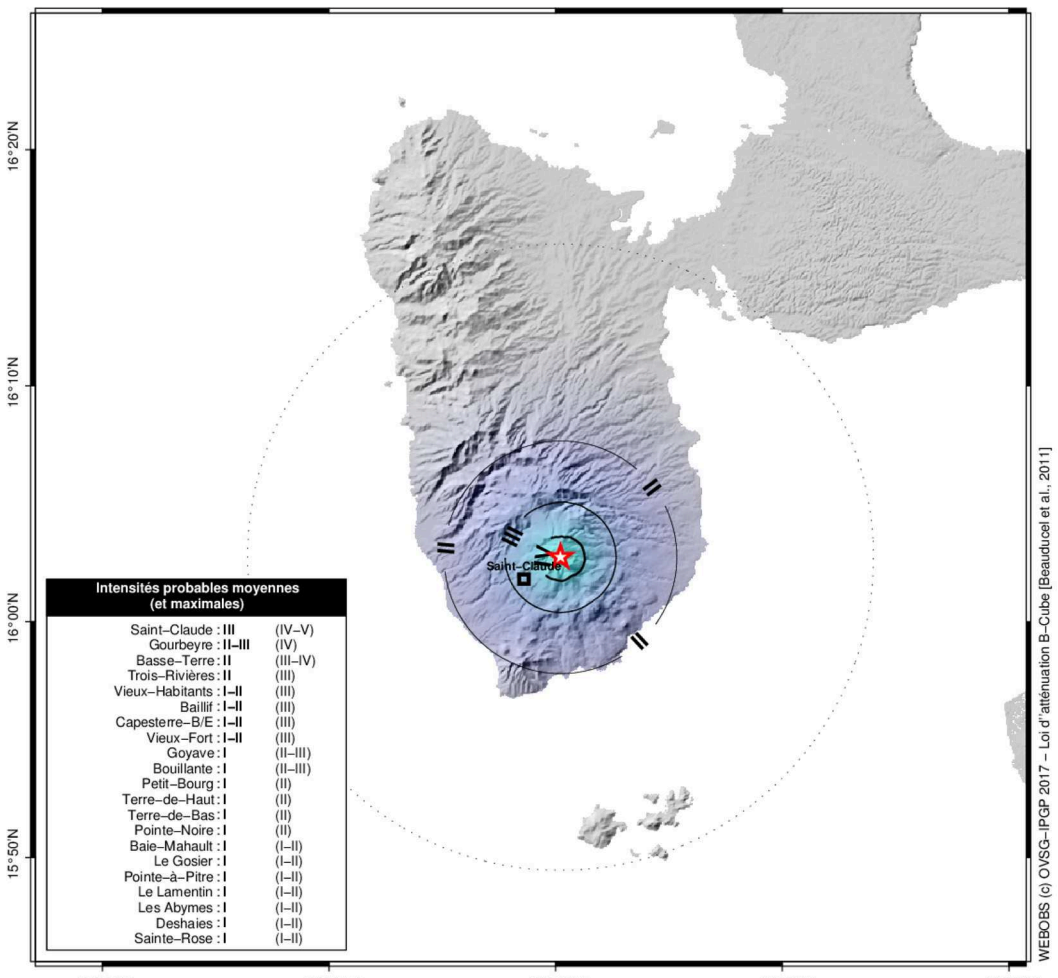

Intensités probables moyennes (et maximales)	
Saint–Claude :	III (IV–V)
Gourbeyre :	II–III (IV)
Basse–Terre :	II (III–IV)
Trois–Rivières :	II (III)
Vieux–Habitants :	I–II (III)
Baillif :	I–II (III)
Capesterre–B/E :	I–II (III)
Vieux–Fort :	I–II (III)
Goyave :	I (II–III)
Bouillante :	I (II–III)
Petit–Bourg :	I (II)
Terre–de–Haut :	I (II)
Terre–de–Bas :	I (II)
Pointe–Noire :	I (II)
Baie–Mahault :	I (I–II)
Le Gosier :	I (I–II)
Pointe–à–Pitre :	I (I–II)
Le Lamentin :	I (I–II)
Les Abymes :	I (I–II)
Deshaies :	I (I–II)
Sainte–Rose :	I (I–II)

Perception Humaine	non ressenti	très faible	faible	légère	modérée	forte	très forte	sévère	violente	extrême
Dégâts Potentiels	aucun	aucun	aucun	aucun	très légers	légers	modérés	importants	destructions	généralisés
Accélérations (mg)	< 1.5	1.5 – 3.2	3.2 – 6.8	6.8 – 15	15 – 32	32 – 68	68 – 150	150 – 320	320 – 680	> 680
Intensités EMS98	I	II	III	IV	V	VI	VII	VIII	IX	X+

(*) **mg** = "milli gé" est une unité d'""accélération correspondant au millième de la pesanteur terrestre
La ligne pointillée délimite la zone où le séisme a pu être potentiellement ressenti.

FIGURE 8 | Example of automatic report for a potentially felt earthquake: Epicenter, mean macroseismic intensities and exhaustive list of towns or neighborhood islands where the event could be felt, with maximum intensity in case of site amplification (data from OVSG/IPGP).

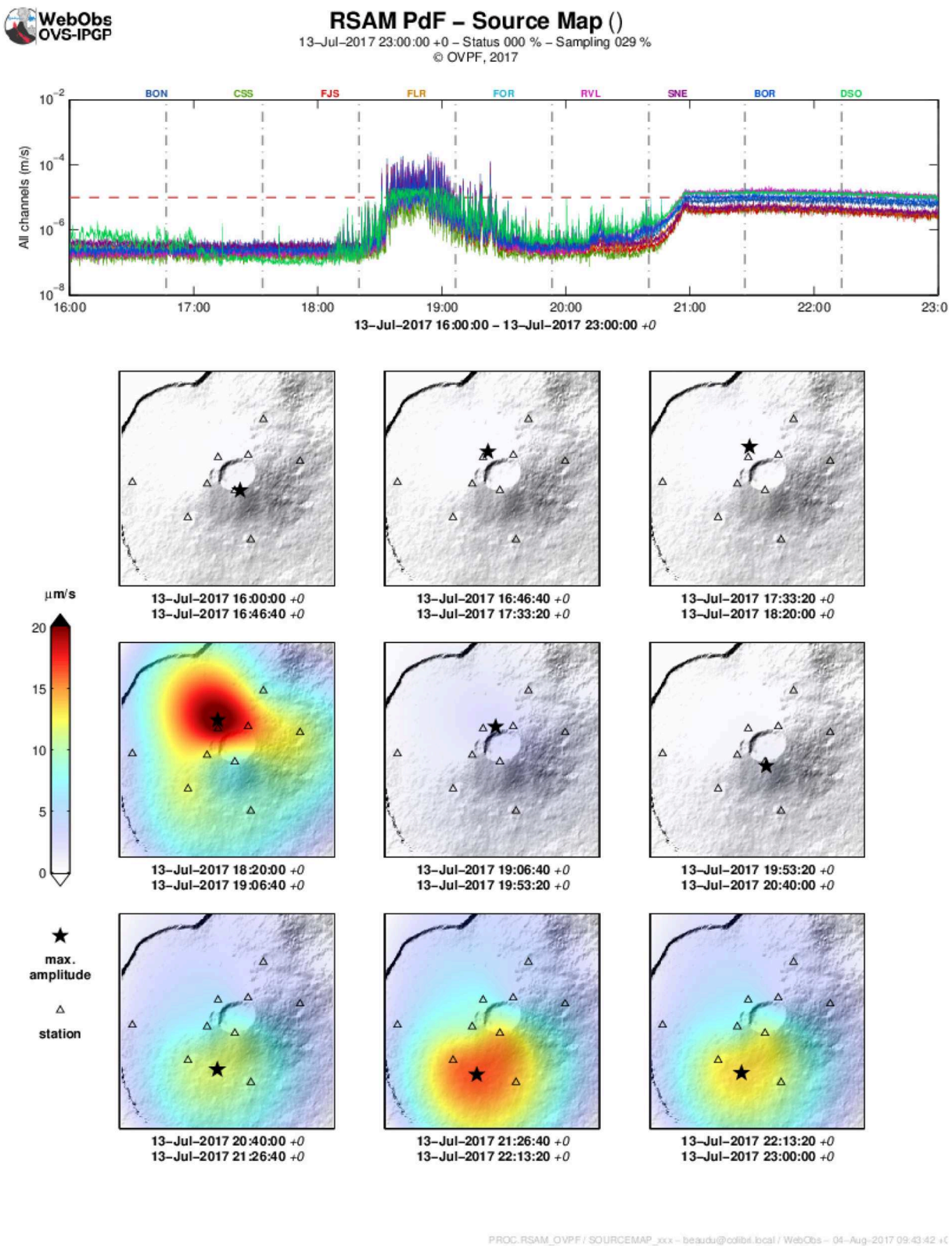

FIGURE 9 | Example of seismic amplitude measurement (RSAM) plots: time series in log scale and arbitrary threshold level, timeline source mapping to locate the eruptive tremor source (data from OVPF/IPGP).

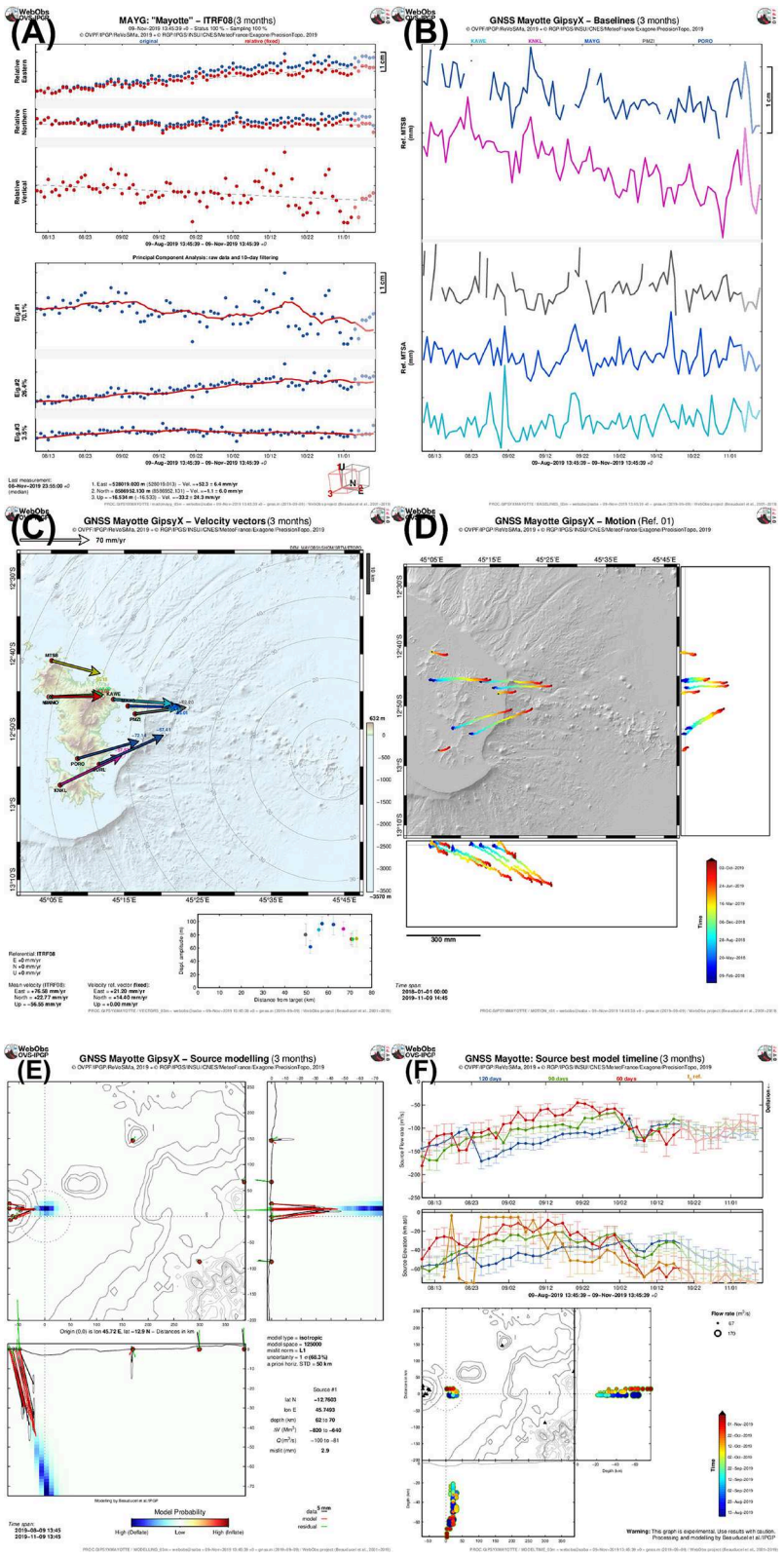

FIGURE 10 | Example of graphs produced by a GNSS proc: **(A)** single node time series of original and relative components, and principal component analysis; **(B)** baselines node pairs time series; **(C)** velocity trend vectors map with amplitude vs. distance from target plot; **(D)** displacement motion map. Background map is made from user-defined bathymetry DEM (Feuillet, 2019) (data from ReVoSiMa). **(E)** Source modeling map using an isotropic point and grid search exploration; **(F)** best models time series showing source flux, depth, and location.

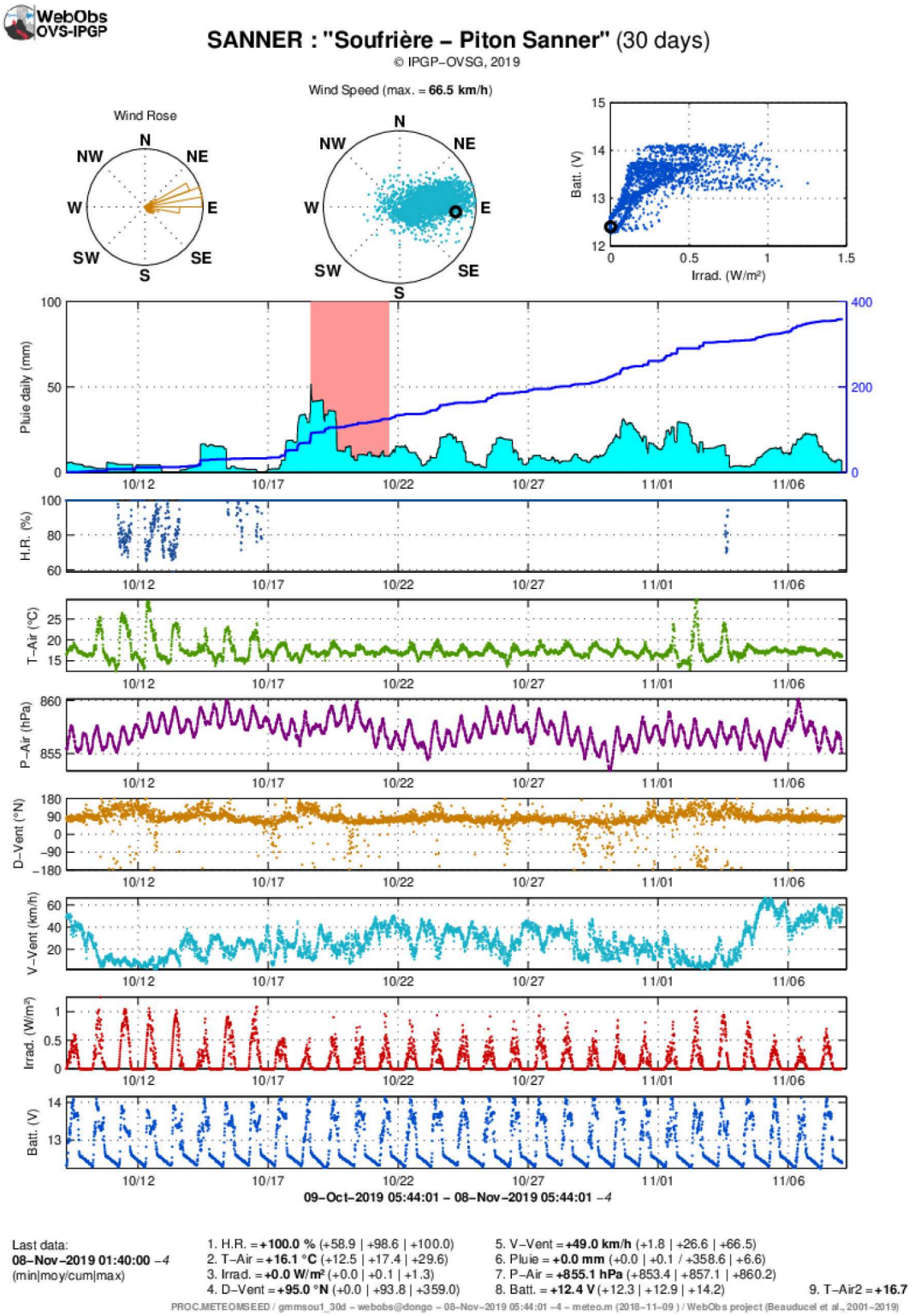

FIGURE 11 | Example of meteorological station graph: wind rose azimuthal histogram, wind direction and speed polar plot, battery voltage vs. solar irradiation, rain gauge using moving sum daily curve, cumulated and alert threshold, other parameters as simple time series (data from OVSG/IPGP).

3.2.12. Hot Springs

This superproc operates physical and chemical parameters from hot springs water sampling on-site measurements and laboratory analysis: air and water temperature, sampling condition, pH, conductivity, cation and anion concentrations, some isotopes. The superproc is able to plot time series of single element or element ratio time (like chlorine/sulfur or carbon/sulfur) and ternary plots (magnesium/calcium/sodium and chlorine/sulfate/carbonate). A specific form is available to manage manual data input in a dedicated database (see **Figure 12** and section 3.3.2).

3.2.13. Weather Station

This superproc is able to handle data from multi-sensor weather station: raingauge, temperature, pressure, humidity, wind speed and direction, irradiation, battery voltage. The plot content can be adapted to the available data. There is a special tool to send an alert based on a rain threshold (in mm/day) and to send an end-of-alert after a delay, using the notification facility of WO (see **Figure 11**).

3.3. Manual Data Forms

The objective of the forms is to handle manual data from human input, edit and validate values associated with a node, i.e., a sampling or measurement site. Each form is adapted to the type of data and scientist needs, but has in common the date and time and the associated node. In particular, input values are checked using specific tests to alert the operator on possible typing error. A table presents the data with date interval, individual node or proc selection, filter on the comments using regular expression, optional ratios, also display the check flag with background colors. Selected data can be exported in simple coma separated value text files.

A web form fits particularly well the observatory needs since it offers the possibility to enter on-site measurement values from or after the field work, then complete the entry when receiving the laboratory analysis, days or weeks after. All authorized operators can view or edit the sample data, while the associated proc produces updated graphs for final check and interpretation.

3.3.1. Volcanic Gas Analysis

This form is dedicated to fumarole physical and chemical parameters from on-site measurements and laboratory analysis. Each data sample has the following channel: temperature, pH, velocity, type of vial sampling (P_2O_5, NaOH, void), major elements (H_2, H_2S, He, Ar, CO, CO_2, CH_4, SO_2, N_2, O_2), isotopes ($\delta_{13}C$, $\delta_{18}O$, ^{222}Rn). The form computes the ratio total sulfur over carbon content.

3.3.2. Water Chemical Analysis

This form is dedicated to water physical and chemical parameters from on-site measurements and laboratory analysis. Each data sample has the following channel: air and water temperature, sampling condition (e.g., primary or secondary griffon, water piping, reservoir, condensate), pH, conductivity, flow rate, water level, cation content (Li^+, Na^+, K^{++}, Mg^{++}, Ca^{++}), anion (F^-, Cl^-, Br^-, NO_3^-, SO_4^{--}, HCO_3^-, I^-), silicate (SiO_2), and isotopes ($\delta_{13}C$, $\delta_{18}O$, δD). The typing check consists in calculating total H^+ ions and the NICB (see **Figures 12A,B**).

3.3.3. Extensometer, Fissurometer, and Electronic Distance Measurement

These forms are dedicated to a specific type of manual measurement on-site, in order to compute an average value and associated uncertainty from repeated measurements by operators on one or three components of displacements. The database stores every measurement and computes the mean and standard deviation value. Checking consists in alerting on abnormal standard deviation values.

4. DISCUSSION

The first years of development, starting in late 2000, have been spent constructing a dedicated solution for the Volcanological and Seismological Observatory of Guadeloupe, which has around 25 different monitoring networks for La Soufrière volcano and the Lesser Antilles regional seismicity and geodesy monitoring network. Early development had been using modest means that might explain some of our initial technical choices. This first relatively stable alpha version has been used efficiently for years and has been specifically adapted to some other observatories (Truong et al., 2009; Cole et al., 2010). A second age of the project started in 2012 and allowed us to expand the concept to other observatories in a more open way, focusing the development on coding barriers breakdown in order to built a real open-source participative software project, as described in this paper.

We can summarize the benefits of the WO system usage that we experienced during the last 19 years in three main points.

4.1. Everyday, Long-Term Monitoring

For daily use, WO has become a hub and unique tool in the French volcanological and seismological observatories (IPGP) for network, equipment, analysis, interpretation and some administrative management. It is the backbone of scientific crisis response during the numerous unrest and eruptive phases that have been experienced by all of the French observatories over the past two decades. It centralizes phenomenological observations as journals and technical maintenance as logs and data catalogs. Manual forms are edited simultaneously from overseas and mainland France analytical laboratories. Periodic graphs are displayed on large screens in the monitoring room and serve as discussion support for weekly meetings, including with distant participants via videoconferencing. Manual requests are extensively used to produce figures for monthly or annual reports as well as for technical and crisis response meetings with authorities, and for public outreach and community awareness. Data export is used by researchers to make their own processing and journal figures.

4.2. Crisis Management

The first application of WO as a support for crisis management was not for a volcanic unrest but a local crustal earthquake, a magnitude 6.3 shallow event that occurred in the Lesser Antilles in 2004 (Bazin et al., 2010). WO helped the Volcanological

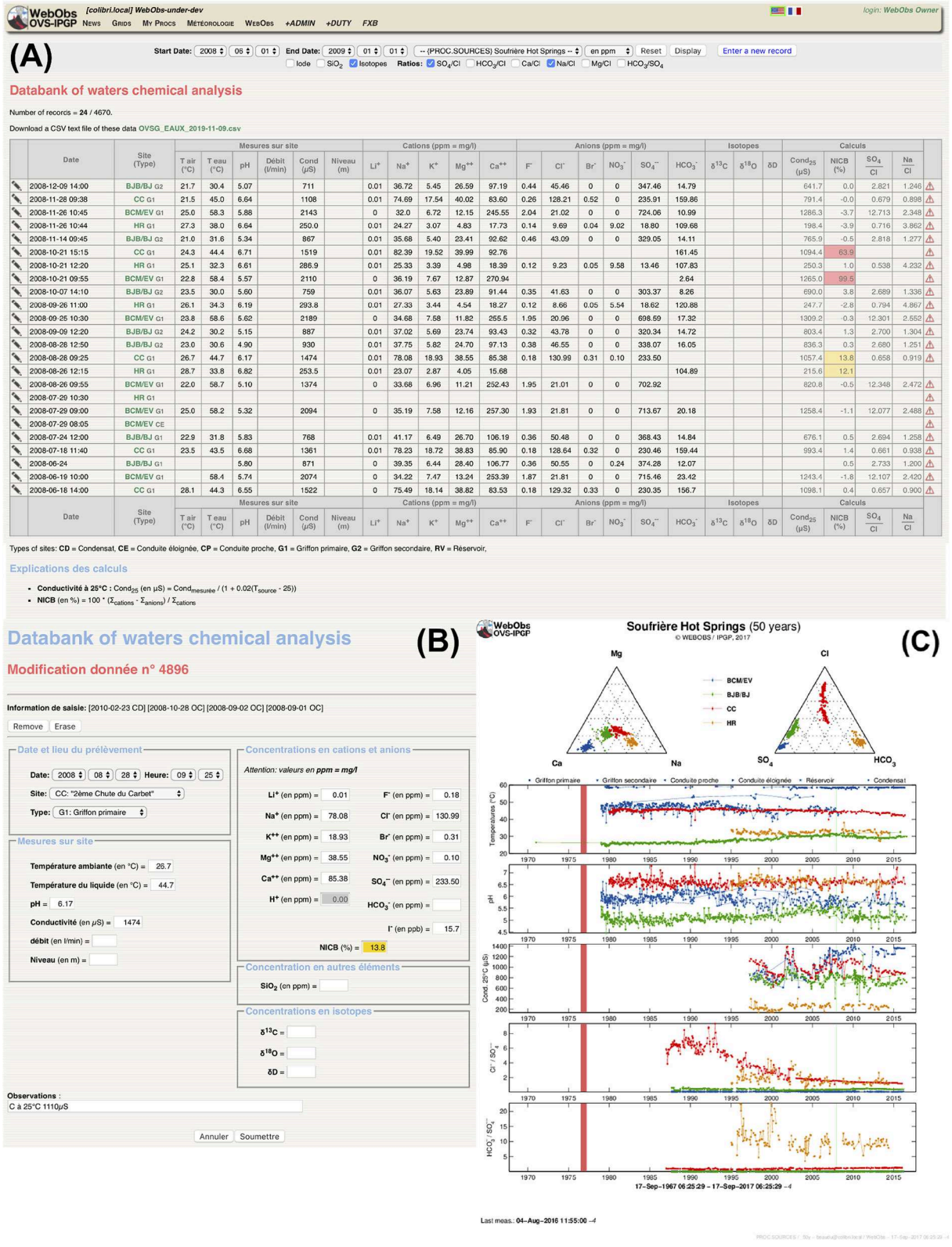

FIGURE 12 | Hot springs data form and associated proc for water chemical analysis: **(A)** table of data samples with search tools, component ratio calculation and colored check flags, **(B)** example of a data form edition (data from OVSG/IPGP); **(C)** summary graph over a 50-year period (data from OVSG/IPGP).

and Seismological Observatory of Guadeloupe in following the aftershocks sequence that lasted for years after the main shock, and in the daily communication with authorities and population after each of the felt event. It has been also easy to develop new dedicated graphs for Omori's law and Gutenberg-Richter statistics and integrate them in the system.

At Piton de la Fournaise (La Réunion), we experienced a typical situation where the observatory had developed already its own dedicated applications for each monitoring techniques, but faced some long-term software maintenance issues. Thus, WO has been installed later and progressively, as a replacement of the obsolete tools, has contributed to improve them with new functionalities and taking advantage of the collaborative open-source project. WO is presently used during each of the eruptions for detecting precursors and following the eruption progress, mainly with seismic and deformations data. In addition, the WO platform is perfectly adapted to allow remote duty scientists from mainland France to assist in real-time to the crisis response on La Réunion thus giving scientists locally time to rest and take some distance from the ongoing unrest and or crisis. This applies also to any unrest and potential eruptive activity at La Soufrière of Guadeloupe (Moretti et al., 2020) or La Montagne Pelée in Martinique.

At Mt. Agung (Bali), WO was installed and used for GNSS data processing during the 2017 crisis paradigm, in order to estimate the magma source volumes at depth from deformation modeling. We were able to adapt data format and some processing strategy due to network specificity and deliver the results to Indonesian authorities within only a few days. Modeling results have contributed to alert level decrease and exclusion zone reduction decision-making (Syahbana et al., 2019).

In 2018, WO was installed very rapidly and used extensively to follow the seismic activity and abnormal deformation due the submarine eruption of a new volcano offshore Mayotte island (REVOSIMA, 2019). Given that a national consortium (REVOSIMA) of many French institutions and universities managed this major crisis, WO gave the possibility to set up a daily monitoring of the activity. Indeed, on-duty scientists performed a check-up of the various parameters using self-generated product graphics of WO. Thus, a wide range of specialists in various fields and from different national institutions participated in the day-today monitoring. Moreover, WO facilitated the share of tasks, like the analysis and localization of seismic signals among different institutes and universities, as it is able to collect data and products from different databases and merge them into one single database (e.g., *SeisComP3* catalog of earthquake events). WO has been pivotal in the complex daily and structured, collegial efficient scientific response to the ongoing Mayotte crisis, especially to create synergies among the scientific response team and to report to authorities in charge of civil protection decisions.

4.3. Research Development Environment

Through the concept of procs and superprocs, the WO environment allows scientists to focus on the testing of ideas and innovative processing on the real-time data, as the import of the source data and the access and export of the results are handled by the system. To develop a new superproc, scientists can use a library of generic functions that read any parameters from the associated proc and import the node's data as numerical vector and matrix, then export graphs in the WO structure. Scientists thus do not have to care about the inputs and outputs and can focus on the processing itself, to create dedicated and complex figures.

In the recent cases of Mt. Agung eruption, the La Soufrière of Guadeloupe unrest, and the ongoing Mayotte eruption, we demonstrated that it was relatively easy to adapt existing superprocs and develop innovative functionalities to answer new requirements. The corresponding developments, made in runtime, have been committed to the open-source repository and became immediately available to other observatories.

DATA AVAILABILITY STATEMENT

The open-source codes, documentation, developers forum and free access to installation packages can be found at the IPGP/WebObs repository: https://github.com/IPGP/webobs. Global elevation models are a merge of SRTM Non-Void Filled: https://doi.org/10.5066/F7K072R7 and ETOPO1: http://doi.org/10.7289/V5C8276M. Sample data are available at Volobsis IPGP data portal: http://volobsis.ipgp.fr, IGN RGP: http://rgp.ign.fr, and Geoscope: http://geoscope.ipgp.fr.

AUTHOR CONTRIBUTIONS

FB was the designer, primary developer, and project manager of the WebObs software. DL has collaborated to the full re-assessment of the code and has built library modules, technical documentation, administration tools, and a setup package. XB, J-MS, and PB were the present main coding contributors with FB. AB and DM have written the Perl codes of the early versions. CB, AL, CA-H, and AN have mainly contributed to the requirements specifications. AF has conducted the first beta-version installation tests at the Merapi volcano observatory.

FUNDING

The WebObs project has been supported mainly by IPGP and CNRS/INSU (SNOV, Observation National Service for Volcanology) funding for the French volcanological and seismological observatories. Additional fundings came from the French Ministry of Ecology (now MTES), the Spirales project from DSI-IRD, the French ANR Domerapi (ANR-12-BS06-0012), the IRD emergency budget, and finally EUROVOLC project that received funding from the European Union's Horizon 2020 research and innovation programme under grant agreement no. 731070. The French volcanological and seismological observatories have benefited from recurrent funding for network and infrastructural development from the

local elected assemblies (Conseil Général de Guadeloupe, Conseil Régional de Guadeloupe, Collectivité Territoriale de Martinique, Conseil Départemental de La Réunion, Conseil Régional de La Réunion), the Préfecture de La Réunion, Préfecture de la Guadeloupe, Préfecture de la Martinique, the French Ministry of Overseas Territories, and from several projects from the European community (FEDER, CPER).

ACKNOWLEDGMENTS

FB warmly thank many colleagues that have extensively used, supported or simply encouraged this project from the early thoughts in 2000 until the implementation at more than 15 observatories today: Jean-Louis Cheminée, Claude Jaupart, Stéphane Acounis, Gilbert Hammouya, Jean-Christophe Komorowski (also for having improved the English of the manuscript), Yves Caristan, Alberto Tarchini, Thierry Kitou, Xavier Lalanne, François Truong, Albert Tarantola, Pierre Briole, Jacques Varet, Frédéric Randriamora, Benoît Coste, Roderick Stewart, Valérie Clouard, Nathalie Feuillet, Cyril Aubaud, Philippe Kowalski, Florent Brenguier, Valérie Ferrazzini, Stephen Roselia, Laura Henriette, Frédérick Massin, Marie-Paule Bouin, Jean-Bernard de Chabalier, I. Gusti Made Agung Nandaka, Éric Lajeunesse, Céline Dessert, Andrea Di Muro, Nicolas Villeneuve, Frédéric Lauret, Jean-Philippe Métaxian (also for having reread the initial manuscript), Agus Budi Santoso, Sulistiyani, Hendra Gunawan, Devy Kamil Syahbana, Benoît Taisne, Chiou Ting Tan, Lauriane Chardot, Christina Widiwijayanti, Aline Peltier, Claudio Satriano, Anne-Marie Lejeune, Roberto Moretti, David Jessop, Sébastien Deroussi, Guillaume Ucciani, Arnaud Burtin, Tristan Didier, Edgar Lenhof, Adolfo Inza, and Anne Le Friant. Special thanks to Steve Tait and Pierre Agrinier for having secured a decisive fund for DL's contract, and to all the daily users for any constructive and beneficial criticism. Many thanks to two enthusiastic reviewers, and to the editor, Fidel Costa. IPGP contribution 4111.

SUPPLEMENTARY MATERIAL

The Supplementary Material for this article can be found online at: https://www.frontiersin.org/articles/10.3389/feart.2020.00048/full#supplementary-material

REFERENCES

Battaglia, M., Cervelli, P. F., and Murray, J. R. (2013). dMODELS: a MATLAB software package for modeling crustal deformation near active faults and volcanic centers. *J. Volcanol. Geother. Res.* 254, 1–4. doi: 10.1016/j.jvolgeores.2012.12.018

Bazin, S., Feuillet, N., Duclos, C., Crawford, W., Nercessian, A., Bengoubou-Valérius, M., et al. (2010). The 2004-2005 les saintes (french west indies) seismic aftershock sequence observed with ocean bottom seismometers. *Tectonophysics* 489, 91–103. doi: 10.1016/j.tecto.2010.04.005

Beauducel, F. (1998). *Structures et comportement mécanique du volcan Merapi (Java): une approche méthodologique du champ de déformations*. (Ph.D. thesis). Université Paris 7, Institut de Physique du Globe de Paris.

Beauducel, F. (2006). Surveillance opérationnelle des volcans français: développements récents à la Guadeloupe. *Géosciences BRGM* 4, 64–68.

Beauducel, F., and Anténor-Habazac, C. (2002). "Quelques éléments d'une surveillance opérationnelle…," in *Journées des Observatoires Volcanologiques* (Paris: Institut de Physique du Globe de Paris).

Beauducel, F., Anténor-Habazac, C., and Mallarino, D. (2004). "WEBOVS: integrated monitoring system interface for volcano observatories," in *IAVCEI General Assembly, Pucon, Chile, 14-16 November 2004* (IAVCEI).

Beauducel, F., Bazin, S., Bengoubou-Valérius, M., Bouin, M., Bosson, A., Anténor-Habazac, C., et al. (2011). Empirical model for rapid macroseismic intensities prediction in Guadeloupe and Martinique. *C. R. Geosci.* 343, 717–728. doi: 10.1016/j.crte.2011.09.004

Beauducel, F., Bosson, A., Randriamora, F., Anténor-Habazac, C., Lemarchand, A., Saurel, J.-M., et al. (2010). "Recent advances in the Lesser Antilles observatories Part 2: WebObs - an integrated web-based system for monitoring and networks management," in *European Geophysical Union General Assembly* (Vienna).

Beauducel, F., and Carbone, D. (2015). A strategy to explore the topography-driven distortions in the tilt field induced by a spherical pressure source: the case of Mt Etna. *Geophys. J. Int.* 201, 1471–1481. doi: 10.1093/gji/ggv076

Beauducel, F., Nurnaning, A., Iguchi, M., Fahmi, A., Nandaka, M., Sumarti, S., et al. (2014). "Real-time source deformation modeling through GNSS permanent stations at Merapi volcano (Indonesia)," in *AGU Fall Meeting Abstracts* (San Francisco, CA).

Cervelli, D., Cervelli, P., Miklius, A., Krug, R., and Lisowski, M. (2002). "VALVE: volcano analysis and visualization environment," in *AGU Fall Meeting Abstracts* (San Francisco, CA).

Cervelli, D., Cervelli, P., and Murray, T. (2004). "New software for long-term storage and analysis of seismic wave data," in *AGU Fall Meeting Abstracts* (San Francisco, CA).

Cervelli, P., Miklius, A., Antolik, L., Parker, T., and Cervelli, D. (2011). "General purpose real-time11 data analysis and visualization software for Volcano observatories," in *AGU Fall Meeting Abstracts*.

Cole, P., Bass, V., Christopher, T., Eligon, C., Murrell, C., Odbert, H., et al. (2010). *Report to the Scientific Advisory Committee on Volcanic Activity at Soufrière Hills Volcano, Montserrat: Report on Activity Between 28 February 2010 and 31 October 2010*. Flemmings: Montserrat Volcano Observatory.

Cornelius, R. R., and Voight, B. (1995). Graphical and PC-software analysis of volcano eruption precursors according to the Materials Failure Forecast Method (FFM). *J. Volcanol. Geother. Res.* 64, 295–320. doi: 10.1016/0377-0273(94)00078-U

Desai, S., Bertiger, W., Garcia-Fernandez, M., Haines, B., Murphy, D., Selle, C., et al. (2014). "Status and plans at the JPL IGS analysis center," in *International GNSS Service 2014 Workshop Compendium, Ed. IGS Central Bureau* (Pasadena, CA: Jet Propulsion Laboratory California Institute of Technology), 53.

Endo, E. T., and Murray, T. (1991). Real-time seismic amplitude measurement (RSAM): a volcano monitoring and prediction tool. *Bull. Volcanol.* 53, 533–545. doi: 10.1007/BF00298154

Feuillet, N. (2019). *MAYOBS1 Cruise, RV Marion Dufresne*. doi: 10.17600/18001217

Herring, T., King, R., and McClusky, S. (2010). *Introduction to Gamit/Globk*. Cambridge, MA: Massachusetts Institute of Technology.

Maggi, A., Ferrazzini, V., Hibert, C., Beauducel, F., Boissier, P., and Amemoutou, A. (2017). Implementation of a multistation approach for automated event classification at Piton de la Fournaise volcano. *Seismol. Res. Lett.* 88, 878–891. doi: 10.1785/0220160189

Moretti, R., Komorowski, J.-C., Ucciani, G., Moune, S., Jessop, D., de Chabalier, J.-B., et al. (2020). The 2018 unrest phase at La Soufrière of Guadeloupe (French West Indies) andesitic volcano: scrutiny of a failed but prodromal phreatic eruption. *J. Volcanol. Geotherm. Res.* 393:106769. doi: 10.1016/j.jvolgeores.2020.106769

Murray, T. L. (1990). *A User's Guide to the PC-Based Time-Series Data-Management and Plotting Program BOB*. Open-file Report 90-56, US Geological Survey.

Newhall, C., Costa, F., Ratdomopurbo, A., Venezky, D., Widiwijayanti, C., Win, N. T. Z., et al. (2017). WOVOdat–an online, growing library of worldwide volcanic unrest. *J. Volcanol. Geother. Res.* 345, 184–199. doi: 10.1016/j.jvolgeores.2017.08.003

REVOSIMA (2019). *Bulletin de L'Activité Sismo-Volcanique à Mayotte*. Technical Report ISSN: 2680-1205, IPGP/BRGM. Available online at: www.ipgp.fr/revosima

Syahbana, D., Kasbani, K., Suantika, G., Prambada, O., Andreas, A., Saing, U., et al. (2019). The 2017–19 activity at Mount Agung in Bali (Indonesia): intense unrest, monitoring, crisis response, evacuation, and eruption. *Sci. Rep.* 9, 1–17. doi: 10.1038/s41598-019-45295-9

Tamburello, G., Moune, S., Allard, P., Venugopal, S., Robert, V., Rosas-Carbajal, M., et al. (2019). Spatio-temporal relationships between fumarolic activity, hydrothermal fluid circulation and geophysical signals at an arc volcano in degassing unrest: La Soufrière of Guadeloupe (French West Indies). *Geosciences* 9:480. doi: 10.3390/geosciences9110480

Truong, F., Lalanne, X., and Chulliat, A. (2009). "MAGIS: the information system of IPGP magnetic observatories," in *Proceedings of the XIIIth IAGA Workshop on Geomagnetic Observatory Instruments, Data Acquisition and Processing, June 9-18 2008* (Golden, CO).

Conflict of Interest: The authors declare that the research was conducted in the absence of any commercial or financial relationships that could be construed as a potential conflict of interest.

frontiers in Earth Science

METHODS
published: 10 July 2020
doi: 10.3389/feart.2020.00205

A New Japan Volcanological Database

Eisuke Fujita, Hideki Ueda and Setsuya Nakada*

National Research Institute for Earth Science and Disaster Resilience, Tsukuba, Japan

For the purpose of the development of volcanology and its practical application to volcanic hazard mitigation, we are conducting a new project named the Integrated Program for Next Generation Volcano Research and Human Resources Development (INeVRH). This project began in 2026 and will end in 2025 and consists of four themes focusing on observation, forecasting, countermeasures, and a data-sharing system. This data-sharing system is named the Japan Volcanological Data Network (JVDN), which will serve as a platform that combines observation, forecast, and countermeasure data to provide information for the judgment at branch nodes of event trees for volcanic crises in the coming decades in Japan.

Keywords: event tree for volcanic crises, INeVRH, JVDN, observation, numerical simulation, countermeasures, database

OPEN ACCESS

Edited by:
Fidel Costa,
Nanyang Technological University, Singapore

Reviewed by:
Sarah Elizabeth Ogburn,
United States Geological Survey (USGS), United States
Christina Widiwijayanti,
Earth Observatory of Singapore, Singapore

****Correspondence:***
Eisuke Fujita
fujita@bosai.go.jp

Specialty section:
This article was submitted to Volcanology, a section of the journal Frontiers in Earth Science

Received: *09 January 2020*
Accepted: *18 May 2020*
Published: *10 July 2020*

Citation:
Fujita E, Ueda H and Nakada S (2020) A New Japan Volcanological Database. Front. Earth Sci. 8:205. doi: 10.3389/feart.2020.00205

INTRODUCTION

In Japan, there are 111 active volcanoes (**Figure 1**), many of which potentially produce hazards and pose risks due to future eruption. Both for mitigation and research purposes, we operate volcano monitoring networks at 50 volcanoes that are managed by various agencies, universities, and institutions. As a consequence, data obtained through monitoring are dispersed across various institutions and in various data formats; therefore, we need to build a common platform to share these various datasets to improve mitigation techniques and to better understand volcanic processes. Doing so will allow us to enhance eruption forecast, hazard evaluation, and risk mitigation.

Our main goal is to build event tree frameworks during volcanic crises to estimate probabilities of possible outcomes of volcanic unrest, which is supported by observational datasets and numerical simulation results, as well as taking into account exposure and vulnerability data. We will construct event trees for volcanic crises using the method proposed by Newhall and Hoblitt (2002) as a standard tool for evaluating volcanic activity to assess hazards and risks as a part of crisis management planning. The event tree systematizes a way to estimate the probabilities of various volcanic phenomena, of which nodes and branches express the subsequent relationships from prior events to final outcomes. In this way, we try to provide more information more quantitatively about the probability of branching at the nodes, i.e., which way the situation will develop. We categorize the event tree into three sections: observation, forecast, and countermeasures (**Figure 2**). The observation section corresponds to the evaluation of volcanic activity, the forecast section corresponds to the branching of volcanic hazards, and the countermeasures section corresponds to the risk evaluation based on exposure and vulnerability.

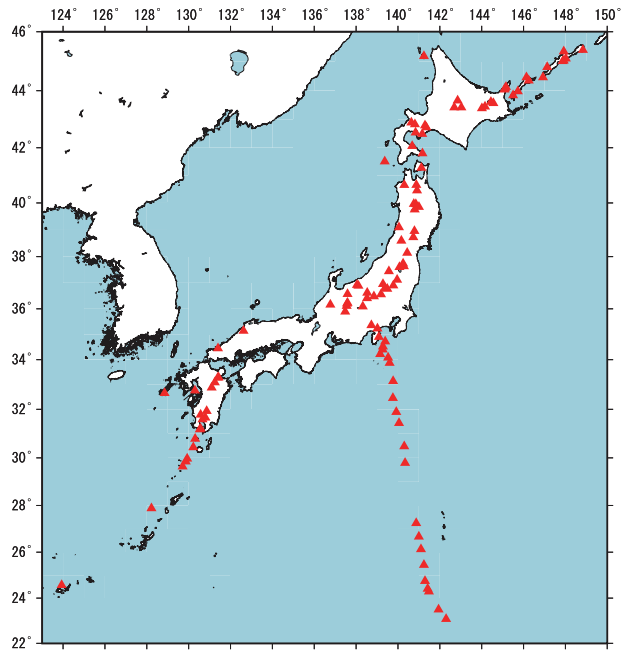

FIGURE 1 | Distribution of active volcanoes in Japan.

The Ministry of Education, Culture, Sports, Science and Technology (MEXT), Japan, has recently launched a new research project, entitled the "Integrated Program for Next Generation Volcano Research and Human Resource Development (INeVRH)" to run from 2016 to 2025. This project consists of four themes, A: Developing a Data-Sharing System of Volcano Observation Data, B: Development of Cutting-edge Volcano Observation Technology, C: Development of Forecasting Technologies for Volcanic Eruptions, and D: Development of Volcano Disaster Countermeasure Technology. The data-sharing system distributed by theme A is the Japan Volcanological Data Network (JVDN). JVDN plans to archive various kinds of data, that is, seismic, geodetic, geochemical, geological, and petrological data. The design for the JVDN system and the data flow is shown in Ueda et al. (2019). Details of the JVDN system are introduced in the next section. Theme B produces the observational data in various categories, namely, Muon, InSAR, optical remote sensing, volcanic gas, and geophysical campaign observation. These are also stored within JVDN. For the forecasting topic, theme C focuses on geological, petrological data, and also numerical simulation of volcanic phenomena, the details of which are explained in sections "Geological and Petrological Data" and "Numerical Simulation Data" of this paper. For the countermeasure information, real-time evaluation of volcanic activity and outreach information such as movies of lectures will be provided based on the research in theme D (Nakada et al., 2019).

Currently, we are in the initial development stage of the JVDN database linking all of the observations, forecasting, and countermeasures, encompassing themes of A–D. We have developed a basic platform to share and to realize static linkage of these for risk management (e.g., hazard maps) and dynamic linkage for crisis management (e.g., updating information about ongoing damage). In this paper, we will summarize the outline of our ongoing project of JVDN database development.

OBSERVATION DATA

We have various kinds of data from observation networks. The Japan Meteorological Agency (JMA) is responsible for issuing warnings and conducts volcanic observation at 50 volcanoes for the purposes of monitoring. Universities also operate observation networks at some active volcanoes for academic research. The National Research Institute for Earth Science and Disaster Resilience (NIED) manages a V-net at 16 volcanoes as a standard volcano observation network, equipped with a borehole high-sensitivity velocity seismometer, borehole tiltmeter, broadband seismometer, and Global Navigation Satellite System (GNSS). The Geospatial Information Authority of Japan (GSI) is responsible for GEONET, the GNSS network encompassing all of Japan. These data are shared between the related organizations, and some data are open to the public or can be used for scientific purposes through registration with each individual system (Ueda et al., 2019).

For the evaluation of volcanic activity and scientific research, the analysis of multi-disciplinary data is pertinent for understanding the state of volcanoes. Our new data platform, JVDN, mainly provides these various kinds of volcanological data, some of which are raw data, while others are meta-data such as the indices about the location, data owner, and their instrument information (**Figure 3**).

For example, raw seismic data is distributed in WIN or WIN32 format, a standard format in Japan (Urabe, 1994). WIN/WIN32 data can be converted into international standard formats, like SAC, SUDS, ASCII, etc., using conversion tools, and users can treat the data as they wish. Ground deformation data from tiltmeters and strainmeters are also stored in WIN/WIN32 format, while GNSS data are stored in RINEX or in meta-data. Discussions are currently underway for other observation data such as magnetic, electric, and gravity observations to determine the most effective methods for analysis and storage.

All these data are designed to be compliant with WOVOdat (Newhall et al., 2017), which has been prepared mainly by the Earth Observatory of Singapore, Nanyang Technological University. WOVOdat distributes data and also analysis visualization, query, and analysis tools with GUI interfaces. Experiences in each volcano observatory and historical volcanic eruptions at a singular volcano are not sufficient to judge forthcoming activity. Therefore, the sharing and comparison of such information between observatories worldwide provide more evidence upon which to judge volcanic activity. The JMA sets the threshold for volcanic warning levels. If we share the unrest/precursory data of a volcanic eruption, we can compare it to other similar events at other volcanoes to estimate the probabilistic outcome of the ongoing observation data for the unrest in question. For

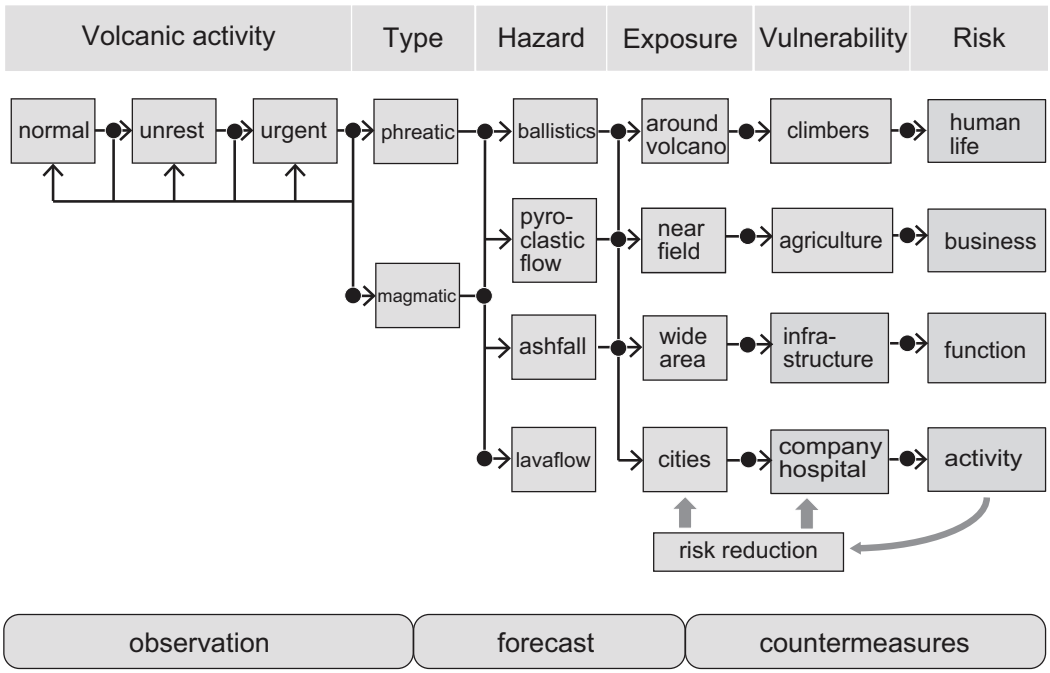

FIGURE 2 | Example of event tree for volcanic crises. We categorize this event tree into three parts: observation, forecast, and countermeasures. The quantitative threshold to judge the branching at each node is investigated by the new project, the Integrated Program for Next Generation Volcano Research and Human Resources Development. Our objective is to deal with all three categories and to propose an adequate countermeasure scheme.

example, at Aso Volcano, Japan, the threshold from level 2 (Do not approach the crater) to level 3 (Do not approach the volcano) is defined as: volcanic tremor amplitude of 4 micro m/s in average tilt change, suggesting volcanic body expansion above 0.02 micro rad/h, and rapid increase in SO_2 gas in excess of 2,000 tons/day (Japan Meteorological Agency, 2016). WOVOdat aims to support this data-sharing concept to improve eruption forecasting and for reaching a better understanding of volcanic processes, and our new JVDN database conforms to WOVOdat.

GEOLOGICAL AND PETROLOGICAL DATA

Geological and petrological studies provide important information about long-term volcanic activity. We obtained many drilling cores during the installation of V-net borehole sensors (Nagai et al., 2011, 2012, 2013a,b) and by geological surveys conducted at many volcanoes by universities and other institutions (Nakagawa et al., 2019). In addition, the INeVRT project is providing new drilling core data at other volcanoes. Precious core samples have to be preserved physically and archived digitally because they disintegrate easily.

National Research Institute for Earth Science and Disaster Resilience has established a drilling core center to manage and store drilling core samples and data in the JVDN database. Such cores can be utilized by researchers worldwide, and the database includes information on the locations, geologic and petrologic descriptions, column diagram, photographs, related background, analysis of results, and other information.

Geological data on units such as ashfall deposits provide information about eruption histories, including sequences of eruptions, modes and scales of eruption, and volumes and temporal development of each eruption (e.g., Suzuki et al., 2013). Drilling core and trench section analysis provide us with detailed information about individual historical eruptions, and we can estimate the branching probability based on multiple empirical data (Nakagawa et al., 2019).

In addition, petrological and laboratory experiment studies provide us with a great deal of information about both the subsurface and surface characteristics of magma behavior. For example, chemical compositions, water content, vesicularity, texture, etc., are the keys to understanding magmatic characteristics as well as the eruptive styles of each volcano. This information can be stored in the database for comparative study (Yoshimoto et al., 2004; Madarigal and Lucke, 2017).

FT-IR measurement of water content in a melt (Yasuda, 2014) is one example of datasets representing magma reservoir characteristics of chemistry, mineralogy, temperature, and water contents for 11 representative active volcanoes that have been archived so far. These petrological data provide information about the conditions and pressure under which magma was stored and can be converted to depth information. From the geophysical observation point of view, we can detect volcanic earthquakes and volcanic tremors beneath volcanoes, as well as their source depth.

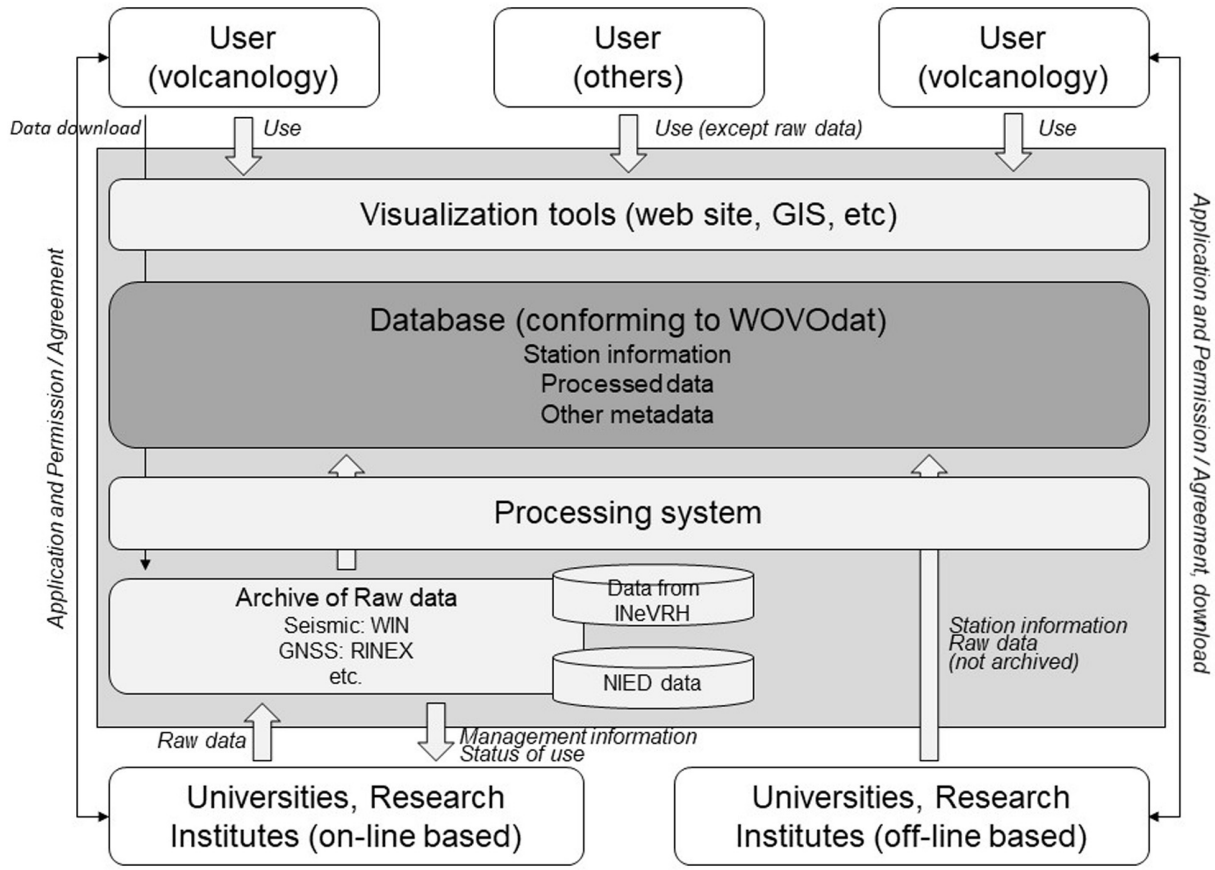

FIGURE 3 | Schematic concepts of the Japan Volcanological Data Network (JVDN).

Geophysical and petrological data give us information on source depth individually. Then, we can choose plausible source mechanisms, for example, vaporized fluid flow for shallow regions and super-critical fluid flow for deeper regions. It may be possible to employ more quantitative models.

Not only is the database designed for the analysis of historical eruptions, it is also designed to help evaluation of ongoing volcanic eruptions. One important objective is to identify the type of eruption, whether it is magmatic or non-magmatic, and to evaluate the possibility of a successive larger eruption event. A quick analysis of volcanic ash, that is, whether it includes juvenile magmatic particles or not, is the key to forecasting the ongoing eruption (e.g., Gaunt et al., 2016). To this end, equipment for automatic ash collection and analysis is under development (Miwa et al., 2018). This enables the precise sequence of the ashfall deposit to be analyzed with time stamping. In addition, ash particles are automatically analyzed and classified in terms of color and shape through an artificial intelligence (AI) system, and the equipment automatically reports the result of the component analysis, allowing the existence of magmatic particles to be assessed in real time. These results will also be uploaded to the JVDN database and will be used for the evaluation of ongoing volcanic activity as well as for countermeasure planning.

NUMERICAL SIMULATION DATA

Numerical simulation is used to evaluate complex volcanic phenomena consisting of both subsurface magmatic processes and surface hazards. In our project, we are building a volcanic hazard evaluation system that enables parallel evaluation of various volcanic hazards, including lava flow, ashfall, ballistics, and others, based on common input parameters such as flux rate (Fujita et al., 2019). Each numerical simulation code is being developed, respectively, and the types of input parameters are set for each individual simulation code. Some background data, e.g., digital elevation maps (DEM) and wind profiles, can also be stored and shared for use in various numerical simulations.

In many cases, numerical calculation is time-consuming, especially for the simulation of complex phenomena like a volcanic plume and multi-phase lava flow. These outputs should also be stored in the relational SQL database associated with the calculation conditions. To express probability in volcanic hazard and risk, we conduct multiple sessions of numerical simulation under plausible sets of input parameters and process these results statistically.

This database of calculation results will also link volcanic hazard to exposures and vulnerability (Fujita et al., 2019). The hazard information is expressed as the inundated area, time,

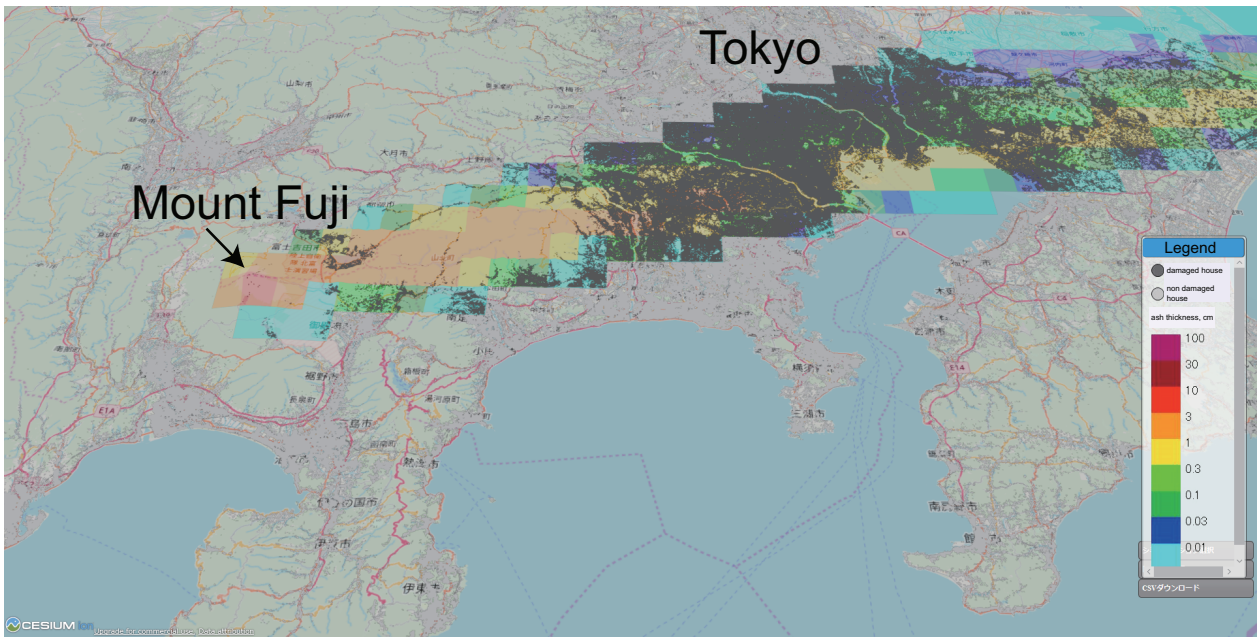

FIGURE 4 | An example of Mount Fuji ashfall simulation by JMA-RATM. The eruption plume was assumed to have the parameters of the Hōei eruption, and the wind profile in December 2016 was applied. The legend indicates the thickness of ashfall after 6 h from the onset of eruption. Gray makers show the buildings, while dark gray markers show those covered by ashfall.

velocity, and other characteristic properties for each type of hazard. As both databases are so-called big data, we need high-speed databases. We convert all of the information in these data into the OGC©, 2020 Moving Features Simple CSV format[1], which enables quick and easy handling. They can also be visualized by using a Geographical Information System (GIS) to plot and overlay them on exposures and vulnerabilities, e.g., the distribution of residential areas, roads, and infrastructure. Through this visualized information, we can estimate the risk of volcanic hazard quantitatively at the target location, and this information is also useful for countermeasures such as the formulation of evacuation plans by disaster mitigation authorities.

Here we introduce some case examples. One of the most widespread and pernicious volcanic hazards is ashfall. Ashfall dispersion is calculated by the JMA-RATM model (Shimbori, 2016). Here, we propose an example of an ashfall due to a Mt. Fuji eruption (**Figure 3**) in which we assume the initial condition of being the same size as the Plinian eruption of Hōei in 1707. Ashfall distribution is strongly controlled by the height of plume and the local wind profile. In the JMA-RATM model, the numerical simulation refers to the weather-forecasting program and obtains detailed distributions. At present, the mesh size of the calculation is 5 km × 5 km, and this will be reduced to a 2 km × 2 km area to provide more detailed information.

We obtain quantitative information of the ashfall deposit for each mesh from the numerical simulation. For risk management, this hazard information can be coupled with the exposure and vulnerability information (**Figure 4**). In general, the simulation mesh and archived mesh in the database are different from each other, so we need to match these different geometries to estimate the inundation area (Figure 4 in Fujita et al., 2019). The building distribution database provided by the Center for Spatial Information Science, The University of Tokyo (2010) is an example of static objects, and it has a much higher resolution than those of the numerical simulation. For the combination of hazard simulation and exposure databases, we need to synchronize the size and geometry of the meshes, applying intersection judgment and interpolation. Our future plan is to provide more quantitative information about the hazard and its risk, for example, using an agent-based model to integrate the ashfall simulation with dynamic information such as dynamic real-time data on humans and transportation. By doing so, we can propose efficient plans for logistics as part of crisis management.

In general, lava flows are less dangerous than the other volcanic hazards, since generally, the flow velocity is not very high, and the damage to human life itself is not very serious. However, a lava flow destroys the surrounding terrain permanently, so the damage inflicted on properties, public facilities, roads, and other infrastructure can be catastrophic. Some examples of lava flow simulation around Mount Fuji are also overlaid on the building infrastructure map (**Figure 5**) using LavaSIM (Hidaka et al., 2005). Most of the important transportation facilities in Japan go through this area, so there would be major economic ramifications if it is damaged by lava flow. A very threatening lava flow occurs when lava flows southward, destroying Shinkansen (bullet train) rail tracks and the Tōmei highway, which are the logistics arteries of Japan.

[1]http://www.ogc.org/ogc/Document

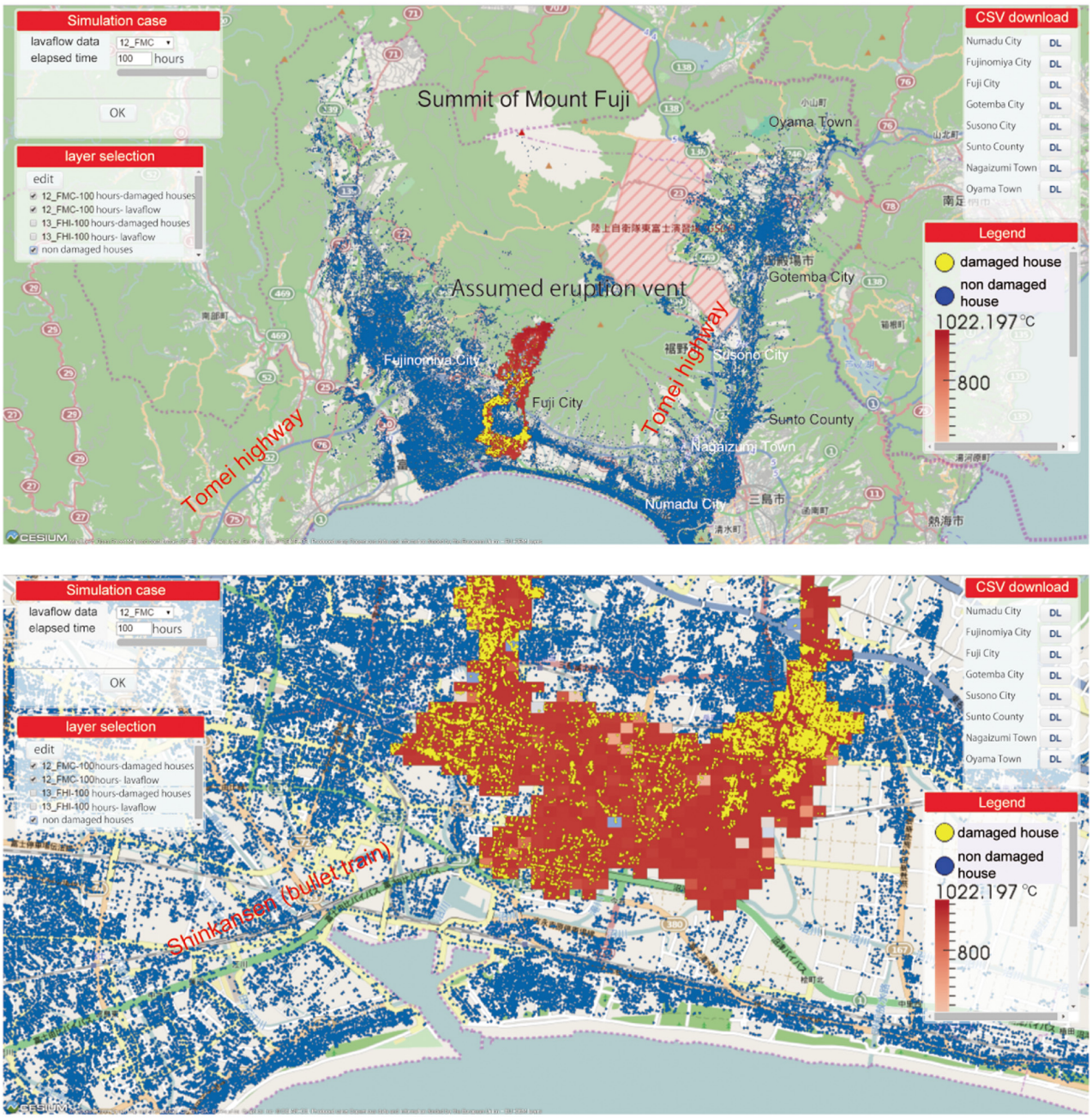

FIGURE 5 | An example of Mount Fuji lava flow simulation using LavaSIM (Hidaka et al., 2005). Blue markers indicate the location of buildings, and red markers show the lava-inundated cells. Yellow markers show the buildings damaged by lava flow. Eruption vent is assumed at the southern flank of Mount Fuji, and the lava flow runs toward the southern flank, damaging the important transportation facilities, Shinkansen (bullet train) and the Tōmei highway, the economic artery of logistics in Japan.

We can delineate the impacted area and estimate the available time before the lava flow impacts and formulate a plan for countermeasures.

We experienced a tragedy caused by ballistics in the eruption of Ontake, Japan, in 2014. Unfortunately, there were many tourists around the summit crater when the phreatic eruption suddenly occurred (Nagano Prefectural Police, 2014; Tsunematsu et al., 2016). Even though it is difficult to issue a warning for a sudden phreatic eruption, it will be essential to understand the risk of ballistic impacts and to make plans for evacuation and shelters around the summit area. We apply the ballistic simulation model using Ballista (Tsunematsu et al., 2014), which can produce outputs regarding the deposits' distribution, energy, and trajectories.

Volcanoes are popular tourist hotspots, and it is important to mitigate possible hazards that can affect volcano climbers. Lessons learned from the tragic Ontake eruption initiated an investigation to obtain real-time tracking of climbers along trails on Mount Fuji trails performed at different times (Tanaka et al., 2018). Tracking devices (beacons) were distributed to each climber, whereby the receivers installed along the trails detected the real-time location of climbers. This dataset shows the speed of the climbers' traffic flow during the most crowded season. A combination of ballistic simulation and this dataset provides a countermeasure plan against ballistics hazards, e.g., the adequate distribution and size of huts and the route to an evacuation path.

We will also evaluate other volcanic hazards such as pyroclastic flow, lahars, etc., and plan to add these to the volcanic disaster evaluation system (Fujita et al., 2019).

COUNTERMEASURE INFORMATION DATA

Volcanologists have information about observation and forecasts for volcanic activities and hazards; however, these outputs are too specialized and difficult to be understood by the general public and therefore are not useful in practical volcanic hazard mitigation procedures for authorities and the general public (Nakada et al., 2019).

As an example, for the quick detection of ashfall distribution and component analysis, NIED developed an information-sharing system via SNS, named "Min'na de kazan," meaning that everyone reports about volcanic activity. Users can upload ashfall information about thickness, ash color, etc., and plot this on a GIS system. We can grasp the distribution of ashfall in real time and can use this to produce contour maps to identify ashfall hazard distribution. This information can be applied to evaluating the damage by ashfall, e.g., against electric power supply lines, roads, railways, and agriculture.

In addition, we are also developing digital volcanic hazard maps, which are converted from the original paper-based volcanic hazard maps issued by individual local governments and are digitized in a GIS-applicable format. Using a combination of hazard maps and social and infrastructure geospatial layers, we can support the countermeasure planning of local governments.

Under our plan, the countermeasure database will also include instructions on how to interpret the observation data and numerical simulation results, some lecture materials about volcanoes for the general public, digital contents including movies of volcanic phenomena, and some standard operating procedure (SOP) information for volcanic disaster management, available for local governments.

CONCLUSION

The ultimate goal of the INeVRH project is to perform evaluation of forthcoming volcanic activity and hazards through the automatic assimilation of observation data. The observation data and its primary data analysis will be stored in the JVDN system. Together with geological and petrological data, these data will be set automatically and/or manually as input to execute various volcanic hazard simulations. Simulation results will then be combined with exposure and vulnerability data to evaluate the risk, which will be utilized on the system as countermeasure information for risk reduction. Since, in most cases, observation data are not sufficient to regulate all input parameters required to run volcanic hazard simulation, some assumptions are used. To obtain the uncertainty and the applicability of the model, we first performed various simulations using the possible range of input parameters. The hazard and risk evaluation are performed using event tree analysis. The most difficult but important part is to obtain threshold values that define toward which branch of the event tree the activity will continue, especially during volcanic crises. We must also remain cognizant that the threshold may not work for a specific volcano, so we should also obtain it at other volcanoes to determine the general applicability. Developing the new Japan volcanological database system capable of integrating observation, forecast, and countermeasure strategy is a challenging task.

DATA AVAILABILITY STATEMENT

All datasets generated for this study are included in the article.

AUTHOR CONTRIBUTIONS

EF conducted general management of INeVRH projects with colleagues, was leading theme C3, the numerical simulation project to develop the volcanic hazard evaluation system, and wrote the manuscript. HU developed the JVDN system and created the figure illustrating the JVDN system. SN managed the countermeasure database project. All authors contributed to the article and approved the submitted version.

FUNDING

This research was funded by the Integrated Program for Next Generation Volcano Research and Human Resource Development, Ministry of Education, Culture, Sports, Science and Technology (MEXT), Japan (http://vivaweb2.bosai.go.jp/kazan-pj/next-generation-volcano-pj-2019-jun).

ACKNOWLEDGMENTS

We are grateful to all participants in the INeVRH. Yosuke Miyagi developed countermeasure tools and provided us with information.

REFERENCES

Center for Spatial Information Science, The University of Tokyo (2010). *Joint Research Program at CSIS*. Available online at: https://joras.csis.u-tokyo.ac.jp/ (accessed April 14, 2020).

Fujita, E., Iriyama, Y., Shimbori, T., Sato, E., Ishii, K., Suzuki, Y., et al. (2019). Evaluating volcanic hazard risk through numerical simulations. *J. Disast. Res.* 14:4. doi: 10.20965/jdr.2019.p0604

Gaunt, H., Bernard, B., Hidalgo, S., Proano, A., Wright, H., Mothes, P., et al. (2016). Juvenile magma recognition and eruptive dynamics inferred from the analysis of ash time series: The 2015 reawakening of *Cotopaxi volcano*. *J. Volcaonol. Geotherm. Res.* 328, 134–146. doi: 10.1016/j.jvolgeores.2016.10.013

Hidaka, M., Goto, A., Umino, S., and Fujita, E. (2005). VTFS project: Development of the lava flow simulation code LavaSIM with a model for three-dimensional convection, spreading, and solidification. *Geochem. Geophys. Geosyst.* 6:7. doi: 10.1029/2004GC000869

Japan Meteorological Agency (2016). Available online at: http://www.data.jma.go.jp/svd/vois/data/tokyo/keikailevelkijunn.html (accessed April 13, 2020).

Madarigal, P., and Lucke, O. (2017). Petrographic analysis of the volcanic bombs and blocks from Poas volcano: April-June 2017 eruption period. *Rev. Geol. Am. Central* 57, 149–159. doi: 10.15517/rgac.v0i57.30336

Miwa, T., Geshi, N., Ito, J., and Tanada, T. (2018). VOLCAT (Visual Observation Laboratory for Capturing Ash Transition) for automatic remote imaging of volcanic ash particle. *Cities Volc.* 10:173.

Nagai, M., Kozono, T., Nakada, S., Kobayashi, T., Kaneko, T., Fujita, E., et al. (2013a). Lithologic Features of the Borehole Cores from the Manzen and Hinamoridai Observation Wells, Kirishima Volcano, Southwestern Japan. *Tech. Natl. Res. Inst. Earth Sci. Disaster Prevent.* 374:49.

Nagai, M., Miyabuchi, Y., Miyoshi, M., Ikebe, S., Watanabe, K., Ohkura, T., et al. (2013b). Lithologic Features of the Borehole Cores from from the Ichinomiya and Hakusui Observation Wells, Aso Volcano, Southwestern Japan. *Tech. Natl. Res. Inst. Earth Sci. Disaster Prevent.* 373:48.

Nagai, M., Nakada, S., Takahashi, M., Asui, M., Ukawa, M., Kozono, T., et al. (2011). Stratigraphy and Lithologic features of the Borehole Core from the Onioshidashi Observation Well, Asama Volcano, Central Japan. *Tech. Natl. Res. Inst. Earth Sci. Disaster Prevent.* 357:32.

Nagai, M., Takahashi, M., Toda, Y., Mori, S., Nakada, S., Yasui, M., et al. (2012). Stratigraphy and Lithologic Features of the Borehole Core from the Takamine Observation Well, Asama Volcano, Central Japan. *Tech. Natl. Res. Inst. Earth Sci. Disaster Prevent.* 366:30.

Nagano Prefectural Police (2014). *Police activity in the volcanic disaster at Mt. Ontake in 2014*. Available online at: https://www.pref.nagano.lg.jp/police/katsudou/ontake/index.html (accessed April 13, 2020).

Nakada, S., Miyagi, Y., Kubo, T., and Fujita, E. (2019). Conveying volcano information effectively to stakeholders – A new project for promotion of next generation volcano research. *J. Disast. Res.* 14:4. doi: 10.20965/jdr.2019.p0623

Nakagawa, M., Matsumoto, A., Kobayashi, K., and Wada, K. (2019). Comparative Petrological Studies of 1962 and 1988–1989 Eruptions of Tokachidake Volcano, Japan: A Case Study for Understanding the Relationship Between Eruption Style and Magma Processes. *J. Disast. Res.* 14:5. doi: 10.20965/jdr.2019.p0766

Newhall, C. G., Costa, F., Ratdomopurubo, A., Venezky, D. Y., Widiwijayanti, C., Thin Zar Win, N., et al. (2017). WOVOdat – An online, growing library of worldwide volcanic unrest. *J. Volcanol. Getherm. Res.* 345, 184–199. doi: 10.1016/j.jvolgeores.2017.08.003

Newhall, C. G., and Hoblitt, R. (2002). Constructing event trees for volcanic crises. *Bull. Volcanol.* 64, 3–20. doi: 10.1007/s004450100173

OGC (2020). OGC© . Available online at: http://www.ogc.org/ogc/Document (accessed April 13, 2020).

Shimbori, T. (2016). Tephra transport: modeling and forecasting. *J. Volocanol. Soc. Jpn.* 61, 399–427.

Suzuki, Y., Yasuda, A., Hokanishi, N., Kaneko, T., Nakada, S., Fujii, T., et al. (2013). Syneruptive deep magma transfer and shallow magma remobilization during the 2011 eruption of Shimoe-dake, Japan-Constraints from melt inclusions and phare equilibria experiments-. *J. Volcanol. Geotherm. Res.* 257, 184–204. doi: 10.1016/j.volgeores.2013.03.017

Tanaka, Y., Fukuzaki, A., Yasumaga, R., Hatanaka, M., Yoshimoto, M., and Honda, R. (2018). Efforts of hiker safety measures utilizing IoT in Mt. Fuji. *Cities Volcanoes* 14:604.

Tsunematsu, K., Chopard, B., Falcone, J. J., and Bonadonna, C. (2014). A numerical model of ballistic transport with collisions in a volcanic setting. *Comput. Geosci.* 63, 62–69. doi: 10.1016/j.cageo.2013.10.016

Tsunematsu, K., Ishimine, Y., Kaneko, T., Yoshimoto, M., Fujii, T., and Yamaoka, K. (2016). Estimation of ballistic block landing energy during 2014 Mount Ontake eruption. *Earth Planet. Sp.* 68:88. doi: 10.1186/s40623-016-0463-8

Ueda, H., Yamada, T., Miwa, T., Nagai, M., and Matsuzawa, T. (2019). Development of a Data sharing system for Japan volcanological data network. *J. Disast. Res.* 14:4.

Urabe, T. (1994). A common format for multi-channel earthquake waveform data. *Seismol. Soc. Jpn. Meet.* 2:384.

Yasuda, A. (2014). A new technique using FT-IR micro-reflectance spectroscopy for measurement of water concentrations in melt inclusions. *EPS* 66:34. doi: 10.1186/1880-5981-66-34

Yoshimoto, M., Fujii, T., Kaneko, T., Yasuda, A., and Nakada, S. (2004). Multiple magma reservoirs for the 1707 eruption of Fuji volcano. *Jpn. Proc. Jpn. Acad. Ser. B* 80, 103–106.

Conflict of Interest: The authors declare that the research was conducted in the absence of any commercial or financial relationships that could be construed as a potential conflict of interest.

frontiers in Earth Science

PERSPECTIVE
published: 23 July 2020
doi: 10.3389/feart.2020.00257

Long-Term Probabilistic Volcanic Hazard Assessment Using Open and Non-open Data: Observations and Current Issues

Pablo Tierz†*

British Geological Survey, The Lyell Centre, Edinburgh, United Kingdom

Probabilistic volcanic hazard assessment (PVHA) has become the paradigm to quantify volcanic hazard over the last decades. Substantial aleatory and epistemic uncertainties in PVHA arise from complexity of physico-chemical processes, impossibility of their direct observation and, importantly, a severe scarcity of observables from past eruptions. One factor responsible for data scarcity is the infrequency of moderate/large eruptions; other factors include lack of discoverability and accessibility to volcanological data. Open-access databases can help alleviate data scarcity and have significantly contributed to long-term PVHA of eruption onset and size, while are less common for data required in other PVHA components (e.g., vent opening). Making datasets open is complicated by economical, technological, ethical and/or policy-related challenges. International synergies (e.g., Global Volcanism Program, WOVOdat, Global Volcano Model, EPOS) will be key to facilitate the creation and maintenance of open-access databases that support *Next-Generation* PVHA. Additionally, clarification of some misconceptions about PVHA can also help progress. Firstly, PVHA should be understood as an expansion of deterministic, scenario-based hazard assessments. Secondly, a successful PVHA should sometimes be evaluated by its ability to deliver useful and usable hazard-related messages that help mitigate volcanic risk. Thirdly, PVHA is not simply an end product but a driver for research: identifying the most relevant sources of epistemic uncertainty can guide future efforts to reduce the overall uncertainty. Broadening of the volcanological community expertise to statistics or engineering has already brought major breakthroughs in long-term PVHA. A vital next step is developing and maintaining more open-access datasets that support PVHA worldwide.

Keywords: probabilistic volcanic hazard assessment, uncertainty quantification, data scarcity, open data, global databases

OPEN ACCESS

Edited by:
Fidel Costa,
Nanyang Technological University, Singapore

Reviewed by:
Mark Bebbington,
Massey University, New Zealand
Chris Newhall,
Mirisbiris Garden and Nature Center, Philippines

***Correspondence:**
Pablo Tierz
pablo@bgs.ac.uk

†***ORCID:***
Pablo Tierz
orcid.org/0000-0001-8889-9900

Specialty section:
This article was submitted to Volcanology, a section of the journal Frontiers in Earth Science

Received: *06 December 2019*
Accepted: *09 June 2020*
Published: *23 July 2020*

Citation:
Tierz P (2020) Long-Term Probabilistic Volcanic Hazard Assessment Using Open and Non-open Data: Observations and Current Issues. Front. Earth Sci. 8:257. doi: 10.3389/feart.2020.00257

INTRODUCTION

Nearly 300,000 people died due to volcanic activity from 1600 to 2010 AD (Auker et al., 2013). Unfortunately, several other deadly eruptions have shocked the world since then. Some because of their lack of clear precursory evidence: Mayon, Philippines, in 2013 (Maeda et al., 2015). Others because of the magnitude of their destructive toll: Fuego, Guatemala, in June 2018

(Naismith et al., 2019) and Krakatau, Indonesia, in December 2018 (Grilli et al., 2019; Williams et al., 2019). One of the most infamous examples of volcano tragedy was the eruption of Mount Pelée, Martinique, in 1902, which claimed the life of around 30,000 people at St Pierre and Morne Rouge (Lacroix, 1904; Fisher et al., 1980). At the time of the eruption, it was assumed that "Mount Pelée would behave in 1902 as it had in 1851 – when a rain of ash [...] did not harm those living under its shadow" (Reed, 2002). However, the timing, location, size and style of volcanic activity tend to change from eruption to eruption and within the same eruption. Thus, properly accounting for and quantifying this natural variability, or aleatory uncertainty, of volcanic eruptions and their associated hazardous phenomena is a basic requirement for volcanic hazard assessment (e.g., Woo, 1999; Connor et al., 2001; Marzocchi et al., 2004). Such assessments should also quantify the epistemic uncertainty related to incomplete knowledge (e.g., Marzocchi et al., 2004; Rougier and Beven, 2013; Tierz et al., 2016a). This can be achieved through probabilistic analyses of the onset, size and location of volcanic eruptions, as well as of the spatio-temporal intensity of hazardous phenomena such as pyroclastic density currents (PDCs) or lahars. Probabilistic volcanic hazard assessment (PVHA) started to develop several decades ago (e.g., Newhall, 1982; Barberi et al., 1990; Connor and Hill, 1995; Connor et al., 2001; Newhall and Hoblitt, 2002; Aspinall et al., 2003; Sparks, 2003) and has now become the standard method for robust, accurate and complete volcanic hazard assessment worldwide (e.g., Marzocchi et al., 2008, 2010; Bayarri et al., 2009; Sobradelo and Martí, 2010; Jenkins et al., 2012; Marzocchi and Bebbington, 2012; Bebbington, 2013, 2014; Del Negro et al., 2013; Hincks et al., 2014; Connor et al., 2015; Neri et al., 2015; Newhall and Pallister, 2015; Whelley et al., 2015; Bevilacqua et al., 2016; Biass et al., 2016; Mead and Magill, 2017; Tierz et al., 2017; Sandri et al., 2018).

Carrying out PVHA requires the collection and use of volcanological data (**Figure 1**) to select and parameterize probability distributions to calculate volcanic hazard, including the critical sources of uncertainty (e.g., Connor and Hill, 1995; Aspinall, 2006; Marzocchi et al., 2008, 2010; Marzocchi and Bebbington, 2012; Bebbington, 2013; Tierz et al., 2016a,b). While these tasks are very data demanding, the vast majority of volcanic systems in the world remain data scarce (e.g., Loughlin et al., 2015). Open data are crucial to help alleviate the widespread issue of data scarcity and, hence, support advancement of PVHA. For instance, open data can be used to *borrow* useful information from *analogue volcanoes* (i.e., volcanoes that have enough similar characteristics as to be considered partially exchangeable) and apply it to perform PVHA at a specific (data-scarce) target volcano (e.g., Marzocchi et al., 2004; Bebbington, 2014; Sheldrake, 2014; Ogburn et al., 2016a; Sheldrake et al., 2016; Newhall et al., 2017; Tierz et al., 2019). Some open-access volcanological databases that contain the necessary data to compute PVHA are currently available: Volcanoes of the world, Global Volcanism Program (Siebert et al., 2010; hereinafter GVP)[1]; WOVOdat (Newhall et al., 2017)[2]; Large Magnitude Explosive Volcanic Eruptions (Crosweller et al., 2012; hereinafter LaMEVE)[3] and others. However, the majority of the volcanological community still heavily relies on non-open data to perform PVHA (e.g., Bevilacqua et al., 2016; Jaquet et al., 2017; Tierz et al., 2018). The predominant use of non-open data reduces the versatility and scope of PVHA methods because researchers worldwide may find it difficult to gain independent insights from the same datasets. Conversely, open-access datasets permit such complementary research to be developed (e.g., Deligne et al., 2010; Sheldrake and Caricchi, 2017; Papale, 2018; Rougier et al., 2018).

In this contribution, I explore the use of open and non-open data in long-term PVHA (i.e., volcanic hazard forecasts on the timescale of years to decades, Marzocchi and Bebbington, 2012) to evidence how the key issue of data scarcity manifests in the predominant and uneven use of non-open data across different components of the probabilistic assessment. Then, I discuss the importance of data scarcity and misconceptions around PVHA as current issues that collectively hinder further and wider development in the field. Finally, I suggest a few potential future directions in the view of an increased availability of open-access datasets to perform long-term PVHA at the individual volcano, regional and global scales.

OPEN AND NON-OPEN DATA IN LONG-TERM PVHA

I have selected a collection of 100 peer-reviewed contributions to analyze long-term PVHA research since 2001 (see **Supplementary Material**). The collection covers, without over-representation, the spectrum of different research groups, volcanic systems, types of PVHA and hazardous phenomena. Although it is not necessarily statistically representative in terms of stratified random sampling, it nevertheless serves to illustrate certain research trends in PVHA over the last two decades. This collection, which I will henceforth denote as the "Sample" is analyzed (**Figure 2**; and **Supplementary Material**), focusing on the use of open, non-open and mixed (i.e., both open and non-open) datasets (see **Definitions**) to assess different components of the long-term forecast: (1) eruption onset and size; (2) eruption vent location; (3) eruption impacts (by hazardous phenomena); and (4) combinations of any of the three, which I term *integrated PVHA*. In the Sample, studies that use either non-open or mixed datasets dominate over those using open datasets to compute long-term PVHA (**Figures 2A,B**). According to the Sample, there have not been major changes in the use of open, non-open and mixed datasets over time (**Figure 2C**).

Eruption Onset and Size

It is the only component of the hazard assessment where open data have been used in isolation (**Figure 2B**) and non-open and mixed data do not dominate (**Figure 2A**). Global databases of the timing and size of volcanic eruptions (principally GVP and

[1]http://www.volcano.si.edu

[2]https://www.wovodat.org/

[3]https://www.bgs.ac.uk/vogripa/view/controller.cfc?method=lameve

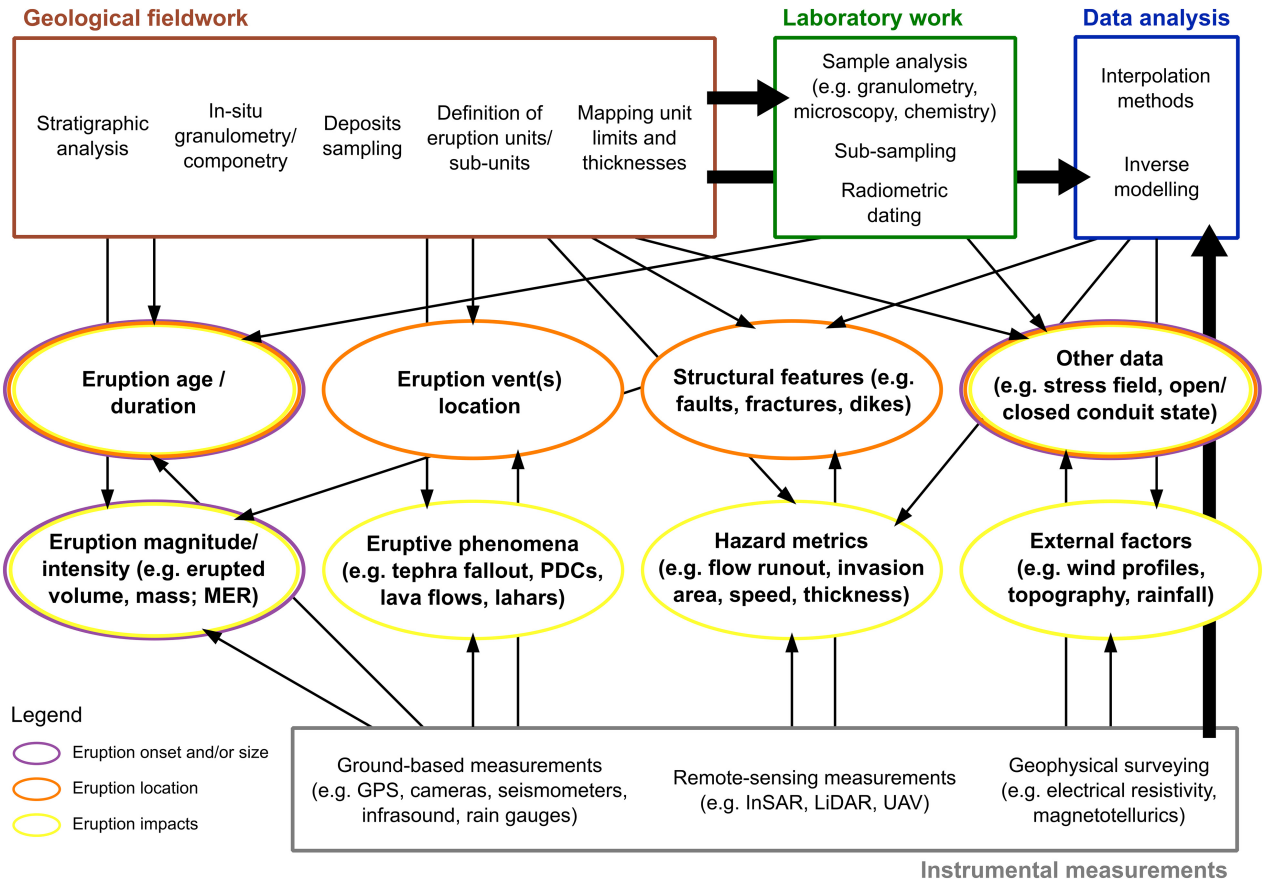

FIGURE 1 | Schematic showing the main types of data (ellipses) that are required to carry out long-term PVHA and some intermediate methods or steps (rectangles) needed to obtain these data. Arrows indicate links between intermediate steps or with derived PVHA data types and variables (ellipses and text within parentheses). Data types are classified according to their use in different components of the hazard assessment: eruption onset and/or size, eruption location and eruption impacts. The majority of the data are generated, directly or indirectly, through geological fieldwork performed on the eruptive products of past volcanic eruptions. Since historical times, direct observations and instrumental measurements of both eruptive parameters as well as external factors (e.g., wind, rainfall, topography) have also become available. MER, Mass Eruption Rate; PDCs, Pyroclastic Density Currents; GPS, Global Positioning System; InSAR, Interferometric Synthetic Aperture Radar; LiDAR, Light Detection And Ranging; UAV, Unmanned Aerial Vehicle.

LaMEVE) have been the key element required for the hazard analysts to conduct PVHA. The Sample suggests that eruption onset-size forecasts were more common during approximately the first decade of the 21st century (**Figure 2D**). This relative decrease could be partially explained by the incorporation of onset-size assessments into integrated PVHA over the second decade of the century (e.g., Sandri et al., 2012, 2014, 2018; Bartolini et al., 2015; Bevilacqua et al., 2017). Recent advances in PVHA of eruption onset and size have focused on alleviating issues around under-recording (Mead and Magill, 2014; Rougier et al., 2016; Sheldrake and Caricchi, 2017) and on the use of covariates to inform the statistical modeling: e.g., open/closed-conduit states (Bebbington, 2014; Whelley et al., 2015); rock geochemistry (Passarelli and Brodsky, 2012); volcano type or tectonic setting (Sheldrake, 2014; Sheldrake and Caricchi, 2017); or a combination of volcanological observations (Dzierma and Wehrmann, 2010, 2014). Moreover, advanced stochastic models to incorporate the epistemic uncertainty in the rates of eruption onsets, and model varied patterns of clustering and recurrent behavior of volcanic eruptions, have been proposed (e.g., Garcia-Aristizabal et al., 2012; Bebbington, 2013; Bevilacqua et al., 2016, 2018).

Eruption Vent Location

It has been exclusively performed using non-open data, according to the Sample (**Figure 2A**). This is strongly related to the fact that the detailed geological data (**Figure 1**) required to derive statistical models for the spatial occurrence of vent locations (e.g., Cappello et al., 2012; Connor et al., 2012; Selva et al., 2012b; Bevilacqua et al., 2015), are rarely available as open-access datasets. The data are available at specific volcanic systems but generalizations about the data-generating process for eruption location are hindered because of the lack of cross-volcano, open-access databases (NB. Le Corvec et al., 2013, could be considered as a "non-open archetype" for such databases). Some recent developments have looked at: (i) constraining the areal extent of vent locations by matching it to potential magma sources identified from geophysical imaging (Deng et al., 2017); or (ii)

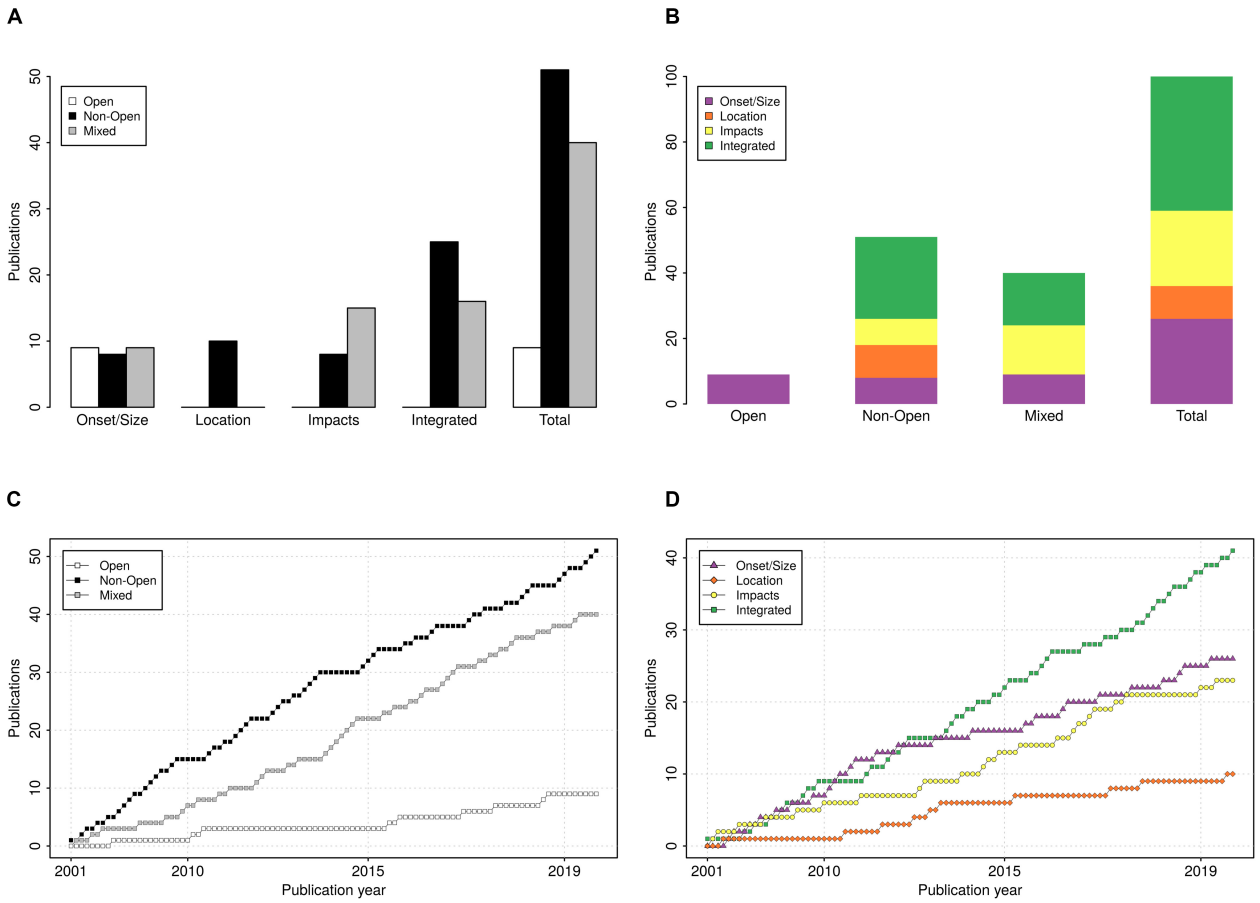

FIGURE 2 | Summary of patterns observed on a collection of 100 publications on long-term PVHA published since 2001. In **(A,B)**: total number of publications partitioned according to the use of open, non-open and mixed datasets **(A)**; and the focus of the PVHA: eruption onset and/or size, eruption location, eruption impacts or integrated PVHA **(B)**. In **(C,D)**: cumulative number of publications according to the same partitions: type of data **(C)** and focus of the PVHA **(D)**. Publications are sorted, in ascending order, by the year of publication and, for those with the same publication year, by alphabetical order. The *x* axis displays the resulting ordinal numbering (*ID* variable in the **Supplementary Material**). Labels on the *x* axis are placed on the first publication of the corresponding publication year.

assessing changes in vent locations due to spatial migration of volcanism in geological time (Jaquet et al., 2017).

Eruption Impacts

Mixed datasets are more commonly used than non-open datasets (**Figure 2A**). This may be due to an increased accessibility to databases of some key elements for the PVHA such as wind profiles for tephra fallout (Kalnay et al., 1996; Dee et al., 2011) or digital elevation models for mass flows (e.g., Shuttle Radar Topography Mission)[4]. Recent advances are linked with: (1) the comprehensive quantification of inter- and intra-eruption-size aleatory variability of quantities such as the mass eruption rate, erupted mass or volume, column height, column-collapse height, etc., (e.g., Biass et al., 2016; Sandri et al., 2016; Tierz et al., 2016b); and (2) the recognition and quantification of diverse sources of epistemic uncertainty, which significantly affect the PVHA (e.g., Stefanescu et al., 2012a,b; Spiller et al., 2014; Tierz et al., 2016a). The parallel development of detailed, yet relatively fast, physical models and versatile statistical models has aided the quantification of the aforementioned uncertainties. Some examples include open-access numerical codes for granular flows (TITAN2D, Patra et al., 2005; *LaharFlow*)[5] and uncertainty quantification techniques ranging from probabilistic graphical models (e.g., Sobradelo et al., 2014; Tonini et al., 2015; Tierz et al., 2017) to polynomial chaos methods (Dalbey et al., 2008; Tierz et al., 2018) and stochastic-process emulators (Bayarri et al., 2009; Spiller et al., 2014; Rutarindwa et al., 2019).

Integrated PVHA

According to the Sample, it has been the most common PVHA over the last years (**Figure 2D**) and it predominantly uses non-open data (**Figure 2A**). Notwithstanding, the range and scope of open-access databases for integrated PVHA seems to be increasing. Long-term programs like GVP have been

[4]https://www2.jpl.nasa.gov/srtm/

[5]https://www.laharflow.bristol.ac.uk/

joined by other efforts such as LaMEVE, FlowDat (Ogburn, 2012)[6], DomeHaz (Ogburn et al., 2015)[7], the Eruption Source Parameter database (Mastin et al., 2009)[8], the Catalog of Icelandic Volcanoes[9], etc. Recent advances have used some of these datasets to parameterize event trees in novel multi-volcano PVHA of tephra fallout (Jenkins et al., 2012) or PDCs (Sandri et al., 2018). Other advances, with potential applicability to integrated PVHA, have designed: (a) community cyberinfrastructure platforms that host or link to other open-access databases and provide online tools to support hazard assessment (Vhub, Palma et al., 2014; Volcanic Hazards Assessment Support System by G-EVER, Takarada, 2017)[10,11]; or (b) methods to identify objective sets of analogue volcanoes from global databases (VOLCANS, Tierz et al., 2019).

DISCUSSION

In my view, further and wider development of long-term PVHA is hindered by data scarcity as well as by some misconceptions and criticism toward PVHA itself.

Data Scarcity in PVHA

Volcanological data (**Figure 1**) are the best possible source of information to quantify aleatory uncertainty in volcanic hazard (e.g., Newhall and Hoblitt, 2002; Marzocchi and Bebbington, 2012; Connor et al., 2015; Pallister et al., 2019). Data discovery can alter this quantification by changing the experimental concept (Marzocchi and Jordan, 2014) and this is especially acute at the scale of individual volcanoes and for infrequent, large-size eruptions. For instance, for some decades, the Campi Flegrei caldera (Italy) was known to have undergone two caldera-forming eruptions, one at ∼39 ka (the Campanian Ignimbrite eruption; Fedele et al., 2003) and another at ∼15 ka (the Yellow Neapolitan Tuff eruption; Deino et al., 2004). Recently, new evidence for a third caldera-forming eruption at ∼29 ka (the Masseria del Monte Tuff eruption) has been found (Albert et al., 2019). This discovery has drastically reduced the expected repose interval for caldera-forming eruptions at Campi Flegrei.

It is also important to distinguish between lack of data discoverability (Loughlin et al., 2015) and lack of data accessibility (see **Definitions**). At present, a number of volcanological datasets, typically collected at specific volcanic systems (e.g., Cioni et al., 2008; Thompson et al., 2015; Bevilacqua et al., 2018), are stored in non-open-access publications and, hence, are not freely available to the entire volcanological community. Open-access publications are becoming more customary, which increases the availability of open data to perform PVHA (e.g., Sobradelo et al., 2011; Biass et al., 2014; Jenkins et al., 2019), but there is still an urgent need to discover, assemble, digitize and store volcanological data in open-access databases (e.g., Geyer and Marti, 2008; Ogburn, 2012; Ogburn et al., 2015, 2016b; Newhall et al., 2017) that help develop *Next-Generation* PVHA. International synergies, such as GVP, the Global Volcano Model[12], European Plate Observing System[13], European Open Science Cloud[14] or EarthCube[15], can play key roles in facilitating the generation and maintenance of such databases, as well as in the transition toward open science in general, for which not only open data but open models and workflows would also be required.

There are significant and varied challenges that play a role in the release of open data. For instance, individual researchers or institutions may be reluctant to release their data until fundamental research has been successfully conducted using those data. Hence, a *grace period* of a few years (e.g., 2 years in WOVOdat)[16] can provide the scope for initial interpretation and publication of results linked to the data. Other difficulties might be: economical and/or logistical (e.g., availability of long-term funding and tailored student supervision to help make existing data accessible), technological (e.g., software and hardware development) and/or legal and policy-related, ranging from intellectual property rights to protection of personal data. For instance, data-protection policies may be different across countries and/or change over time, within a given country or region (e.g., General Data Protection Regulation of May 2018 in Europe[17]). Particularly in volcanology, expert elicitation has become an important tool to extract data for PVHA (e.g., Aspinall, 2006; Selva et al., 2012a; Hincks et al., 2014; Thompson et al., 2015; Christophersen et al., 2018). The elicitation process has ethical and legal implications (e.g., Hemming et al., 2018), such as anonymity of the generated data, that need to be carefully considered while moving toward more open-data and open-science environments that facilitate PVHA worldwide.

Misconceptions Around PVHA

I focus here on three that I consider the most relevant. First, probabilistic approaches are sometimes criticized because of their overall complexity. However, it should be noted that PVHA is an expansion of deterministic approaches (Marzocchi and Bebbington, 2012). That is, a probabilistic hazard product can be converted into a "deterministic" one while the contrary does not hold. The versatility of PVHA should be an asset, not a detriment. For instance, a collection of hazard curves covering a spatial grid actually represents a set of probability and hazard maps that can be derived from the hazard curves by using thresholds in either the hazard-intensity measure (e.g., flow speed) or the probability of exceedance, respectively (e.g., Selva et al., 2014; Tonini et al., 2015; Tierz et al., 2018). The

[6]https://vhub.org/resources/2076
[7]https://vhub.org/resources/1742
[8]https://www.bgs.ac.uk/research/volcanoes/esp/search.cfc?method=viewHome
[9]http://icelandicvolcanos.is/
[10]https://vhub.org/
[11]http://volcano.g-ever1.org/
[12]https://globalvolcanomodel.org/
[13]https://epos-ip.org/
[14]https://ec.europa.eu/research/openscience/index.cfm?pg=open-science-cloud
[15]https://earthcube.org
[16]https://wovodat.org/about/about.php
[17]https://ec.europa.eu/info/law/law-topic/data-protection/data-protection-eu_en

latter case is effectively equivalent to producing a scenario-based hazard map with known probability of exceedance. One key difference in deterministic, scenario-based hazard maps is that the associated probability of exceedance is not known (e.g., Esposti Ongaro et al., 2008; Charbonnier and Gertisser, 2012; Capra et al., 2015). Nevertheless, it is also important to acknowledge that probabilistic and deterministic approaches should not be seen as an "either-or choice" (e.g., Newhall and Pallister, 2015; Rouwet et al., 2017): both methods are reciprocally informative and beneficial for the goal of improving volcanic hazard assessments (e.g., Marzocchi et al., 2008; Marzocchi and Bebbington, 2012; Newhall and Pallister, 2015).

Secondly, validation of probabilistic hazard forecasts is necessary (Marzocchi and Bebbington, 2012; Marzocchi and Jordan, 2014; Connor et al., 2015) but not always there are enough data (**Figure 1**) available for such purpose (e.g., Marzocchi et al., 2004, 2008). In this context, a successful volcanic hazard assessment should be seen as one that efficiently delivers vital messages that help mitigation of volcanic risk (Pallister et al., 2019). Depending on the volcanological and socio-political context, the nature of this message can vary remarkably: from evidencing the possibility of far-reach PDCs during escalating phases of unrest (e.g., Mount Pinatubo, in June 1991: Newhall and Punongbayan, 1996; Newhall and Pallister, 2015) to raising awareness of the relevance of volcanic hazard at under-studied explosive volcanic systems with long repose intervals (e.g., Main Ethiopian Rift: Vye-Brown et al., 2016). In densely populated, heavily industrialized areas built on or surrounded by several volcanoes (e.g., the metropolitan area of Napoli, Italy, ∼3 M inhabitants), long-term PVHA represents a vital asset to deliver effective hazard-related messages. Considering Somma-Vesuvius and Campi Flegrei separately, long-term PDC hazard is most crucially controlled by different aspects at the two volcanoes. At Somma-Vesuvius, the size of the next eruption is a key factor controlling the volume and spatial reach of PDCs (Gurioli et al., 2010; Tierz et al., 2016a,b; Sandri et al., 2018) while vent-opening variability (Tadini et al., 2017) has a limited influence, partly due to major topographic controls on PDC propagation exerted by the stratocone and Mount Somma (Esposti Ongaro et al., 2008; Tierz et al., 2016a, 2018). At Campi Flegrei, eruption size has a more restricted effect on the volume and spatial reach of PDCs, for the most-likely explosive eruption sizes (Orsi et al., 2004, 2009; Neri et al., 2015; Tierz et al., 2016b). However, the location of the next eruptive vent (Selva et al., 2012b; Bevilacqua et al., 2015; Rivalta et al., 2019) has a paramount importance, given the complex intra-caldera topography and the smaller PDC invasion areas at Campi Flegrei (Tierz et al., 2016b; Bevilacqua et al., 2017; Sandri et al., 2018).

Finally, PVHA is often solely seen as an end product while it should also be considered a driver for research. If epistemic uncertainties are comprehensively quantified and ranked (e.g., Stefanescu et al., 2012a,b; Rougier and Beven, 2013; Spiller et al., 2014; Tierz et al., 2016a), then sensitivity of PVHA outputs can be explicitly explored (e.g., Tierz et al., 2016a; Bevilacqua et al., 2017; Sandri et al., 2018), and data collection can be aimed at reducing the overall uncertainty to improve volcanic hazard assessment (e.g., Tierz et al., 2016a; Trolese et al., 2019). The above example of PVHA of PDCs at the metropolitan area of Napoli exemplifies how research can focus on the most critical, volcano-specific aspects linked to PDC hazard: e.g., spatial probability of vent opening at Campi Flegrei and probability of eruption size at Somma-Vesuvius.

FUTURE DIRECTIONS

I propose four major steps to improve long-term PVHA in the context of an increased availability of open-access datasets:

1. *Unraveling the links between global and local frequency-magnitude distributions:* there is still debate about the portability of global frequency-magnitude distributions (Papale, 2018; Rougier et al., 2018) to regional (Sheldrake and Caricchi, 2017) and individual-volcano scales (Bebbington, 2014). Bayesian hierarchical models are a structured approach to accommodate end-member interpretations (Ogburn et al., 2016a) but different exchangeability assumptions between analogue volcanoes should be investigated to improve such models. Novel tools to identify objective sets of analogue volcanoes will facilitate such analyses (VOLCANS, Tierz et al., 2019);
2. *Toward the use of data-generating processes to model vent locations:* it would be preferable to use the data-generating process itself (i.e., magma transfer to the surface), instead of mostly focusing of past-vents data, to derive spatial PDFs of vent opening. Further developments in: (a) testing the spatial distributions of past vent locations against meaningful geological and geophysical data (Martin et al., 2004; Runge et al., 2016); and/or (b) applying hybrid physical-statistical approaches to simulate dike propagation trajectories and calculate spatial probabilities for future vent locations (Rivalta et al., 2019) are promising ways forward;
3. *Increased granularity in intra-eruption forecasting*: almost every PVHA of hazardous phenomena aggregates volcanic activity at the level of the single eruption (e.g., Jenkins et al., 2012; Becerril et al., 2014; Sandri et al., 2018) but very few incorporate the dynamic nature of intra-eruption phenomenology (e.g., Wolpert et al., 2018; Bebbington and Jenkins, 2019). More effort should be put in this direction and open-access, global datasets will be a fundamental resource for probabilistic models that incorporate this level of granularity in eruption dynamics (Cassidy et al., 2018);
4. *From hazard summation to hazard interaction in multi-hazard assessments at volcanoes:* the majority of volcanic multi-hazard assessments analyze hazardous phenomena separately and then combine or add their resulting hazard footprints (e.g., Sandri et al., 2014; Bartolini et al., 2015). There are very few examples where the hazard interaction is explicitly quantified (e.g., Volentik et al., 2009; Tierz et al., 2017). Probabilistic graphical

models (Koller and Friedman, 2009) can help quantify such critical interactions and their construction could strongly benefit from techniques such as machine learning (Anantrasirichai et al., 2019), if enough open volcanological data (**Figure 1**) were available.

The volcanological community has been able to enlarge its collective expertise over the last decades by engaging with scientists from diverse fields such as statistics, engineering or computer science. This has already resulted in major breakthroughs in long-term PVHA (e.g., Barberi et al., 1990; Wadge et al., 1994; Connor and Hill, 1995; Newhall and Hoblitt, 2002; Bayarri et al., 2009; Marzocchi et al., 2010; Jenkins et al., 2012; Bebbington, 2014, 2015; Jaquet et al., 2017; Tierz et al., 2017; Sandri et al., 2018). A vital next step relates to creating, expanding and maintaining more open-access volcanological datasets, as well as open-source software and workflows (e.g., data processing), that can support long-term PVHA worldwide.

DEFINITIONS

Open Data

Any type of data that any user can access and re-use, entirely free of charge, through a device equipped with an Internet connection (NB. Data in the GVP database is considered as open data, even prior to its release as an open-access database in 2002, Siebert and Simkin, 2002). Please note that *fully open data* would also imply free availability of the software and workflows used to generate these data. A simplified approach, where open data refers only to data used to compute long-term PVHA (see **Figure 1**), was taken here for the sake of facilitating the analysis shown in **Figure 2** and the Electronic **Supplementary Material**.

Non-open Data

Any type of data that does not comply with the definition given for open data. For example, all data found in subscription-based or pay-per-view articles is considered non-open. Please note that many authors may be willing to grant open access to their data upon publication. However, from the user point of view, data accessibility ultimately depends on the specific access policy associated with each published article.

Data Scarcity

General lack of data for any given volcano or group of volcanoes, independently of the reason behind this scarcity.

Data Discoverability

Quality of any kind of data for a given volcano or group of volcanoes of being able to be *discovered* through identification, description, measurement, sampling, etc.

Data Accessibility

Quality of any kind of data for a given volcano or group of volcanoes of being able to be accessed (and re-used) as open data. Please note that the concept of data accessibility may contain finer gradations (e.g., data in repositories, supplementary material files; maps drawn on an article; data available from author upon request, etc.), which would result in more data categories than the three distinguished in this manuscript: open, non-open and mixed. A simplified categorisation was chosen here for the sake of facilitating the analysis shown in **Figure 2** and the Electronic **Supplementary Material**.

Data Availability

Quality of any kind of data for a given volcano or group of volcanoes of being available for its re-use as open data. In the context of the manuscript, synonym of data accessibility.

AUTHOR'S NOTE

New data used in this study are shown in the figures presented and available in the **Supplementary Material**. Figures were generated using Inkscape software (Harrington, 2004–2005) and R programming language (R Core Team, 2013) and color schema were based on www.ColorBrewer.org (Brewer, 2018).

DATA AVAILABILITY STATEMENT

All datasets generated for this study are included in the article/**Supplementary Material**.

AUTHOR CONTRIBUTIONS

PT conceived this perspective, collected and processed the data, analyzed the results, generated the figures, wrote the manuscript, and approved all its versions.

FUNDING

The research leading to these results has been supported by Global Geological Risk Platform of the British Geological Survey NC-ODA grant NE/R000069/1: Geoscience for Sustainable Futures.

ACKNOWLEDGMENTS

I would like to thank the Topic Editors: Elisa Trasatti, Fidel Costa, and Michelle Parks, for having invited me to submit a manuscript to their research topic. I am very grateful to Mark Bebbington, Chris Newhall, and an anonymous reviewer for their thorough revisions and insightful comments, which helped me improve the clarity and completeness of the manuscript, and to Fidel Costa and Valerio Acocella for their helpful feedback and editorial support. I wholeheartedly thank Susan Loughlin for encouraging me to write this perspective and for all her invaluable feedback; and her and Eliza Calder for the very insightful conversations we have shared about volcanoes and volcanic hazard and risk. Using the 1902 eruption at Mount Pelée as an example of the importance of quantifying aleatory uncertainty in PVHA

was an idea envisaged by Elaine Spiller. I would like to thank Andrea Di Vico for helpful conversations. I profoundly thank Laura Sandri and Warner Marzocchi for allowing me to learn so much about statistics and volcanic hazard assessment from them. For having also contributed to increasing my understanding of volcanic systems and volcanic hazard assessment, I will try to summarize my warmest thanks to: Marceliano Lago, Carlos Galé, Teresa Ubide, Patricia Larrea, Joan Martí, Paolo Papale and all the NEMOH family, Antonio Costa, Roberto Sulpizio, Mauro Antonio Di Vito, Lucia Zaccarelli, Jacopo Selva, Abani Patra, Ramona Stefanescu, Greg Valentine, Sarah Ogburn, Sylvain Charbonnier, Henry Odbert, Mark Woodhouse, Jeremy Phillips, Ben Clarke, Elaine Spiller, and Bruce Pitman. Many other colleagues, reviewers and editors have played a crucial role in discussions that have made me improve my knowledge and perspectives on probabilistic volcanic hazard assessment and volcanoes in general. I would like to sincerely thank them all. Published with permission of the Executive Director of British Geological Survey (NERC-UKRI).

SUPPLEMENTARY MATERIAL

The Supplementary Material for this article can be found online at: https://www.frontiersin.org/articles/10.3389/feart.2020.00257/full#supplementary-material

REFERENCES

Albert, P. G., Giaccio, B., Isaia, R., Costa, A., Niespolo, E. M., Nomade, S., et al. (2019). Evidence for a large-magnitude eruption from campi flegrei caldera (Italy) at 29 ka. *Geology* 47, 595–599. doi: 10.1130/g45805.1

Anantrasirichai, N., Biggs, J., Albino, F., and Bull, D. (2019). A deep learning approach to detecting volcano deformation from satellite imagery using synthetic datasets. *Remote Sens. Environ.* 230:111179. doi: 10.1016/j.rse.2019.04.032

Aspinall, W. P. (2006). "Structured elicitation of expert judgment for probabilistic hazard and risk assessment in volcanic eruptions," in *Statistics in Volcanology*, eds H. M. Mader, S. G. Coles, C. B. Connor, and L. J. Connor (London: Geological Society), 15–30. doi: 10.1144/iavcei001.2

Aspinall, W. P., Woo, G., Voight, B., and Baxter, P. J. (2003). Evidence-based volcanology: application to eruption crises. *J. Volcanol. Geotherm. Res.* 128, 273–285. doi: 10.1016/s0377-0273(03)00260-9

Auker, M., Sparks, R., Siebert, L., Crosweller, H., and Ewert, J. (2013). A statistical analysis of the global historical volcanic fatalities record. *J. Appl. Volcanol.* 2:2.

Barberi, F., Macedonio, G., Pareschi, M. T., and Santacroce, R. (1990). Mapping the tephra fallout risk: an example from Vesuvius, Italy. *Nature* 344, 142–144. doi: 10.1038/344142a0

Bartolini, S., Bolós, X., Martí, J., Pedra, E. R., and Planagumà, L. (2015). Hazard assessment at the quaternary la garrotxa volcanic field (NE Iberia). *Nat. Hazards* 78, 1349–1367. doi: 10.1007/s11069-015-1774-y

Bayarri, M. J., Berger, J. O., Calder, E. S., Dalbey, K., Lunagomez, S., Patra, A. K., et al. (2009). Using statistical and computer models to quantify volcanic hazards. *Technometrics* 51, 402–413. doi: 10.1198/tech.2009.08018

Bebbington, M. S. (2013). Assessing probabilistic forecasts of volcanic eruption onsets. *Bull. Volcanol.* 75:783.

Bebbington, M. S. (2014). Long-term forecasting of volcanic explosivity. *Geophys. J. Int.* 197, 1500–1515. doi: 10.1093/gji/ggu078

Bebbington, M. S. (2015). Spatio-volumetric hazard estimation in the Auckland volcanic field. *Bull. Volcanol.* 77:39.

Bebbington, M. S., and Jenkins, S. F. (2019). Intra-eruption forecasting. *Bull. Volcanol.* 81:34.

Becerril, L., Bartolini, S., Sobradelo, R., Martí, J., Morales, J. M., and Galindo, I. (2014). Long-term volcanic hazard assessment on El Hierro (Canary Islands). *Nat. Hazards Earth Syst. Sci.* 14, 1853–1870.

Bevilacqua, A., Bursik, M., Patra, A., Bruce Pitman, E., Yang, Q., Sangani, R., et al. (2018). Late Quaternary eruption record and probability of future volcanic eruptions in the Long Valley volcanic region (CA, USA). *J. Geophys. Res. Solid Earth* 123, 5466–5494. doi: 10.1029/2018jb015644

Bevilacqua, A., Flandoli, F., Neri, A., Isaia, R., and Vitale, S. (2016). Temporal models for the episodic volcanism of campi flegrei caldera (Italy) with uncertainty quantification. *J. Geophys. Res. Solid Earth* 121, 7821–7845. doi: 10.1002/2016jb013171

Bevilacqua, A., Isaia, R., Neri, A., Vitale, S., Aspinall, W. P., Bisson, M., et al. (2015). Quantifying volcanic hazard at Campi Flegrei caldera (Italy) with uncertainty assessment: 1. Vent opening maps. *J. Geophys. Res. Solid Earth* 120, 2309–2329. doi: 10.1002/2014jb011775

Bevilacqua, A., Neri, A., Bisson, M., Esposti Ongaro, T., Flandoli, F., Isaia, R., et al. (2017). The effects of vent location, event scale, and time forecasts on pyroclastic density current hazard maps at campi flegrei caldera (Italy). *Front. Earth Sci.* 5:72. doi: 10.3389/feart.2017.00072

Biass, S., Bonadonna, C., Connor, L., and Connor, C. (2016). TephraProb: a MATLAB package for probabilistic hazard assessments of tephra fallout. *J. Appl. Volcanol.* 5:10.

Biass, S., Scaini, C., Bonadonna, C., Folch, A., Smith, K., and Höskuldsson, A. (2014). A multi-scale risk assessment for tephra fallout and airborne concentration from multiple Icelandic volcanoes–Part 1: hazard assessment. *Nat. Hazards Earth Syst. Sci.* 14, 2265–2287. doi: 10.5194/nhess-14-2265-2014

Brewer, C. A. (2018). Available online at: http://www.colorbrewer.org (accessed November 15, 2019). doi: 10.5194/nhess-14-2265-2014

Cappello, A., Neri, M., Acocella, V., Gallo, G., Vicari, A., and Del Negro, C. (2012). Spatial vent opening probability map of Etna volcano (Sicily. Italy). *Bull. Volcanol.* 74, 2083–2094. doi: 10.1007/s00445-012-0647-4

Capra, L., Gavilanes-Ruiz, J. C., Bonasia, R., Saucedo-Giron, R., and Sulpizio, R. (2015). Re-assessing volcanic hazard zonation of Volcán de Colima, México. *Nat. Hazards* 76, 41–61. doi: 10.1007/s11069-014-1480-1

Cassidy, M., Manga, M., Cashman, K., and Bachmann, O. (2018). Controls on explosive-effusive volcanic eruption styles. *Nat. Commun.* 9, 1–16.

Charbonnier, S. J., and Gertisser, R. (2012). Evaluation of geophysical mass flow models using the 2006 block-and-ash flows of merapi volcano, java, indonesia: towards a short-term hazard assessment tool. *J. Volcanol. Geotherm. Res.* 231, 87–108. doi: 10.1016/j.jvolgeores.2012.02.015

Christophersen, A., Deligne, N. I., Hanea, A. M., Chardot, L., Fournier, N., and Aspinall, W. P. (2018). Bayesian Network modeling and expert elicitation for probabilistic eruption forecasting: pilot study for Whakaari/White Island, New Zealand. *Front. Earth Sci.* 6:211. doi: 10.3389/feart.2017.00211

Cioni, R., Bertagnini, A., Santacroce, R., and Andronico, D. (2008). Explosive activity and eruption scenarios at somma-vesuvius (Italy): towards a new classification scheme. *J. Volcanol. Geotherm. Res.* 178, 331–346. doi: 10.1016/j.jvolgeores.2008.04.024

Connor, C., Bebbington, M., and Marzocchi, W. (2015). "Probabilistic volcanic hazard assessment," in *The Encyclopedia Of Volcanoes*, 2nd Edn, eds H. Sigurdsson, B. Houghton, S. McNutt, H. Rymer, and J. Stix (Cambridge: Academic Press), 897–910. doi: 10.1016/b978-0-12-385938-9.00051-1

Connor, C. B., and Hill, B. E. (1995). Three nonhomogeneous poisson models for the probability of basaltic volcanism: application to the yucca mountain region, nevada. *J. Geophys. Res. Solid Earth* 100, 10107–10125. doi: 10.1029/95jb01055

Connor, C. B., Hill, B. E., Winfrey, B., Franklin, N. M., and Femina, P. C. (2001). Estimation of volcanic hazards from tephra fallout. *Nat. Hazards Rev.* 2, 33–42. doi: 10.1061/(asce)1527-6988(2001)2:1(33)

Connor, L. J., Connor, C. B., Meliksetian, K., and Savov, I. (2012). Probabilistic approach to modeling lava flow inundation: a lava flow hazard assessment for a nuclear facility in Armenia. *J. Appl. Volcanol.* 1:3.

Crosweller, H. S., Arora, B., Brown, S. K., Cottrell, E., Deligne, N. I., Guerrero, N. O., et al. (2012). Global database on large magnitude explosive volcanic eruptions (LaMEVE). *J. Appl. Volcanol.* 1:4.

Dalbey, K., Patra, A. K., Pitman, E. B., Bursik, M. I., and Sheridan, M. F. (2008). Input uncertainty propagation methods and hazard mapping of geophysical mass flows. *J. Geophys. Res. Solid Earth* 113:B05203. doi: 10.1029/2006JB004471

Dee, D. P., Uppala, S. M., Simmons, A. J., Berrisford, P., Poli, P., Kobayashi, S., et al. (2011). The ERA-Interim reanalysis: configuration and performance of the data assimilation system. *Q. J. R. Meteorol. Soc.* 137, 553–597.

Deino, A. L., Orsi, G., de Vita, S., and Piochi, M. (2004). The age of the Neapolitan Yellow Tuff caldera-forming eruption (Campi Flegrei caldera–Italy) assessed by 40Ar/39Ar dating method. *J. Volcanol. Geotherm. Res.* 133, 157–170. doi: 10.1016/s0377-0273(03)00396-2

Del Negro, C., Cappello, A., Neri, M., Bilotta, G., Hérault, A., and Ganci, G. (2013). Lava flow hazards at mount etna: constraints imposed by eruptive history and numerical simulations. *Sci. Rep.* 3:3493.

Deligne, N. I., Coles, S. G., and Sparks, R. S. J. (2010). Recurrence rates of large explosive volcanic eruptions. *J. Geophys. Res. Solid Earth* 115:B06203. doi: 10.1029/2009jb006554

Deng, F., Connor, C. B., Malservisi, R., Connor, L. J., White, J. T., Germa, A., et al. (2017). A geophysical model for the origin of volcano vent clusters in a colorado plateau volcanic field. *J. Geophys. Res. Solid Earth* 122, 8910–8924. doi: 10.1002/2017jb014434

Dzierma, Y., and Wehrmann, H. (2010). Statistical eruption forecast for the chilean southern volcanic zone: typical frequencies of volcanic eruptions as baseline for possibly enhanced activity following the large 2010 concepción earthquake. *Nat. Hazards Earth Syst. Sci.* 10, 2093–2108. doi: 10.5194/nhess-10-2093-2010

Dzierma, Y., and Wehrmann, H. (2014). Probabilities of future VEI $\geq$ 2 eruptions at the Central American Volcanic Arc: a statistical perspective based on the past centuries' eruption record. *Int. J. Earth Sci.* 103, 2029–2042. doi: 10.1007/s00531-012-0803-2

Esposti Ongaro, T., Neri, A., Menconi, G., De'Michieli Vitturi, M., Marianelli, P., Cavazzoni, C., et al. (2008). Transient 3D numerical simulations of column collapse and pyroclastic density current scenarios at Vesuvius. *J. Volcanol. Geotherm. Res.* 178, 378–396. doi: 10.1016/j.jvolgeores.2008.06.036

Fedele, F. G., Giaccio, B., Isaia, R., and Orsi, G. (2003). "The campanian ignimbrite eruption, heinrich event 4, and palaeolithic change in europe: a high-resolution investigation," in *Volcanism and the Earth's Atmosphere*, eds A. Rob and C. Oppenheimer (Hoboken: John Wiley & Sons), 301–325. doi: 10.1029/139gm20

Fisher, R. V., Smith, A. L., and Roobol, M. J. (1980). Destruction of St. Pierre, Martinique, by ash-cloud surges, May 8 and 20, 1902. *Geology* 8, 472–476.

Garcia-Aristizabal, A., Marzocchi, W., and Fujita, E. (2012). A Brownian model for recurrent volcanic eruptions: an application to Miyakejima volcano (Japan). *Bull. Volcanol.* 74, 545–558. doi: 10.1007/s00445-011-0542-4

Geyer, A., and Marti, J. (2008). The new worldwide collapse caldera database (CCDB): a tool for studying and understanding caldera processes. *J. Volcanol. Geotherm. Res.* 175, 334–354. doi: 10.1016/j.jvolgeores.2008.03.017

Grilli, S. T., Tappin, D. R., Carey, S., Watt, S. F. L., Ward, S. N., Grilli, A. R., et al. (2019). Modelling of the tsunami from the December 22, 2018 lateral collapse of Anak Krakatau volcano in the sunda straits. *Indonesia. Sci. Rep.* 9, 1–13.

Gurioli, L., Sulpizio, R., Cioni, R., Sbrana, A., Santacroce, R., Luperini, W., et al. (2010). Pyroclastic flow hazard assessment at Somma–Vesuvius based on the geological record. *Bull. Volcanol.* 72, 1021–1038. doi: 10.1007/s00445-010-0379-2

Harrington, B. (2004–2005). *Inkscape*. Available online at: http://www.inkscape.org/ (accessed November 15, 2019). doi: 10.1007/s00445-010-0379-2

Hemming, V., Burgman, M. A., Hanea, A. M., McBride, M. F., and Wintle, B. C. (2018). A practical guide to structured expert elicitation using the IDEA protocol. *Methods Ecol. Evol.* 9, 169–180. doi: 10.1111/2041-210x.12857

Hincks, T. K., Komorowski, J.-C., Sparks, S. R., and Aspinall, W. P. (2014). Retrospective analysis of uncertain eruption precursors at La Soufrière volcano, Guadeloupe, 1975–77: volcanic hazard assessment using a Bayesian Belief Network approach. *J. Appl. Volcanol.* 3:3. doi: 10.1111/2041-210x.12857

Jaquet, O., Lantuéjoul, C., and Goto, J. (2017). Probabilistic estimation of long-term volcanic hazard under evolving tectonic conditions in a 1 Ma timeframe. *J. Volcanol. Geotherm. Res.* 345, 58–66. doi: 10.1016/j.jvolgeores.2017.07.010

Jenkins, S., Magill, C., McAneney, J., and Blong, R. (2012). Regional ash fall hazard I: a probabilistic assessment methodology. *Bull. Volcanol.* 74, 1699–1712. doi: 10.1007/s00445-012-0627-8

Jenkins, S. F., Goldstein, H., Bebbington, M. S., Sparks, R. S. J., and Koyaguchi, T. (2019). Forecasting explosion repose intervals with a non-parametric bayesian survival model: application to sakura-jima volcano, Japan. *J. Volcanol. Geotherm. Res.* 381, 44–56. doi: 10.1016/j.jvolgeores.2019.04.008

Kalnay, E., Kanamitsu, M., Kistler, R., Collins, W., Deaven, D., Gandin, L., et al. (1996). The NCEP/NCAR 40-year reanalysis project. *Bull. Am. Meteorol. Soc.* 77, 437–472.

Koller, D., and Friedman, N. (2009). *Probabilistic Graphical Models: Principles And Techniques*. Cambridge, MA: MIT press.

Lacroix, A. (1904). *La Montagne Pelée Et Ses Éruptions*. France: Masson.

Le Corvec, N., Spörli, K. B., Rowland, J., and Lindsay, J. (2013). Spatial distribution and alignments of volcanic centers: clues to the formation of monogenetic volcanic fields. *Earth Sci. Rev.* 124, 96–114. doi: 10.1016/j.earscirev.2013.05.005

Loughlin, S. C., Vye-Brown, C., Sparks, R. S. J., Brown, S. K., Barclay, J., Calder, E., et al. (2015). "An introduction to global volcanic hazard and risk," in *Global Volcanic Hazards And Risk*, eds S. C. Loughlin, R. S. J. Sparks, S. K. Brown, S. F. Jenkins, and C. Vye-Brown (Cambridge: Cambridge University Press), 1–80. doi: 10.1017/cbo9781316276273.003

Maeda, Y., Kumagai, H., Lacson, R., Figueroa, M. S., Yamashina, T., Ohkura, T., et al. (2015). A phreatic explosion model inferred from a very long period seismic event at Mayon Volcano. Philippines. *J. Geophys. Res. Solid Earth* 120, 226–242. doi: 10.1002/2014jb011440

Martin, A. J., Umeda, K., Connor, C. B., Weller, J. N., Zhao, D., and Takahashi, M. (2004). Modeling long-term volcanic hazards through Bayesian inference: an example from the Tohoku volcanic arc, Japan. *J. Geophys. Res. Solid Earth* 109:B10208. doi: 10.1029/2004JB003201

Marzocchi, W., and Bebbington, M. S. (2012). Probabilistic eruption forecasting at short and long time scales. *Bull. Volcanol.* 74, 1777–1805. doi: 10.1007/s00445-012-0633-x

Marzocchi, W., and Jordan, T. H. (2014). Testing for ontological errors in probabilistic forecasting models of natural systems. *Proc. Natl. Acad. Sci. U.S.A.* 111, 11973–11978. doi: 10.1073/pnas.1410183111

Marzocchi, W., Sandri, L., Gasparini, P., Newhall, C., and Boschi, E. (2004). Quantifying probabilities of volcanic events: the example of volcanic hazard at mount vesuvius. *J. Geophys. Res. Solid Earth* 109:B11201. doi: 10.1029/2004JB003155

Marzocchi, W., Sandri, L., and Selva, J. (2008). BET_EF: a probabilistic tool for long-and short-term eruption forecasting. *Bull. Volcanol.* 70, 623–632. doi: 10.1007/s00445-007-0157-y

Marzocchi, W., Sandri, L., and Selva, J. (2010). BET_VH: a probabilistic tool for long-term volcanic hazard assessment. *Bull. Volcanol.* 72, 705–716. doi: 10.1007/s00445-010-0357-8

Mastin, L. G., Guffanti, M., Servranckx, R., Webley, P., Barsotti, S., Dean, K., et al. (2009). A multidisciplinary effort to assign realistic source parameters to models of volcanic ash-cloud transport and dispersion during eruptions. *J. Volcanol. Geotherm. Res.* 186, 10–21. doi: 10.1016/j.jvolgeores.2009.01.008

Mead, S., and Magill, C. (2014). Determining change points in data completeness for the Holocene eruption record. *Bull. Volcanol.* 76:874.

Mead, S. R., and Magill, C. R. (2017). Probabilistic hazard modelling of rain-triggered lahars. *J. Appl. Volcanol.* 6:8.

Naismith, A. K., Watson, I. M., Escobar-Wolf, R., Chigna, G., Thomas, H., Coppola, D., et al. (2019). Eruption frequency patterns through time for the current (1999–2018) activity cycle at Volcán de Fuego derived from remote sensing data: Evidence for an accelerating cycle of explosive paroxysms and potential implications of eruptive activity. *J. Volcanol. Geotherm. Res.* 371, 206–219. doi: 10.1016/j.jvolgeores.2019.01.001

Neri, A., Bevilacqua, A., Esposti Ongaro, T., Isaia, R., Aspinall, W. P., Bisson, M., et al. (2015). Quantifying volcanic hazard at Campi Flegrei caldera (Italy) with uncertainty assessment: 2. Pyroclastic density current invasion maps. *J. Geophys. Res. Solid Earth* 120, 2330–2349. doi: 10.1002/2014jb011776

Newhall, C., and Hoblitt, R. (2002). Constructing event trees for volcanic crises. *Bull. Volcanol.* 64, 3–20. doi: 10.1007/s004450100173

Newhall, C. G. (1982). *A Method For Estimating Intermediate- And Long-Term Risks From Volcanic Activity, With An Example From Mount st. Helens*. Washington, DC: U.S. Geological Society.

Newhall, C. G., Costa, F., Ratdomopurbo, A., Venezky, D. Y., Widiwijayanti, C., Win, N. T. Z., et al. (2017). WOVOdat–an online, growing library of worldwide

volcanic unrest. *J. Volcanol. Geotherm. Res.* 345, 184–199. doi: 10.1016/j.jvolgeores.2017.08.003

Newhall, C. G., and Pallister, J. S. (2015). "Using multiple data sets to populate probabilistic volcanic event trees," in *Volcanic Hazards, Risks, Disasters*, eds P. Papale, J. C. Eichelberger, S. Nakada, S. Loughlin, and H. Yepes (Amsterdam: Elsevier), 203–232. doi: 10.1016/b978-0-12-396453-3.00008-3

Newhall, C. G., and Punongbayan, R. S. (1996). *Fire and Mud: Eruptions And Lahars Of Mount Pinatubo, Philippines*. Seattle: University of Washington Press.

Ogburn, S. E. (2012). *FlowDat: Mass Flow Database*. Available online at: https://vhub.org/groups/massflowdatabase (accessed November 24, 2019).

Ogburn, S. E., Berger, J., Calder, E. S., Lopes, D., Patra, A., Pitman, E. B., et al. (2016a). Pooling strength amongst limited datasets using hierarchical Bayesian analysis, with application to pyroclastic density current mobility metrics. *Stat. Volcanol.* 2:1. doi: 10.5038/2163-338x.2.1

Ogburn, S. E., Harpel, C. J., Pesicek, J. D., and Wellik, J. (2016b). *The Eruption Forecasting Information System: Volcanic Eruption Forecasting Using Databases*. Washington, DC: American Geophysical Union.

Ogburn, S. E., Loughlin, S. C., and Calder, E. S. (2015). The association of lava dome growth with major explosive activity (VEI $\geq$ 4): DomeHaz, a global dataset. *Bull. Volcanol.* 77:40.

Orsi, G., Di Vito, M. A., and Isaia, R. (2004). Volcanic hazard assessment at the restless campi flegrei caldera. *Bull. Volcanol.* 66, 514–530. doi: 10.1007/s00445-003-0336-4

Orsi, G., Di Vito, M. A., Selva, J., and Marzocchi, W. (2009). Long-term forecast of eruption style and size at Campi Flegrei caldera (Italy). *Earth Planet. Sci. Lett.* 287, 265–276. doi: 10.1016/j.epsl.2009.08.013

Pallister, J., Papale, P., Eichelberger, J., Newhall, C., Mandeville, C., Nakada, S., et al. (2019). Volcano observatory best practices (VOBP) workshops-a summary of findings and best-practice recommendations. *J. Appl. Volcanol.* 8:2.

Palma, J. L., Courtland, L., Charbonnier, S., Tortini, R., and Valentine, G. A. (2014). Vhub: a knowledge management system to facilitate online collaborative volcano modeling and research. *J. Appl. Volcanol.* 3:2.

Papale, P. (2018). Global time-size distribution of volcanic eruptions on Earth. *Sci. Rep.* 8:6838.

Passarelli, L., and Brodsky, E. E. (2012). The correlation between run-up and repose times of volcanic eruptions. *Geophys. J. Int.* 188, 1025–1045. doi: 10.1111/j.1365-246x.2011.05298.x

Patra, A. K., Bauer, A. C., Nichita, C. C., Pitman, E. B., Sheridan, M. F., Bursik, M., et al. (2005). Parallel adaptive numerical simulation of dry avalanches over natural terrain. *J. Volcanol. Geotherm. Res.* 139, 1–21. doi: 10.1016/j.jvolgeores.2004.06.014

R Core Team (2013). *R: A Language and Environment for Statistical Computing*. Geneva: R Core Team.

Reed, C. (2002). *Mount Pelée, Martinique 1902-2002*. Croatia: Geotimes.

Rivalta, E., Corbi, F., Passarelli, L., Acocella, V., Davis, T., and Di Vito, M. A. (2019). Stress inversions to forecast magma pathways and eruptive vent location. *Sci. Adv.* 5:eaau9784. doi: 10.1126/sciadv.aau9784

Rougier, J., Sparks, R. S. J., Cashman, K. V., and Brown, S. K. (2018). The global magnitude–frequency relationship for large explosive volcanic eruptions. *Earth Planet. Sci. Lett.* 482, 621–629. doi: 10.1016/j.epsl.2017.11.015

Rougier, J., Sparks, S. R., and Cashman, K. V. (2016). Global recording rates for large eruptions. *J. Appl. Volcanol.* 5:11.

Rougier, J. C., and Beven, K. J. (2013). "Model limitations: the sources and implications of epistemic uncertainty," in *Risk and Uncertainty Assessessment for Natural Hazards*, eds J. C. Rougier, R. S. J. Sparks, and L. J. Hill (Cambridge: Cambridge University Press), 40–63. doi: 10.1017/cbo9781139047562.004

Rouwet, D., Constantinescu, R., and Sandri, L. (2017). "). Deterministic versus probabilistic volcano monitoring: not 'or' but 'and'. volcanic unrest," in *Advances in Volcanology*, eds J. Gottsmann, J. Neuberg, and B. Scheu (Cham: Springer), 35–46. doi: 10.1007/11157_2017_8

Runge, M. G., Bebbington, M. S., Cronin, S. J., Lindsay, J. M., and Moufti, M. R. (2016). Integrating geological and geophysical data to improve probabilistic hazard forecasting of Arabian Shield volcanism. *J. Volcanol. Geotherm. Res.* 311, 41–59. doi: 10.1016/j.jvolgeores.2016.01.007

Rutarindwa, R., Spiller, E. T., Bevilacqua, A., Bursik, M. I., and Patra, A. K. (2019). Dynamic probabilistic hazard mapping in the long valley volcanic region CA: integrating vent opening maps and statistical surrogates of physical models of pyroclastic density currents. *J. Geophys. Res. Solid Earth.* 124, 9600–9621. doi: 10.1029/2019jb017352

Sandri, L., Costa, A., Selva, J., Tonini, R., Macedonio, G., Folch, A., et al. (2016). Beyond eruptive scenarios: assessing tephra fallout hazard from Neapolitan volcanoes. *Sci. Rep.* 6:24271.

Sandri, L., Jolly, G., Lindsay, J., Howe, T., and Marzocchi, W. (2012). Combining long-and short-term probabilistic volcanic hazard assessment with cost-benefit analysis to support decision making in a volcanic crisis from the Auckland Volcanic Field, New Zealand. *Bull. Volcanol.* 74, 705–723. doi: 10.1007/s00445-011-0556-y

Sandri, L., Thouret, J.-C., Constantinescu, R., Biass, S., and Tonini, R. (2014). Long-term multi-hazard assessment for El Misti volcano (Peru). *Bull. Volcanol.* 76, 1–26.

Sandri, L., Tierz, P., Costa, A., and Marzocchi, W. (2018). Probabilistic hazard from pyroclastic density currents in the neapolitan Area (Southern Italy). *J. Geophys. Res. Solid Earth* 123:890. doi: 10.1002/2017JB014890

Selva, J., Costa, A., Sandri, L., Macedonio, G., and Marzocchi, W. (2014). Probabilistic short-term volcanic hazard in phases of unrest: a case study for tephra fallout. *J. Geophys. Res. Solid Earth* 119, 8805–8826. doi: 10.1002/2014jb011252

Selva, J., Marzocchi, W., Papale, P., and Sandri, L. (2012a). Operational eruption forecasting at high-risk volcanoes: the case of Campi Flegrei, Naples. *J. Appl. Volcanol.* 1:5.

Selva, J., Orsi, G., Di Vito, M. A., Marzocchi, W., and Sandri, L. (2012b). Probability hazard map for future vent opening at the campi flegrei caldera, Italy. *Bull. Volcanol.* 74, 497–510. doi: 10.1007/s00445-011-0528-2

Sheldrake, T. (2014). Long-term forecasting of eruption hazards: a hierarchical approach to merge analogous eruptive histories. *J. Volcanol. Geotherm. Res.* 286, 15–23. doi: 10.1016/j.jvolgeores.2014.08.021

Sheldrake, T., and Caricchi, L. (2017). Regional variability in the frequency and magnitude of large explosive volcanic eruptions. *Geology* 45, 111–114. doi: 10.1130/g38372.1

Sheldrake, T. E., Sparks, R. S. J., Cashman, K. V., Wadge, G., and Aspinall, W. P. (2016). Similarities and differences in the historical records of lava dome-building volcanoes: Implications for understanding magmatic processes and eruption forecasting. *Earth-Science Rev.* 160, 240–263. doi: 10.1016/J.EARSCIREV.2016.07.013

Siebert, L., and Simkin, T. (2002). *Volcanoes of the World: an Illustrated Catalog of Holocene Volcanoes and their Eruptions. Smithsonian Inst, Global Volcanism Prog Digital Inf Ser GVP-3*. Available online at: http://www.volcano.si.edu (accessed May 8, 2018).

Siebert, L., Simkin, T., and Kimberly, P. (2010). *Volcanoes of The World*. Berkeley: University of California Press.

Sobradelo, R., Bartolini, S., and Martí, J. (2014). HASSET: a probability event tree tool to evaluate future volcanic scenarios using Bayesian inference. *Bull. Volcanol.* 76:770.

Sobradelo, R., and Martí, J. (2010). Bayesian event tree for long-term volcanic hazard assessment: application to Teide-Pico Viejo stratovolcanoes, Tenerife, Canary Islands. *J. Geophys. Res. Solid Earth* 115:B05206. doi: 10.1029/2009JB006566

Sobradelo, R., Martí, J., Mendoza-Rosas, A. T., and Gómez, G. (2011). Volcanic hazard assessment for the Canary Islands (Spain) using extreme value theory. *Nat. Hazards Earth Syst. Sci.* 11, 2741–2753. doi: 10.5194/nhess-11-2741-2011

Sparks, R. S. J. (2003). Forecasting volcanic eruptions. *Earth Planet. Sci. Lett.* 210, 1–15.

Spiller, E. T., Bayarri, M. J., Berger, J. O., Calder, E. S., Patra, A. K., Pitman, E. B., et al. (2014). Automating emulator construction for geophysical hazard maps. *SIAM/ASA J. Uncertain. Quantif.* 2, 126–152. doi: 10.1137/120899285

Stefanescu, E. R., Bursik, M., Cordoba, G., Dalbey, K., Jones, M. D., Patra, A. K., et al. (2012a). Digital elevation model uncertainty and hazard analysis using a geophysical flow model. *Proc. R. Soc. Math. Phys. Eng. Sci.* 468, 1543–1563. doi: 10.1098/rspa.2011.0711

Stefanescu, E. R., Bursik, M., and Patra, A. K. (2012b). Effect of digital elevation model on Mohr-Coulomb geophysical flow model output. *Nat. Hazards* 62, 635–656. doi: 10.1007/s11069-012-0103-y

Tadini, A., Bevilacqua, A., Neri, A., Cioni, R., Aspinall, W. P., Bisson, M., et al. (2017). Assessing future vent opening locations at the Somma-Vesuvio volcanic complex: 2. Probability maps of the caldera for a future Plinian/sub-Plinian

event with uncertainty quantification. *J. Geophys. Res. Solid Earth* 122, 4357–4376. doi: 10.1002/2016jb013860

Takarada, S. (2017). The volcanic hazards assessment support system for the online hazard assessment and risk mitigation of quaternary volcanoes in the world. *Front. Earth Sci.* 5:102. doi: 10.3389/feart.2017.00102

Thompson, M. A., Lindsay, J. M., Sandri, L., Biass, S., Bonadonna, C., Jolly, G., et al. (2015). Exploring the influence of vent location and eruption style on tephra fall hazard from the Okataina Volcanic Centre. *New Zeal. Bull. Volcanol.* 77:38.

Tierz, P., Loughlin, S. C., and Calder, E. S. (2019). VOLCANS: an objective, structured and reproducible method for identifying sets of analogue volcanoes. *Bull. Volcanol.* 81:76. doi: 10.1007/s00445-019-1336-3

Tierz, P., Sandri, L., Costa, A., Sulpizio, R., Zaccarelli, L., Vito, M. A. D., et al. (2016a). "Uncertainty assessment of pyroclastic density currents at mount vesuvius (italy) simulated through the energy cone model," in *Natural Hazard Uncertainty Assessment: Modeling and Decision Support*, eds P. Webley, K. Riley, and M. P. Thompson (Hoboken: John Wiley & Sons), 125–145. doi: 10.1002/9781119028116.ch9

Tierz, P., Sandri, L., Costa, A., Zaccarelli, L., Di Vito, M. A., Sulpizio, R., et al. (2016b). Suitability of energy cone for probabilistic volcanic hazard assessment: validation tests at Somma-Vesuvius and campi flegrei (Italy). *Bull. Volcanol.* 78:1073. doi: 10.1007/s00445-016-1073-9

Tierz, P., Stefanescu, E. R., Sandri, L., Sulpizio, R., Valentine, G. A., Marzocchi, W., et al. (2018). Towards quantitative volcanic risk of pyroclastic density currents: probabilistic hazard curves and maps around Somma-Vesuvius (Italy). *J. Geophys. Res. Solid Earth* 123:383. doi: 10.1029/2017JB015383

Tierz, P., Woodhouse, M. J., Phillips, J. C., Sandri, L., Selva, J., Marzocchi, W., et al. (2017). A framework for probabilistic multi-hazard assessment of rain-triggered lahars using bayesian belief networks. *Front. Earth Sci.* 5:73. doi: 10.3389/feart.2017.00073

Tonini, R., Sandri, L., and Thompson, M. A. (2015). PyBetVH: a python tool for probabilistic volcanic hazard assessment and for generation of Bayesian hazard curves and maps. *Comput. Geosci.* 79, 38–46. doi: 10.1016/j.cageo.2015.02.017

Trolese, M., Cerminara, M., Ongaro, T. E., and Giordano, G. (2019). The footprint of column collapse regimes on pyroclastic flow temperatures and plume heights. *Nat. Commun.* 10:2476.

Volentik, A. C. M., Connor, C. B., Connor, L. J., and Bonadonna, C. (2009). "Aspects of volcanic hazard assessment for the bataan nuclear power plant, luzon Peninsula, Philippines," in *Volcanic and Tectonic Hazard Assessment for Nuclear Facilities*, eds C. Connor, N. Chapman, and L. Connor (New York, NY: Cambridge University Press), 229–256. doi: 10.1017/cbo9780511635380.010

Vye-Brown, C., Sparks, R. S. J., Lewi, E., Mewa, G., Asrat, A., Loughlin, S. C., et al. (2016). Ethiopian volcanic hazards: a changing research landscape. *Geol. Soc. Lond. Spec. Publ.* 420, 355–365. doi: 10.1144/sp420.16

Wadge, G., Young, P. A. V., and McKendrick, I. J. (1994). Mapping lava flow hazards using computer simulation. *J. Geophys. Res. Solid Earth* 99, 489–504. doi: 10.1029/93jb01561

Whelley, P. L., Newhall, C. G., and Bradley, K. E. (2015). The frequency of explosive volcanic eruptions in Southeast Asia. *Bull. Volcanol.* 77:1.

Williams, R., Rowley, P., and Garthwaite, M. C. (2019). Reconstructing the Anak Krakatau flank collapse that caused the December 2018 Indonesian tsunami. *Geology* 47, 973–976. doi: 10.1130/g46517.1

Wolpert, R. L., Spiller, E. T., and Calder, E. S. (2018). Dynamic statistical models for pyroclastic density current generation at Soufrière Hills Volcano. *Front. Earth Sci.* 6:55. doi: 10.3389/feart.2018.00055

Woo, G. (1999). *The Mathematics of Natural Catastrophes*. London: Imperial College Press.

Conflict of Interest: The author declares that the research was conducted in the absence of any commercial or financial relationships that could be construed as a potential conflict of interest.

frontiers in Earth Science

ORIGINAL RESEARCH
published: 24 March 2021
doi: 10.3389/feart.2020.510514

Water Vapor Tomography of the Lower Atmosphere from Multiparametric Inversion: the Mt. Etna Volcano Test Case

Massimo Aranzulla[1], *Claudia Spinetti*[2]*, *Flavio Cannavò*[1], *Vito Romaniello*[2], *Francesco Guglielmino*[1], *Giuseppe Puglisi*[1] *and Pierre Briole*[1,3]

[1]*Istituto Nazionale di Geofisica e Vulcanologia, OE, Catania, Italy,* [2]*Istituto Nazionale di Geofisica e Vulcanologia, ONT, Roma, Italy,* [3]*Ecole Normale Supérieure–PSL Research University–UMR CNRS 8538, Paris, France*

Space techniques based on GPS and SAR interferometry allow measuring millimetric ground deformations. Achieving such accuracy means removing atmospheric anomalies that frequently affect volcanic areas by modeling the tropospheric delays. Due to the prominent orography and the high spatial and temporal variability of weather conditions, the active volcano Mt. Etna (Italy) is particularly suitable to carry out research aimed at estimating and filtering atmospheric effects on GPS and DInSAR ground deformation measurements. The aim of this work is to improve the accuracy of the ground deformation measurements by modeling the tropospheric delays at Mt. Etna volcano. To this end, data from the monitoring network of 29 GPS permanent stations and MODIS multispectral satellite data series are used to reproduce the tropospheric delays affecting interferograms. A tomography algorithm has been developed to reproduce the wet refractivity field over Mt. Etna in 3D, starting from the slant tropospheric delays calculated by GPS in all the stations of the network. The developed algorithm has been tested on a synthetic atmospheric anomaly. The test confirms the capability of the software to faithfully reconstruct the simulated anomaly. With the aim of applying this algorithm to real cases, we introduce the water vapor content measured by the MODIS instrument on board Terra and Aqua satellites. The use of such data, although limited by cloud cover, provides a two-fold benefit: it improves the tomographic resolution and adds feedback for the GPS wet delay measurements. A cross-comparison between GPS and MODIS water vapor measurements for the first time shows a fair agreement between those indirect measurements on an entire year of data (2015). The tomography algorithm was applied on selected real cases to correct the Sentinel-1 DInSAR interferograms acquired over Mt. Etna during 2015. Indeed, the corrected interferograms show that the differential path delay reaches 0.1 m (i.e. 3 C-band fringes) in ground deformation, demonstrating how the atmospheric anomaly affects precision and reliability of DInSAR space-based techniques. The real cases show that the tomography is often able to capture the atmospheric effect at the large scale and correct interferograms, although in limited areas. Furthermore, the introduction of MODIS data significantly improves by ~80% voxel resolution at the critical layer (1,000 m). Further improvements will be suitable for monitoring active volcanoes worldwide.

Keywords: tomography, GPS, etna, earth observation data, SAR, water vapor

OPEN ACCESS

Edited by:
Michelle Parks,
Icelandic Meteorological Office, Iceland

Reviewed by:
Giovanni Nico,
Istituto Per Le Applicazioni Del Calcolo "Mauro Picone", Italy
Halldor Geirsson,
University of Iceland, Iceland

***Correspondence:**
Claudia Spinetti
claudia.spinetti@ingv.it

Specialty section:
This article was submitted to Volcanology, a section of the journal Frontiers in Earth Science

Received: *06 November 2019*
Accepted: *24 December 2020*
Published: *24 March 2021*

Citation:
Aranzulla M, Spinetti C, Cannavò F, Romaniello V, Guglielmino F, Puglisi G and Briole P (2021) Water Vapor Tomography of the Lower Atmosphere from Multiparametric Inversion: the Mt. Etna Volcano Test Case. Front. Earth Sci. 8:510514. doi: 10.3389/feart.2020.510514

INTRODUCTION

Measurements of ground displacements play a key role for understanding geophysical processes, especially in active volcanic areas. In volcano geodesy, the global positioning system (GPS) is widely used for this purpose in combination with the differential interferometry synthetic aperture radar (DInSAR) technique. The interferograms are obtained through the difference between two SAR images acquired in two different periods with the same viewing geometry. Expressed in values of phase rotation of the backscattered radar wave, they are the measurement of the differential path delays in the line of sight (LOS), imaged according to a grid related to the sampling frequency (Ulabay et al., 1981; Massonnet et al., 1993). The differential phase can be estimated with an accuracy of a few degrees; therefore, DInSAR can measure differential propagation delay with millimetric accuracy as in the case of the C-band synthetic aperture radars of the European Sentinel-1 satellites. Changes in the delays can be due to ground deformation, changes in the path delay in the troposphere, or other causes. When using DInSAR to measure ground deformations, the tropospheric delay is in general the most significant effect and the most difficult to correct (Zebker et al., 1997; Delacourt et al., 1998; Williams et al., 1998). It is an integrated function of pressure, temperature, and humidity along the ray path. In the domain of X-band, C-band, L-band, and GPS signals, it does not depend on the frequency. GPS has amply demonstrated to be applicable to measure the integrated amount of water vapor in the atmosphere (Bevis et al., 1992; Tregoning et al., 1998; Gradinarsky and Jarlemark, 2004; Nilsson and Elgered, 2007; Champollion et al., 2009; Notarpietro et al., 2011; Chen and Liu, 2014; Benevides et al., 2015b; Benevides et al., 2016). Yuval et al. (2015) propose the use of dense regional GPS networks for extracting tropospheric zenith delays and ionospheric total electron content maps in order to produce tropospheric and ionospheric correction maps, respectively, for InSAR images. By measuring the integrated amount of water vapor in several directions from a number of locations in a local GPS network, it is possible to estimate the 3-D structure of the atmospheric water vapor by applying a tomographic method. This technique is known as GPS tomography (e.g., Flores et al., 2001; Champollion et al., 2009). Different works have described GPS tomography experiments aimed at sounding the atmosphere in time, that is, 4-D tomography (Flores et al., 2000; Perler et al., 2011; Benevides et al., 2018). Others have considered additional measurements (e.g., remote sensing data from different types of satellites or different constellations) to enhance the accuracy of the tomography (e.g., Benevides et al., 2015a; Heublein et al., 2019; Zhao et al., 2019). The orography of the studied area plays a key role in the resolution capabilities of the technique (Flores et al., 2001).

Here, we focus on the case of Mt. Etna volcano (Italy). This high volcano (more than 3,300 m a.s.l.) has a prominent and complex topography. With the Mediterranean Sea to the east and exposed to dominant winds from/on the west, it has varying microclimates on its different flanks. Several studies have been carried out on Mt. Etna to estimate and correct the tropospheric delay in SAR interferograms, using various approaches: 1) empirical data to predict atmospheric conditions through numerical models (Delacourt et al., 1998; Webley et al., 2004), 2) use of the relation between InSAR phase and elevation (Beauducel et al., 2000), 3) use of the tropospheric delays derived from GPS analysis (Wadge et al., 2002; Aranzulla and Puglisi, 2015).

In this work, for the first time, an entire year of GPS tropospheric delays has been combined with integrated water vapor contents measured with MODIS instruments on board Terra and Aqua satellites in order to calculate the tropospheric spatial and temporal variability delay. The use of MODIS data in the tomographic modeling of the troposphere has proved to be fruitful by Benevides et al., 2015a. However, in this study, we expand this approach in very harsh experimental conditions dominated by the prominent topography of Mt. Etna. The Earth Observation (EO) data are the only ones that can be systematically used for water vapor content measurements over Mt. Etna. Following Kämpfer (2012), operational techniques for water vapor retrievals include ground-based instruments (microwave radiometer, Sun photometer, Lidar, and FTIR spectrometer), *in situ* methods (radiosonde and airborne instruments), and remote sensing (IR, and visible and microwave sensors). This last technique allows global coverage, but no retrievals can be obtained during cloudy and rainy weather (for visible and IR sensors) or over land (for microwave sensors). During a series of weather conditions, it was recognized that the coverage by terrestrial measurements is insufficient to correctly characterize the three-dimensional water vapor field (Bernot et al., 2014). Moreover, in the case of Mt. Etna, *in situ* radiosonde data are not available, and the closest daily soundings are performed at Trapani, 220 km to the west of Mt. Etna (Wadge et al., 2002).

The fact that the SAR satellites are side-looking radar makes the need for accurate tropospheric tomography more critical than the case of radar systems measuring at nadir where the lateral heterogeneities require only along track correction. In DInSAR, the radar observes the scene through an off-nadir angle ranging between 20° and 40°, depending on the satellite system used. Starting from the previous studies (Bonforte et al., 2001; Bruno et al., 2007; Aranzulla and Puglisi, 2015), we propose a refined method to obtain an accurate tomography of the lower troposphere, specifically tied to the delays measured by the network of permanent GPS stations deployed around Mt. Etna. We use an algorithm commonly used in tomography based on linear regularized least squares (RLS) (Tarantola, 2005) to which we add an adaptive step to tune the algorithm automatically and verify the tomography outcomes with DInSAR data.

In the following, we first present the method to obtain the 3-D refractivity field, and then the GPS analysis data and the MODIS integration to obtain the tropospheric delay along any line of sight, followed by the result and the comparison with Sentinel-1A interferograms, from May to November 2015.

THEORETICAL BACKGROUND AND METHODS

The Refractivity

The refractive index n is a dimensionless complex number that characterizes the velocity of light through a material. It is the factor by which the speed of the radiation is reduced, at a given wavelength, with respect to its speed in the vacuum. Its real part corresponds to the propagation delay through the material, and its imaginary part corresponds to the amount of absorption loss. Its value depends on the frequency of the considered wave. For the atmosphere, the highest values of n are reached for waves between 50 and 70 GHz, and it remains almost constant for waves below 20 GHz (Karmakar, 2017; Balal and Pinhasi, 2019). In the domain of space geodetic instruments (below 20 GHz), the refractivity index can then be considered frequency independent. The absorption does not significantly affect the propagation delay in GPS and DInSAR, and it can be neglected (Curlander and McDonough, 1991; Hofmann-Wellenhof et al., 2001). The refractive index n in the atmosphere assumes values very close to 1; thus, it is usually replaced by the so-called refractivity N which represents the departure of the refractive index n from unity, expressed in parts per million:

$$N = 10^6 (n - 1) \tag{1}$$

In the neutral atmosphere (i.e., excluding the effects of charged particles), the real part of the refractivity N is a function of temperatures and densities of atmospheric gases (Debye, 1929; Essen and Froome, 1951). The refractivity applied to GPS signal has the following expression (Rueger, 2002a; Rueger, 2002b; Healy, 2011):

$$N = k_1 \frac{p_d}{T} + k_2 \frac{p_w}{T} + k_3 \frac{p_w}{T^2} = N_h + N_w \tag{2}$$

where p_d is the total pressure of dry air (expressed in [hPa]), T the atmospheric temperature (expressed in [K]), p_w the partial pressure of water vapor (expressed in [hPa]), and k_1, k_2, and k_3 the empirical constants determined in the literature by laboratory measurements (Thayer, 1974; Hill et al., 1982; Bevis et al., 1994; Rueger 2002a; Rueger, 2002b). For k_2 and k_3, we use the numerical values of 71.2952 K/hPa and 375463 K^2/hPa, respectively (Rueger 2002a). The value of k_1 = 77.6904 K/hPa was computed assuming the worst 2015 level of carbon dioxide concentration of 400 ppm. N_h and N_w are named hydrostatic refractivity and wet refractivity, respectively. The hydrostatic refractivity N_h depends only on the total density of dry air, while the wet refractivity N_w depends on the partial pressure of water vapor and the temperature. As the liquid water droplets are very small (usually below 1 mm) compared to the GPS wavelength (about 20 cm), their contribution to the refractivity can be neglected even during heavy rains (Solheim et al., 1999).

The Slant Path Delay

The optical path of an electromagnetic (EM) microwave in a neutral heterogeneous medium, in the absence of free charges, like the troposphere, is obtained from Maxwell equations considering the spatial component of the wave (Helmholtz's equation), which yields the Eikonal equation (Nilsson et al., 2013). The solution of the Eikonal equation therefore corresponds to a geometric description of the propagation of the wave. The slant path delay (*SPD*) is the difference between the travel time of a signal from a satellite to a ground-based receiver and the travel time that would occur if there were no atmosphere affecting the signal propagation (Bevis et al., 1992; Hofmann-Wellenhof et al., 2001). Considering that we can express the delays in terms of variations in path length by dividing them for the EM velocity, the *SPD* can be formulated as the following:

$$SPD = \int_s [n(s) - 1] ds + [S - G] \tag{3}$$

where s is the actual path of the EM wave through the atmosphere and n is the atmospheric refractive index, S is the geometric length of the actual propagation path of the ray (Fermat principle path), and G is the geometric length of the straight path of the ray (vacuum path). The first term is due to the slowing effect, and the second term is due to bending, which for an elevation angle greater than 15° can be neglected (Ichikawa et al., 1995; Hofmann-Wellenhof et al., 2001). We can use the straight ray path and a linear inversion, which simplifies the tomographic problem. Combining the **Eqs. 1**–**3**, the *SPD* can be expressed with the following equation:

$$SPD = 10^{-6} \int_s N ds = 10^{-6} \int_s (\mathrm{N_h} + \mathrm{N_w}) ds = SDD + SWD \tag{4}$$

where *SDD* and *SWD* are "slant dry delay" and "slant wet delay," respectively. The *SWD* is caused by tropospheric water vapor along the ray path, and *SDD* (larger than the *SWD*) by all other atmospheric constituents (Rocken et al., 1995). The *SDD* can be accurately modeled by using the pressure and temperature at the ground level and the altitude of the ground (Hopfield, 1969). The *SWD* is much more variable in time and space and is therefore complicated to model accurately. For these reasons, here we assume that we can estimate the *SDD*, and thus we consider the *SWD* observables only to compute the wet refractivity tomography.

The Tomography Algorithm

The algorithm to calculate the tomography consists of different steps summarized in the block diagram of **Figure 1**. The first step is the tomographic geometry setup. Three key elements are considered: the GPS satellites, the receivers on the Earth surface, and the volume of the atmosphere whose refractivity we aim to investigate. The tomographic volume is discretized into a number of boxes (voxel parameterization) in which the refractivity is considered constant. According to **Eq. 4**, the *i-th* wet refractivity delay amount along the ray of the satellite–receiver pair can be described by linear combination of the crossed voxels refractivity.

$$SWD_\mathrm{i} = 10^{-6} \sum_{j=1}^{n_{vox}} A_{ij} (N_w)_j \tag{5}$$

where SWD_i is the wet delay of the *i-th* receiver–satellite pair, n_{vox} is the number of voxels, A_{ij} is the length of the *i-th* ray in the *j-th*

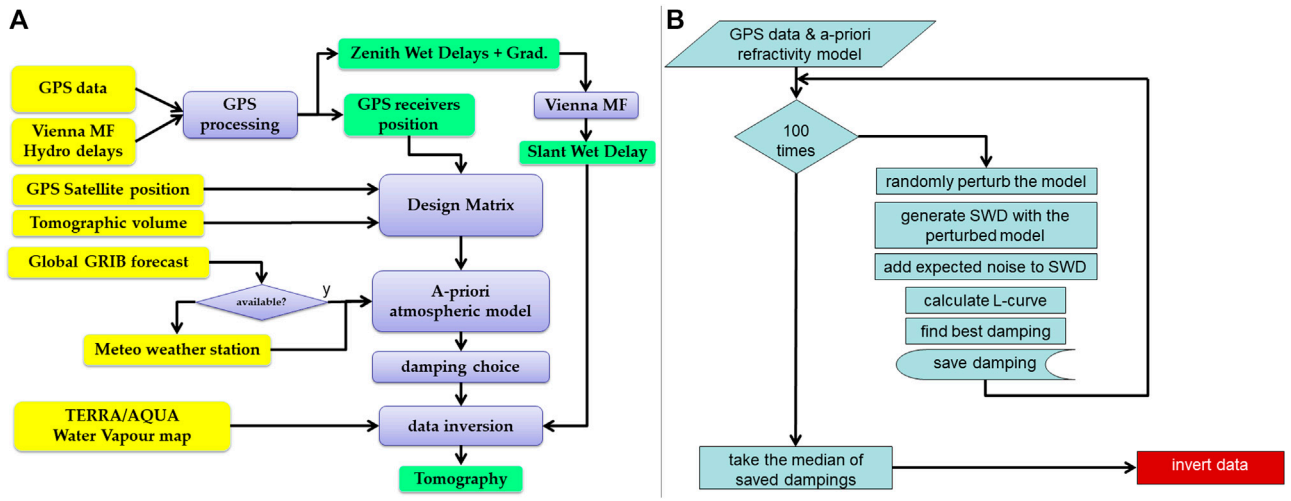

FIGURE 1 | (A) Block diagram of the processing chain. In yellow, the blocks with external data; in violet, the processing blocks; in green, the blocks with calculated parameters from GPS and the block of final inversion for tomography calculation. **(B)** Zoom of the "damping choice" block: flow diagram of the algorithm to estimate a damping factor for a robust tomography. The damping factor followed an iterative process: for each iteration, we selected the best damping factor (by L-curve) to reconstruct a randomly perturbed model where real measured noise was added. The single L-curve was calculated in a fixed set of 10 damping values. At the end of the process, the damping factor used for the real data inversion was the median of the ones obtained from the iterations.

voxel, and $(N_w)_j$ represents the wet refractivity value of the *j-th* voxel. Summarizing the entire system of equations in a matrix form, the following can be written:

$$SWD = 10^{-6} A N_w \tag{6}$$

Although the number of rays crossing the voxels exceeds the number of unknowns, the linear system in **Eq. 6** is usually underdetermined. This is so because, for example, a voxel in the grid may not be crossed and thus be undetermined. Then, we introduce a regularization process, namely, damped least squares approach (Tarantola, 2005), that minimizes the following cost function:

$$\left|SWD - 10^{-6} A N_w\right|^2 + \gamma \left|10^{-6} N_w\right|^2 \tag{7}$$

Minimizing the first term of the cost function (7) gives the model that better fits the data in the least-squares sense. The regularization term, although introducing biases in solutions, penalizes large solution values; reduces variance, the mean square error; and helps improve the prediction accuracy.

The "damping-factor" γ controls the reduction of variance against an increase of bias (Tarantola, 2005). The damped least square has a closed form solution given by:

$$10^{-6} N_w = \left(A^T A + \gamma I\right)^{-1} A^T SWD \tag{8}$$

Where I is the identity matrix.

The most important part in the data inversion algorithm is the choice of the best damping factor that balances solution variance and bias, given the available data.

The "damping-factor" is usually set empirically, by running a series of single iteration inversions aimed at exploring a wide range of damping values, and plotting data misfit vs. model variance L-curve method (Tarantola, 2005; Hirahara, 2000). To make this choice robust to data changes, a Monte Carlo sampling was introduced in the inversion algorithm (see **Figure 1B**). In particular, for an inversion, 100 synthetic cases are produced at first. Each case consists of a new model generated from the actual *a priori* model by randomly selecting half of the voxels and modifying the refractivity by superimposing random values whose standard deviation is 10% of their *a priori* refractivity values (hence, simulating sparse anomalies, difficult to retrieve). For each of the new models, new GPS data are simulated. The simulated data are then added with a Gaussian noise with standard deviation of the same order of magnitude as the associated uncertainties of current measurements. The best damping factor for each synthetic case is retrieved as the coefficient with the minimum residual norm and the minimum norm of refractivity model which corresponds to the point with maximum curvature on the L-curve (Hirahara, 2000; Tarantola, 2005). The final damping factor is chosen as the median of the best factors retrieved from the synthetic cases. This choice allows us to avoid extreme scattered solutions and make solutions robust against changes in data, either GPS network configuration and/or measurement uncertainties, as shown in Aranzulla and Puglisi, 2015.

The N_w refractivity values were finally selected by the method of Toomey and Foulger (1989) and for the Mt. Etna test site (Aranzulla and Puglisi, 2015).

The Atmospheric Model

The atmospheric *a priori* model we use is divided into layers where atmospheric refractivity varies only with the altitude. In ideal experimental conditions, we can initialize the tomographic model, by computing the refractivity at an arbitrary altitude using the atmospheric measurements of weather balloons, through **Eq. 2**. In the case of Mt. Etna, the radiosonde data performed in

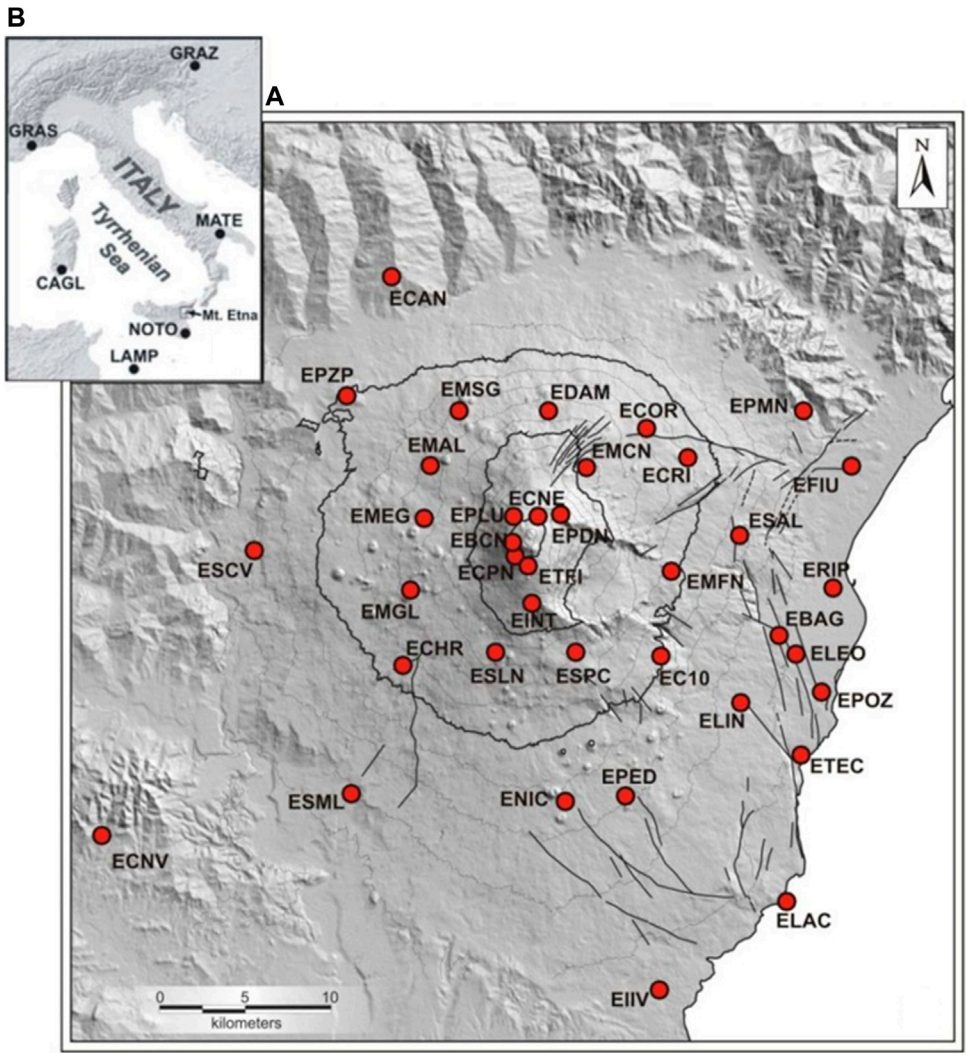

FIGURE 2 | (A) The permanent GPS stations over Mt. Etna volcano. 1,000 m contour lines are shown. **(B)** IGS stations included in the International Terrestrial Reference Frame (ITRF).

Trapani station are therefore not suitable to describe the actual atmosphere around the volcano, which is located too far away. To overcome this problem, we used two strategies, depending on the data availability for the studied period. For this study, we use the NCEP GFS 0.25° global forecast grid historical archive (NOAA http://dx.doi.org/10.5065/D65D8PWK). In particular, we extract the parameters of **Eq. 2** relevant to the 26 physical levels of the NCEP GFS grids, and compute the refractivity at each altitude by averaging the values of adjacent pixels within the investigation volume. However, if NCEP GFS grids are not available, the model is able to predict T, p_d, and p_w at any altitude, and then compute the refractivity profile for the *a priori* model of atmospheric refractivity, starting from the atmospheric measurements of pressure (p_0), temperature (T_0), and relative humidity (H_0) at the ground level (Saastamoinen 1972a; Saastamoinen, 1972b). Since we cannot exactly know p_w at a defined elevation, we estimated a variation range for that value. Since the highest value of p_w at each height corresponds to the saturated water vapor pressure, we can consider the two extreme cases: the first, called dry condition (which estimates the hydrostatic refractivity N_h) and the second, called saturated condition (which estimates the $N_h + N_{w(saturated)}$ term of refractivity). Thus, it is possible to calculate the refractivity and consequently the propagation velocity corresponding to different heights from sea level, for the two limit conditions: dry and saturated. Consequently, we are able to evaluate whether or not the refractivity tomography results are physically acceptable solutions.

The Global Positioning System Measurements

Since 2000, a continuous GPS array has operated to monitor the ground deformations of Mt. Etna volcano (Palano et al., 2010). The actual array consists of 42 stations that provide a dense coverage of the volcano (**Figure 2**).

Among the whole GPS array, we used a subset of 29 stations where a full data archive is available for the studied period (2015). The stations are equipped with low-multipath choke-ring antennas, and we apply elevation-dependent corrections for the antenna phase centers (Schmid et al., 2005). We processed the GPS data using the GAMIT package developed by the Massachusetts Institute of Technology (Herring et al., 2010). This software uses double-differenced GPS phase observations to estimate for each observing span (in our case 24 h) a single set of station coordinates and orbital parameters together with piecewise linear models of zenith tropospheric delay (ZTD) and gradients at each station. Standard models for precession, nutation, Earth rotation, and solid Earth and ocean tides are applied (IERS Conventions). The motions of the GPS satellites are taken from the Final Orbits of the International GNSS Service (https://www.igs.org/), which typically have an accuracy of ~2 cm. We processed our data with the data from six surrounding IGS stations (**Figure 2**), used as reference stations to tie our network to the International Terrestrial Reference Frame (ITRF). Although GAMIT's output separately provides dry and wet tropospheric delay, caused by the high spatial and temporal variability, only the wet component is important for our purposes (**Figure 1A**). Zenith wet delay (ZWD) is estimated during the GPS processing by assuming a 2-h interval and interpolated through time by a spline approach. Then, the delay along the line of sight between the station and the satellite, slant wet delay (SWD), is computed by properly mapping the zenith wet delay (ZWD) through the so-called Vienna Mapping Function 1 (VMF1) which improves the quality of GPS solutions (Boehm et al., 2006). This estimation process is overall summarized as "Vienna MF" in **Figure 1A**. We included only data with elevation angle above 15° in order to minimize multipath effects and errors in the mapping functions because, at such elevation, the ray bending effect is negligible. The first-order ionospheric delay is removed by forming the "ionosphere-free" combination of the L1 and L2 phases. After estimating station coordinates and atmospheric parameters from the modeling of the double-differenced phase, GAMIT can produce residuals for the undifferenced phases by estimating clock corrections that the double-difference observations cancel (Alber, et al., 2000). Although the undifferenced post-fit phase residuals and SWD are suitable for atmospheric tomography, we chose to use only the SWD data in order to have a more reliable and stable estimation of the atmospheric effect to EM signal.

Moderate Resolution Imaging Spectroradiometer Data and Integration

The MODIS (Moderate Resolution Imaging Spectroradiometer) instruments operate on board the Aqua and Terra satellites. The sensors collect data in 36 spectral bands within the range 0.4–14.4 μm and at different spatial resolutions (2 bands at 250 m, 5 bands at 500 m and 29 bands at 1 km). The satellites are operated by NASA (https://modis.gsfc.nasa.gov/) and cover the entire Earth every 1–2 days; in particular, the Mt. Etna area is covered two times per day, so these data are particularly suitable for the aim of this study. NASA web services disseminate MODIS data at different levels of processing as well as derived products for land, ocean, and atmospheric applications. The MODIS has the appropriate absorption bands to retrieve water vapor content in the atmospheric column (Spinetti 2004 and Buongiorno, 2007). Here, we use the IPWV (integrated precipitable water vapor) product of the multispectral EO data series that is stored and delivered at 5 km pixel resolution. **Figure 3** shows one of MODIS IPWV related to a night passage of the Aqua satellite for the day August 22, 2015.

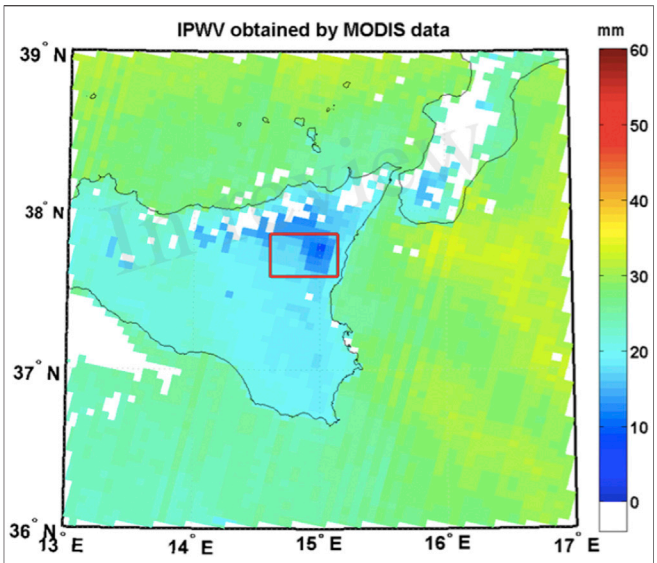

FIGURE 3 | IPWV map acquired by the MODIS on August 22, 2015 at 01:10 UTC. The red box indicates the area defined to perform the comparison between MODIS and GPS IPWV. White pixels correspond to no data (clouds).

In order to add these IPWV as observable in our tomographic model of Mt. Etna (**Figure 1A**), we must first verify that they are consistent with the IPWV values estimated from the processing of our GPS data. The ZWD is directly proportional to Precipitable Water Vapor by a factor calculated during GPS processing (Bevis et al., 1994). The comparison has been performed for the entire year 2015 considering GPS and MODIS-retrieved water vapor data at the same time as satellites pass. In particular, 612 Terra and Aqua satellite acquisitions (both diurnal and nocturnal) were employed in the comparison, and 33 stations of the overall network were considered for GPS measurements.

The comparison was made by averaging the measurements within a considered common area (box in **Figure 3**). The averages result from all the pixels falling in the box for MODIS data and from all acquisitions by the GPS stations within the same box. **Figure 4** shows the comparison results. MODIS data overestimate the GPS ones by ~7%, and the resulting Pearson correlation is equal to 0.91. Considering these differences, it can be stated that the IPWV measurements derived by MODIS data are usable as input for the tomographic model. Finally, it is worth to note that only the clear sky condition enables obtaining reliable IPWV measurements.

We used the daily IPWV data from the MODIS as input for model of **Eq. 6** together with SWD from GPS measurements gathered every epoch throughout the day. The SWD was retrieved every 2 h, and we considered the values interpolated by spline. In

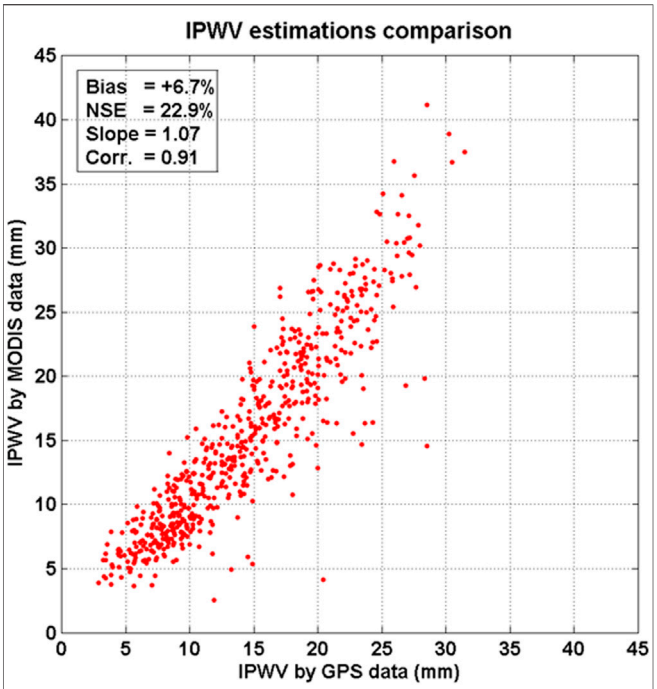

FIGURE 4 | Scatterplot of IPWV comparison between MODIS and GPS of one year of data (2015).

particular, we considered the mean value of the interpolated SWD in the range ±15 min around the considered time of MODIS acquisition.

Sentinel-1A DInSAR Image

We performed a DInSAR analysis of C-band Sentinel-1-A data referring to selected images acquired between 18 May and November 26, 2015. These data are acquired from the Sentinel-1A satellite operating under the Copernicus program of the European Space Agency (ESA) available from https://scihub.copernicus.eu/dhus/. The processed images were acquired in TopSAR (Terrain Observation with Progressive Scans SAR) Interferometric Wide (IW) mode (VV polarization; vertical transmit and receive polarization), along the descending orbit.

The Sentinel-1A data were processed by GAMMA software (Wegmüller et al., 2015), using a spectral diversity method, and a procedure able to co-register the image pairs with extremely high precision (<0.01 pixel). The interferograms were produced by applying a two-pass DInSAR processing and multi-looking pixels (5 × 1 in range and in azimuth) in order to maintain the full ground resolution (11 × 13 m). The topographic phase was removed from the interferograms by using the SRTM V4 digital elevation model (DEM) generated by Shuttle Radar Topography Mission (SRTM) with three arc-second ground resolution (about 90 m) (Jarvis et al., 2008).

RESULTS AND DISCUSSION

The results are divided into two parts. The first subsection concerns the synthetic tests aimed at evaluating if the problem formulation is correct and if the implemented code is suitable to map the refractivity field. In the second subsection, results of selected test cases of 2015 are reported and discussed. Following the results obtained in Aranzulla and Puglisi (2015), the tomographies are computed by using a tomography volume of $54 \times 54 \times 10\ km^3$, equally spaced in $7 \times 7 \times 5$ voxels centered on the summit craters of Mt. Etna. The tomographic volume setup is shown in **Figure 5**. We set the lower layer at 1,000 m, rather than 2,000 m as in Aranzulla and Puglisi (2015), in order to maximize the benefit of the use of MODIS data for improving the information about the lowermost layer of the atmosphere (i.e., that with the highest expected water vapor content). We kept the same order of the tomographic matrix used in Aranzulla and Puglisi (2015) ($7 \times 7 \times 5$ voxels) because it has proven to be suitable for studying the atmosphere over Mt. Etna with a GPS network composed by 30–40 stations.

The Synthetic Test

For applying the method described in *The Tomography Algorithm*, we first need to compute the test's tomography and evaluate the quality of the results. The test has been carried out by using GPS data only, by following the same approach adopted to test a previous tomographic tool implemented by Aranzulla and Puglisi (2015). Because water vapor circulates in the form of bubbles or masses in the atmosphere, we assumed a bubble anomaly structure (i.e., a discretized volume having a shape similar to a bubble), in which the wet refractivity varies by 25% from the surrounding space, with respect to the maximum allowed range (peak to peak value) of the modified layer. Starting from the position of satellites, GPS receivers and the refractivity field containing the "anomaly" ($N_{perturbed}$), for the *i-th* ray, we computed the theoretical slant wet delay ($SWD_{perturbed}$) by using **Eq. 5** and then, to simulate actual data, adding the noise according to the following equation:

$$\mathrm{SWD_{noisy}} = \mathrm{SWD_{perturbed}} + \mathrm{noise}\ (\%, n\sigma) \qquad (9)$$

We added a normally distributed random noise of *10%* within 2σ, that is, about twice the typical GAMIT SWD error magnitude. The SWD_{noisy} represents the perturbed and noised slant wet delay value of the *ith* ray inside the tomography volume. Coming from $N_{perturbed}$, SWD_{noisy} contains the effect of the set perturbation.

Figure 6 shows the tomography results of the bubble structure synthetic test obtained, assuming the GPS array geometry of October 8, 2014 (28 operational stations). By adopting the approach described in Aranzulla and Puglisi (2015), the damping factor value is 18,400, and the spread function (SF) threshold above which the results are valid is 0.8. **Figure 6A** shows the values of the wet refractivity field (tomography) for all the voxels, while **Figure 6B** shows the matrices of the assumed perturbation model (bubble) and the tomographic results. **Figure 6** allows comparing the tests performed in a synoptic way. The result of the tomography is consistent with the assumed model, that is, the tomography reveals the right perturbations in the right place. The expected (modeled) and estimated (tomographic) values of the refractivity are coincident at the layers 1,000, 5,000, and 7,000 m. Robust conclusions cannot be drawn at the highest and lowest layers. Indeed, at the layer 1,000 m, only one result is acceptable within the fixed

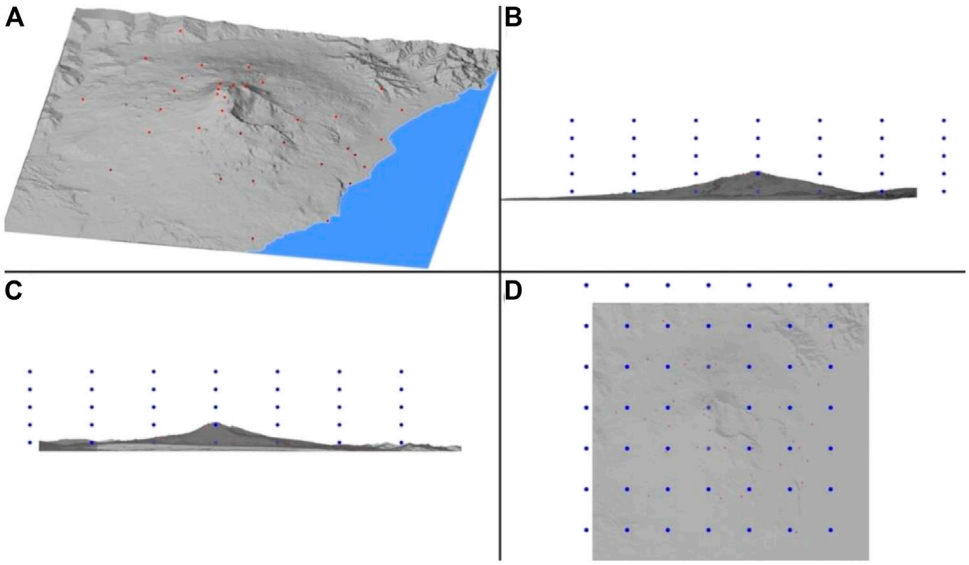

FIGURE 5 | 3D Tomographic model 3-D setup; the volume size of 54 × 54 × 10 km is equally spaced in 7 × 7 × 5 voxels centered on Mt. Etna's summit craters: **(A)** whole volcano (red dots represent GPS stations); **(B)** layers on the eastern flank; **(C)** layers on the northeastern flank; **(D)** Nadir view. The blue dots represent the voxel centers.

thresholds. The statistical reliability of remaining voxels is too low, even though the results are close to the expected model (blue line in **Figure 6A**). At layer 9,000 m, the estimated anomalies are small as expected (because at that elevation, the temperature is extremely low and the troposphere contains almost no water), but too close to the associated uncertainties, thus preventing any statistical assessment at this elevation.

The Actual Tests

The outcomes of the previous section allow us to apply the tomography in real cases of Sentinel-1 interferograms. It is worth noting that for each interferogram, we have to use two tomographies. Five test cases have been selected from the interferograms produced over Mt. Etna by using C-band Sentinel-1A data. Due to the topography of Mt. Etna, the atmospheric artefacts on the interferogram in general have a concentric pattern and high-frequency local perturbation in the north-northeastern flank of the volcano. To select the actual case, we processed all Sentinel-1A available data for 2015 and then identified, by visual inspection criterion, the interferograms with the most evident atmospheric artefacts (**Table 1**). With reference to the flowchart of **Figure 1**, starting from the GAMIT GPS ZWD and gradients output, the GPS receiver and satellite positions, the IPWV MODIS data, and the global numerical weather prediction model computed by the U.S. National Weather Service (NWS), we set the tomography volume and computed the A matrix of **Eq. 6**. **Table 1** shows the selected test cases together with GPS at the time of Sentinel-1A passes, the IPWV MODIS data, and the available GPS receiver data. The tomographies were computed considering only the nocturnal acquisitions of the MODIS, as the closest in time to the Sentinel-1A acquisition time. The cloudy sky of 21 October and 26 November compromised the possibility to measure the water vapor content from MODIS data, excluding cloudy areas as observables. This is why the damping factor γ of **Eq. 7** is different for those two cases (see **Table 1**). As previously mentioned, the SF and γ thresholds govern the selection of the representative voxels. The last column of **Table 1** represents the percentage of the resolved voxels where the 21 October and 26 November cases show the effect of the lack of MODIS data clearly. **Figure 7** shows the tomography results of the actual test cases with the corresponding parameters in **Table 1**, where it is evident that the number of resolved voxels, and hence the covered area, is greater for 17 July and 22 August. The availability of the retrieved MODIS data also allows computing the voxel refractivities of the western flank of the volcano, especially in the lower layers where the highest contribution of water vapor is expected.

The number of resolved voxels is statistically greater with the introduction of MODIS data (18 May, 17 July and 22 August) as shown in **Table 1**, which demonstrates how the addition of the MODIS improves the overall resolution of the tomography. Indeed, the average of the total resolved voxels ranges from 37.1% without MODIS data (cloudy weather conditions) to 45% with MODIS data (clear sky weather conditions), with an increase of 7.9%. In particular, in the lowest layer (1,000 m), the resolved voxel percentage increases on average by 10.2%, from 12.2% without MODIS data to 22.4% with MODIS data. This percentage represents an improvement of about 80% in resolving the voxels of the lowest layer (1,000 m) in relation to the use of GPS data only (**Figure 8**).

In order to use the results of tomographies to correct SAR interferograms, it is necessary to calculate the Sentinel-1A line of sight (LOS) delay stored during the whole transition period of the radar signals in the troposphere. To this end, we implemented a specific routine in the tomographic tool, able to compute the LOS delay by **Eq. 5** using the obtained refractivity results. As the LOS cannot be calculated without knowing the refractivity value of all the voxels of the investigated volume, it is important to properly

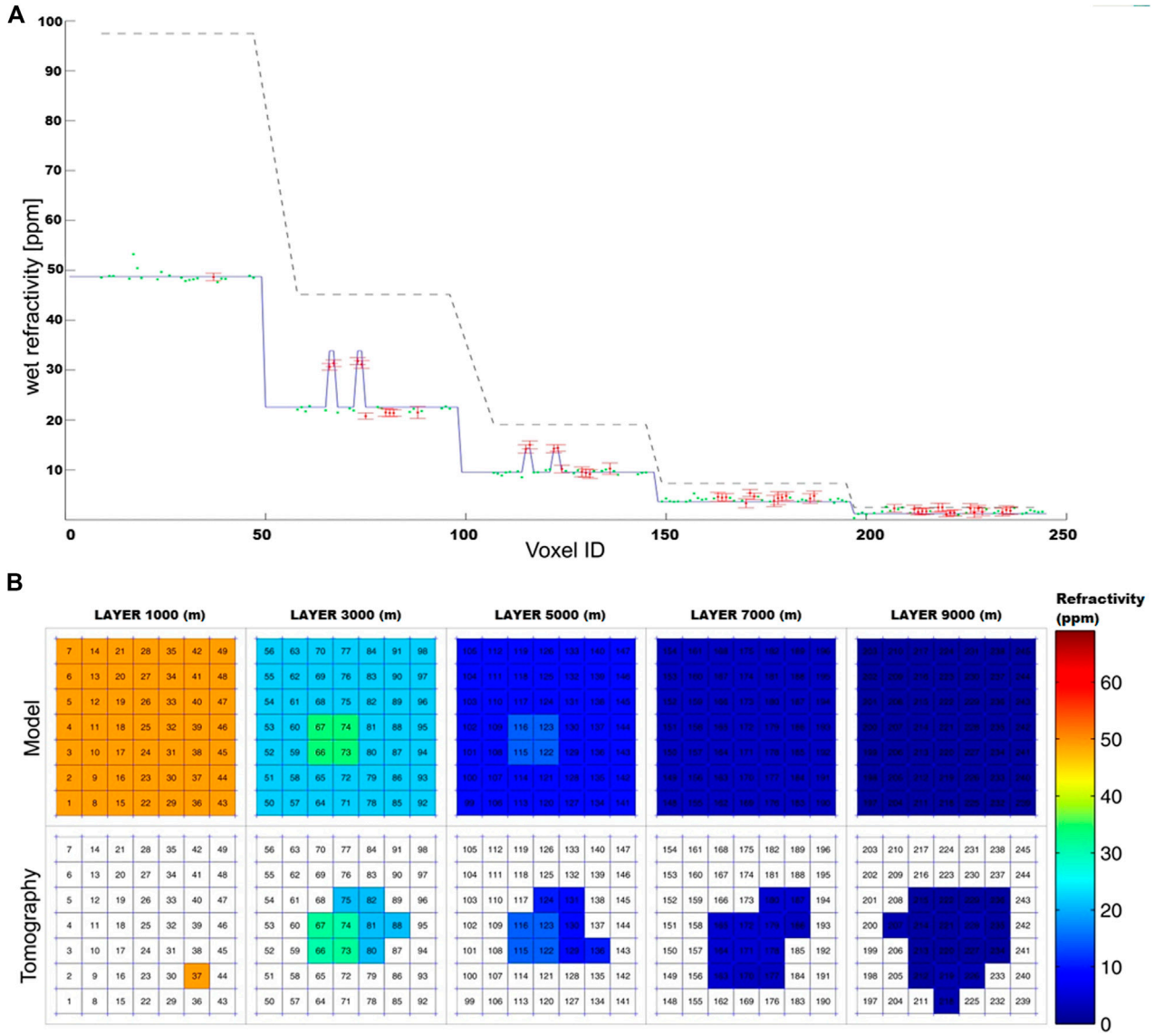

FIGURE 6 | (A) Wet refractivity field vs. voxel, ranked according to the position of the voxel in the matrix **(B)**. Dashed black lines represent the physical constraints for the tomographic solution (saturation at the different elevations). The blue line is the wet refractivity starting model. The green points are the numeric results of all the voxels in which it is possible to calculate a refractivity value. The red points represent the refractivity values of the voxels considered to be acceptable according to the fixed thresholds (damping and SF), that is, the result of the tomography. **(B)** tomography results: the first row refers to the reference model, and the second row is the reconstructed tomography. The voxels are numbered from lower to upper layer and from south to north, in cardinal numbers. The tomography images show only the voxels over the SF threshold, the others are blank. Results are plotted according to the color scale on the right. The considered volume refers to the model shown in **Figure 5**.

set the refractivity values for the unresolved voxels, which were set to the starting values, corresponding to the NCEP grid parameters. **Figure 9** shows the wet delay LOS maps referred to Sentinel-1A descending orbit actual cases, computed by using the tomography results.

Finally, we used those wet delay LOS map results of **Figure 9** to correct the atmospheric effects in the real SAR interferograms. To do so, such results were converted in four simulated interferograms of differential delay (DInDelay) by adopting a differential approach and by using 18 May as the reference date. **Figure 10** shows in the second row the resulting phase of simulated interferograms (DInDelay) together with the corresponding real Sentinel-1A interferograms shown in the first row. In the end, we corrected the phase interferograms by applying the DInDelay to the Sentinel-1A interferograms (third row in **Figure 10**).

Results shown in **Figure 10** allow drawing several observations about the suitability of the proposed tomographic model to correct the DInSAR data and making suggestions for future developments. Besides the differences in the spatial resolution between the Sentinel-1A data and the tomography, due to the intrinsic differences in the pixel sizes in the two datasets, overall, the

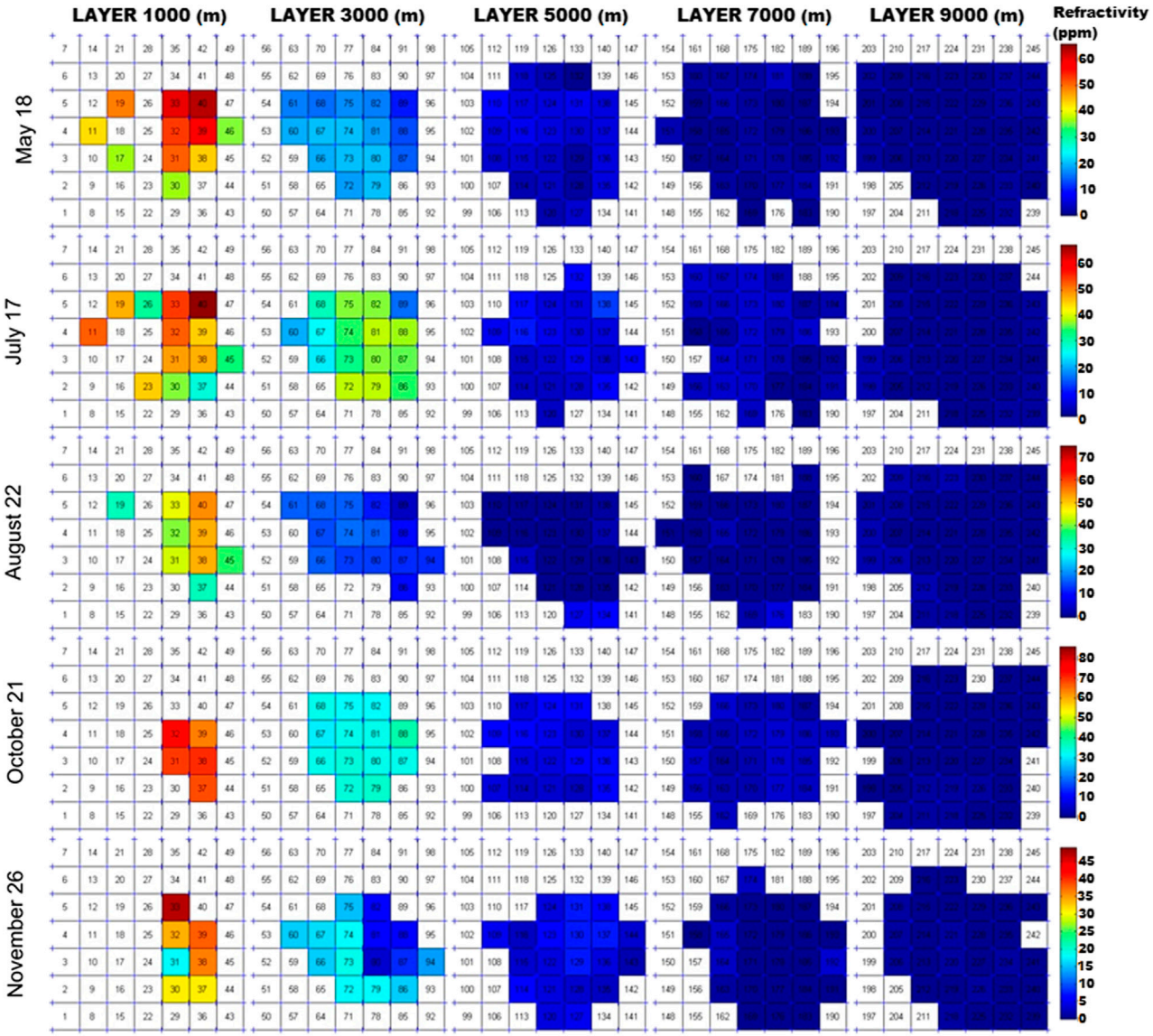

FIGURE 7 | Wet refractivity tomography of the selected actual cases. Each test case has a different color scale in order to appreciate the variations of the individual test case.

TABLE 1 | Selected test cases (UTC hour ranges from 05:04 to 05:06 acquisition time of Sentinel-1A).

Date	MODIS acquisition time (UTC)	MODIS cloud coverage(%)	GPS available stations	Damping factor	Total resolved voxels	Resolved voxels layer 1,000 m
May 18, 2015 (reference)	01:10	0	23	3,300	116/245 (47.3%)	11/49 (22.4%)
Jul 17, 2015	01:35	0	29	3,300	112/245 (45.7%)	13/49 (26.5%)
Aug 22, 2015	01:10	0	27	3,300	103/245 (42.0%)	9/49 (18.3%)
Oct 21, 2015	00:35	95	23	5,200	88/245 (35.9%)	5/49 (10.2%)
Nov 26, 2015	01:10	100	26	5,200	94/245 (38.4%)	7/49 (14.2%)

DInDelay shows the same fringes pattern of the SAR interferograms. It confirms that at the first order, the selected SAR interferograms contain significant atmospheric contributions as we supposed.

The corrected interferograms (third row of **Figure 10**) show two notable characteristics. 1) The pattern of the fringes often mimics the boundary of the voxels ("boxiness"); this is particularly evident in the south-eastern (along the coast line),

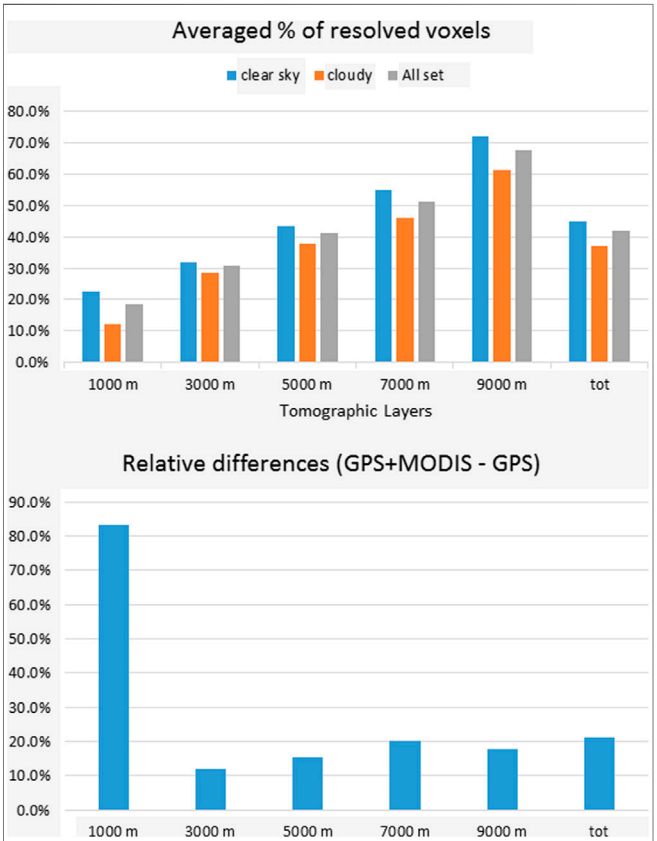

FIGURE 8 | Resolved Voxels Statistics. In the upper histogram, the averaged percentage of the resolved voxels are plotted, for the different layers (1,000 m, 3,000 m, 5,000 m, 7,000 m, and 9,000 m) and the whole set of the tomographies; the "clear sky" values refer to the 18 May, 17 July, and 22 August tomographies; the "cloudy" values refer to the 21 October and 26 November tomographies; "all set" values refer to all tomographies. In the lower histogram, the relative difference between "clear sky" (GPS + MODIS) and "cloudy" (GPS) vs. "cloudy" (GPS) tomographies, for the different layers (1,000 m, 3,000 m, 5,000 m, 7,000 m, and 9,000 m) and the whole set of the tomographies.

western and north-western flanks of the volcano. This effect, which prevents the analysis of subtle "small" features such as local faults, is somewhat expected due to the large dimension of the voxels, and might be overcome in the future by reducing the voxel dimensions. 2) There remains an evident spatial high-frequency perturbation in the right and upper-right part of 18 May–21 October and 18 May–26 November (corresponding to the eastern and northeastern flanks of the volcano). This characteristic indicates that only in these parts of the SAR interferograms are the corrections not appropriate. This was somewhat expected as strong turbulence of the lower atmosphere is often visible in the interferograms of these parts of the volcano. It is worth noting that also MODIS data showed the cloudy weather conditions on those dates (**Table 1**). This characteristic was not captured by the atmospheric tomography probably because the spatial resolution of our tomography is too poor compared to the small scale of this phenomenon. Just as for the "boxiness," the high-frequency perturbation can be properly estimated by the reduction of the voxel dimensions to improve the effectiveness of the tomographic correction.

Besides the high-frequency residuals in the eastern and northeastern flanks of the volcano, the application of the atmospheric correction mostly reduces the number of concentric fringes in the corrected interferograms of 18 May–17 July, 18 May–21 October, and 18 May–26 November. The most successful correction is visible in the images relevant to 18 May–21 October. While the original SAR interferogram shows the highest number of fringes (about three fringes) of deformation at the top of the volcano, the DInDelay mimics the pattern of the experimental fringes well, and the corrected interferograms show values varying by about one fringe, especially in the western and southwestern flanks. Only in the southeastern flank do we observe a voxel-shaped anomaly, likely produced by the poor estimation of the atmospheric anomalies in some voxels due to poor GPS network geometry in this area. Indeed, the same voxel-shaped anomaly is observed in the corrected interferograms of 18 May–17 July and 18 May–26 November. The latter shows a residual in the western flank, indicating an approach of the ground surface to the radar sensor which cannot be associated either to the inflation or to the spreading of the volcano, both phenomena often observed in this flank (Bonforte et al., 2008). Indeed, by independently processing the GPS time series for the same period, with GIPSY 6.4 software (https://gipsy-oasis.jpl.nasa.gov/), we cannot observe any significant deformation consistent with these residuals (**Figure 11**). The maximum deformation in LOS among all the stations is in fact less than 1 cm and is recorded at the ECHR station. Thus, the residuals might be related to turbulent atmosphere that cannot be modeled by the tomography.

It is worth noting that for all actual cases, except for the 18 May–22 August pair, the slope of the Sentinel-1A experimental fringes is consistent with the slope of the fringes of the model. The inconsistency relevant to the 18 May–22 August pair might be due to non-modeled atmosphere conditions or to pitfalls in the tomographic inversion. Indeed, we noticed that it includes the tomography with the highest refractivity at the 3,000 m layer (**Figure 7**) due possibly to inaccurate NCEP parameters on 22 August or to fast changes in the lower atmosphere that the time delay between SAR and the MODIS passes cannot take into account.

CONCLUSION

One of the sources of uncertainty in measuring deformation by using satellite platforms (GPS and SAR) is the effect of the lower atmosphere in the propagation of the EM signals, mainly due to tropospheric water vapor contents. We implemented a new algorithm to perform a 3-D tomography of the wet refractivity by integrating data from GPS, MODIS, and weather models. This algorithm is an improvement on the step forward from a previous tool derived from the seismic tomography (Aranzulla and Puglisi, 2015). The algorithm has been tested and applied to Mt. Etna 2015 test cases. The study shows that by using GPS IPWV alone, the wet

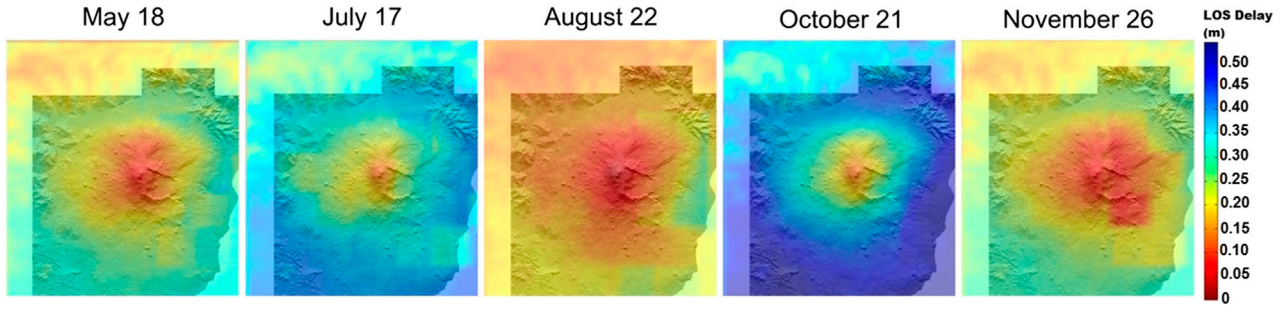

FIGURE 9 | Wet delay line of sight maps referred to the five actual cases selected according to Sentinel-1A descending orbit acquisitions.

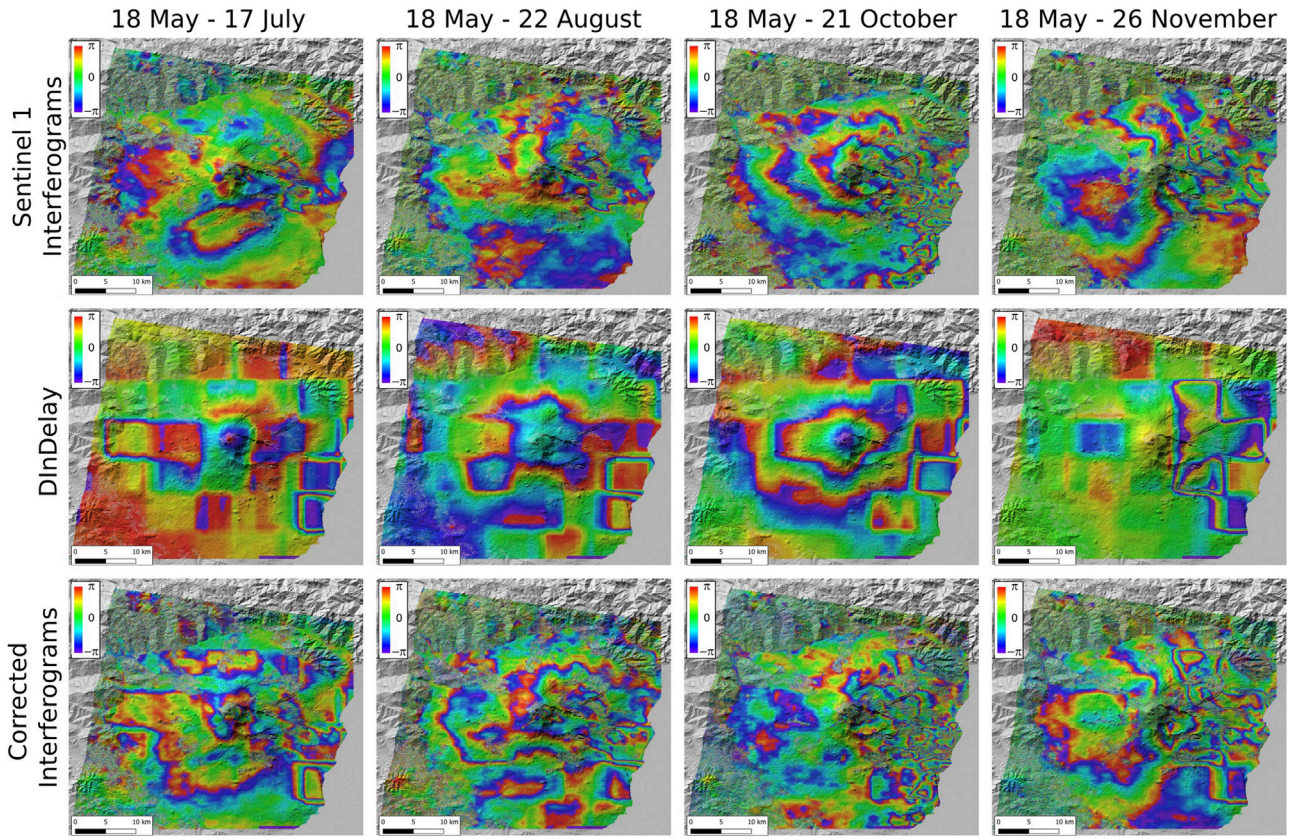

FIGURE 10 | Sentinel-1 interferograms, DInDelay (Differential Interferograms Delay) and Sentinel-1 corrected interferograms. On the first row the DInSAR data are shown, on the second and third rows the corresponding DInDelay and corrected interferograms. All the images are shown in phase ($-\pi$, π; 2π phase corresponds to 28 mm). In the 18 May–26 November interferogram the high-frequency atmospheric perturbation is in the northeastern flank.

refractivity tomography results in about 37% of resolved voxels. Adding MODIS IPWV data increases on average the number of resolved voxels by about 8%. In the lower critical layer (1,000 m), the resolved voxels improve by about 80% in relation to the use of GPS data only. Introducing the GRIB file from NOAA global forecast analysis has allowed us to initialize the tomographic computation with reliable atmospheric conditions and assign the wet refractivity values in the remaining unresolved voxel. One of the main advantages of the availability of a tomographic model of the lower atmosphere is the possibility to estimate the LOS travel time of the SAR signals. To this end, the tomographic tools have been updated with a routine able to compute the LOS delay.

We tested the model by assuming a bubble-shaped anomaly at the lower atmosphere. The simulation shows that the results are consistent with the expected values. Furthermore, the tool has been applied to real Sentinel-1A interferograms during 2015, for which we computed the relevant tomographies, the corresponding wet delays, and the simulated interferograms (DInDelay). The real

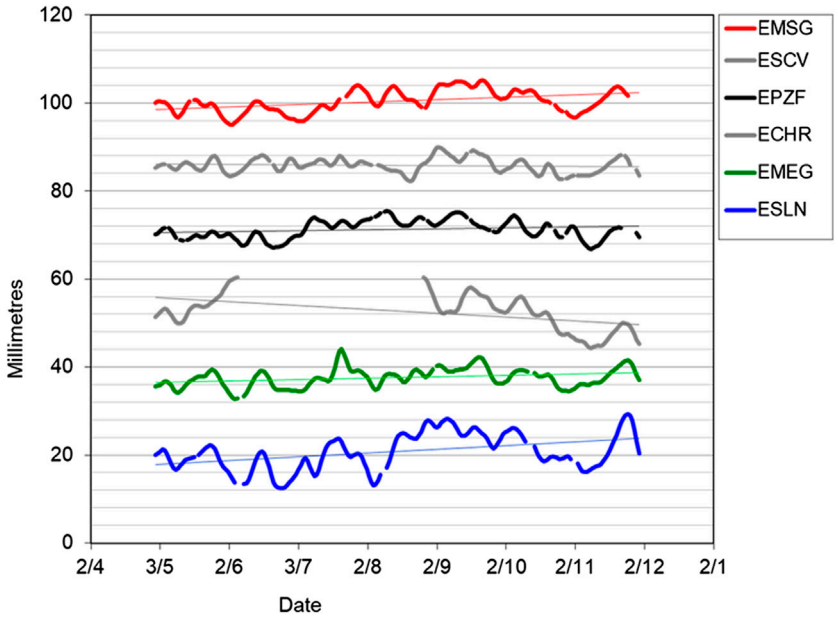

FIGURE 11 | GPS LOS displacement time series of the stations located in the western flank of Mt. Etna and their linear trends. For the distribution of the stations refer to **Figure 2**.

cases show that often, although in limited areas, the tomography is able to capture the atmospheric effect at the large scale and correct the Sentinel-1A interferograms. This work proves that the proposed method can be used to correct atmospheric effects in areas with prominent topography and on interferograms with severe atmospheric artefacts, even in cloudy conditions. Future studies will allow us to overcome the main limit of the method (e.g., reduction of the voxel dimensions) and to improve its effectiveness, also by including other GNSS constellation data.

Further improvements will be suitable for monitoring active volcanoes worldwide where a local GPS network is operating.

DATA AVAILABILITY STATEMENT

The datasets generated for this study are available on request to the corresponding author.

AUTHOR CONTRIBUTIONS

MA, CS, FG, GP, and PB contributed conception and design of the study; MA, FC, and VR developed the tool; MA, CS, FC, VR, and FG performed the analysis; MA and CS wrote the first draft of the manuscript; MA, CS, and VR, wrote sections of the manuscript. All authors contributed to manuscript revision, and read and approved the submitted version.

FUNDING

This study has been carried out in the frame of the EC FP7 Mediterranean Supersite Volcanoes project (ECGA 308665) funded by the European Commission and supported by H2020 EVEREST project funded by the European Commission. Copernicus Sentinel-1 data (2015) are provided by ESA in the framework of GEO-GSNL initiative and available at the Copernicus Open Access Hub (https://scihub.copernicus.eu). The MODIS dataset were acquired by the INGV-ONT real-time KSG multi-mission satellite acquisition system funded by Italian Presidenza del Consiglio dei Ministri – Dipartimento della Protezione Civile (DPC).

ACKNOWLEDGMENTS

We thank S. Conway for his editing precious help and the Reviewers that help us to substantially improve the work.

REFERENCES

Alber, C., Ware, R., Rocken, C., and Braun, J. (2000). Obtaining single path phase delays from GPS double differences. *Geophys. Res. Lett.* 27 (17), 2661–2664. doi:10.1029/2000GL011525

Aranzulla, M., and Puglisi, G. (2015). GPS tomography tests for DInSAR applications on Mt. Etna. *Ann. Geophys.* 58 (3), S0329. doi:10.4401/ag-6750

Balal, Y., and Pinhasi, Y. (2019). Atmospheric effects on millimeter and sub-millimeter (THz) satellite communication paths. *J. Infrared Millim. Terahertz Waves* 40 (2), 219–230. doi:10.1007/s10762-018-0554-7

Beauducel, F., Briole, P., and Froger, J. L. (2000). Volcano wide fringes in ERS SAR interferograms of Etna: deformation or tropospheric eect?. *J. Geophys. Res.* 105, 16391–16402, doi:10.1029/2000JB900095

Benevides, P., Catalao, J., Nico, G., and Miranda, P. M. (2018). 4D wet refractivity estimation in the atmosphere using GNSS tomography initialized by

radiosonde and AIRS measurements: results from a 1-week intensive campaign. *GPS Solut.* 22 (4), 91. doi:10.1007/s10291-018-0755-5

Benevides, P., Catalao, J., Nico, G., and Miranda, P. M. (2015a). Inclusion of high resolution MODIS maps on a 3D tropospheric water vapor GPS tomography model. in remote sensing of clouds and the atmosphere XX. *Inte. Soc. Opt. Photonics* 9640, 96400. doi:10.1117/12.2194857

Benevides, P., Nico, G., Catalão, J., and Miranda, P. M. (2015b). Bridging InSAR and GPS tomography: a new differential geometrical constraint. *IEEE Trans. Geosci. Rem. Sens.* 54 (2), 697–702. doi:10.1109/TGRS.2015.2463263

Benevides, P., Nico, G., Catalão, J., and Miranda, P. M. (2016). Analysis of Galileo and GPS integration for GNSS tomography. *IEEE Trans. Geosci. Rem. Sens.* 55 (4), 1936–1943. doi:10.1109/TGRS.2016.2631449

Bernot, H., Walpersdorf, A., Reverdy, M., van Baelen, J., Ducrocq, V., Champollion, C., et al. (2014). A GPS network for tropospheric tomography in the framework of the Mediterranean hydrometeorological observatory Cévennes-Vivarais (southeastern France). *Atmos. Meas. Tech.* 7, 553–578. doi:10.5194/amt-7-553-2014

Bevis, M., Businger, S., Herring, T. A., Rocken, C., Anthes, R. A., and Ware, R. H. (1992). GPS meteorology: remote sensing of atmospheric water vapor using the global positioning system. *J. Geophys. Res.* 97 (D14), 15787–15801. doi:10.1029/92JD01517.

Bevis, M., Businger, S., Chiswell, S., Herring, T. A., Anthes, R. A., Rocken, C., et al. (1994). GPS meteorology: mapping zenith wet delays onto precipitable water. *J. Appl. Meteorol.* 33 (3), 379–386. doi:10.1175/1520-0450(1994)033<0379:gmmzwd>2.0.co;2

Boehm, J. B., Werland Schuh, H., (2006). Troposphere mapping functions for GPS and very long baseline interferometry from European Centre for Medium-Range Weather Forecasts operational analysis data, *J. Geophys. Res.* 111, B02406. doi:10.1029/2005JB003629

Bonforte, A., Ferretti, A., Prati, C., Puglisi, G., and Rocca, F. (2001). Calibration of atmospheric eects on SAR interferograms by gps and local atmosphere models: rst results. *J. Atmos. Sol. Terr. Phys.* 63, 1343–1357. doi:10.1016/s1364-6826(00)00252-2

Bonforte, A., Bonaccorso, A., Guglielmino, F., Palano, M., and Puglisi, G. (2008). Feeding system and magma storage beneath Mt Etna as revealed by recent inflation/deflation cycles. *J. Geophys. Res.* 113, B05406. doi:10.1029/2007JB005334

Bruno, V., Aloisi, M., Bonforte, A., Immè, J., and Puglisi, G. (2007). Atmospheric anomalies over mt. Etna using GPS signal delays and tomography of radio wave velocities. *Ann. Geophys.* 50 (2), 267–282. doi:10.4401/ag-4417

Champollion, C., Flamant, C., Bock, O., Masson, F., Turner, D., and Weckwerth, T. (2009). Mesoscale GPS tomography applied to the 12 June 2002 convective initiation event of IHOP_2002. *Q. J. R. Meteorol. Soc.* 135 (640), 645–662. doi:10.1002/qj.386

Chen, B., and Liu, Z. (2014). Voxel-optimized regional water vapor tomography and comparison with radiosonde and numerical weather model. *J. Geodes.* 88 (7), 691–703. doi:10.1007/s00190-014-0715-y

Curlander, J. C., and McDonough (1991). *Synthetic aperture radar*: Wiley Interscience. New York, Vol. 11.

Debye, P. (1929). *Polar molecules*. New York: Dover.

Delacourt, C., Briole, P., and Achache, J. (1998). Tropospheric corrections of SAR interferograms with strong topography, application to Etna. *Geophys. Res. Lett.* 25, 2849–2852. doi:10.1029/98gl02112

Essen, L., and Froome, K. D. (1951). The refractive indices and dielectric constants of air and its principal constituents at 24,000 mc/s. *Proc. Phys. Soc. B* 64 (10), 862–875. doi:10.1088/0370-1301/64/10/303

Flores, A., De Arellano, J.-G., Gradinarsky, L. P., and Rius, A. (2001). Tomography of the lower troposphere using a small dense network of GPS receivers. *IEEE Trans. Geosci. Rem. Sens.* 39 (2), 439–447. doi:10.1109/36.905252

Flores, A., Ruffini, G., and Rius, A. (2000). 4D tropospheric tomography using GPS slant wet delays. *Ann. Geophys.* 18 (2), 223–234. doi:10.1007/s00585-000-0223-7

Gradinarsky, L. P., and Jarlemark, P. (2004). Groundbased GPS tomography of water vapor: analysis of simulated and real data. *J. Meteorol. Soc. Jpn.* 82 (1B), 551–560. doi:10.2151/jmsj.2004.551

Healy, S. B. (2011). Refractivity coecients used in the assimilation of GPS radio occultation measurements. *J. Geophys. Res.* 116, 1–10. doi:10.1029/2010JD014013

Herring, T. A., King, R. W., and McClusky, S. C. (2010). *Gamit reference manual, release 10.4.* Cambridge, MA, USA: Massachusetts Institute of Technology.

Heublein, M., Alshawaf, F., Erdnüß, B., Zhu, X. X., and Hinz, S. (2019). Compressive sensing reconstruction of 3D wet refractivity based on GNSS and InSAR observations. *J. Geodes.* 93 (2), 197–217. doi:10.1007/s00190-018-1152-0

Hill, R. J., Lawrence, R. S., and Priestley, J. T. (1982). Theoretical and calculation aspects of the radio refractive index of water vapor. *Radio Sci.* 17 (5), 1251–1257. doi:10.1029/RS017i005p01251

Hirahara, K. (2000). Local gps tropospheric tomography, Earth. *Planets Space* 52 (11), 935–939. doi:10.1186/BF03352308

Hofmann-Wellenhof, B., Lichtenegger, H., and Collins, J. (2001). *Global positioning system: theory and practice*. 5th Edn. Verlag Wien, New York: Springer.

Hopfield, H. S. (1969). Oceans and atmospheres, 4487-4499. Two-quartic tropospheric refractivity profile for correcting satellite data. *J. Geophys. Res.* 74, 18. doi:10.1029/JC074i018p04487

Ichikawa, R., Kasahara, M., Mannoji, N., and Naito, I. (1995). Estimations of atmospheric excess path delay based on three-dimensional numerical prediction model data. *J. Geod. Soc.* 41 (4), 379–408. doi:10.11366/sokuchi1954.41.379

Jarvis, A., Reuter, H. I., Nelson, A., and Guevara, E. (2008). Hole-filled SRTM for the globe version 4, available from the CGIAR-CSI SRTM 90m Database. Available at: http://srtm.csi.cgiar.org. (Accessed January 15, 2016).

Kämpfer, N. (2012). *Monitoring atmospheric water vapor*, New York, NY: Springer Vol. 2012, 326.

Karmakar, P. K. (2017). *Microwave propagation and remote sensing: atmospheric influences with models and applications*. Boca Raton, Florida, United States: CRC Press.

Massonnet, D., Rossi, M., Carmona, C., Adragna, F., Peltzer, G., Feigl, K., et al. (1993). The displacement eld of the landers earthquake mapped by radar interferometry. *Nature* 364, 138–142. doi:10.1038/364138a0

Nilsson, T., and Elgered, G. (2007). Water vapor tomography using GPS phase observations: results from the ESCOMPTE experiment. *Tellus Dyn. Meteorol. Oceanogr.* 59 (5), 674–682. doi:10.1111/j.1600-0870.2007.00247.x

Nilsson, T., Böhm, J., Wijaya, D. D., Tresch, A., Nafisi, V., and Schuh, H. (2013). "Path delays in the neutral atmosphere". in *Atmospheric effects in space geodesy*, Berlin, Heidelberg: Springer 73–136.

Notarpietro, R., Cucca, M., Gabella, M., Venuti, G., and Perona, G. (2011). Tomographic reconstruction of wet and total refractivity fields from GNSS receiver networks. *Adv. Space Res.* 47 (5), 898–912. doi:10.1016/j.asr.2010.12.025

Palano, M., Rossi, M., Cannavò, F., Bruno, V., Aloisi, M., Pellegrino, D., et al. (2010). A geodetic reference frame for mt. Etna GPS networks. *Ann. Geophys. Italy* 53, 49–57. doi:10.4401/ag-4879

Perler, D., Geiger, A., and Hurter, F. (2011). 4D GPS water vapor tomography: new parameterized approaches. *J. Geodes.* 85 (8), 539–550. doi:10.1007/s00190-011-0454-2

Rocken, C., van Hove, T., Johnson, J., Solheim, F., Ware, R., Bevis, M., et al. (1995). GPS/STORM—GPS sensing of atmospheric water vapor for meteorology. *J. Atmos. Ocean. Technol.* 12 (3), 468–478. doi:10.1175/1520-0426(1995)012<0468:gsoawv>2.0.co;2

Rueger, J. M. (2002a). "Refractive index formulae for radio waves," in Proc. XXII FIG international congress American Society for Photogrammetry and Remote Sensing (Kansas, USA: Addison-Wesley Publishing Company Advanced Book Program/World Science Division). Available at: https://www.fig.net/resources/proceedings/fig_proceedings/fig_2002/Js28/JS28_rueger.pdf.

Rueger, J. M. (2002b). Refractive indices of light, infrared and radio waves in the atmosphere, Technical report the university of new south wales, Australia. School of Surveying and Spatial Information Systems, Technical Paper Unisurv S-68.

Saastamoinen, J. (1972a). Introduction to practical computation of astronomical refraction. *Bull. God.* 106, 383–397. doi:10.1007/BF02522047

Saastamoinen, J. (1972b). "Atmospheric correction for the troposphere and stratosphere in radio ranging of satellites," in *The use of artificial satellites for geodesy*. Editors S. W. Henriksen, A. Mancini, and B. H. Chovitz (Wiley: New York), 247–251.

Schmid, R., Rothacher, M., Thaller, D., and Steigenberger, P. (2005). Absolute phase center corrections of satellite and receiver antennas. Impact on GPS

solutions and estimation of azimuthal phase center variations of the satellite antenna. *GPS Solut.* 9, 283–293. doi:10.1007/s10291-005-0134-x

Solheim, F. S., Vivekanandan, J., Ware, R. H., and Rocken, C. (1999). Propagation delays induced in GPS signals by dry air, water vapor, hydrometeors, and other particulates. *J. Geophys. Res.* 104 (D8), 9663–9670. doi:10.1029/1999jd900095

Spinetti, C., and Buongiorno, M. F. (2007). Volcanic Aerosol Optical Characteristics of Mt. Etna Tropospheric Plume Retrieved by Means of Airborne Multispectral Images, *J Atmos. and Solar-Terrestrial Physic*. 69 (9) 981–994.doi:10.1016/j.jastp.2007.03.014

Spinetti, C., and Buongiorno, M. F. (2004). "Volcanic water vapor abundance retrieved by using hypespectral Data," in IEEE International Geoscience and Remote Sensing Symposium, Sept 2004, Anchorage, Alaska, USA, 1487–1490. doi:10.1109/IGARSS.2004.1368702

Tarantola, A. (2005). *Inverse problem theory and methods for model parameter estimation*, Philadelphia, USA: Society of Industrial and Applied Mathematics (SIAM), 342. doi:10.1137/1.978089871792

Thayer, G. D. (1974). An improved equation for the radio refractive index of air. *Radio Sci.* 9 (10), 803–807. doi:10.1029/RS009i010p00803

Toomey, D., and Foulger, G. (1989). Tomographic inversion of local earthquake data from the hengill-grensdalur central volcano complex, Iceland. *J. Geophys. Res.* 94, 497–510. doi:10.1029/jb094ib12p17497

Tregoning, P., Boers, R., O'Brien, D., and Hendy, M. (1998). Accuracy of absolute precipitable water vapor estimates from GPS observations. *J. Geophys. Res. Atmosphere* 103 (D22), 28701–28710. doi:10.1029/98jd02516

Ulaby, F. T., Moore, R. K., and Fung, A. K. (1981). "Volume 1-Microwave remote sensing fundamentals and radiometry active and passive," in *Book microwave remote sensing*.

Wadge, G., Webley, P., James, I. N., Bingley, R., Dodson, A., Waugh, S., et al. (2002). Atmospheric models, GPS and InSAR measurements of the tropospheric water vapor field over mount Etna. *Geophys. Res. Lett.* 29 (19), 11-1–11-4. doi:10.1029/2002gl015159

Webley, P., Wadge, G., and James, I. N. (2004). Determing radio wave delay by non-hydrostatic atmospheric modelling of water vapor over mountains. *Phys. Chem. Earth* 29, 139–148. doi:10.1016/j.pce.2004.01.013

Wegmüller, U., Werner, C., Strozzi, T., Wiesmann, A., Frey, O., and Santoro, M. (2015). "Sentinel-1 support in the GAMMA software," in Proceedings of fringe 2015: advances in the science and applications of SAR interferometry and sentinel-1 InSAR workshop, ESA ESRIN, Frascati, Italy, March 2015 23–27.

Williams, S., Bock, Y., and Fang, P. (1998). Integrated satellite interferometry: tropospheric noise and gps estimates and implications for interferometric synthetic aperture radar products. *J. Geophys. Res.* 103 (B1127), 27051–27067. doi:10.1029/98jb02794

Zebker, H. A., Rosen, P. A., and Henseley, S. (1997). Atmospheric eects in interferometric synthetic aperture radar surface deformation and topographic maps. *J. Geophys. Res.* 102 (B4), 7547–7563. doi:10.1029/96JB03804

Zhao, Q., Yao, Y., Cao, X., and Yao, W. (2019). Accuracy and reliability of tropospheric wet refractivity tomography with GPS, BDS, and GLONASS observations. *Adv. Space Res.* 63 (9), 2836–2847. doi:10.1016/j.asr.2018.01.021

Conflict of Interest: The authors declare that the research was conducted in the absence of any commercial or financial relationships that could be construed as a potential conflict of interest.

Advantages of publishing in Frontiers

OPEN ACCESS
Articles are free to read for greatest visibility and readership

FAST PUBLICATION
Around 90 days from submission to decision

HIGH QUALITY PEER-REVIEW
Rigorous, collaborative, and constructive peer-review

TRANSPARENT PEER-REVIEW
Editors and reviewers acknowledged by name on published articles

Frontiers
Avenue du Tribunal-Fédéral 34
1005 Lausanne | Switzerland

Visit us: www.frontiersin.org
Contact us: frontiersin.org/about/contact

REPRODUCIBILITY OF RESEARCH
Support open data and methods to enhance research reproducibility

DIGITAL PUBLISHING
Articles designed for optimal readership across devices

FOLLOW US
@frontiersin

IMPACT METRICS
Advanced article metrics track visibility across digital media

EXTENSIVE PROMOTION
Marketing and promotion of impactful research

LOOP RESEARCH NETWORK
Our network increases your article's readership